ornl

NUREG/CR-3744
Volume 1
ORNL/TM-9154/V1

OAK RIDGE
NATIONAL
LABORATORY

MARTIN MARIETTA

Heavy-Section Steel Technology Program Semiannual Progress Report for October 1983–March 1984

C. E. Pugh

Prepared for the U.S. Nuclear Regulatory Commission
Office of Nuclear Regulatory Research
Under Interagency Agreements DOE 40-551-75 and 40-552-75

OPERATED BY
MARTIN MARIETTA ENERGY SYSTEMS, INC.
FOR THE UNITED STATES
DEPARTMENT OF ENERGY

Printed in the United States of America. Available from
National Technical Information Service
U.S. Department of Commerce
5285 Port Royal Road, Springfield, Virginia 22161

Available from

GPO Sales Program
Division of Technical Information and Document Control
U.S. Nuclear Regulatory Commission
Washington, D.C. 20555

NUREG/CR-3744
Volume 1
ORNL/TM-9154/V1
Dist. Category RF

Engineering Technology Division

HEAVY-SECTION STEEL TECHNOLOGY PROGRAM SEMIANNUAL PROGRESS REPORT FOR OCTOBER 1983–MARCH 1984

C. E. Pugh

Manuscript Completed – May 14, 1984
Date Published – June 1984

Prepared for the
U.S. Nuclear Regulatory Commission
Office of Nuclear Regulatory Research
under Interagency Agreements DOE 40-551-75 and 40-552-75

NRC FIN No. B0119

Prepared by the
OAK RIDGE NATIONAL LABORATORY
Oak Ridge, Tennessee 37831
operated by
MARTIN MARIETTA ENERGY SYSTEMS, INC.
for the
U.S. DEPARTMENT OF ENERGY
under Contract No. DE-AC05-840R21400

* *

NOTICE

This current report is the first Heavy-Section Steel Technology Program Progress Report that will be issued on a semiannual basis. Prior to FY 1984, the reports were issued on a quarterly basis.

* *

CONTENTS

	Page
LIST OF FIGURES	vii
LIST OF TABLES	xiii
PREFACE	xvii
SUMMARY	xix
ABSTRACT	1
1. PROGRAM MANAGEMENT	2
References	3
2. FRACTURE METHODOLOGY AND ANALYSIS	5
2.1 Comparison of Sharp Crack and Blunt Crack Finite-Element Analyses of an ITV Subjected to Pressurized Thermal Shock	5
2.2 Elastic-Ideally-Plastic PTS Analysis for a Deep, Continuous, Internal, Longitudinal Crack in a Cylinder	7
2.3 Investigation of Damping and of the Cleavage-Fibrous Transition in Reactor-Grade Steel	13
2.3.1 Cleavage-fibrous transition studies	13
2.3.1.1 Determination of the temperature for loss of cleavage in A36, A514, and A533B steels	13
2.3.1.2 Fractographic examination of A508 specimens	14
2.3.1.3 Investigations of weld metal	15
2.3.2 Plastic zone studies	17
2.3.3 Dynamic run-arrest calculations	20
References	25
3. MATERIAL CHARACTERIZATION AND PROPERTIES	27
4. ENVIRONMENTALLY ASSISTED CRACK-GROWTH TECHNOLOGY	28
4.1 Introduction	28
4.2 Fatigue Crack-Growth Results	28
4.3 Static Load Testing	34
4.4 Characterization of Test Environments Through Free Corrosion Potential Measurements	36
4.5 International Cyclic Crack-Growth Rate Group	42
4.5.1 Test methods and results group	43
4.5.2 Mechanisms group	44
4.5.3 Data collection and evaluation group	44
References	44

		Page
5.	CRACK-ARREST TECHNOLOGY	46
	5.1 Crack-Arrest Studies at ORNL	46
	5.1.1 Preliminary wide-plate test planning	46
	5.1.2 Preliminary wide-plate test analyses	48
	5.2 Crack-Arrest Studies at the University of Maryland	55
	5.2.1 Analyses and experiments in support of wide-plate tests	55
	5.2.2 ASTM round robin on K_{Ia} testing	56
	5.3 Crack-Arrest Studies at BCL	57
	5.3.1 Overcooling experiment support	57
	5.3.2 Low-upper-shelf-energy weld from vessel V-8A	60
	5.3.3 Crack-arrest test refinement	64
	5.3.4 Data base	67
	References	72
6.	IRRADIATION EFFECTS STUDIES	76
	6.1 Third HSST Irradiation Series	76
	6.2 Fourth HSST Irradiation Series	76
	6.3 Irradiation-Induced K_{Ic} Curve Shift	98
	6.4 Irradiated Crack-Arrest Studies	99
	6.5 Irradiated Stainless Steel Cladding	102
	6.5.1 Introduction	102
	6.5.2 Materials	103
	6.5.3 Irradiation history	103
	6.5.4 Results and discussion	103
	6.5.5 Conclusions and recommendations for future work	114
	References	118
7.	CLADDING EVALUATIONS	120
8.	INTERMEDIATE VESSEL TESTS AND ANALYSES	121
9.	THERMAL-SHOCK TECHNOLOGY	122
	9.1 Summary	122
	9.2 Thermal-Shock Experiment TSE-8	122
	9.3 Modifications to OCA-P	126
	9.3.1 Crack arrest on the upper shelf	126
	9.3.2 Consideration of multiple flaw zones	126
	9.3.3 Methods for accelerating the convergence of $P(F\|E)$	129
	9.3.4 Error analysis	130
	9.3.5 Simulation of the flaw depth	132
	9.4 Influence Coefficients for Cladding	133

Page

9.5 Integrated Pressurized-Thermal-Shock Program Studies ... 134

9.5.1 Contribution to P(F|E) of flaws in the circumferential welds and the base material 135
9.5.2 Sensitivity analysis 136
9.5.3 Summary of results for Oconee-I 137

9.6 Thermal-Shock Investigations Related to HDR Reactor Vessel 137

References 140

10. PRESSURIZED-THERMAL-SHOCK TECHNOLOGY 142

10.1 Experimental Planning 142

10.2 PTSE Test Facility and Vessel Preparation 147

10.3 Analysis of PTSE-1 150

10.3.1 PTSE-1A pretest analysis by OCA/USA 150
10.3.2 Crack-depth analyses for the PTSE-1 test series 151

10.4 Results and Analyses of PTSE-1 159

10.4.1 Results of PTSE-1A 159
10.4.2 Test PTSE-1B 161
10.4.3 Test PTSE-1C 166

10.5 Conclusions 171

References 173

CONVERSION FACTORS 175

LIST OF FIGURES

Figure		Page
1.1	Level-2 work breakdown structure for HSST Program	3
2.1	Segment of ITV with outer surface crack analyzed at time t = 199 s in PTS transient PTSE-1A	5
2.2	Cut ring model of cylinder containing continuous longitudinal surface crack	8
2.3	Ideally plastic model of uncracked ligament in cylinder containing internal longitudinal surface crack	9
2.4	(*a*) SEM view of transverse section showing small cavities and carbide cluster in contact with bottom of each cavity; and (*b*) optical microscope view of transverse section showing single cavity and carbide cluster in contact with bottom of cavity	15
2.5	Transverse section views of region below main fracture surface in CVN specimen of A508 steel showing branch of cleavage separation that was bypassed by main fracture surface	16
2.6	Isochromatic fringe patterns in birefringent coating on CT specimen of 7075 aluminum alloy (circles marked on each photograph are of diameter = $2r_y$)	18
2.7	Crack-arrest toughness as function of temperature for TSE and Cooperative Program steels	21
2.8	(*a*) Predicted crack extension vs time behavior for second jump in TSE-5 and (*b*) predicted stress-intensity factor vs time behavior for second jump in TSE-5	22
2.9	Predicted crack extension vs time for fourth jump in TSE-5A	24
2.10	Predicted crack extension vs time for second jump in TSE-6	24
4.1	Fatigue crack-growth results for high sulfur heat CQ2, showing effect of temperature on results at R = 0.7 in simulated PWR environment	30
4.2	Fatigue crack-growth results for specimen CQ2-5 tested at R = 0.2, 288°C in simulated PWR environment	31

Figure		Page
4.3	Effect of frequency on fatigue crack-growth for high sulfur heat CQ2 at R = 0.7, 288°C in simulated PWR environment	32
4.4	Fatigue crack behavior of two low sulfur heats of A533B steel tested at R = 0.2, 288°C in simulated PWR environment	33
4.5	Photograph of electrochemical measurement apparatus	37
4.6	Inside of white box showing separate small pressure vessel for checking out various measurement devices	38
4.7	Close-up of potential measurement devices installed in separate test chamber	39
4.8	Instrumentation for zirconia plug ac impedance studies	41
5.1	Schematic of a pull-plate assembly for a wide-plate test	47
5.2	Through-the-thickness variation of K_I for initial crack-depth ratio $a_o/w = 0.2$	49
5.3	Through-the-thickness variation of K_I for arrested crack-depth ratio $a_f/w = 0.45$	50
5.4	Initiation vs arrest stress-intensity values for crack arrest at a/w = 0.45, and for various initial crack depths	52
5.5	Maximum crack-arrest values vs final crack depth based on load capacity of NBS machine (P = 6000 kips = 26.7 MN) and on average remaining ligament stress equal to 484 MPa (70 ksi)	53
5.6	Crack-arrest toughness values vs arrested crack depth calculated by various empirical equations for far-field stress of 121 MPa and initial $a_o/w = 0.20$	54
5.7	Strain gage outputs recorded as functions of time at locations 12.7 and 25.4 ahead of notch tip, 12.7 mm above crack line, in CT specimen (W = 152 mm)	55
5.8	Crack-arrest toughness of steel from PTSE-1 material	60

Figure		Page
5.9	Results of crack-arrest tests on submerged-arc weld from vessel V-8A	61
5.10	Load-displacement record associated with reloading arrested-cleavage crack	65
5.11	Double-displacement records of reloading specimens that contained arrested cracks	66
5.12	Trace of strain gage response derived from calibration experiment	68
5.13	Maximum strain gage response as a function of gage response	68
5.14	Weibull plots of K_{Ic} obtained using various test techniques	71
5.15	Weibull plot of combined thermal-shock and reinitiation K_{Ic} values	71
6.1	Tensile specimen configurations	80
6.2	Tensile strength of irradiated and unirradiated weld 65W	81
6.3	Tensile strength of irradiated and unirradiated weld 70W	87
6.4	Tensile strength of irradiated and unirradiated weld 71W	87
6.5	Typical J-R curve from ORNL microcomputer testing system	95
6.6	Fracture toughness of irradiated and unirradiated plate 02	95
6.7	Fracture toughness of unirradiated weld 68W	96
6.8	Fracture toughness of irradiated and unirradiated weld 69W	96
6.9	Fracture toughness of unirradiated weld 70W	97
6.10	Fracture toughness of irradiated and unirradiated weld 71W	97
6.11	Macroetched cross section of weldment HSST-73W	100

Figure		Page
6.12	Effect of irradiation on Charpy impact energy of type 308 stainless steel cladding	105
6.13	Fracture surfaces of irradiated type 308 stainless steel cladding Charpy impact specimens	106
6.14	SEMs of fracture surfaces of nonirradiated type 308 stainless steel cladding Charpy impact specimens	107
6.15	Fracture surfaces of irradiated stainless steel cladding Charpy impact specimens (nominally type 309) clearly showing bright, faceted type 309 weld metal pass directly below notch and duller type 308 weld metal comprising rest of specimen	108
6.16	SEM of fracture face of unirradiated Charpy specimen CPL-516 (nominally type 309) tested at −32°C in transition region	109
6.17	Detailed views of type 309 weld metal fracture surface of specimen CPL-516 showing predominantly flat fracture with islands of fibrous tearing	110
6.18	Detailed views of type 308 weld metal fracture surface of specimen CPL-516 showing mixed mode fracture	111
6.19	SEM of fracture surface of unirradiated nominally type 309 Charpy specimen CPL-524 tested at 177°C on upper shelf	112
6.20	Charpy impact energy of unirradiated nominally type 309 cladding divided into low- and high-energy populations based on fraction of type 308 weld metal composing specimen ligament	115
6.21	Charpy impact energy of irradiated nominally type 309 cladding divided into low- and high-energy populations based on fraction of type 308 weld metal composing the specimen ligament	116
6.22	Effect of irradiation on Charpy impact energy of high- and low-energy populations of nominal type 309 cladding specimens	117
9.1	Critical-crack-depth curves for TSE-8 indicating flow path using blunted flaw	124

Figure		Page
9.2	Conceptual schematic of LN_2-spray thermal-shock test facility	125
9.3	Illustration of method of selecting $(K_{Ia})_{max}$	127
9.4	Stress distributions used in superposition technique for including effect of cladding on K_I	134
9.5	P(F|E) vs EFPY for Oconee-I postulated OCAs	138
10.1	K_{Ic} data for PTSE-1 vessel	144
10.2	K_{Ia} data for PTSE-1 vessel	144
10.3	Piecewise linear stress-strain relationship assumed for ADINA-ORVIRT pretest analysis of PTSE-1	145
10.4	Plan for PTSE-1, the evolution of K_I and crack-tip K_{Ic} and K_{Ia} values for ideal experiment	145
10.5	PTSE-1 test vessel geometry	148
10.6	PTSE-1 test vessel after instrumentation was applied	149
10.7	Pressure transients planned for PTSE-1A, -1B, and -1C	151
10.8	Critical-crack-depth loci from the PTSE-1A pretest analysis	152
10.9	K_I vs time and a/w from the PTSE-1A pretest analysis, based on 2-D analysis	153
10.10	a/w vs CMOD for proposed PTSE-1A transient, $55 \leq t \leq 115$ s	155
10.11	a/w vs ΔCMOD for proposed PTSE-1A transient, $55 \leq t \leq 115$ s, offset by CMOD for a/w = 0.08	156
10.12	a/w vs ΔCMOD for PSTE-1B transient, $50 \leq t \leq 130$ s, $h = 6250\ W \cdot m^{-2} \cdot K^{-1}$, offset by CMOD for a/w = 0.08	157
10.13	a/w vs ΔCMOD for PTSE-1C transient, $50 \leq t \leq 130$ s, offset by CMOD for a/w = 0.15	158
10.14	Actual PTSE-1A pressure transient and other test parameters	159
10.15	Results (parameters vs time) of posttest OCA/USA analysis of PTSE-1A	160

Figure		Page
10.16	Results (parameters vs T) of posttest OCA/USA analysis of PTSE-1A	160
10.17	Critical-crack-depth loci from PTSE-1B pretest analysis	163
10.18	K_I and K_{Ic} vs T for a/w = 0.077 from PTSE-1B pretest analysis	164
10.19	Actual PTSE-1B pressure transient and other test parameters	164
10.20	Results (parameters vs time) of the posttest OCA/USA analysis of PTSE-1B	165
10.21	Results (parameters vs T) of posttest OCA/USA analysis of PTSE-1B	165
10.22	Results (critical-crack-depth loci) of posttest OCA/USA analysis of PTSE-1B	166
10.23	ΔCMOD vs axial position along crack front at time of crack initiation in test PTSE-1B	167
10.24	Critical-crack-depth loci from PTSE-1C pretest analysis	168
10.25	Actual PTSE-1C pressure transient and other test parameters	169
10.26	Results (parameters vs time) of the posttest OCA/USA analysis of PTSE-1C	169
10.27	Results (parameters vs T) of posttest OCA/USA analysis of PTSE-1C	170
10.28	Results (critical-crack-depth loci) of posttest OCA/USA analysis of PTSE-1C	170
10.29	Comparison of curves representing small-specimen K_{Ic} and K_{Ia} data with Sect. XI curves and results of PTSE-1 experiment	172

LIST OF TABLES

Table		Page
2.1	Analysis of ITV with outer surface crack at time t = 199 s in test transient PTSE-1A	6
2.2	Conditions for tests with large plastic zones	19
2.3	Measured displacements for specimens tested with large plastic zones	19
2.4	Comparison between predicted and observed crack jumps in ORNL thermal-shock experiments TSE-5, TSE-5A, and TSE-6	23
4.1	Test matrix for study of frequency and temperature effects for high sulfur A533B steel	29
4.2	Status of bolt-loaded specimens in simulated PWR environment	35
4.3	Fatigue crack-growth rate testing to complement static load tests	36
4.4	Impedance results measured on porous zirconia plugs in 0.1 M KCl	40
5.1	Crack-arrest toughness of steel from PTSE-1 material	58
5.2	Samples types	59
5.3	Crack-arrest tests of duplex compact specimens fabricated from piece V8A-D, low-toughness weld	62
5.4	Estimation of crack-arrest load	64
5.5	Classification of data-base contents	69
5.6	Distribution functions for K_{Ic}	72
6.1	Chemical composition of submerged-arc welds for Third HSST Irradiation Series	77
6.2	Tensile properties of unirradiated welds for Third HSST Irradiation Series	78
6.3	Tensile properties of irradiated welds for Third HSST Irradiation Series	79

Table		Page
6.4	Average tensile strength for Third HSST Irradiation Series	80
6.5	Average total elongation for Third HSST Irradiation Series	81
6.6	Charpy property degradation of low-copper welds and plate produced by irradiation to 2.20×10^{23} neutrons/m^2 (288°C)	83
6.7	Chemical composition of plate 02 and submerged-arc welds for Fourth HSST Irradiation Series	84
6.8	Tensile properties of unirradiated welds and plates for Fourth HSST Irradiation Series	85
6.9	Tensile properties of irradiated welds and plates for Fourth HSST Irradiation Series	86
6.10	Average tensile strength for Fourth HSST Irradiation Series	88
6.11	Average total elongation for Fourth HSST Irradiation Series	88
6.12	ORNL transition region test data summary of unirradiated 1TCS specimens	89
6.13	MEA transition region test data summary of unirradiated 1TCS specimens	90
6.14	ORNL upper-shelf J-R curve data summary of unirradiated 1TCS specimens	91
6.15	MEA upper-shelf J-R curve data summary of unirradiated 1TCS specimens	92
6.16	ORNL transition region test data summary of irradiated 1TCS specimens (preliminary data)	93
6.17	ORNL upper-shelf J-R curve data summary of irradiated 1TCS specimens (preliminary data)	94
6.18	Fracture toughness parameters summary for Fourth HSST Irradiation Series	98
6.19	Average chemical compositions of materials for the Fifth HSST Irradiation Series	101

Table		Page
6.20	Mechanical properties of HSST welds 72W and 73W	102
6.21	Tensile properties of stainless steel cladding before and after irradiation	104
6.22	Charpy impact energy of unirradiated nominally type 309 stainless steel cladding	113
6.23	Charpy impact energy of nominally type 309 stainless steel cladding irradiated to 2×10^{23} neutrons/m^2 (E > 1 MeV) at 288°C	114
9.1	TSE-8 test conditions corresponding to Fig. 9.1	123
9.2	Influence of number of simulated crack depths on P(I|E)	132
9.3	Parameters simulated in OCA-P	136
9.4	Effect of including WPS in calculation of P(F|E) at 32 EFPY	139
10.1	Characteristics of PTSE-1 vessel used in OCA/USA pretest analysis	146
10.2	PTSE-0 test conditions	147
10.3	Calculated midplane CMODs for selected crack-depth ratios a/w in test vessel PTSE-1 (internal pressure p = 1 MPa)	153
10.4	Calculated midplane CMOD for selected crack-depth ratios a/w and times t in test transient PTSE-1B (internal pressure p = 0)	154
10.5	Calculated CMODs for crack-depth ratios a/w = 0.08 and 0.30 in two proposed PTSE-1B test transients	155
10.6	Basis for planned transients for PTSE-1A, -1B, and -1C pretest analyses	162

PREFACE

The Heavy-Section Steel Technology (HSST) Program, which is sponsored by the Nuclear Regulatory Commission, is an engineering research activity devoted to extending and developing the technology for assessing the margin of safety against fracture of the thick-walled steel pressure vessels used in light-water-cooled nuclear power reactors. The program is being carried out in close cooperation with the nuclear power industry. This report covers HSST work performed in October 1983–March 1984. The work performed by Oak Ridge National Laboratory (ORNL) and by subcontractors is managed by the Engineering Technology Division. Major tasks at ORNL are carried out by the Engineering Technology Division and the Metals and Ceramics Division. Prior progress reports on this program are ORNL-4176, ORNL-4315, ORNL-4377, ORNL-4463, ORNL-4512, ORNL-4590, ORNL-4653, ORNL-4681, ORNL-4764, ORNL-4816, ORNL-4855, ORNL-4918, ORNL-4971, ORNL/TM-4655 (Vol. II), ORNL/TM-4729 (Vol. II), ORNL/TM-4805 (Vol. II), ORNL/TM-4914 (Vol. II), ORNL/TM-5021 (Vol. II), ORNL/TM-5170, ORNL/NUREG/TM-3, ORNL/NUREG/TM-28, ORNL/NUREG/TM-49, ORNL/NUREG/TM-64, ORNL/NUREG/TM-94, ORNL/NUREG/TM-120, ORNL/NUREG/TM-147, ORNL/NUREG/TM-166, ORNL/NUREG/TM-194, ORNL/NUREG/TM-209, ORNL/NUREG/TM-239, NUREG/CR-0476 (ORNL/NUREG/TM-275), NUREG/CR-0656 (ORNL/NUREG/TM-298), NUREG/CR-0818 (ORNL/NUREG/TM-324), NUREG/CR-0980 (ORNL/NUREG/TM-347), NUREG/CR-1197 (ORNL/NUREG/TM-370), NUREG/CR-1305 (ORNL/NUREG/TM-380), NUREG/CR-1477 (ORNL/NUREG/TM-393), NUREG/CR-1627 (ORNL/NUREG/TM-401), NUREG/CR-1806 (ORNL/NUREG/TM-419), NUREG/CR-1941 (ORNL/NUREG/TM-437), NUREG/CR-2141/Vol. 1 (ORNL/TM-7822), NUREG/CR-2141, Vol. 2 (ORNL/TM-7955), NUREG/CR-2141, Vol. 3 (ORNL/TM-8145), NUREG/CR-2141, Vol. 4 (ORNL/TM-8252), NUREG/CR-2751, Vol. 1 (ORNL/TM-8369/V1), NUREG/CR-2751, Vol. 2 (ORNL/TM-8369/V2), NUREG/CR-2751, Vol. 3 (ORNL/TM-8369/V3), NUREG/CR-2751, Vol. 4 (ORNL/TM-8369/V4), NUREG/CR-3334, Vol. 1 (ORNL/TM-8787/V1), NUREG/CR-3334, Vol. 2 (ORNL/TM-8787/V2), and NUREG/CR-3334, Vol. 3 (ORNL/TM-8787/V3).

SUMMARY

1. PROGRAM MANAGEMENT

The total program tasks were slightly arranged during this period into ten tasks: (1) program management, (2) fracture methodology and analysis, (3) material characterization and properties, (4) environmentally assisted crack-growth studies, (5) crack-arrest technology, (6) irradiation effects studies, (7) stainless steel cladding evaluations, (8) intermediate vessel tests and analyses, (9) thermal-shock technology, and (10) pressurized-thermal-shock technology. Starting with this issue, progress reports will be issued on a semiannual basis, and the chapters will correspond to the ten tasks. A detailed 5-year program plan was completed during this period, and it addresses each of the ten tasks.

The work performed at Oak Ridge National Laboratory (ORNL) and under existing research and development subcontracts is included in this report. During the report period, 23 program briefings, reviews, or presentations were made, and four technical documents were published. The meetings included the Eleventh Nuclear Regulatory Commission (NRC) Water Reactor Safety Research Information Meeting, where this program made four technical contributions.

2. FRACTURE METHODOLOGY AND ANALYSIS

Finite-element analyses were performed of pressurized-thermal-shock loadings to confirm the superposition calculations of the OCA/USA computer program, to ensure agreement between ORNL/IBM and ORNL/CYBER versions of the ORMGEN/ADINA/ORVIRT, and to compare sharp and blunt crack models. Previous closed-form solutions were extended to cover deep, continuous, internal, longitudinal surface cracks subjected to pressure as well as thermal loadings with complete ligament yielding.

At the University of Maryland, testing was begun on three-point-bend specimens of A508 steel to determine the loss-of-cleavage temperature for this material. The presence of carbide clusters in the cavities observed fractographically in regions of fibrous sepa-ation in A508 and A533B steel was confirmed. A topical report was prepared on the two-dimensional dynamic finite-element program SAMCR. Further results were obtained using photoelastic coatings on compact tension specimens regarding the recoverability of nonlinear crack-opening-displacements during crack-arrest testing.

3. MATERIAL CHARACTERIZATION AND PROPERTIES

Development of crack-arrest testing technology continued at ORNL, and scoping tests for the American Society for Testing and Materials (ASTM) round robin were completed at RT_{NDT} + 29°C. Specimens for both

ORNL and University of Maryland round-robin testing were fabricated. A prototype system was developed for performing fatigue crack-growth and J-R testing using the potential drop technique.

4. ENVIRONMENTALLY ASSISTED CRACK-GROWTH TECHNOLOGY

A new matrix of tests has been initiated for a heat of A533B steel with high sulfur to study cyclic crack-growth rates as a function of temperature and loading frequency in the light-water reactor (LWR) environment. Crack growth under sustained loads continued through the use of bolt-loaded specimens. A second test of reference electrodes was initiated as a part of efforts to continuously monitor the environment by measurement of electrochemical potential.

5. CRACK-ARREST TECHNOLOGY

Preliminary plans were made for performing crack-arrest tests of single-edge notch wide-plate specimens under tensile load and transverse temperature gradient. An interagency agreement was established to permit the National Bureau of Standards (NBS), Gaithersburg, to perform these tests in their large tensile machine. Preliminary analyses were performed to assess the range of capability of the NBS test system. The University of Maryland developed sample wide-plate test scenarios and also performed model tests to demonstrate the feasibility of using strain gages to monitor crack behavior in fracture specimens such as the wide plates. In connection with the ASTM round robin, blanks for all three test materials were shipped to participants.

In the Battelle Columbus Laboratories support program, crack-arrest tests were completed on pressurized-thermal-shock test (PTSE-1) material and low-upper-shelf weld material from intermediate vessel ITV-8A. K_{Ia} values for PTSE-1 were slightly above the American Society of Mechanical Engineers (ASME) K_{IR} curve up to a temperature just above the onset of the Charpy upper shelf. The range of test temperatures for V-8A was more limited, but this material also exhibited values close to K_{IR}. The crack-arrest data base was expanded to 344 points. Statistical analyses of toughness vs temperature are presented; they result in simple expressions for the mean and standard deviation for both K_{Ic} and K_{Ia}.

6. IRRADIATION EFFECTS STUDIES

Tensile tests of the four low-upper-shelf weldments used in the Third HSST Irradiation Series were completed, and the property values are summarized for both unirradiated and irradiated conditions. Charpy V-notch (CVN) tests were completed for a Federal Republic of Germany material that was included in the Fourth Irradiation Series. Cooperative testing by Materials Engineering Associates and ORNL continued for the

first three capsules of the fourth series, with tensile testing being completed along with all unirradiated 1TCS tests. Scoping tests of the irradiated 1TCS specimens were initiated. Concerning the Fifth Irradiation Series, two-thirds of the 0.25% copper weldments and one-third of the 0.35% copper weldments were received from the fabricator. Specimens of the high copper weldments are being assembled in the first two capsules (each containing two 4TCS and twelve CVN specimens). Design of the capsules for the 1TCS and 2TCS specimens were nearing completion.

To provide an initial evaluation of the potential degradation of properties for weld-deposited stainless steel cladding, tensile, CVN, and precracked Charpy specimens from a single-wire cladding were irradiated to about 2×10^{23} neutrons/m^2 ($E > 1$ MeV) at 288°C. Tensile and CVN tests were completed, and the data were compared with unirradiated test results.

7. CLADDING EVALUATIONS

The FY 1984 program plan deferred work in this task until data are available on the effects of irradiation on the fracture properties of stainless steel cladding. However, a subcontract is in place with Combustion Engineering to provide three-wire series-arc clad plates for future studies, and delivery is now expected in the second half of FY 1984.

8. INTERMEDIATE VESSEL TESTS AND ANALYSES

During this reporting period, as had been planned, no significant work was done on this task. In the next reporting period, the posttest evaluation and reporting on V-8A will be performed.

9. THERMAL-SHOCK TECHNOLOGY

Preliminary exploratory fracture-mechanics (FM) calculations were conducted for proposed thermal-shock experiment TSE-8, an objective of which is to investigate crack behavior in the upper-transition and upper-shelf temperature regimes. The study suggests that the present liquid-nitrogen test facility and associated experimental technique will not be adequate; however, use of a higher initial temperature (~300°C), a long axial initially blunted flaw, "instantaneous" sharpening of the flaw during the transient, and spray application of liquid nitrogen to induce the thermal shock will result in satisfactory test conditions.

Modifications were made to the deterministic-probabilistic FM computer code, OCA-P, to include crack arrest on the upper shelf, multiple flaw zones, importance sampling, error analysis, and an increase in the number of flaw depths simulated. The latter modification was made after conducting a detailed study to determine the effect of the number and relative values of the flaw depths simulated.

Stress-intensity factor influence coefficients, which had previously been calculated for 6/1 and 1.8-m-long semielliptical inner-surface flaws in the absence of cladding, were calculated for the cladding effect for the same two flaw geometries and were then added to OCA-P and OCA-II.

The probabilistic FM study for the Oconee-I vessel for the Integrated Pressurized-Thermal-Shock (IPTS) Program was completed, and a preliminary feasibility study associated with the possibility of conducting TSEs with the German HDR facility was begun.

10. PRESSURIZED-THERMAL-SHOCK TECHNOLOGY

The first pressurized-thermal-shock test, PTSE-1, of a pressure vessel was performed. The objectives of the test were to investigate (1) the effects of warm prestressing on initiation of propagation of an existing crack and (2) to determine the nature of arrest of a rapidly propagating crack at temperatures on the ductile upper shelf. In PTSE-1 the intended conditions were produced, and a preliminary study of the information collected in the experiment indicates that the desired objectives were attained. Two crack initiations and arrests occurred after a succession of warm prestressing episodes. Preliminary analyses imply that the initiations occurred at stress-intensity factor K_I values of 157 and 221 MPa$\cdot\sqrt{m}$ at temperatures T of 100 and 120°C, respectively. The corresponding arrest values were K_I = 177 and 265 MPa$\cdot\sqrt{m}$ at T = 157 and 168°C, respectively.

In preparation for PTSE-1, final modifications to the test facility were completed; test material characterization tests were performed; a preliminary shakedown test series, PTSE-0, was performed; extensive fracture analyses based on characterization data were performed; and the PTSE-1 vessel was flawed, instrumented, and tested.

HEAVY-SECTION STEEL TECHNOLOGY PROGRAM SEMIANNUAL PROGRESS REPORT FOR OCTOBER 1983–MARCH 1984*

C. E. Pugh

ABSTRACT

The Heavy-Section Steel Technology Program is conducted for the Nuclear Regulatory Commission. The studies relate to all areas of the technology of materials fabricated into thick-section primary-coolant containment systems of light-water-cooled nuclear power reactors. The focus is on the behavior and structural integrity of steel pressure vessels containing cracklike flaws. Starting with FY 1984, the program was reorganized from seven into ten tasks: (1) program management, (2) fracture methodology and analysis, (3) material characterization and properties, (4) environmentally assisted crack-growth studies, (5) crack-arrest technology, (6) irradiation effects studies, (7) cladding evaluations, (8) intermediate vessel tests and analysis, (9) thermal-shock technology, and (10) pressurized-thermal-shock (PTS) technology. PTS analyses were performed to confirm the OCA/USA computer program. Previous closed-form solutions were extended to cover longitudinal, internal, surface cracks subjected to pressure and thermal loadings. A topical report was drafted on the dynamic fracture code SAMCR. A new matrix of cyclic crack-growth rate tests was initiated for a high sulfur heat of A533B steel. Preliminary plans were developed for performing crack arrest tests of wide-plate specimens exposed to tensile loads and a transverse temperature gradient. A subcontract was placed to initiate a study of viscoplastic effects on run-arrest events in specimens such as the wide plates. Test material was sent to participants in the American Society of Testing and Materials round robin on crack arrest. Tensile testing was completed in the Third Irradiation Series. Cooperative testing continued for the Fourth Irradiation Series. Initial specimens (4TCS and CVN) were fabricated from the high copper weldments for the Fifth Irradiation Series. One-wire process stainless steel cladding specimens were irradiated and tested. Preliminary calculations were carried out on a possible TSE-8 to examine crack behavior in the upper-shelf temperature regime. A probabilistic fracture-mechanics study for Oconee-I vessel was completed. The first PTS experiment (PTSE-1) was performed after final facility preparations were made, the vessel was flawed and instrumented, material properties data were evaluated, extensive analyses were performed, and a detailed shakedown test (PTSE-0) was performed.

---

*Conversion from SI to English units for all SI quantities are listed on a foldout page at the end of this report.

1. PROGRAM MANAGEMENT

C. E. Pugh

The Heavy-Section Steel Technology (HSST) Program, a major safety program sponsored by the Nuclear Regulatory Commission (NRC) at the Oak Ridge National Laboratory (ORNL), is concerned with the structural integrity of the primary systems [particularly the reactor pressure vessels (RPVs)] of light-water-cooled nuclear power reactors. The structural integrity of these vessels is ensured by (1) designing and fabricating RPVs according to standards set by the code for nuclear pressure vessels, (2) detecting flaws of significant size that occur during fabrication and in service, and (3) developing methods of producing quantitative estimates of conditions under which fracture could occur. The program is concerned mainly with developing pertinent fracture technology, including knowledge of (1) the material used in these thick-walled vessels, (2) the flaw-growth rate, and (3) the combination of flaw size and load that would cause fracture and thus limit the life and/or the operating conditions of this type of reactor plant.

The program is coordinated with other government agencies and with the manufacturing and utility sectors of the nuclear power industry in the United States and abroad. The overall objective is a quantification of safety assessments for regulatory agencies, for professional code-writing bodies, and for the nuclear power industry. Several activities are conducted under subcontract by research facilities in the United States and through informal cooperative effort on an international basis. Three research and development subcontracts are currently in force, and two additional subcontracts are being finalized at this time.

Effective with the beginning of FY 1984 (October 1, 1983), the program tasks were rearranged according to the work breakdown structure shown in Fig. 1.1. Accordingly, the chapters of this progress report correspond to these ten tasks. During this period, a 5-year program plan[1] was completed and is being used as the reference document for management reporting to the NRC. The plan will be distributed to the NRC-RF category early in the next report period.

NRC granted approval for two foreign technical specialists to be assigned temporarily to the HSST program: Dr. Robert Wanner of the Swiss Federal Institute for Reactor Research for 1 year, and Dr. Hermann Stamm of the Institute für Reaktorbauelemente, Karlsruhe, Federal Republic of Germany for 9 months. Steps to obtain ORNL and Department of Energy approval of these assignments were initiated.

During this quarter, 23 program briefings, reviews, or presentations were made by the HSST staff at technical meetings and at program reviews for the NRC staff or visitors. This includes four contributions[2-5] to the Eleventh NRC Water Reactor Safety Research Information Meeting, which was held October 24–28, 1983. One technical progress report[6] and one topical report[7] were published during the quarter.

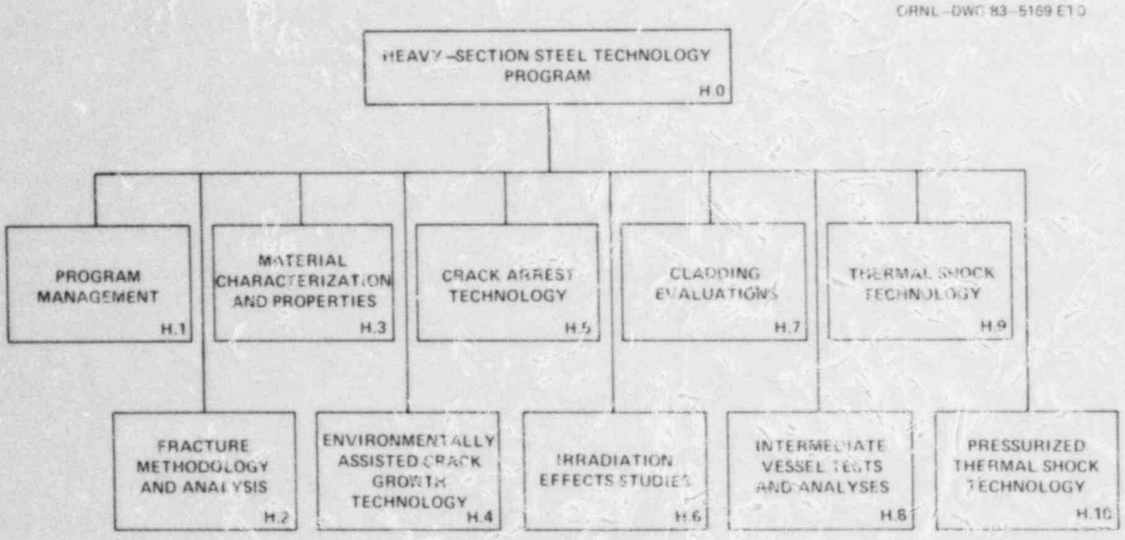

Fig. 1.1. Level-2 work breakdown structure for HSST Program.

References

1. ORNL Staff, *Heavy-Section Steel Technology Five-Year Plan FY 1983–1987*, NUREG/CR-3595 (ORNL/TM-9008), Union Carbide Nuclear Div., Oak Ridge Natl. Lab., Draft, November 30, 1983.

2. J. G. Merkle, "Evaluations of the Irwin Adjustment for Small Specimen Fracture Toughness Data," *Proceedings of Eleventh Water Reactor Safety Research Information Meeting at the NBS, Gaithersburg, Md., October 26 and 27, 1983*, NUREG/CP-0048, Vol. 4, U.S. Nuclear Regulatory Commission (1983).

3. B. R. Bass, "Computational Methods for Fracture Analysis of HSST Pressure Vessel Experiments," *Proceedings of Eleventh Water Reactor Safety Research Information Meeting at the NBS, Gaithersburg, Md., October 26 and 27, 1983*, NUREG/CP-0048, Vol. 4, U.S. Nuclear Regulatory Commission (1983).

4. R. D. Cheverton, D. G. Ball, and S. E. Bolt, "Finite-Flaw Extension Under Thermal Shock: TSE-7 Test and Evaluation," *Proceedings of Eleventh Water Reactor Safety Research Information Meeting at the NBS, Gaithersburg, Md., October 26 and 27, 1983*, NUREG/CP-0048, Vol. 4, U.S. Nuclear Regulatory Commission (1983).

5. R. D. Cheverton, and D. G. Ball, "The ORNL Probabilistic Fracture-Mechanics Code OCA-P," *Proceedings of Eleventh Water Reactor Safety Research Information Meeting at the NBS, Gaithersburg, Md., October 26 and 27, 1983*, NUREG/CP-0048, Vol. 4, U.S. Nuclear Regulatory Commission (1983).

6. C. E. Pugh, *Heavy-Section Steel Technology Program Quart. Prog. Rep. April–June 1983*, NUREG/CR-3334, Vol. 2 (ORNL/TM-8787/V2), Union Carbide Corp. Nuclear Div., Oak Ridge Natl. Lab., December 1983.

7. D. G. Ball et al., *OCA-II, A Code for Calculating the Behavior of 2-D and 3-D Surface Flaws in a Pressure Vessel Subjected to Temperature and Pressure Transients*, NUREG/CR-3491 (ORNL-5934), Union Carbide Nuclear Div., Oak Ridge Natl. Lab., February 1984.

2. FRACTURE METHODOLOGY AND ANALYSIS

2.1 Comparison of Sharp Crack and Blunt Crack Finite-Element Analyses of an ITV Subjected to Pressurized Thermal Shock

B. R. Bass

A cylindrical vessel (ITV) with an outer surface crack subjected to pressurized-thermal-shock (PTS) loading was analyzed with the ORMGEN/ADINA/ORVIRT[1-3] fracture-mechanics (FM) system. This study utilized both linear and nonlinear material models, three different three-dimensional (3-D) finite-element geometries, and the OCA/USA FM program. The objectives of the analysis were three-fold: (1) to compare the response of a sharp crack model with a blunt crack model utilizing linear and nonlinear constitutive relations and different mesh refinement, (2) to confirm the superposition calculations from the OCA/USA computer program, and (3) to ensure agreement between the Oak Ridge IBM version and the CYBER 205 version of the ORMGEN/ADINA/ORVIRT system.

Figure 2.1 depicts a segment of the ITV containing an outer surface crack with a depth ratio of a/w = 0.08, a width of w = 147.6 mm, and an

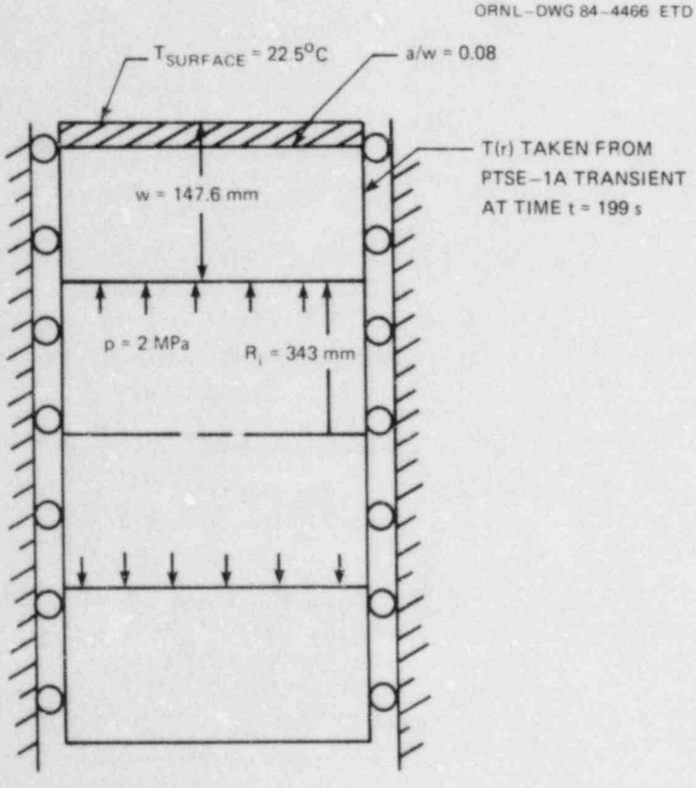

Fig. 2.1. Segment of ITV with outer surface crack analyzed at time t = 199 s in PTS transient PTSE-1A.

inner radius of R_i = 343 mm. The cylinder is subject to plane strain boundary constraints, an internal pressure p = 2 MPa, and a thermal gradient attained at time t = 199 s in PTS test transient PTSE-1A (see Chap. 10 of this report). The cylinder was analyzed with the ORMGEN/ADINA/ORVIRT system using the three different finite-element models summarized in Table 2.1. The sharp crack model utilized quarter-point nodes around the crack tip to introduce a $1/\sqrt{r}$ stress singularity approprite for linear-elastic fracture mechanics. Collapsed prism elements with midside nodes were employed in the blunt crack model for the appropriate 1/r singularity of elastic-plastic material response.[4] Models 1 and 2 utilized 26 nodes between the outer surface and the crack front, while for model 3 the corresponding number of nodes was 14.

The results of the analysis from the 3-D finite-element models are presented in Table 2.1. For the linear thermoelastic material model, results from the sharp crack model 1 and from the blunt crack model 2(a) differ by 2%. Both 3-D calculations differ by <1% from the OCA/USA 2-D superposition calculation of K_I. When the crack-tip region of blunt model 2(b) is allowed to yield, crack-mouth-opening-displacement (CMOD) values are increased by 2.5% and K_I values are reduced by 13%. When

Table 2.1. Analysis of ITV with outer surface crack at time t = 199 s in test transient PTSE-1A[a]

3-D Model			Description	CMOD (mm)	K_I (MPa·$\sqrt{m}$)
No.	Nodes	Elements			
1	1930	318	Sharp crack with linear thermoelastic material model, quarter-point nodes around crack tip	0.2498	151.4[b]
2	1944	318	(a) Blunt crack with linear thermoelastic material model	0.2502	149.0
			(b) Blunt crack with multilinear deformation plasticity material model	0.2564	129.0
3	654	79	(a) Blunt crack with linear thermoelastic material model	0.2446	144.8
			(b) Blunt crack with multilinear deformation plasticity material model	0.2574	126.7

[a] PTSE-1A transient is described in Chap. 10 of this report.

[b] The corresponding result from an OCA/USA 2-D superposition calculation is given by K_I = 150 MPa·$\sqrt{m}$.

model 2 is replaced by the relatively coarse mesh of model 3, the calculated K_I values are reduced by ~3%. This change is due in part to the coarse mesh of model 3 being relatively stiffer than the model 2 mesh.

The set of 3-D calculations in Table 2.1 corresponding to models 1 and 2 were performed on both the CYBER 205 version and the IBM version of ORMGEN/ADINA/ORVIRT and produced results that were identical.

2.2 Elastic-Ideally-Plastic PTS Analysis for a Deep, Continuous, Internal, Longitudinal Crack in a Cylinder

J. G. Merkle

In previous progress reports, closed-form solutions were presented for analyzing (1) the effects of thermal-shock loading under elastic conditions on deep, continuous, internal, longitudinal,[5] and circumferential[6] surface cracks in pressure vessels; and (2) the effects of complete ligament yielding without strain hardening in the case of internal longitudinal cracks.[7] More recently it has become necessary to consider the effects of vessel internal pressure as well as those of thermal-shock loading. Therefore, a previous analysis was developed in support of the design of ITV experiments using internal pressure, external flaws, and external thermal-shock loading.[8] The objective of the analysis to be presented here is to extend the previous analyses to cover deep, continuous, internal, longitudinal surface cracks subjected to pressure as well as thermal loading with complete ligament yielding, but without strain hardening.

Because the crack is assumed to be deep, it is reasonable to adopt the strip-yield model philosophy by assuming that yielding occurs only on the plane ahead of the crack tip. When the ligament is completely yielded, the stress distribution directly ahead of the crack is an ideally plastic stress distribution, and the crack-plane displacements are the elastic ring bending displacements corresponding to the applied loading and the crack-plane tractions.[7]

To calculate the elastically induced displacements of the crack faces, a section of the cylinder is modeled as a cut ring, with one end fixed and the other end free (Fig. 2.2). For $\phi_{max} = 2\pi$ and radially symmetric loading, $X_a = 0$; the total relative displacements of the crack faces are equal to the elastically calculated displacements of the free end, given by

$$\begin{Bmatrix} \theta \\ \Delta_y \end{Bmatrix} = \frac{1}{EI} \begin{bmatrix} 2\pi r & -2\pi r^2 \\ -2\pi r^2 & 3\pi r^3 \end{bmatrix} \begin{Bmatrix} M_a \\ Y_a \end{Bmatrix} , \tag{2.1}$$

where positive displacements and rotations are defined as those occurring in the directions of the positive tractions.

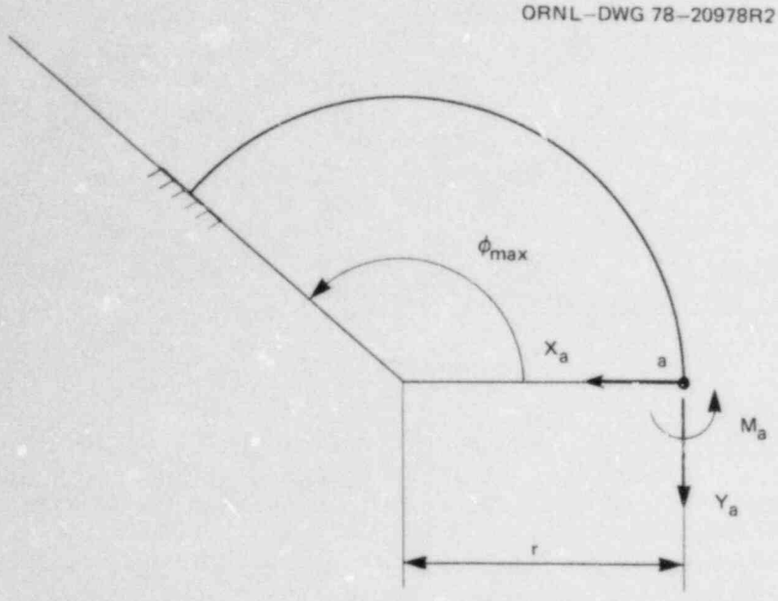

Fig. 2.2. Cut ring model of cylinder containing continuous longitudinal surface crack.

Referring to Fig. 2.3, the moment, causing bending deflections, that acts on the crack plane is given by

$$M_a = -M_B + \sigma_Y \left[-d^2 + dw - \left(\frac{bw}{2} - \frac{b^2}{2} \right) \right] , \tag{2.2}$$

where M_B is the moment of the total stress distribution acting in the uncracked ring taken about the neutral axis of the uncracked ring cross section. The moment M_B can be represented by

$$M_B = \frac{\sigma_B w^2}{6} , \tag{2.3}$$

where σ_B is the linearized inside surface thermal stress. The force, causing bending deflections, that acts on the crack plane is given by

$$Y_a = -\sigma_Y (2d - b) - \sigma_p w , \tag{2.4}$$

where

$$\sigma_p = p \left(\frac{r_i}{w} \right) . \tag{2.5}$$

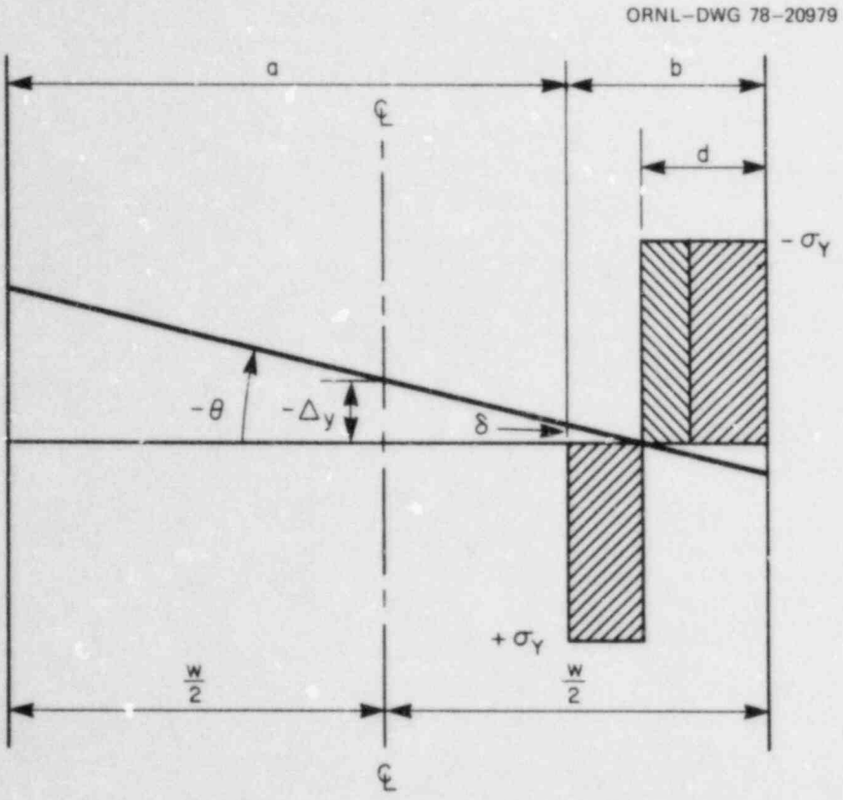

Fig. 2.3. Ideally plastic model of uncracked ligament in cylinder containing internal longitudinal surface crack.

Referring again to Fig. 2.3, the crack-plane displacement-rotation relations are given by

$$+\Delta_y = \theta\left(\frac{W}{2} - d\right) , \tag{2.6}$$

and

$$\delta = -\theta(b - d) . \tag{2.7}$$

Note that the sign convention adopted here results in the crack-tip-opening displacement δ being positive when the crack-opening angle θ is negative for an internal surface crack.

The problem solution is obtained by using Eq. (2.6) to eliminate Δ_y in Eq. (2.1), then eliminating θ, and solving Eq. (2.1) for (d/b). This locates the hinge point, which is the point of stress reversal in the fully yielded remaining ligament. The resulting equation for (d/b) is

$$\left(\frac{b}{w}\right)^2 \left(\frac{d}{b}\right)^3 - C_2\left(\frac{d}{b}\right)^2 + C_1\left(\frac{d}{b}\right) - C_0 = 0 \,, \tag{2.8}$$

where

$$C_0 = \left[1 - \frac{\left(\frac{\sigma_p}{\sigma_Y}\right)}{\left(\frac{b}{w}\right)}\right] \frac{1}{2}\left(\frac{r}{w}\right)\left(3\,\frac{r}{w} + 1\right) + \left(\frac{r}{w} + \frac{1}{2}\right) \times \left[+\frac{1}{6}\,\frac{\left(\frac{\sigma_B}{\sigma_Y}\right)}{\left(\frac{b}{w}\right)} + \frac{1}{2}\left(1 - \frac{b}{w}\right)\right] , \tag{2.9}$$

$$C_1 = 3\left(\frac{r}{w}\right)^2 + \left(2 + \frac{b}{w} - \frac{\sigma_p}{\sigma_Y}\right)\left(\frac{r}{w}\right) + \frac{1}{2} + \frac{1}{6}\left(\frac{\sigma_B}{\sigma_Y}\right) + \frac{1}{2}\left(\frac{b}{w}\right)\left(1 - \frac{b}{w}\right), \tag{2.10}$$

and

$$C_2 = 3\left(\frac{b}{w}\right)\left(\frac{r}{w} + \frac{1}{2}\right) \,. \tag{2.11}$$

For the case of $(d/b) > 0$, corresponding to the hinge point located inside the remaining ligament, Eq. (2.8) can be solved by iteration, using the rearranged form

$$\left(\frac{d}{b}\right) = \frac{C_0 + C_2\left(\frac{d}{b}\right)^2 - \left(\frac{b}{w}\right)^2\left(\frac{d}{b}\right)^3}{C_1} \,. \tag{2.12}$$

The crack-plane moment can be obtained by noting that

$$\left(\frac{d}{w}\right) = \left(\frac{d}{b}\right)\left(\frac{b}{w}\right) , \tag{2.13}$$

and then combining Eqs. (2.2) and (2.3) to read

$$\frac{M_a}{M_B} = -1 - \frac{6}{(\sigma_B/\sigma_Y)} \left[\left(\frac{d}{w}\right)^2 - \left(\frac{d}{w}\right) + \frac{1}{2} \left(\frac{b}{w}\right) \left(1 - \frac{b}{w}\right) \right] . \qquad (2.14)$$

The crack-plane bend angle and centerline vertical displacement are given by

$$\frac{\theta}{2\pi\varepsilon_Y} = 2 \left(\frac{r}{w}\right) \left(\frac{\sigma_B}{\sigma_Y}\right) \left(\frac{M_a}{M_B}\right) + 12 \left(\frac{r}{w}\right)^2 \times \left[- \left(\frac{b}{w}\right) + 2 \left(\frac{d}{w}\right) + \left(\frac{\sigma_p}{\sigma_Y}\right) \right] , \qquad (2.15)$$

and

$$\frac{-\Delta_y}{2\pi\varepsilon_Y r} = 2 \left(\frac{r}{w}\right) \left(\frac{\sigma_B}{\sigma_Y}\right) \left(\frac{M_a}{M_B}\right) + 18 \left(\frac{r}{w}\right)^2 \times \left[- \left(\frac{b}{w}\right) + 2 \left(\frac{d}{w}\right) + \left(\frac{\sigma_p}{\sigma_Y}\right) \right] . \qquad (2.16)$$

Finally, the crack-tip opening displacement (COD) is calculated by rearranging Eq. (2.7) to read

$$\delta = -\theta w \left(\frac{b}{w}\right) \left(1 - \frac{d}{b}\right) . \qquad (2.17)$$

Referring to Fig. 2.3 when the distance d is reduced to zero, the remaining ligament becomes completely yielded in tension, although a strain gradient still exists in the ligament. For this condition, Eq. (2.8) reduces to

$$C_0 = 0 . \qquad (2.18)$$

Consequently, using Eq. (2.9), the ligament size for a given loading at which the ligament becomes completely yielded in tension is given by the

solution to the quadratic equation,

$$\left(\frac{b}{w}\right)^2 - \left(\frac{b}{w}\right)\left[\frac{\left(\frac{r}{w}\right)\left(3\,\frac{r}{w}+1\right)}{\left(\frac{r}{w}+\frac{1}{2}\right)}+1\right] - \left[\frac{1}{3}\left(\frac{\sigma_B}{\sigma_Y}\right) - \left(\frac{\sigma_p}{\sigma_Y}\right)\frac{\left(\frac{r}{w}\right)\left(3\,\frac{r}{w}+1\right)}{\left(\frac{r}{w}+\frac{1}{2}\right)}\right] = 0 \,. \quad (2.19)$$

Also by rearranging Eq. (2.19), the pressure at the onset of complete tensile yielding in the remaining ligament for a given ligament size and thermal loading is

$$\frac{\sigma_p}{\sigma_Y} = \frac{b}{w} + \frac{\left(\frac{r}{w}+\frac{1}{2}\right)}{\left(\frac{r}{w}\right)\left(3\,\frac{r}{w}+1\right)}\left[\left(\frac{b}{w}\right) - \left(\frac{b}{w}\right)^2 + \frac{1}{3}\left(\frac{\sigma_B}{\sigma_Y}\right)\right]. \quad (2.20)$$

For the case of $(d/b) = 0$, the crack-plane moment, bend angle, centerline vertical displacement, and the COD can all be obtained from Eqs. (2.14)—(2.17) by setting $(d/b) = 0$.

For the case of the remaining ligament fully yielded in tension with the hinge point located outside the ligament, the stress distribution in the ligament is independent of the hinge point location, being the same as for $d = 0$. Therefore, using Eq. (2.14), the crack-plane bending moment is given by

$$\frac{M_a}{M_B} = \frac{-3\left(\frac{b}{w}\right)\left(1-\frac{b}{w}\right)}{\left(\frac{\sigma_B}{\sigma_Y}\right)} - 1 \,. \quad (2.21)$$

The crack-plane bend angle and vertical centerline displacement are given by

$$\frac{\theta}{2\pi\epsilon_Y} = 2\left(\frac{r}{w}\right)\left(\frac{\sigma_B}{\sigma_Y}\right)\left(\frac{M_a}{M_B}\right) + 12\left(\frac{r}{w}\right)^2\left(\frac{\sigma_p}{\sigma_Y} - \frac{b}{w}\right), \quad (2.22)$$

and

$$\frac{-\Delta_y}{2\pi\varepsilon_Y r} = 2\left(\frac{r}{w}\right)\left(\frac{\sigma_B}{\sigma_Y}\right)\left(\frac{M_a}{M_B}\right) + 18\left(\frac{r}{w}\right)^2\left(\frac{\sigma_p}{\sigma_Y} - \frac{b}{w}\right) . \tag{2.23}$$

Finally, using Fig 2.3, the COD is given by

$$\delta = -\Delta_y + \theta w\left(\frac{1}{2} - \frac{b}{w}\right) . \tag{2.24}$$

For purposes of comparison with elastic analysis, the calculated CODs can be expressed in terms of equivalent stress-intensity factors by using the conversions

$$J = \sigma_Y \delta , \tag{2.25}$$

and

$$K_J = \sqrt{EJ} . \tag{2.26}$$

2.3 Investigation of Damping and of the Cleavage-Fibrous Transition in Reactor-Grade Steel*

W. L. Fourney† R. J. Sanford†
G. R. Irwin† C. W. Schwartz†
R. Chona† X-J. Zhang†

2.3.1 Cleavage-fibrous transition studies

2.3.1.1 Determination of the temperature for loss of cleavage in A36, A514, and A533B steels. Two techniques are being used to determine the temperature elevation necessary for loss of dominant cleavage fracturing. One method employs fractographic examination of the fracture surfaces of standard Charpy V-Notch (CVN) impact specimens, whereas the other uses larger (25- to 50-mm-thick) side-grooved specimens, in which the initial fibrous crack extension from a fatigue precrack is converted to rapid cleavage by using a spring plate in series with the load train of a stiff testing machine. The steels examined have A36, A514, and A533B designations.

---

*Work sponsored by HSST Program under UCC-ND Subcontract 7778 between UCC-ND and the University of Maryland.

†Department of Mechanical Engineering, University of Maryland, College Park.

No significant differences have been found in the loss-of-cleavage temperature determined from the two methods except in the case of the air-cooled A36 bridge steel for which the required temperature concluded from the CVN data was somewhat higher.

Comparisons of the same kind are in progress using 61-mm-thick three-point-bend specimens of A508 steel, tempered at 613°C to provide properties similar to the cylinders used for ORNL tests TSE-6 and -7. CVN impact test results were used to estimate the value of RT_{NDT} as 46°C. During fatigue precracking of the large bend specimens, rapid crack propagation occurred as the crack exited the chevron in the first two specimens prepared. For the first of the two specimens, the one-second K_{Ic} estimate was in the range of 80 to 90 MPa$\cdot\sqrt{m}$, and the crack did not arrest in the specimen. In the second specimen, the one-second K_{Ic} value was 59 MPa$\cdot\sqrt{m}$, and the crack arrested at an a/w of 0.7. Results from this test can therefore be usefully employed. Additional A508 material has been received from ORNL and a complete series of tests will be made during the next reporting period.

2.3.1.2 Fractographic examination of A508 specimens. It was previously suggested[9] that carbide clusters were associated with the small cavities typically seen in regions of fibrous (hole-joining) separations in A508 and A533B steels. This feature is of potential importance in understanding the fracture transition behavior in these steels. Although it is difficult to prepare an accurate transverse section through a small cavity (typically 3 to 6 μm in size), partial success has been achieved. Figure 2.4(*a*) shows a scanning electron microscope (SEM) section view in which two cavities are reasonably clear. In each case, a carbide cluster is in contact with the bottom of the cavity. Figure 2.4(*b*) shows an optical microscope view in which a single cavity can clearly be seen. A thin coating of chromium was applied by evaporation to the fracture surface prior to nickel plating and sectioning. Once again, a carbide cluster is in contact with the bottom of the cavity. Investigations of the relationship between voids and carbides are continuing.

A CVN specimen of A508 steel was broken at a relatively low temperature (−40°C) for comparison purposes. Fractographic examinations clearly showed the tendency of connections between non-coplanar cleavage elements to separate in a tearing or fibrous manner. Figure 2.5 shows transverse section views of a 1.5-mm branch of cleavage separation that was bypassed by the main fracture surface. The branch cracks have been highlighted by arrows in the figure. During initial examinations of this section, the collection of debris in the branch crack opening was objectionable, and efforts were made to eliminate this by nickel plating and additional polishing. The resulting deposition of nickel into the crack openings can be seen in Fig. 2.5.

The final opening of the branch crack decreases steadily with distance from the main fracture surface. It is obvious from the tip-region crack openings that cleavage cracking involves negligible plastic strain. The increase of the crack opening at smaller distances from the main crack can be ascribed to plastic strains at branch crack connections that developed during deformation and fracture of late-breaking connections on the main fracture surface.

ORNL PHOTO 2171-84

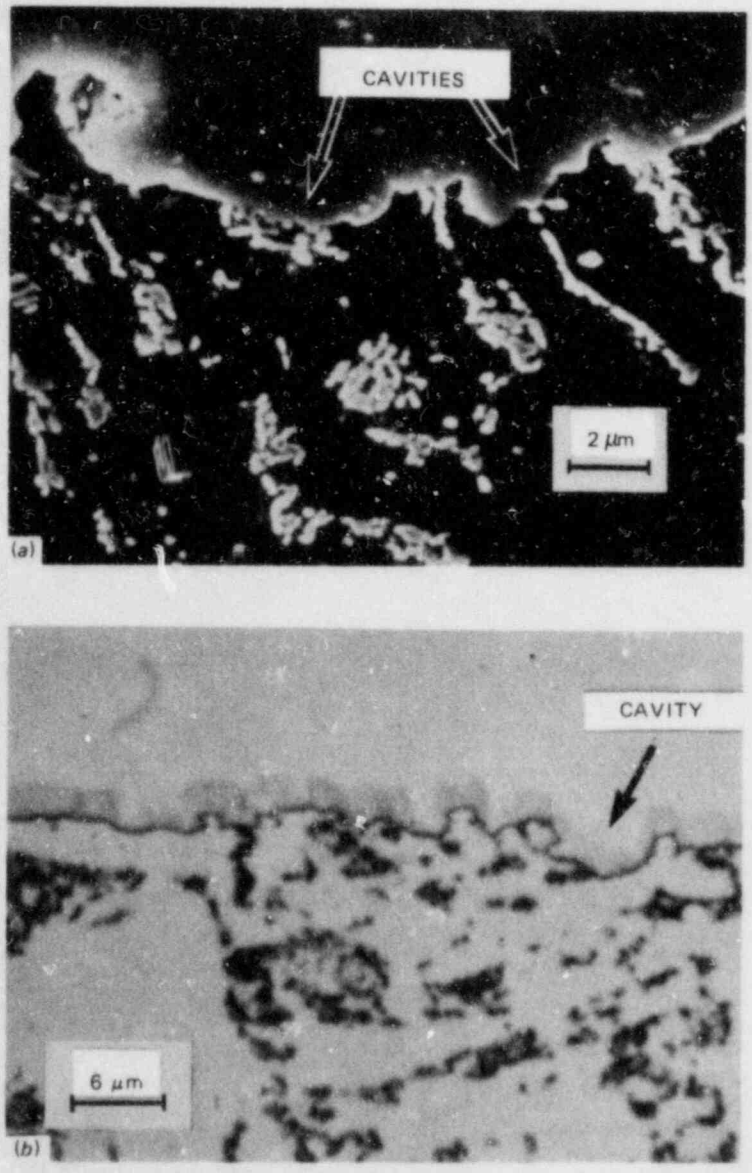

Fig. 2.4. (*a*) SEM view of transverse section showing small cavities and carbide cluster in contact with bottom of each cavity; and (*b*) optical microscope view of transverse section showing single cavity and carbide cluster in contact with bottom of cavity.

2.3.1.3 Investigations of weld metal. Inquiries have been received from utility personnel on whether this project will include investigations of weld metal. Arrangements have been made with ORNL to obtain a small block of low-upper-shelf weld metal. It is believed that fractographic and microstructural examinations using only CVN impact specimens will be of considerable value with regard to these inquiries.

ORNL PHOTO 2172-84

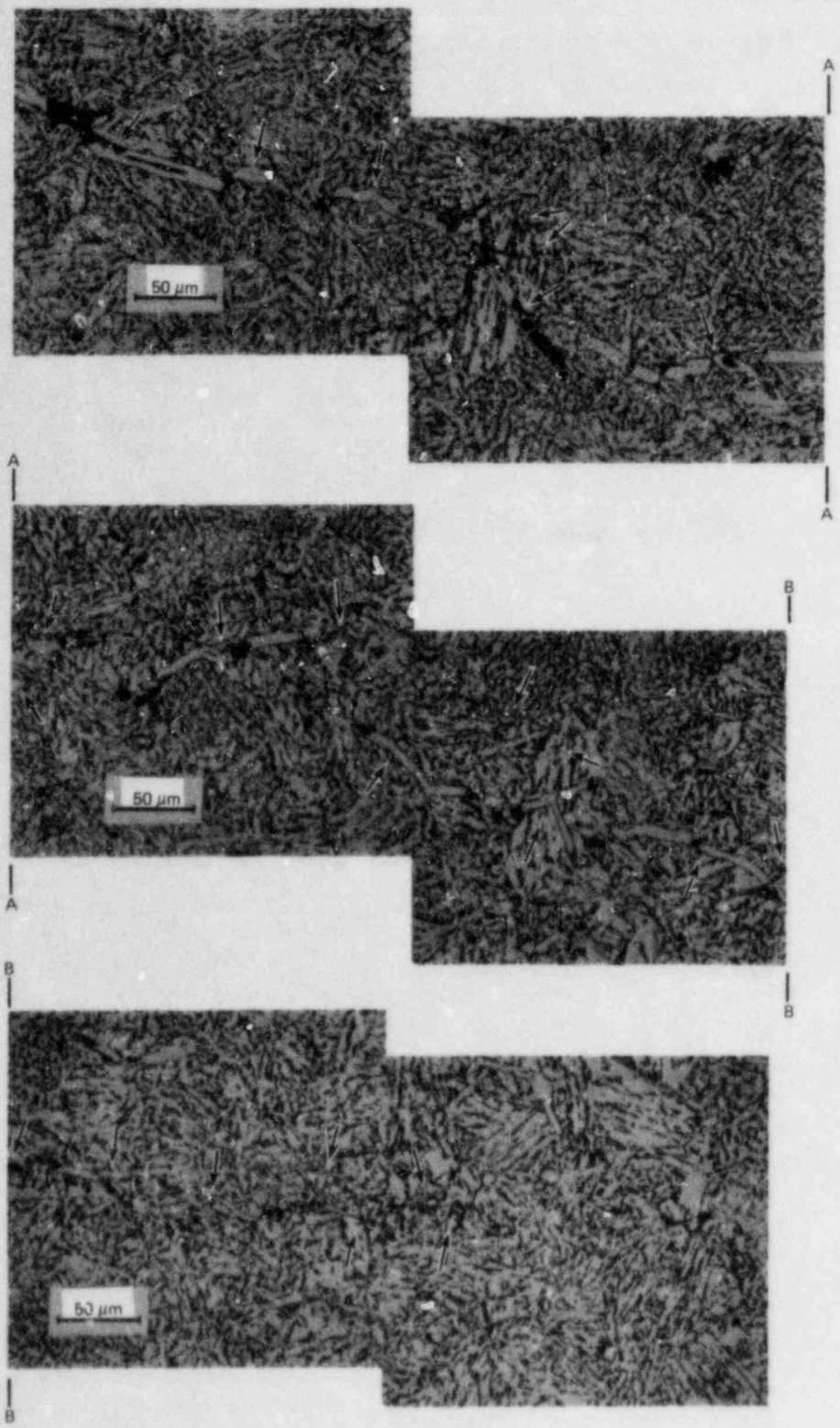

Fig. 2.5. Transverse section views of region below main fracture surface in CVN specimen of A508 steel showing branch of cleavage separation that was bypassed by main fracture surface. The branch crack is highlighted by arrows.

2.3.2 Plastic zone studies

The correct manner of handling a sizeable plastic zone around the initial starter notch is presently of some interest with regard to crack-arrest testing. The presence of this plastic zone gives rise to nonlinear load-displacement records and consequently affects the calculated values of K_Q and K_a, which are based upon the measured CMODs. An unresolved question is how much of the nonlinear displacement component should be included for purposes of evaluating K_Q and K_a.

A series of experiments were conducted earlier[10] in which compact tension (CT) specimens of 7075 aluminum alloy with a blunt, sawcut "crack" were loaded to some maximum load, unloaded, and crack extension simulated by extending the crack in a quasi-static manner with a fine (0.25-mm-thick) jeweler's saw. The specimens had a birefringent coating bonded onto one face, and examination of the fringe pattern as well as measurements of fiducial marks placed at the crack mouth indicated that most of the "residual" opening displacement present after unloading was recovered when the crack was extended past the plastically deformed region. However, as pointed out in Ref. 10, those results were preliminary and represented plastic zone sizes of the order of $2r_Y/W = 12.5\%$.

Examination of this problem continued during the current period. Several tests were conducted with larger plastic zones, using both monotonic loading and sequential load-unload cycling, as called for in the proposed American Society for Testing and Materials (ASTM) crack-arrest toughness measurement procedure. These tests used specimens similar to those used earlier, namely CT specimens fabricated from 6.4-mm-thick 7075-T651 aluminum alloy with a 1-mm-thick birefringent coating (Photolastic PS-1) bonded onto one face, a width W of 152 mm, and a sawcut crack terminating in a drilled hole at an a/w of 0.42.

Typical results are shown in Fig. 2.6; it shows the fringe patterns in the coating at (*a*) maximum load, (*b*) after unloading to zero load before crack extension, and (*c*) after extension of the crack with a jeweler's saw. There is little evidence in the fringe pattern of Fig. 2.6(*c*) of the initial plastic zone, other than the low-order disturbance related to the permanent stretch in the plastic zone and comparable in size to the $2r_Y$ value of 38 mm calculated for this test ($2r_Y/W = 25\%$). Measurements of the CMOD showed that, of the maximum opening of 5.6 mm for this test, 0.69 mm was still present after unloading to zero load. Extension of the crack past the plastically deformed region led to the recovery of most of this residual opening, and the final permanent opening displacement was 0.076 mm, which is 1.4% of the maximum opening displacement recorded.

A total of three tests were conducted, two using monotonic loading and one using sequential load-unload cycling. The results from all three tests were similar and are summarized in Tables 2.2 and 2.3. These results confirm the indications obtained previously: most of the nonlinear displacement component is recoverable when the crack is extended past the plastically deformed region. It remains unclear at this time as to when this recovery occurs. This question will be investigated further during the next reporting period.

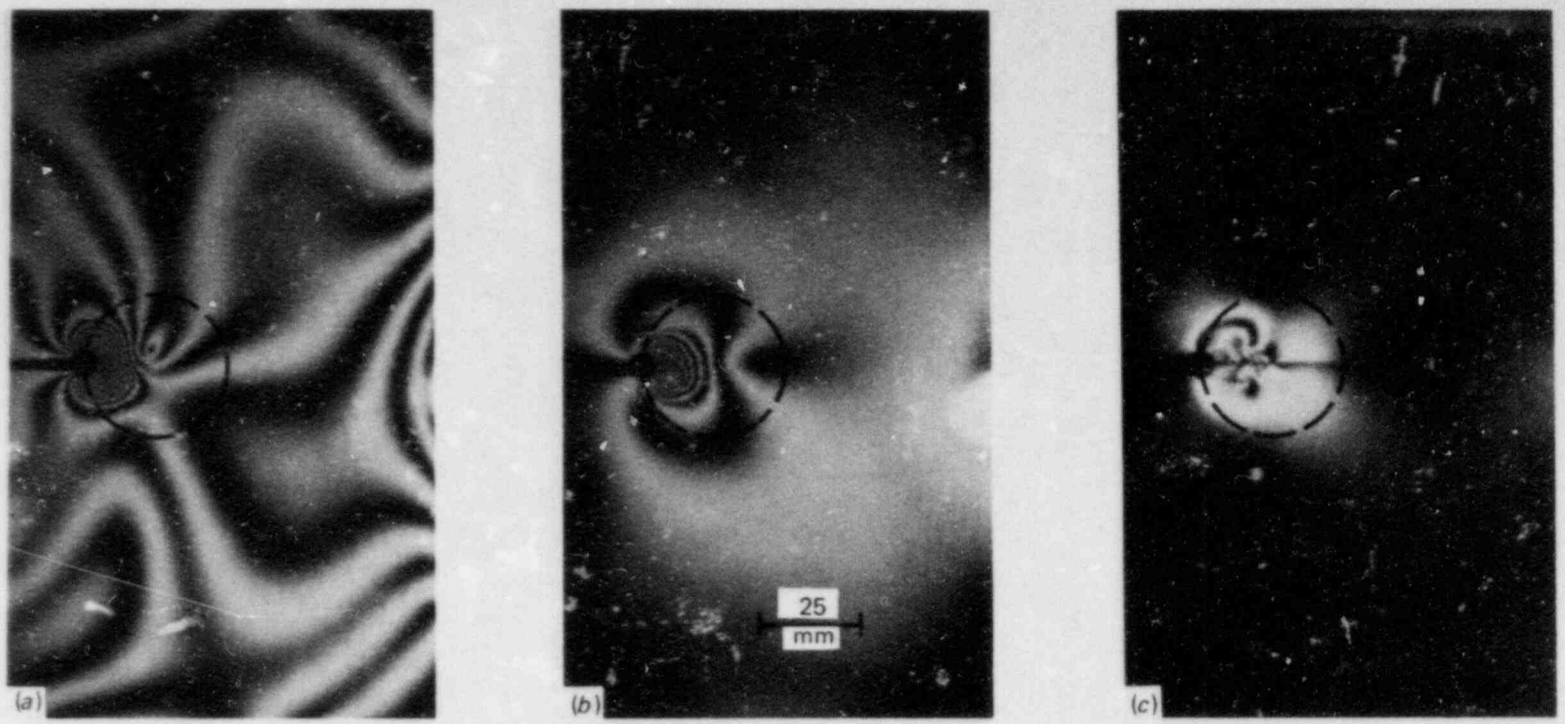

Fig. 2.6. Isochromatic fringe patterns in birefringent coating on CT specimen of 7075 aluminum alloy showing (*a*) stress field at maximum load; (*b*) redistributed elastic residual stress field caused by presence of a region of plastic deformation ahead of notch tip — after unloading to zero load and before extending crack; and (*c*) permanent residual field remaining after extension of crack by sawcutting. (Circles marked on each photograph are of diameter = $2r_y$.)

Table 2.2. Conditions for tests with large plastic zones

Test No. and loading	a_o/w	K_o^a (MPa$\cdot\sqrt{m}$)	a_{eff}/w	K_{eff}^b (MPa$\cdot\sqrt{m}$)	r_Y (mm)	$2r_Y/W$ (%)
I (Monotonic)	0.42	196	0.55	167	19.1	25
II (Monotonic)	0.42	189	0.53	167	19.1	25
V (Sequential)	0.42	157	0.51	141	13.5	18

[a] K_o = K-value calculated using a_o/w and the measured crack mouth opening, Δ_o.

[b] K_{eff} = K-value calculated iteratively using $a_{eff} = a_o + r_Y$ and Δ_o.

Table 2.3. Measured displacements for specimens tested with large plastic zones

Test No. and loading	Δ_o[a] (mm)	Δ_r[b] (mm)	Δ_r/Δ_o (%)	Δ_p[c] (mm)	Δ_p/Δ_o (%)
I (Monotonic)	5.61	0.69	12	0.08	1.4
II (Monotonic)	5.54	0.66	12	0.10	1.8
V (Sequential)	4.57	0.74	16	0.08	1.7

[a] Δ_o = CMOD at maximum load; measured with a clip gage.

[b] Δ_r = CMOD after unloading to zero load, before extending crack; measured with a clip gage and from fiducial marks on specimen.

[c] Δ_p = CMOD after extending the crack by sawcutting; measured from fiducial marks on specimen.

2.3.3 Dynamic run-arrest calculations

During the current reporting period, efforts concerning the dynamic fracture code SAMCR have focused on

1. incorporating thermal effects into the SAMCR code formulation;
2. performing dynamic run-arrest analyses of the different events in ORNL thermal-shock tests TSE-5, -5A, and -6; and
3. preparing a topical report on dynamic run-arrest calculations as well as a user's manual for the SAMCR code.

The run-arrest events observed in ORNL Thermal-Shock Experiments TSE-5, -5A, and -6 were modeled using SAMCR. Attention was focused on the second event in TSE-5, the third and fourth events in TSE-5A, and the second event in TSE-6. A 180° segment of the test cylinder was modeled in each case, with the crack oriented along the positive branch of the x-axis. A change in mesh between the TSE-5 series and TSE-6 was necessitated by the smaller wall thickness in the latter.

Input data pertaining to the radial temperature distribution and initial crack depth for each event were obtained from ORNL. The static finite-element program, DOASIS, was used to generate the initial displacement and thermal strain distribution in the cylinder wall prior to each dynamic event. The temperature transient associated with a particular event was assumed to remain unchanged during the run-arrest segment. The variation with temperature of the arrest toughness K_{Ia} of A508 steel was modeled by the dashed curve shown in Fig. 2.7. The data in Fig. 2.7 represent a compilation of the static analysis test results from the TSE experiments and the mean values obtained from the A533B steel tested in the Cooperative Program on Crack-Arrest Testing. The last piece of input data required by SAMCR, namely the relationship between crack-tip stress-intensity factor K and crack speed c, was obtained from Rosenfield et al.,[11] where it is suggested that for RPV steels

$$K(c, T) = K_{Ia}(T) \cdot f(c) , \tag{2.27}$$

where

$$f(c) = \begin{cases} 1, & c \leq 340 \text{ m/s} \\ (828 + 2.45c)/(2000 - c), & c > 340 \text{ m/s} \end{cases} . \tag{2.28}$$

A comparison of the experimental and SAMCR-predicted crack jumps for each event analyzed is presented in Table 2.4. A better picture of the predicted crack extension behavior is, however, obtained from an examination of Figs. 2.8(*a*) and (*b*), that show, respectively, crack extension vs time and stress-intensity factor vs time from the analysis results for the second jump in TSE-5. The crack [Fig. 2.8(*a*)] starts out with a relatively large velocity, which decreases at about 50 μs and remains nearly constant thereafter until crack arrest occurs. As with the modified compact tension (MCT) analyses discussed previously[10] numerous

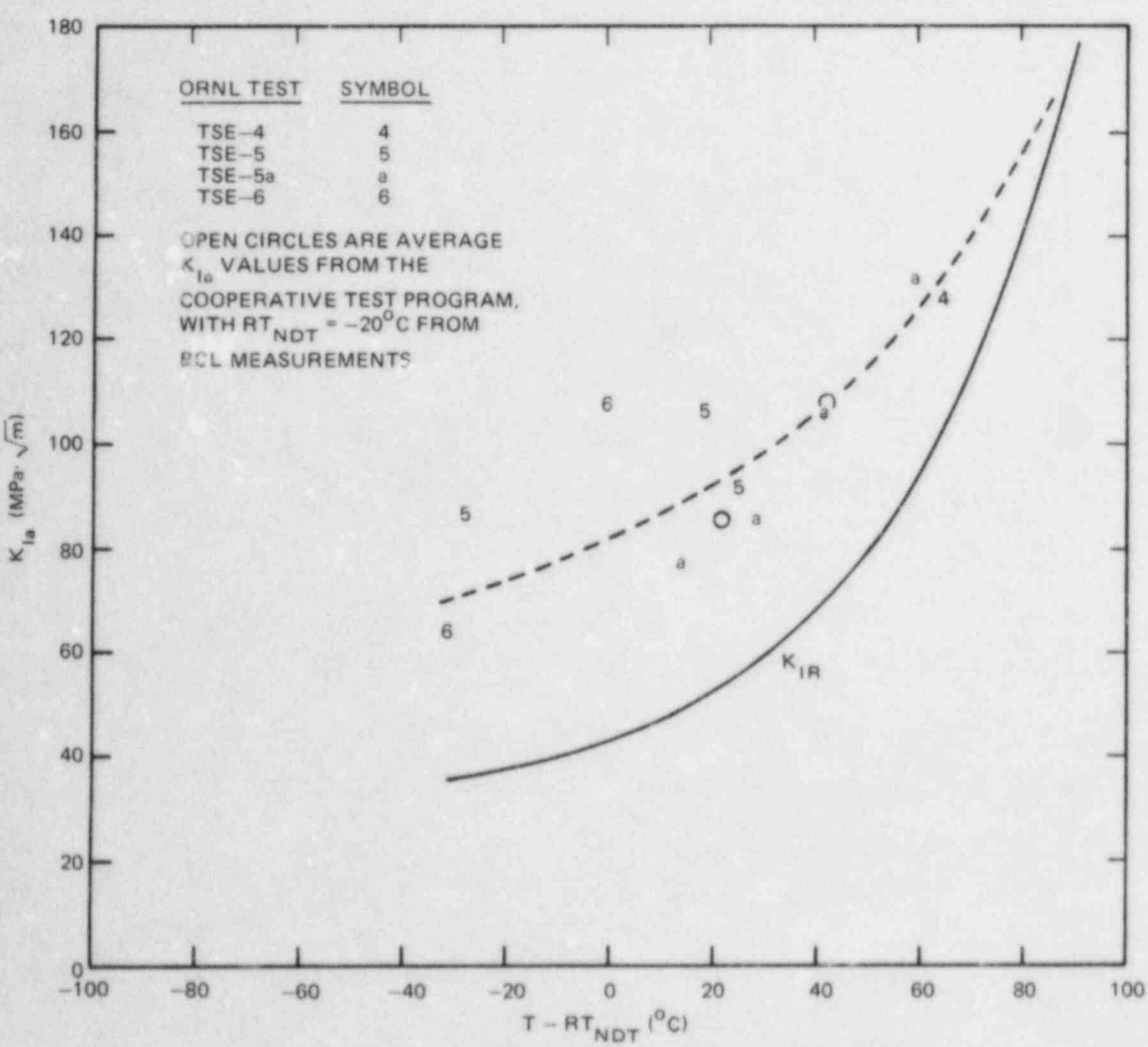

Fig. 2.7. Crack-arrest toughness as function of temperature for TSE and Cooperative Program steels.

short segments of run-arrest are seen within the overall crack extension history. This is more readily understood by an examination of Fig. 2.8(*b*) in conjunction with Eqs. (2.27) and (2.28). The computed dynamic K-value falls sharply at first, but then follows a gradually rising trend before peaking at about 375 μs, after which it begins to fall. This is consistent with the static K_I vs crack-depth behavior calculated for this transient by Cheverton.[12] However, in the dynamic analysis, this behavior in the computed K-value has the effect of keeping K just above or just below the threshold K_{Ia} value. From Eqs. (2.27) and (2.28), it is then obvious that the crack speed will vary somewhat discontinuously between a value of ~350 m/s and 0. This is confirmed by the predicted instantaneous crack speed vs time data.

The large initial velocity is also a consequence of the constitutive relation specified. The steadily increasing nature of the c-K relationship defined by Eqs. (2.27) and (2.28) allows large crack speeds

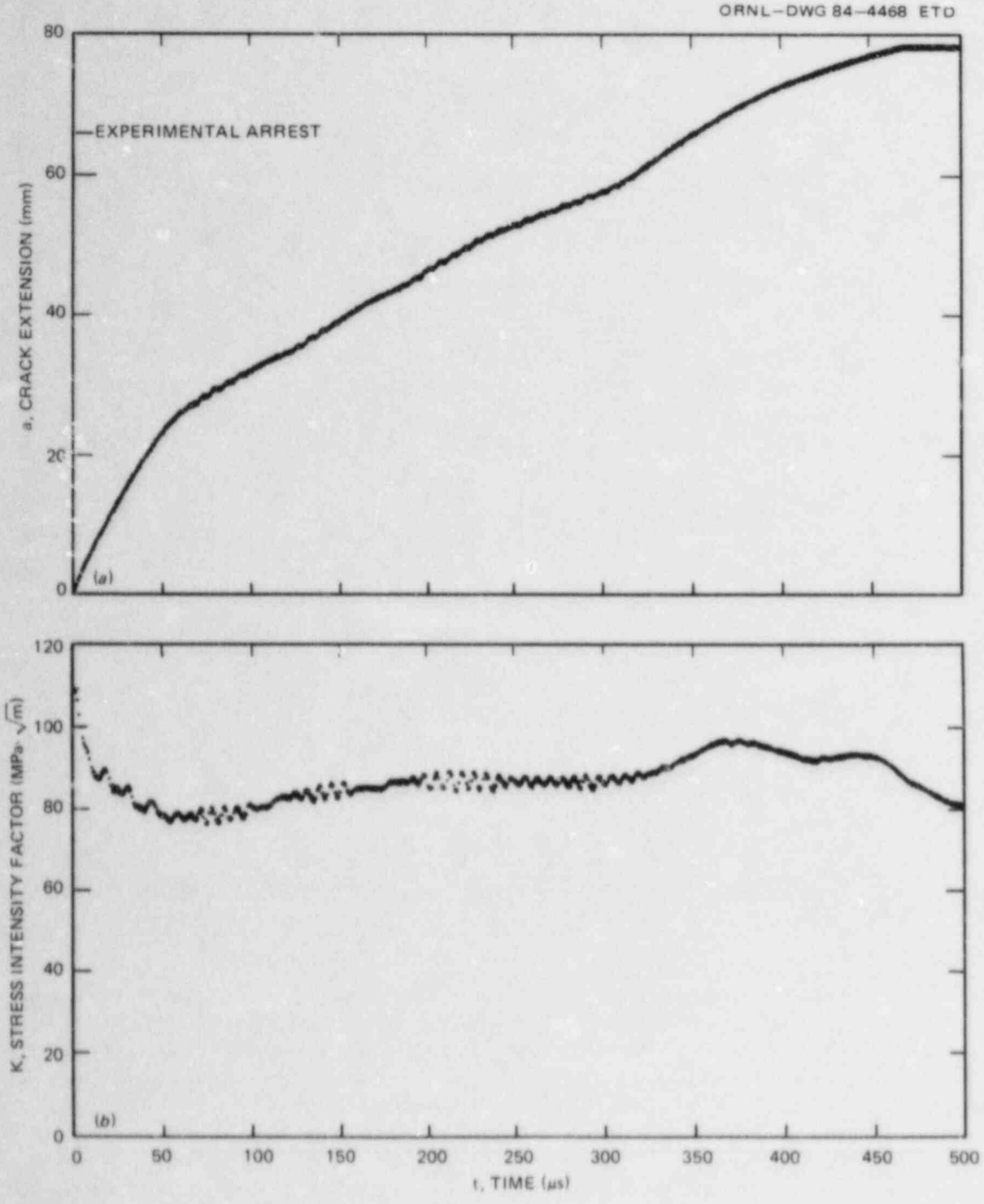

Fig. 2.8. (*a*) Predicted crack extension vs time behavior for second jump in TSE-5 and (*b*) predicted stress-intensity factor vs time behavior for second jump in TSE-5.

Table 2.4. Comparison between predicted and observed crack jumps in ORNL thermal-shock experiments TSE-5, -5A, and -6

TSE event	Experimental crack jump (mm)	Predicted crack jump (mm)	Run-arrest time (m/s)	Average crack velocity (m/s)
TSE-5 jump 2	65.5	77.9	473	165
TSE-5A jump 3	18.3	16.3	368	44
TSE-5A jump 4	33.0	39.4	454	87
TSE-6[a] jump 2	50.3	47.2	460	103

[a]Analysis of TSE-6 jump 2 was halted when the forward leg of the J-contour passed outside the finite-element mesh. Crack velocity at this time was 25.4 m/s.

(in excess of 10% of shear wave speed) during the early stages of the analysis, even though the K-value is falling. A large segment of the total crack extension therefore occurs during this period. The difference between predicted and observed crack jump (78 mm vs 65.5 mm) is thus closely linked to the nature of the c-K relationship that has been used and about which little is known. The overall picture of a slowly advancing crack that does not exhibit large dynamic effects over most of its propagation history is in agreement with the expectations of what would happen in a large structure such as the test cylinder.

Figures 2.9 and 2.10 show crack extension vs time for the fourth jump in TSE-5A and the second jump in TSE-6, respectively. In neither instance does one see the large initial velocities of Fig. 2.8(*a*). This is probably due to differences in K-levels for these jumps and/or different crack-tip temperatures, which placed these events lower down on the c-K curve at initiation. An observation from Fig. 2.10 (TSE-6 jump 2) is the indication in the computations of an intermediate arrest for 40 μs, after the crack had jumped about 35.6 mm. This is consistent with the COD and fracture-surface observations made by Cheverton[13] for this test. Unfortunately, the analysis for this event was halted at 460 μs after initiation, when the crack depth became large enough for the leading edge of the J-integral contour to pass outside of the finite-element mesh being used. The crack had extended 47.2 mm from its starting position at that time and was moving with a very low velocity (of the order of 25.4 m/s). By comparison with the other TSE analyses performed, it could therefore be expected to arrest without penetrating the cylinder wall much further.

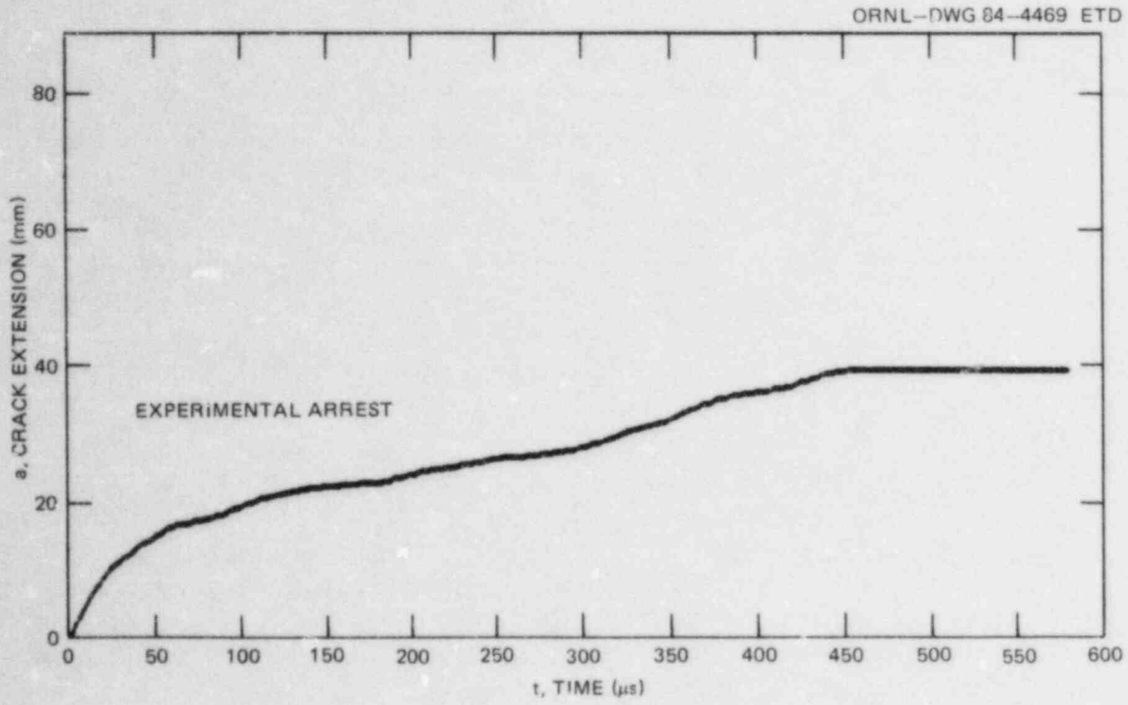

Fig. 2.9. Predicted crack extension vs time for fourth jump in TSE-5A.

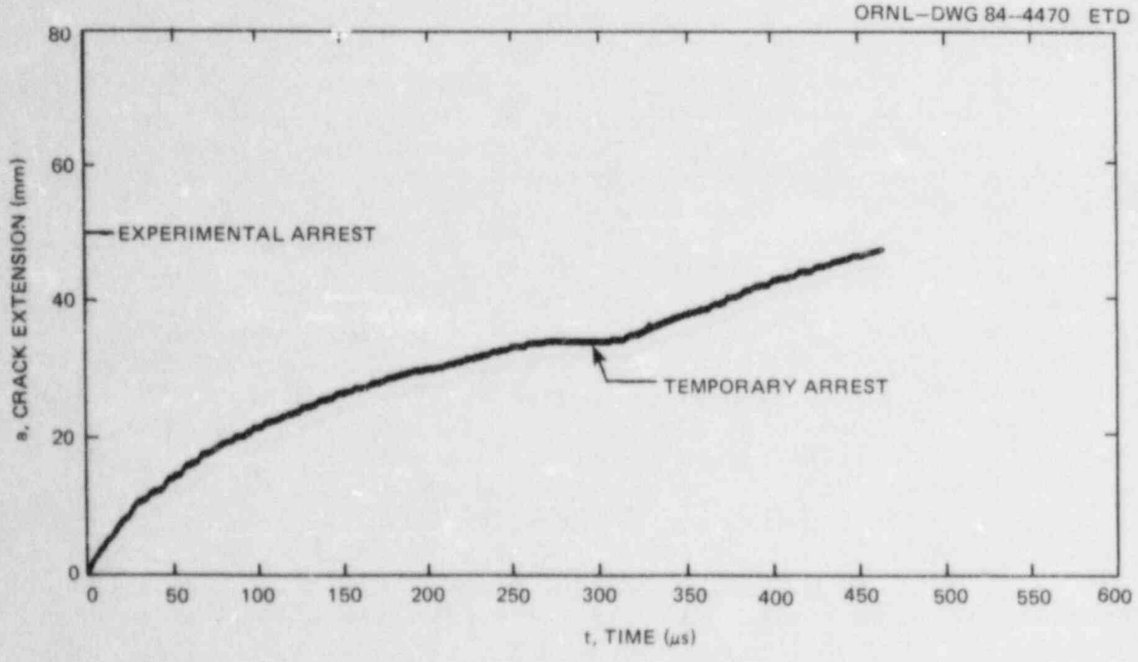

Fig. 2.10. Predicted crack extension vs time for second jump in TSE-6.

Note that the small internodal spacing in the r-direction required to accurately model the thermal gradients, when combined with the size of the cylinder, required the use of ~1400 nodal points to model the thermal-shock problem. The increase in computational time over some of the other analyses that have been performed with SAMCR was therefore very large. The time-step size used was typically of the order of 0.2 μs, and a computation for 400 to 500 μs extended over 2000 or more time steps.

References

1. B. R. Bass and J. W. Bryson, *Applications of Energy Release Rate Technique to Part-Through Cracks in Plates and Cylinders, Volume 1, ORMGEN-3D: A Finite Element Mesh Generator for 3-Dimensional Crack Geometries*, NUREG/CR-2997, Vol. 1 (ORNL/TM-8527/V1), Union Carbide Corp. Nuclear Div., Oak Ridge Natl. Lab., December 1982.

2. K. J. Bathe, *ADINA — A Finite Element Program for Automatic Dynamic Incremental Nonlinear Analysis*, Report 82448-1, Massachusetts Institute of Technology, Cambridge, Mass., September 1975 (revised December 1978).

3. B. R. Bass and J. W. Bryson, *Applications of Energy Release Rate Techniques to Part-Through Cracks in Plates and Cylinders, Volume 2. ORVIRT: A Finite Element Program for Energy Release Rate Calculations for 2-D and 3-D Crack Models*, NUREG/CR-2997, Vol. 2 (ORNL/TM-8527/V2), Union Carbide Corp. Nuclear Div., Oak Ridge Natl. Lab., February 1983.

4. R. S. Barsoum, "Triangular Quarter-Point Elements as Elastic and Perfectly-Plastic Crack Tip Elements," *Int. J. Numerical Methods in Eng.* 11, 85—98 (1977).

5. J. G. Merkle, "An Approximate Stress Intensity Factor Solution for a Deep Inside-Surface Longitudinal Crack in a Cylinder Under Thermal Loading," pp. 5—25 in *HSST Program Quart. Prog. Rep. October—December 1975*, ORNL/NUREG/TM-3, Union Carbide Corp. Nuclear Div., Oak Ridge Natl. Lab.

6. J. G. Merkle, "Approximate Stress Intensity Factor Calculations for Continuous Inside-Surface Circumferential Cracks in a Cylinder Under Thermal Loading," pp. 3—15 in *HSST Program Quart. Prog. Rep. January—March 1976*, ORNL/NUREG/TM-28, Union Carbide Corp. Nuclear Div., Oak Ridge Natl. Lab.

7. J. G. Merkle, "Analysis of Crack Behavior Under Thermal Shock Loading," pp. 3—12 in *HSST Program Quart. Prog. Rep. July—September 1978*, ORNL/NUREG/TM-275, Union Carbide Corp. Nuclear Div., Oak Ridge Natl. Lab.

8. J. G. Merkle, "Elastic-Ideally Plastic PTS Analysis for a Deep Continuous External Longitudinal Crack in a Cylinder," pp. 103–111 in *HSST Program Quart. Prog. Rep. January–March 1983*, NUREG/CR-3334, Vol. 1, ORNL/TM-8787/V1, Union Carbide Corp. Nuclear Div., Oak Ridge Natl. Lab.

9. W. L. Fourney et al., "Investigation of Damping and of the Cleavage-Fibrous Transition in Reactor Grade Steel," *HSST Program Quart. Prog. Rep. July–September 1983*, NUREG/CR-3334, Volume 3, ORNL/TM-8787/V3, Union Carbide Corp. Nuclear Div., Oak Ridge Natl. Lab.

10. W. L. Fourney et al. "Investigation of Damping and of the Cleavage-Fibrous Transition in Reactor Grade Steel," pp. 25–44 in *HSST Program Quart. Prog. Rep. April–June 1983*, NUREG/CR-3334, Volume 2, ORNL/TM-8787/V2, Union Carbide Corp. Nuclear Div., Oak Ridge Natl. Lab.

11. A. R. Rosenfield et al., "BCL HSST Support Program," pp. 3–30 in *HSST Program Quart. Prog. Rep. April–June 1982*, NUREG/CR-2751, Volume 2, ORNL/TM-8369/V2, Union Carbide Corp. Nuclear Div., Oak Ridge Natl. Lab.

12. R. D. Cheverton et al., "Thermal Shock Investigations," pp. 52–74 in *HSST Program Quart. Prog. Rep. July–September 1979*, NUREG/CR-1197, ORNL/NUREG/TM-370, Union Carbide Corp. Nuclear Div., Oak Ridge Natl. Lab.

13. R. D. Cheverton et al., "Thermal Shock Investigations," pp. 52–89 in *HSST Program Quart. Prog. Rep. October–December 1981*, NUREG/CR-2141, Volume 4, ORNL/TM-8252, Union Carbide Corp. Nuclear Div., Oak Ridge Natl. Lab.

3. MATERIAL CHARACTERIZATION AND PROPERTIES

R. K. Nanstad J. J. McGowan
W. R. Corwin D. P. Edmonds

A section of the test cylinder for Thermal-Shock Experiment No. 7 (TSE-7) was received and prepared for sectioning into specimens for metallographic and scanning electron fractographic analyses. Prior to sectioning, photographs were taken of the fracture surface. The scanning electron fractography will specifically examine the arrest and reinitiation regions for evidence of ductile-dimple fractures.

Development of crack-arrest testing technology in the laboratory has continued. Our primary activities have revolved around the American Society for Testing and Materials (ASTM) round robin on crack-arrest toughness. We have completed most of the scoping tests with 50-mm-thick compact crack-arrest specimens (2TCCA) of A533 grade B class 1 steel for the round robin. Those tests were performed at temperatures up to 29°C above the RT_{NDT} (RT_{NDT} + 29°C). The next series of scoping tests will be performed at temperatures up to RT_{NDT} + 50°C in an attempt to measure crack-arrest toughness K_{Ia} values as high above RT_{NDT} as possible. The results from the scoping tests will be used to determine the temperature range and specific test temperatures for the round-robin testing of the A533 material.

The testing system has been upgraded with the installation of a new electronic conditioning package and the installation of a hot-air system for testing at temperatures above room temperature. Additionally, we have completed the fabrication of fixturing for testing of CCA specimens with planar dimensions from 100 by 100 mm to 200 by 200 mm with both right-side up and inverted-split pin configurations. We have fabricated the A533 grade B class 1 2TCCA specimens for both Oak Ridge National Laboratory (ORNL) and University of Maryland round-robin test series. An optimization of welding procedures program was conducted to minimize cracking tendencies of the Hard-X N weld crack starter.

A prototype system for performing fatigue crack-growth and J-R testing using the potential drop technique has been developed. The system is completely microcomputer driven and yields report-quality graphs upon test completion. Resolution of crack extension measurements has been achieved as low as 5 μm. The advantages of this technique are (1) the potential for obtaining continuous J vs crack extension measurements, thus eliminating the need for the unloading step inherent in the unloading compliance technique; (2) the potential for performance of dynamic J-R curves; and (3) the flexibility allowed for complex loadings. The elimination of the unloading steps is particularly advantageous for remote testing in the hot cell environment. Activities during the next report period will involve investigations of loading rate effects and direct comparisons with unloading compliance results.

Regarding the wide-plate crack-arrest program, plans for material characterization have been completed and sectioning of the test plate has begun. A piece has been removed for metallographic examination and hardness testing to determine the gradient through the thickness.

4. ENVIRONMENTALLY ASSISTED CRACK-GROWTH TECHNOLOGY*

W. H. Bamford† R. J. Jacko†
L. J. Ceschini†

4.1 Introduction

The objective of this task is to characterize the crack-growth rate properties of light-water reactor (LWR) materials exposed to primary-coolant environments. The work now being conducted falls into four major areas:

1. corrosion fatigue crack-growth tests in simulated pressurized-water reactor (PWR) environment;
2. static load K_{ISCC} tests in simulated PWR environment;
3. fractographic examination of specimen fracture surfaces; and
4. characterization of environment by measurement of electrochemical potential.

4.2 Fatigue Crack-Growth Results

Recent results in corrosion fatigue crack-growth rate testing have shown that there can be significantly different levels of environmental enhancement for different heats of the same steel. This enhancement was related to the sulfur content of the steels, as rather conclusively demonstrated by a test matrix conducted in this program and as previously reported.[1,2]

A new matrix of tests has now been formulated to provide more detailed information on the behavior of a steel that is expected to show a high level of environmental enhancement. The heat chosen for study is a pressure vessel steel with a sulfur content of 0.025 wt %, among the highest contents that are known and typical of the oldest materials in service in operating plants. (As time has passed, vessel steels have been produced with lower sulfur contents to improve the fracture toughness.) The fatigue crack-growth characteristics of this material will be studied as a function of temperature and frequency at two values of R ratio (K_{min}/K_{max}). A preliminary matrix of tests to evaluate these parameters has been provided in Table 4.1.

During this report period testing began on this matrix, and a number of results have been obtained. The first step was to perform basic tests to benchmark the material relative to other materials that have been characterized in this program. This was done by testing standard 2TCT

---

*Work sponsored by HSST Program under Union Carbide Corporation-Nuclear Division (UCC-ND) Subcontract 11X-21598C between UCC-ND and Westinghouse Electric Corporation, Nuclear Technology Division.

†Westinghouse Electric Corporation, Power Systems, Nuclear Technology Division, Pittsburgh, Pa. 15230.

Table 4.1. Test matrix for study of frequency and temperature effects for high sulfur A533B steel

Test temperature (°C)	R ratio = 0.2		R ratio = 0.7	
	Frequency (cpm)	Specimen	Frequency (cmp)	Specimen
288	1	CQ2-5	1	CQ2-6
			10	CQ2-11
204			1	CQ2-7
93				

(5.08-cm-thick) specimens under sinusoidal loadings at 1 cpm. These tests were completed, and the result for R ratio = 0.7 is shown in Fig. 4.1 for specimen CQ2-6. Figure 4.1 indicates that this material shows an irregular crack-growth behavior at high R ratio, with the growth rate both increasing and decreasing as the test progressed. Overall, the crack-growth rate showed somewhat less environmental acceleration than had been expected based on previous tests of similar materials, but the lack of sustainable high growth rates at high R has been observed many times before. Specimen CQ2-5 was tested at low R ratio (R = 0.20), and the crack-growth behavior was much more accelerated, as seen in Fig. 4.2. This behavior falls in with the higher levels of crack-growth rate observed earlier at this value of R ratio, as seen by comparison with the American Society of Mechanical Engineers (ASME) reference curve. Thus, further study of this material apparently will be valuable in better characterizing the older vessel steels.

The high R ratio testing was carried further during this report period to study the effects of temperature and frequency on crack growth. Thus far, data scatter makes strong conclusions difficult, but some observations are in order. Figure 4.1 shows results obtained at two temperatures (204 and 288°C), and the behavior is very similar for each. There is a great deal of acceleration and deceleration in crack-growth rate for both tests, but the highest observed crack-growth rates were found at 288°C.

A preliminary view of the effect of frequency can be seen in Fig. 4.3, where tests conducted at 1 and 10 cpm are shown. Again there are many accelerations and decelerations in the crack-growth rate in both these tests, but it is clear that the growth rate at 1 cpm is much greater than those at 10 cpm.

During the next reporting period, further testing will be carried out on this matrix, and the range of temperatures and frequencies will be expanded.

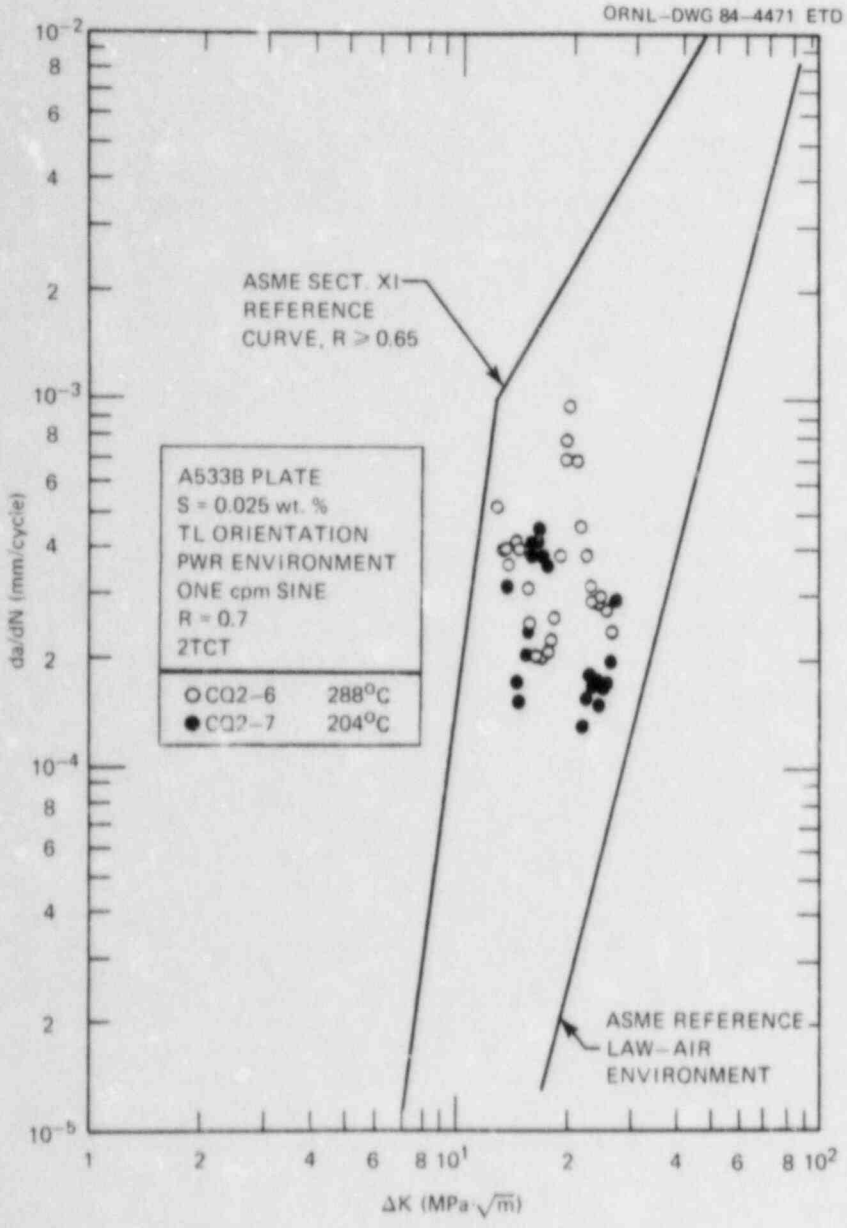

Fig. 4.1. Fatigue crack-growth results for high sulfur heat CQ2, showing effect of temperature on results at R = 0.7 in simulated PWR environment.

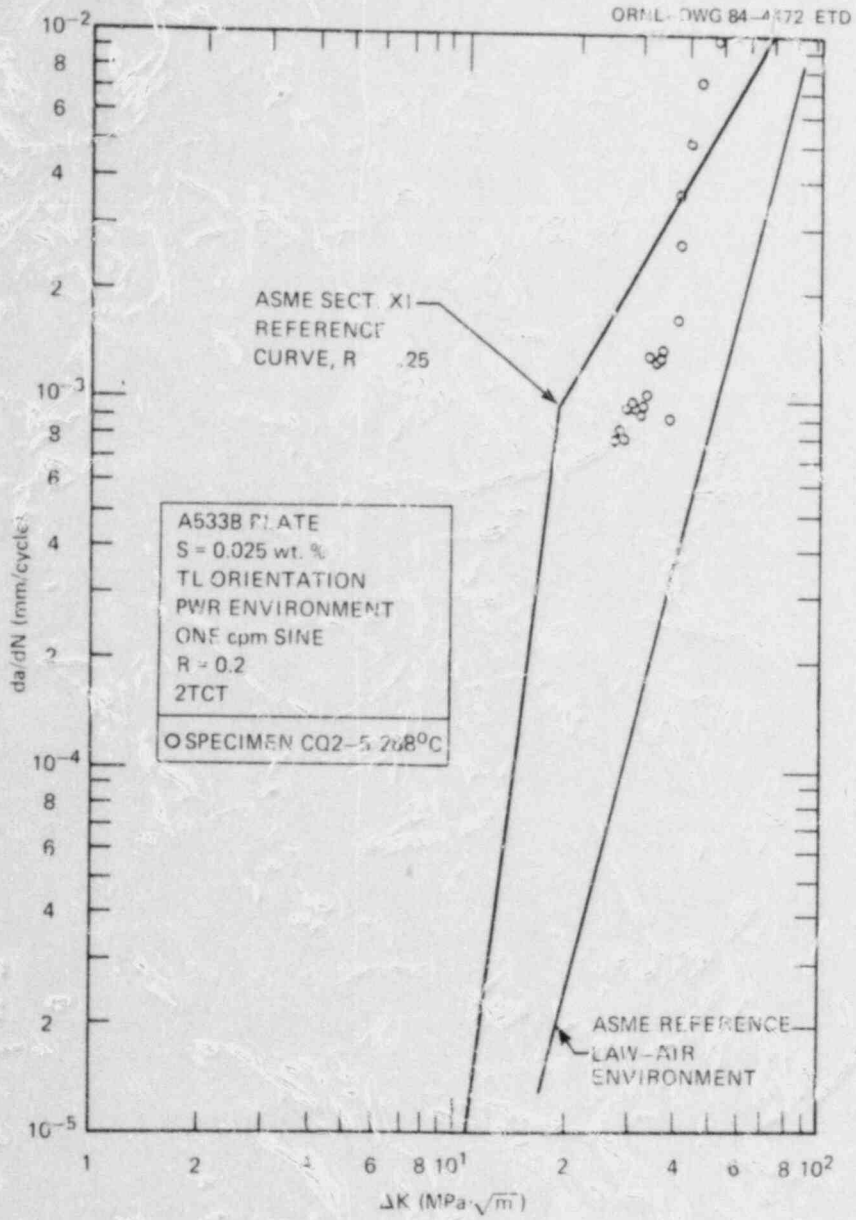

Fig. 4.2. Fatigue crack-growth results for specimen CQ2-5 tested at R = 0.2, 288°C in simulated PWR environment.

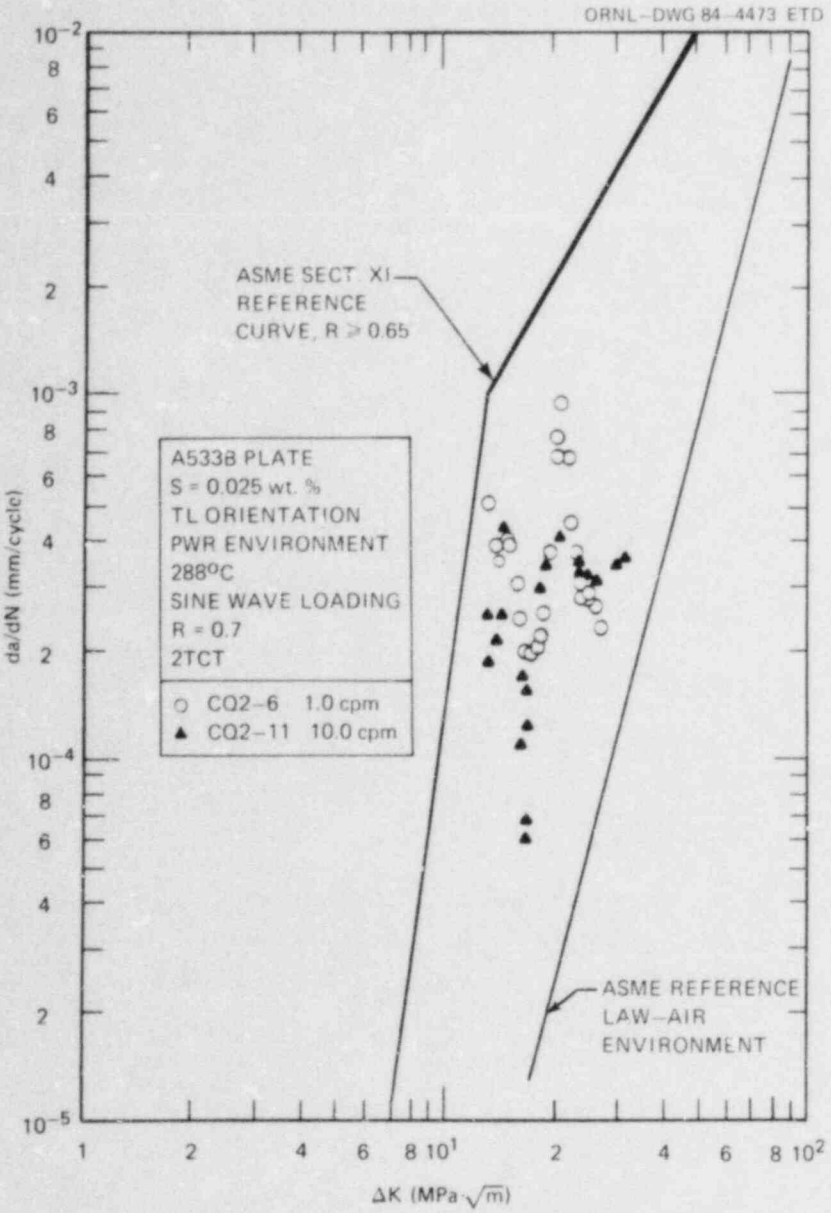

Fig. 4.3. Effect of frequency on fatigue crack-growth for high sulfur heat CQ2 at R = 0.7, 288°C in simulated PWR environment.

A second area of investigation during this report period involved the level of crack-growth rate enhancement for low sulfur steels in water environments. Earlier tests of two heats of A533B class 1 steel with nominally the same sulfur content (0.004 wt %) resulted in remarkably different behaviors, as shown in Fig. 4.4, for specimens W7-2C7 and TW-1. These two heats were tested under identical conditions, so that no difference in behavior was expected. Several tests of heat TW were conducted under these conditions and resulted in similar behavior,[1] so during this report period a second test was conducted on heat "W7." Results of this test are

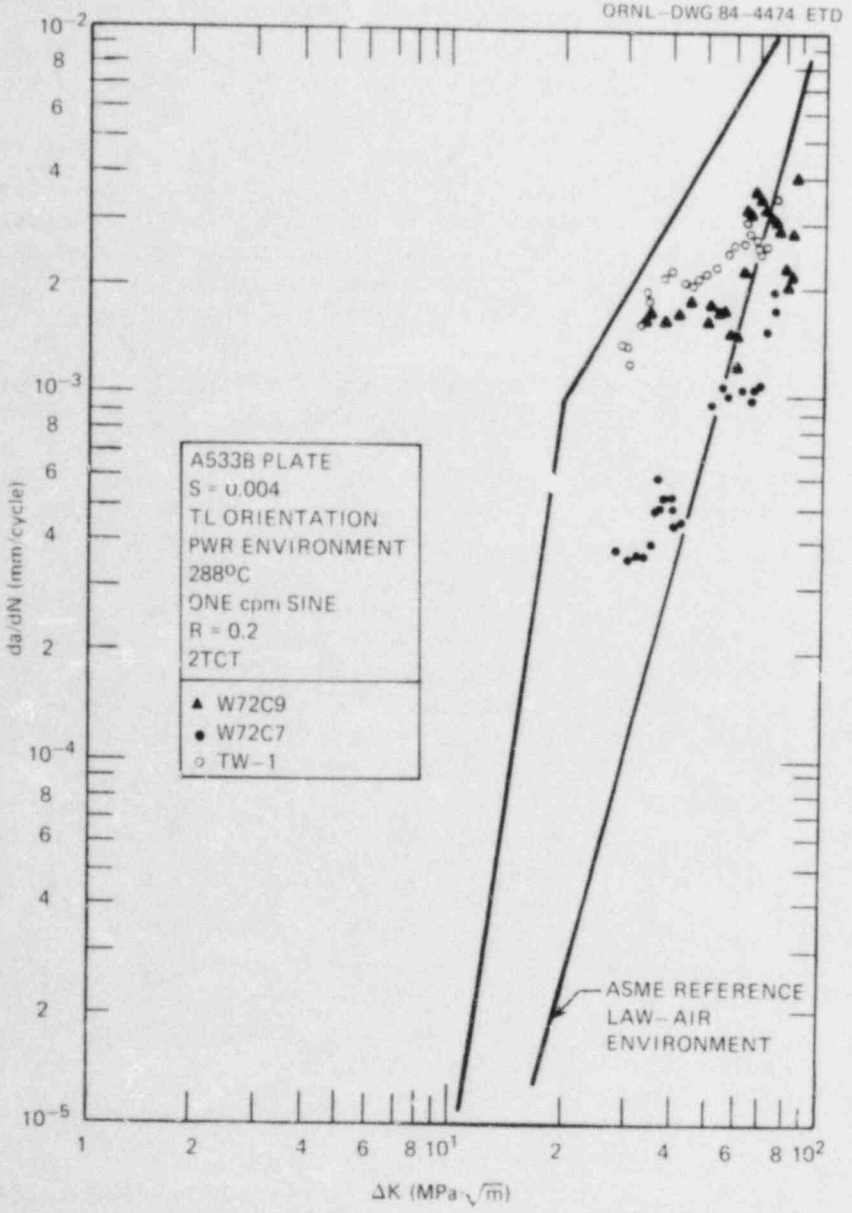

Fig. 4.4. Fatigue crack behavior of two low sulfur heats of A533B steel tested at R = 0.2, 288°C in simulated PWR environment.

also presented in Fig. 4.4 and show a behavior similar to that obtained for heat "TW." Thus, two tests of heat "W7" are now available that show much different crack-growth rates. This difference in behavior is too great to be the result of data scatter, so further investigation is under way.

4.3 Static Load Testing

The behavior of cracks in the pressure vessel steels and welds of interest in the PWR environment has been under investigation using bolt-loaded specimens since 1974. The specimens are WOL type, 2.54 cm thick, and loaded to a fixed displacement by a bolt of the same material. The specimens are positioned in the bottom of two of the operating corrosion fatigue autoclaves. A summary of the information generated thus far in this portion of the program appears in Ref. 3.

Cracking under static load has been observed in several of the heat-affected zone (HAZ) materials and in a single heat of A533B class 1 plate. The incubation time for the HAZs has been rather short, around 2,000 h, but for the plate material the time to first cracking exceeded 37,000 h in the environment. No cracking has occurred in the welds or forging material as yet, after over 70,000 h, 48,000 in the environment. Table 4.2 shows the status of all specimens tested to date.

A total of 25 specimens have undergone testing in the environment, including specimens from A533B class 1, A508 class 2, and welds and HAZs made with Linde 80, Linde 124, and Linde 0091 fluxes. Twenty specimens remain in testing. The specimens have all been prepared in the same manner. They are precracked in air at low loadings in compliance with ASTM E399 requirements, then loaded to a predetermined value of stress-intensity factor K, which is obtained by tightening the bolt until the face opening of the specimen corresponds to that K, as determined by a compliance relationship. If the crack propagates, it should stop at a length that corresponds to the threshold for stress corrosion cracking K_{ISCC}. This value is easily calculated from the final crack length, because the face opening of the specimen remains constant even though the load drops as the crack propagates. Thus, the applied K will decrease as the crack propagates, stopping at $K = K_{ISCC}$. This process is complicated considerably by the fact that incubation times are involved that may be very long in some cases. Even when cracking occurs, as it has in some specimens, it is irregular and occurs by fits and starts. The method used to expose the specimens to the environment is somewhat deficient because the crack length can only be monitored periodically as the autoclave is opened for specimen insertion or repair of seals. Nonetheless, through numerous removals, considerable information has been obtained on the behavior of these specimens.

As can be seen in Table 4.2, some crack extension appears to be still occurring in a few specimens, with a tendency for cracks to propagate unevenly at first and then to even out on each side. As the cracks propagate into the specimen, the applied stress-intensity factor K decreases and should reach a common value for a given material, regardless of initial loading. This appears to be happening to a degree, but the

Table 4.2. Status of bolt-loaded specimens in simulated PWR environment (March 1, 1984)

Material	Specimen	Applied stress-intensity factor (MPa•√m)	Total time loaded (h)	Time in environment (h)
A533 class 1 plate (HSST plate 4)	04A-112	110	70,630	48,638
	04A-114	90	70,630	48,994
	04A-116	88	70,630	48,994
A508 class 2 forging	F-13	110	71,650	51,430
	F-14	99	71,650	51,430
	F-15	88	71,650	51,430
Linde 124 weld	C-13	110	71,650	51,430
	C-14	99	71,650	51,430
Linde 124 weld HAZ	CQ-1-HAZ	110	24,320 (1,816)[a]	12,394 (1,262)
	CQ-2-HAZ	99	24,320	12,394
	CQ-3-HAZ	88	24,748 (3,360)	12,274 (2,616)
Linde 0091 weld HAZ	D-7HAZ	99	22,420	10,368
	D-8HAZ[b]	88	22,420 (7,196)	10,368 (4,160)
	D-9HAZ	77	22,420	10,368
Linde 124 weld HAZ	K-3HAZ	66	360	336
	K-4HAZ	77	360	336
	K-5HAZ	88	360	336
Linde 0091 weld HAZ	DD-3HAZ	66	192	168
	DD-4HAZ	77	192	168
	DD-5HAZ	88	192	168

[a]Hours at first observed crack extension.

[b]Extension since last report.

uneven crack propagation makes accurate calculation of the applied stress-intensity factor difficult. The stress-intensity factor has been calculated based on the average of the two side measurements from the specimen. The applied K values appear to be stablizing in a range of 44 to 55 MPa•√m.

Two new materials were added to those in testing during this report period, to provide further insight into the behavior of a wide range of pressure vessel steels and welds. In conjunction with these tests, fatigue crack-growth rate tests are being carried out on the same materials, to provide further insight into the mechanisms involved (see Table 4.3). A review of efforts to date to relate crack-growth rates in fatigue to those obtained under constant load was provided in a previous progress report.[4]

Table 4.3. Fatigue crack-growth rate testing to complement static load tests

Test material	R = 0.2		R = 0.7	
	Frequency (cpm)	Specimen	Frequency (cpm)	Specimen
Linde 124 weld HAZ material "C"	1	C-24-HAZ-1	1	C-23-HAZ-1
Linde 124 weld HAZ material "CQ"	1	CQ-1 HAZ	1	CQ-2 HAZ
			5	CQ-3 HAZ
Linde 80 weld HAZ material "C"	1	C-3 HAZ	1	C-4 HAZ
A533B plate "04"	1	2D 3Q-6	1	02GB-2
	1	2D 3Q-5	1	2D1Q-2
Linde 0091 weld material "D"	1	D-1 HAZ	1	D-2 HAZ
			1	D-4 HAZ
			1	D-6 HAZ
Linde 124 weld material "KH"	Test results not yet available			
Linde 0091 weld material "DD"				

4.4 Characterization of Test Environments Through Free Corrosion Potential Measurements

The objective of this phase of the work is to monitor the environment-material interaction with time by continuous measurement of electrochemical potential. Different reference electrodes have been incorporated into the corrosion fatigue test loops: an external silver-silver chloride (Ag/AgCl) reference electrode and two paladium-hydrogen (Pd/H) reference electrodes. One Pd/H reference electrode has been placed in the corrosion fatigue chamber. The tip of the electrode is adjacent to the notch of the CT test specimen. Other electrodes are located in a separate electrode chamber in the autoclave effluent line. The current experimental arrangement is shown in Figs. 4.5–4.7. The electrode chamber presently contains an Ag/AgCl reference electrode, a Pd/H reference electrode, a A508 steel sample, a thermocouple, and a Pt counter electrode.

Limited experiments have been conducted during this reporting period, and those were confined to measuring the free corrosion potential of the A508 and Pt coupons vs the Pd/H and Ag/AgCl reference electrodes in the test chamber. Both reference electrodes appeared to operate satisfactorily during initial qualification tests. A posttest calibration test on

ORNL PHOTO 2176-84

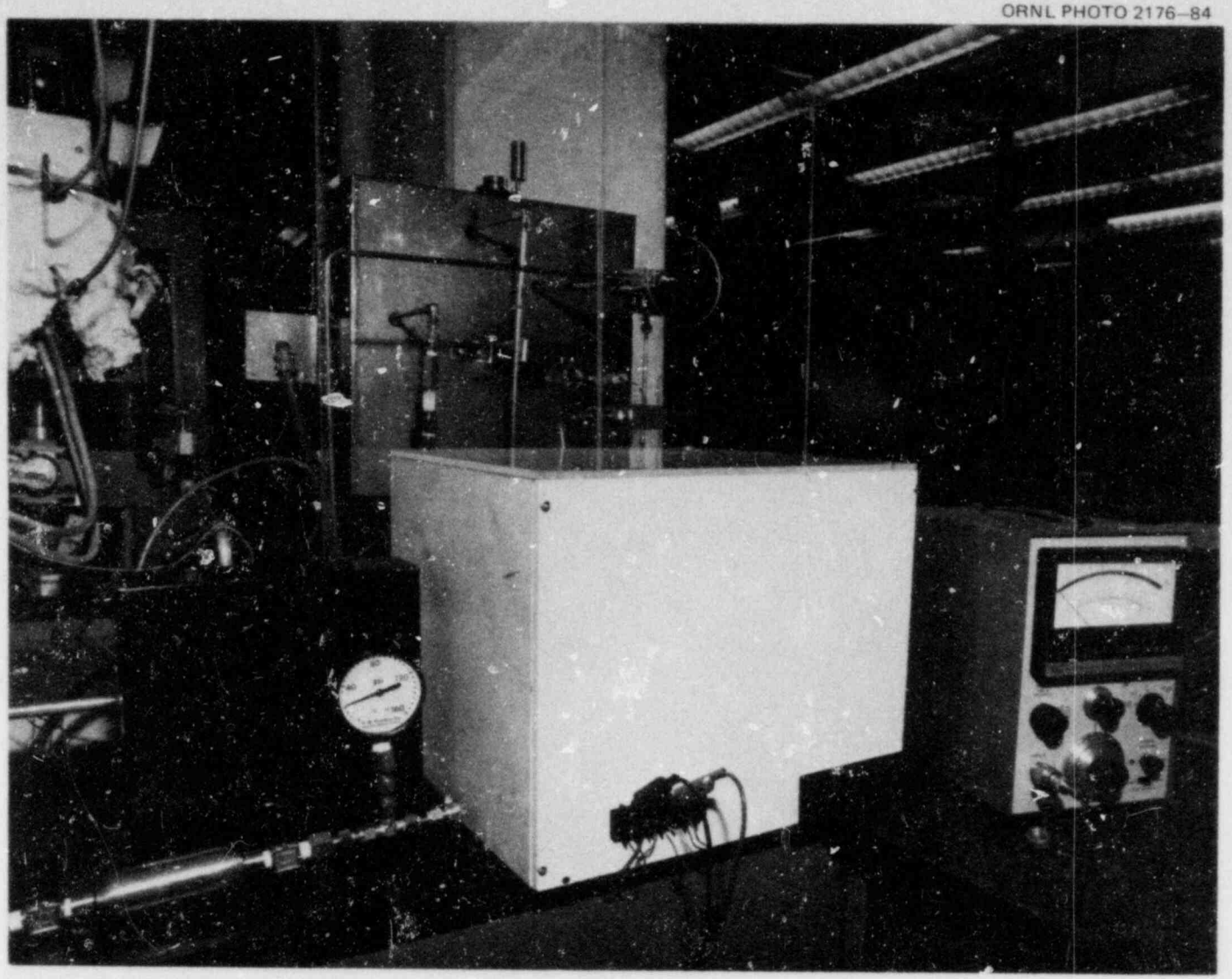

Fig. 4.5. Photograph of electrochemical measurement apparatus. Note that inside white box in foreground is separate test chamber for checking out various measurement devices, as shown in Fig. 4.6.

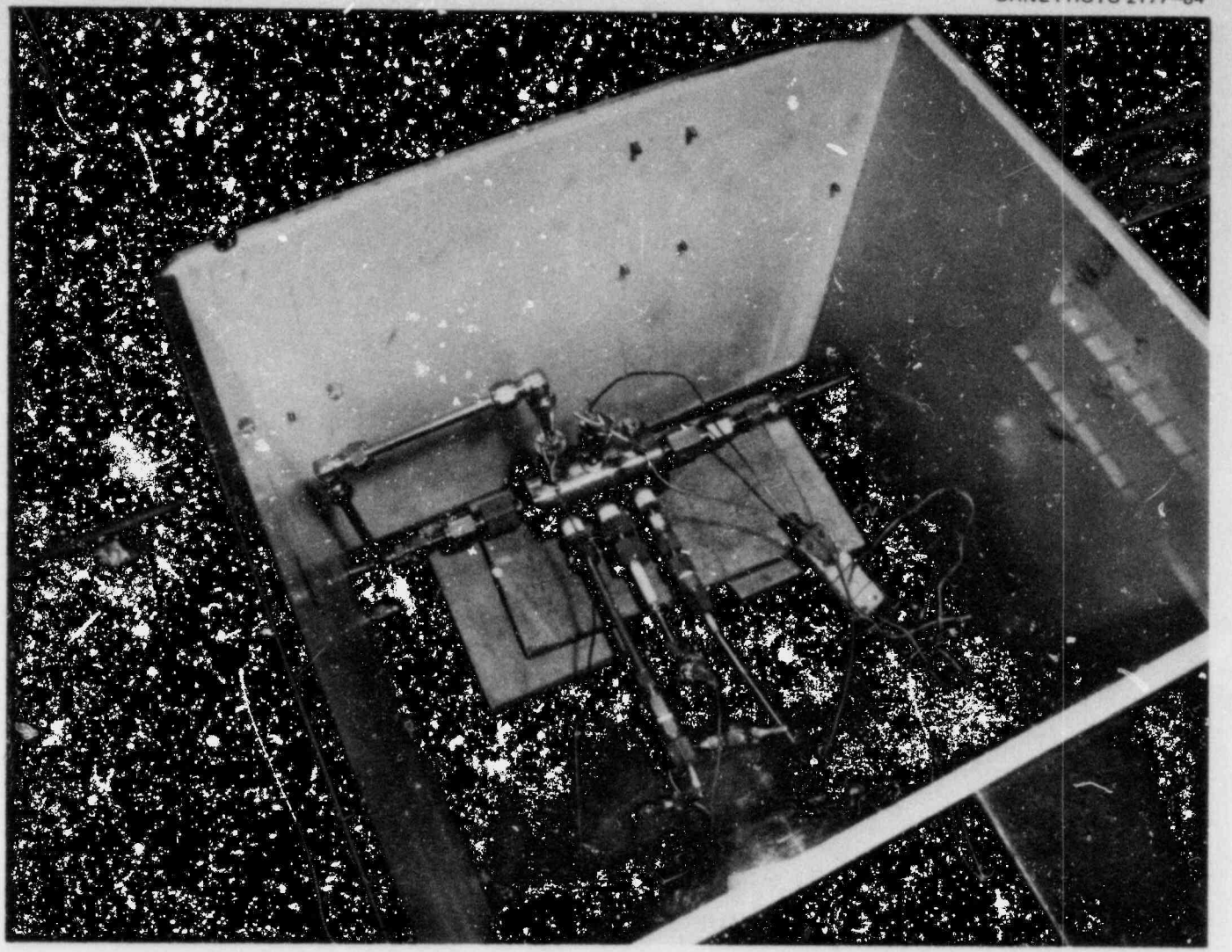

Fig. 4.6. Inside of white box showing separate small pressure vessel for checking out various measurement devices.

ORNL PHOTO 2178-84

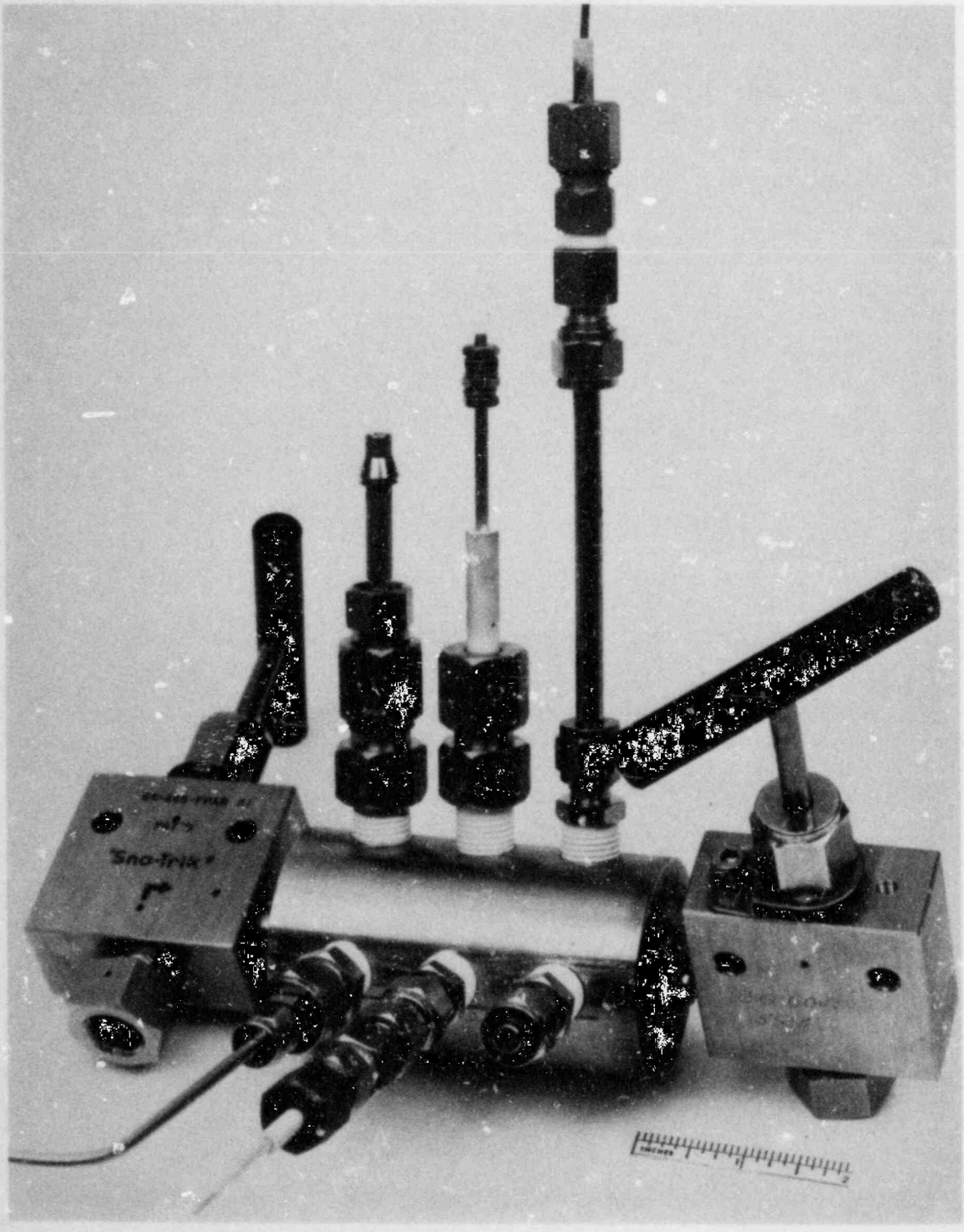

Fig. 4.7. Close-up of potential measurement devices installed in separate test chamber.

the Ag/AgCl reference electrode revealed that the electrode potential had changed by <18 mV over the 200-h exposure at test temperature of 288°C.

In an effort to optimize the Ag/AgCl electrode performance, impedance tests have been performed to optimize the zirconia plug that acts as an ion exchange barrier between the test environment and the dilute KCl internal electrolyte. The ac impedance studies have been performed on several batches of zirconia and commercial reference junctions. The objective of the testing is to determine a qualification test that will index the behavior of the plug. This will be correlated with the plug stability and the long-term electrode performance. Figure 4.8 is a block diagram of the experimental apparatus used for the impedance studies. An ac current is passed through a known resistance and across the plug that is emersed in 0.1 M KCl. Assuming that the electrode impedance is mainly resistive at the frequency of the measurement, the impedance of the plug in the cell is given by:

$$R_x = R_s[V_x/V_s] \ , \qquad (4.1)$$

where

R_x = impedance across the cell,
R_s = impedance across the known resistor,
V_x = voltage drop across the cell,
V_s = voltage drop across the whole resistor.

The voltages are measured using Keithley 169 voltmeters that have input impedances of >10 MΩ and are shunted by <100 pF. These instruments provided useful readings over the frequency range from 30 Hz to 5 KHz. Sample test data from duplicate specimens from two batches of zirconia are listed in Table 4.4. The measured impedances are higher than expected.

Table 4.4. Impedance results measured on porous zirconia plugs in 0.1 M KCl

Frequency (Hz)	Plug B1 (MΩ)	Plug B2 (MΩ)	Plug C1 (MΩ)	Plug C2 (MΩ)
30	11.11	9.68	10.80	10.81
100	9.89	9.85	10.24	9.81
300	7.56	7.41	8.47	4.55
1K	3.12	3.11	4.04	2.76
3K	1.19	1.19	1.59	1.03
5K	0.83	0.85	1.11	0.72
10K	0.61	0.60	0.80	0.52

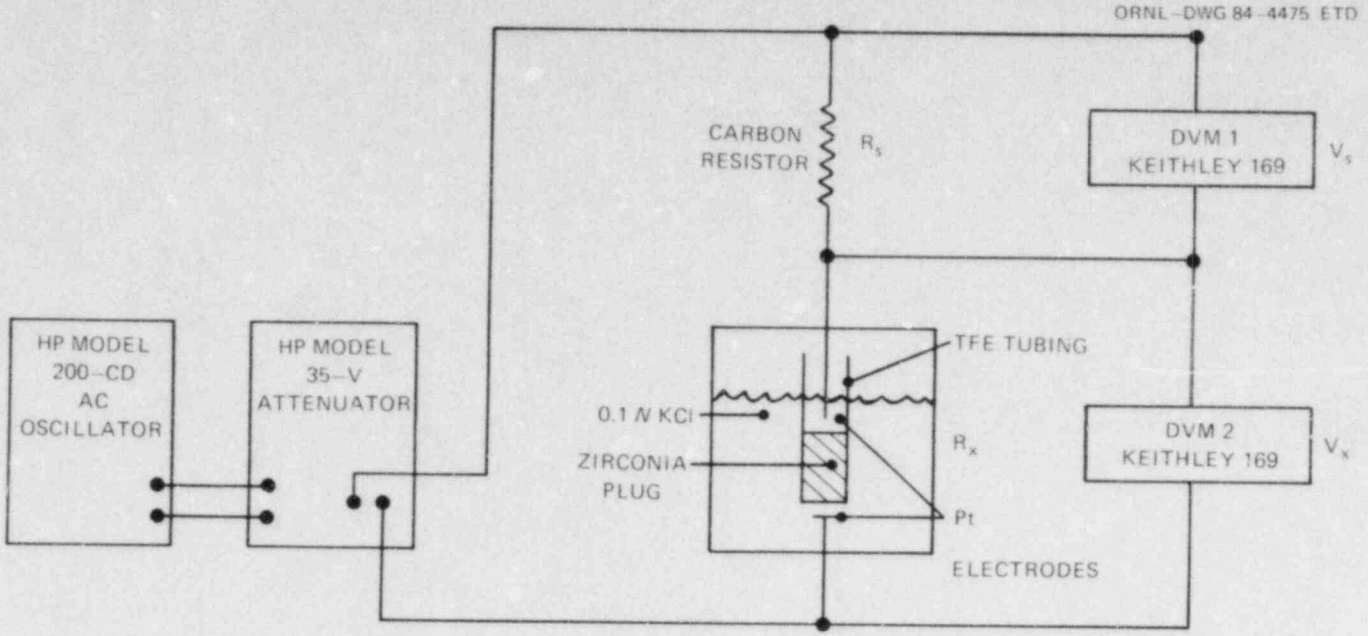

Fig. 4.8. Instrumentation for zirconia plug ac impedance studies.

Impedance values ranging from 20 to 200 KΩ were expected based on similar measurements made by Andresen on zirconia plugs used for similar reference electrode applications. Apparently, the zirconia that is being used in this project has much less porosity than that used by Andresen. The influence of the higher electrode impedance on the Ag/AgCl reference electrode performance is being investigated.

A second test of the reference electrodes has been initiated. The test stand is being slowly heated from room temperature to 288°C. The autoclave is being allowed to stabilize at several temperatures during the process of heating. At 150°C, the free corrosion potential of the A508 was approximately −250 mV with respect to the Ag/AgCl reference electrode containing 0.01 M KCl. Once the appropriate temperature has been obtained, the present intent is to allow the reference electrodes to operate for time periods in excess of 500 h. Some polarization measurements will also be performed using the A508 coupon in the test cell.

4.5 International Cyclic Crack-Growth Rate Group

The International Group on Cyclic Crack-Growth Rates (ICCGR Group) is an interdisciplinary group set up to share information on corrosion fatigue. The group was formed in 1977 at the initiative of the Nuclear Regulatory Commission (NRC) and Electric Power Research (EPRI), the two major U.S. sponsors of research in corrosion fatigue of pressure vessel steels in light-water reactor (LWR) environments. They realized that a systematic study of the variables affecting corrosion fatigue and their possible synergistic interactions would be prohibitively expensive and time consuming if undertaken by a single organization. This initiative received enthusiastic support in Western Europe and Japan and resulted in the formal charter of the ICCGR Group in November 1978. A review of the group's function and achievements in its first 4 years of existence has been given by Slama and Jones.[5]

The general objective of the ICCGR Group is to coordinate the research and development efforts on environment-assisted cyclic crack growth in pressure boundary materials in light-water service environments undertaken in Western Europe, North America, and Japan. Specific objectives are to

1. provide a forum for the timely interchange of information, ideas, and test data between research workers;
2. plan and perform cooperative research programs;
3. develop consensus test procedures and data reduction methods and encourage the transfer of such procedures and methods to the appropriate "standards" activities;
4. develop well-qualifed crack-growth rate data bases and improved understanding of the rate determining factors; and
5. make recommendations on the application of research results and laboratory test data to engineering practice and encourage the transfer of this information by organizing symposia, interacting with code committees and regulatory bodies, etc.

The focus of the group activities to date has been on the pressure vessel steels A533B1, A508-C12, and A508-C13, but work on other nuclear pressure boundary materials is also reported and discussed during the semiannual meetings, which alternate between the United States and Western Europe. Currently, 36 organizations from 11 countries participate in the activities of the ICCGR Group. Members include experts in mechanics, corrosion chemistry, and metallurgy; as required, additional experts are invited to the meetings. Task groups were formed to concentrate on specific topics. Three such task groups are active at present in the areas of Test Methods and Results, Mechanisms, and Data Collection and Evaluation.

Participation in the ICCGR meetings is one of the key elements of this work, because it is the best forum presently available for exchanging information on current research in the areas of corrosion and corrosion fatigue in LWR materials. Therefore, the status of the group's activities will be reviewed periodically in these reports. The most recent meeting of this group was held in Schenectady, New York, in October 1983, and the discussions held in each of the areas of technical interest of the group are reviewed below.

4.5.1 Test methods and results group

The emphasis of this subgroup has been to develop standardized methods of testing and data analysis and reporting. The testing methods have been refined through round-robin testing and other comparisons, and now good agreement is found between virtually all member laboratories for tests performed under similar loading conditions. A good summary of the way in which this was accomplished is found in Ref. 5. The present emphasis in the area of test methods is measuring the open circuit electrochemical potential on a test specimen. This information is presently viewed as the best characterization of the overall water environment. Recent work has been aimed at developing reliable long-term measurement devices and developing a method of reporting electrochemical potential measurements relative to a standard hydrogen scale. Two separate measurement surveys have been carried out and have resulted in significant improvements in measurement techniques in a relatively short period of time. Presently the most reliable measurement techniques are the Ag/AgCl electrode developed by Andresen[6] and the Pd/H electrode; work is continuing to further refine these two methods.

The second area of interest to this group involves sharing of recent results in both corrosion and corrosion fatigue tests. Apparently, two major parameters can affect the results of fatigue crack-growth rate tests, which are otherwise conducted under the same range of applied stress-intensity factor and water chemistry. These parameters are the flow rate of the water environment and the inclusion content of the steel, often characterized by the sulfur content. It is clear that the amount of enhancement in crack growth due to the water environment is strongly increased in steels with high sulfur content and for tests conducted under lower flow conditions. A great deal of experimental work is presently under way to further investigate the conditions that can exist in the

crack-tip region, because it is becoming clear that the level of environmental enhancement is controlled by the events occurring in this region. The sulfur content affects crack growth because the manganese sulfide inclusions dissolve, releasing sulfur into the water and causing acidification. The bulk flow rate of the test environment affects the level of enhancement, because it controls the refreshment rate of the crack-tip environment. A series of tests have recently demonstrated these conclusions qualitatively.

4.5.2 Mechanisms group

The thrust of the work by this subgroup has been to provide mechanistically based explanations for the differences observed in corrosion and corrosion fatigue data in the water environment. Thus, the work of this group involves close interaction with the efforts of the test methods and results subgroup. The work includes developing and proving theories concerning the mechanisms involved through small-scale tests, study of available data, and study of fracture surfaces of tested specimens. It presently appears that most available crack-growth rate results can be explained in terms of the crack-tip strain rate and the quantities that affect it, for example, the passivation rate, liquid diffusion rates, and oxide rupture rates. This approach has resulted in the beginnings of a quantitative understanding of the effects of sulfur and bulk flow rate.

4.5.3 Data collection and evaluation group

This subgroup has responsibility for establishing a data base of the existing corrosion and corrosion fatigue crack-growth data and developing reference laws for the prediction of crack extension. Validation tests are also designed to test the usefulness of predictive models. This subgroup works in close cooperation with the MPC/PVRC working group on crack propagation technology, whose task is to develop reference curves for ASME Code pressure vessels and piping. The work of this subgroup is now accelerating, as the testing methods have been refined for consistency and the mechansims are now beginning to be understood. Recent efforts of the group have included contributions to development of a reference crack-growth rate curve for stainless steels and a consideration of spectrum load and component tests for validation of reference crack-growth laws.

References

1. W. H. Bamford, R. Jacko, and L. J. Ceschini, "Environmentally Assisted Crack Growth in Light Water Reactors," in *Heavy-Section Steel Technology Program Quart. Prog. Rep. July–September 1983*. ORNL/TM-8787/V3 (NUREG/CR-3334, Vol. 3), Union Carbide Corp. Nuclear Div., Oak Ridge Natl. Lab., February 1984.

2. W. H. Bamford, "Environmental Cracking of Pressure Boundary Materials, and the Importance of Metallurgical Considerations," in *Aspects of Fracture Mechanics in Pressure Vessel and Piping*, ASME Publication PVP-vol. 58, 1982.

3. W. H. Bamford, D. M. Moon, and L. J. Ceschini, "Studies of Statically and Dynamically Loaded Cracks in Simulated Pressurized Water Environment," presented as paper No. 12, *Corrosion* 83, Anaheim, Calif., April 1983 (submitted for publication in *Corrosion*).

4. W. H. Bamford, D. M. Moon, and L. J. Ceschini, "Environmentally Assisted Crack Growth in Light Water Reactors," in *Heavy-Section Steel Technology Program Quart. Prog. Rep. October–December 1982*, ORNL/TM-8369/V4, (NUREG/CR-2751, Vol. 4), Union Carbide Corp. Nuclear Div., Oak Ridge Natl. Lab., May 1983.

5. G. Slama and R. Jones, "International Cooperative Group on Cyclic Crack Growth Rate," in *Proceedings, Sixth SMiRT Conference, Post Conference Session 8, Paris, France, 1981.*

6. *Mechanisms of Environmental Cracking in Systems Peculiar to the Power Generator Industry*, prepared by General Electric Co., F. P. Ford, principal investigator, EPRI NP-2589 (Final Report), September 1982.

5. CRACK-ARREST TECHNOLOGY

5.1 Crack-Arrest Studies at ORNL

5.1.1 Preliminary wide-plate test planning (C. E. Pugh)

During this report period, plans were made for the performance of a series of six crack-arrest tests on plate specimens whose dimensions are about 1 × 1 × 0.1 m. The plans were developed after an exploratory discussion between the Nuclear Regulatory Commission (NRC) and Japanese organizations revealed that a practicable cooperative program using Japanese test systems could not be forthcoming. After assessing the suitability and availability of existing large-capacity tensile equipment, it was decided that the tests would be performed at the National Bureau of Standards (NBS) in Gaithersburg, Maryland. The NBS was selected, in part, because of the ease of Oak Ridge National Laboratory (ORNL) working with another federally owned facility and because of supplemental NBS studies that will be carried out. The NBS machine has a tensile load capacity to 26.7 MN (6 million pounds). Although this loading capacity is considerably less than the 100 MN (22 million pounds) that the Japanese machine can apply, very meaningful tests can be performed.

The objectives of the test are threefold: (1) develop crack-arrest-toughness data at temperatures high in the transition region and hopefully in the upper-shelf region of Charpy test data; (2) provide data, such as crack velocities, dynamic strain fields, and loadings, that will be used to validate or improve elastic and vicoplastic dynamic fracture-mechanics (FM) models; and (3) provide improved experimental dynamic fracture methods. The basic test begins by initiating the propagation of a crack in the cold region of a single-edge-notched (SEN) wide plate that is loaded transverse to the crack path and that has a linear temperature gradient in the direction of the propagation. The crack is then to arrest in a warm region where the crack-arrest toughness K_{Ia} is much higher. The specimen is to be attached to pull tabs that are sufficiently long (see Fig. 5.1) so that stress waves will not be reflected from the pull-pin region until after the run-arrest event has been completed. To obtain meaningfully high K_{Ia} values, a warm prestressing (WPS) technique is to be used to permit application of an initial load that is greater (by as much as a factor of 2 or more) than that required for the stress intensity K to be equal to K_{Ic}. Professor G. R. Irwin of the University of Maryland suggested, in private communications, procedures similar to those shown below.

Step 1. Heat the entire plate up to or above the temperature where arrest is expected to take place.
Step 2. Apply tensile load so that K is equal to the desired initiation level (e.g., $K_I = K_o$).
Step 3. Unload specimen by about 10% while maintaining uniform temperature.
Step 4. Apply the temperature gradient across specimen that is to be used in the test.
Step 5. Increase load until initiation occurs.

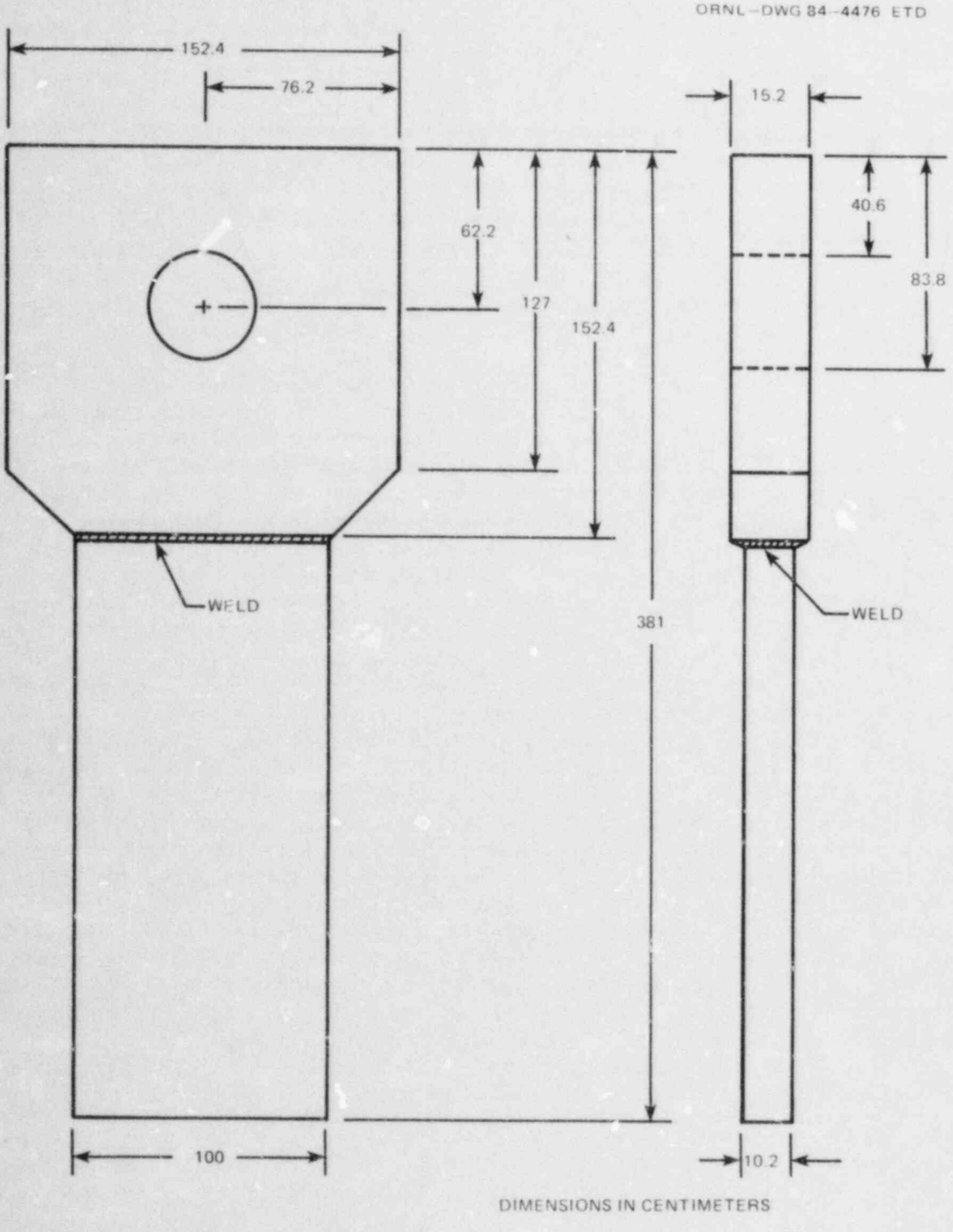

Fig. 5.1. Schematic of a pull-plate assembly for a wide-plate test.

The test specimens are to be taken from the Heavy-Section Steel Technology (HSST) plate 13-A of A533 grade B class 1 steel, which has vendor-provided property values: yield stress of 414 MPa, ultimate tensile stress of 550 MPa, and nil ductility temperature of 29°C. The material is to be fully characterized by tensile, Charpy, fracture toughness, and crack-arrest toughness through the use of laboratory specimens. This same material will also be used in the viscoplastic characterization studies to be carried out at the Southwest Research Institute as part of Task 2 of the HSST Program. The effectiveness of the WPS procedure is to be studied by the NBS (Boulder) through some beam tests (101 × 152 × 762 mm).

5.1.2 Preliminary wide-plate test analyses (B. R. Bass, J. W. Bryson, J. G. Merkle, C. E. Pugh, and D. A. Steinert)

During this report period, scoping analyses were conducted in support of defining the series of SEN wide-plate crack-arrest tests. Basically, the analyses considered the test configuration proposed in Ref. 1. In particular, the test plate has a width and length equal to 1 m, and the specimen is attached to upper and lower pull plates (see Fig. 5.1). Tentatively, the plate thickness will be 100 mm, with 12.5 percent-of-thickness side grooves to control crack-plane and crack-front straightness. The scoping analyses considered initial cracks having a depth ratio a_o/w in the range of 0.029 to 0.20. These cracks would initiate under the applied tensile load and thermal gradient and would arrest at an a_f/w value in the range of 0.40 to 0.60.

First, finite-element analyses were performed for one case to estimate the through-thickness variation of K_I values; the computed K_I values were also compared with results from selected empirical formulas. Three-dimensional finite-element models of the SEN specimen (without side grooves) were generated and analyzed with the ORMGEN/ADINA/OKVIRT FM system. Here the plate thickness t = 76.2 mm, initial crack-depth ratio $a_o/w = 0.2$, and arrest ratio $a_f/w = 0.45$. Because of symmetry considerations, only a quarter of the plate was modeled. Analyses for the inital crack-depth ratio $a_o/w = 0.2$ utilized both linear and nonlinear material models. In the linear-elastic calculations, quarter-point elements were used at the crack front for a $1/\sqrt{r}$ singularity in the stress and strain fields; the finite-element model consisted of 2858 holes and 570 20-noded isoparametric elements. For the elastic-plastic calculations, collapsed prism elements were used to allow for a 1/r singularity at the crack front. The nonlinear material response was modeled by the Ramberg-Osgood power-hardening law that in the uniaxial case takes the form

$$\varepsilon/\varepsilon = \sigma/\sigma_o + \alpha\,(\sigma/\sigma_o)^n \,. \qquad (5.1)$$

Materials constants were selected to approximate the response of A533B pressure vessel steel: Young's Modulus $E = 2.07 \times 10^5$ MPa, Poisson's ratio $\nu = 0.3$, yield stress $\sigma_o = 414$ MPa, strain-hardening exponent $n = 10$, and constant $\alpha = 0.05$.

For the SEN models having $a_o/w = 0.20$, a uniform tensile stress σ = 120.7 MPa was applied on the transverse plane located 1 m from the plane

of the crack. The through-thickness K_I distribution from the linear model is given in Fig. 5.2, along with the pseudo-K_I values obtained from the nonlinear calculation of J and from the relation $K_I = \sqrt{E/J(1 - 2\nu)}$. Also included in the figure is the K_I value computed from the empirical formula from Ref. 2,

$$K_I = \sigma \sqrt{\pi a_o}\, F(a_o/w) \ , \tag{5.2}$$

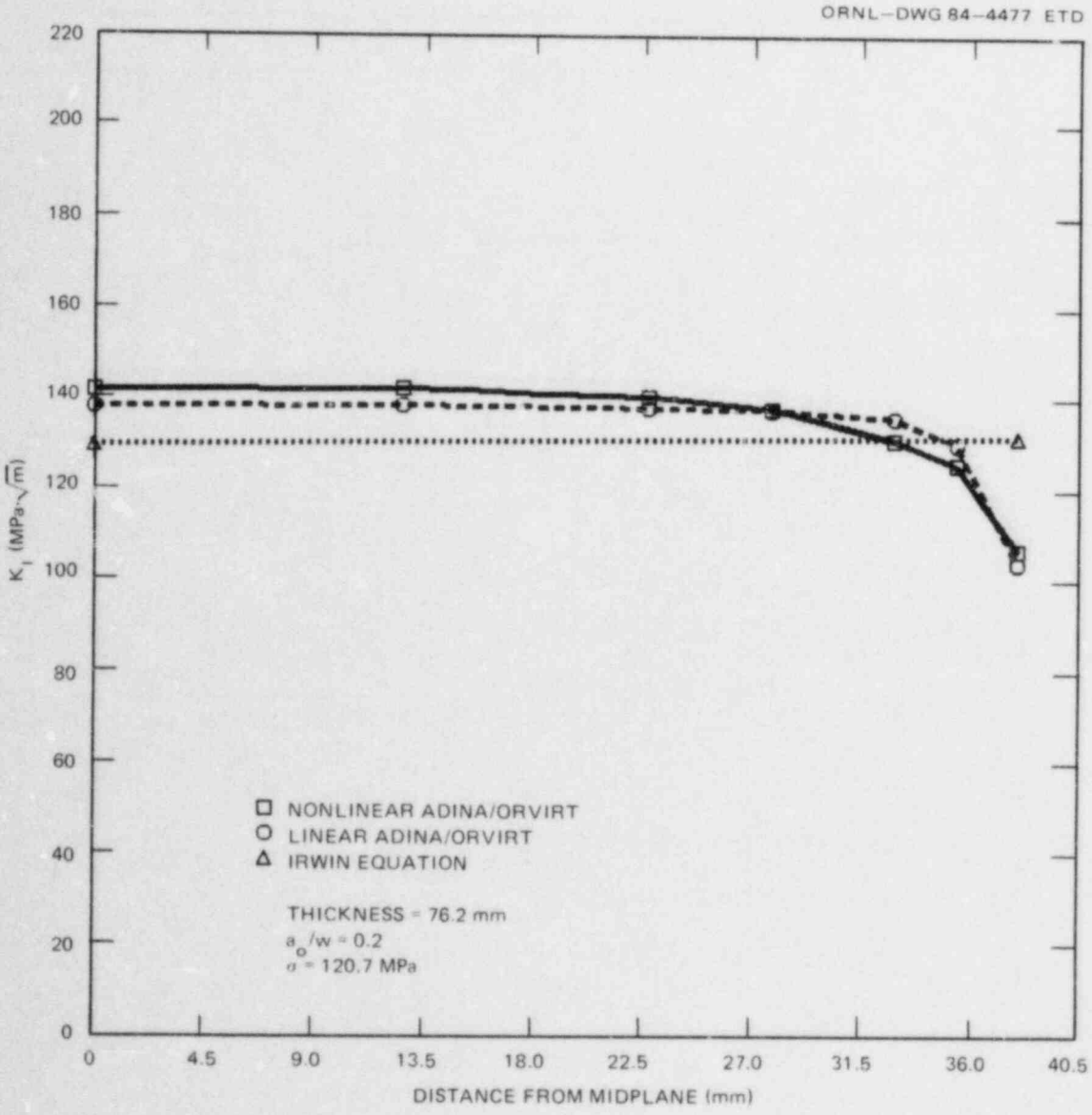

Fig. 5.2. Through-the-thickness variation of K_I for initial crack-depth ratio $a_o/w = 0.2$.

where

$$F(a/w) = \sqrt{\left(\frac{2w}{\pi a}\right)\tan\left(\frac{\pi a}{2w}\right)}\;\frac{0.752 + 2.02(a/w) + 0.37\left[1 - \sin\left(\frac{\pi a}{2w}\right)\right]^3}{\cos\left(\frac{\pi a}{2w}\right)} . \quad (5.3)$$

In Fig. 5.3, the SEN model having the arrested crack-depth ratio a_f/w = 0.45 was analyzed for two different boundary conditions assuming a linear-elastic material model. The K_I distribution for the applied load case was obtained using the same stress boundary condition (σ =120.7 MPa) that was applied to the models of a_o/w = 0.2. For the applied displacement case,

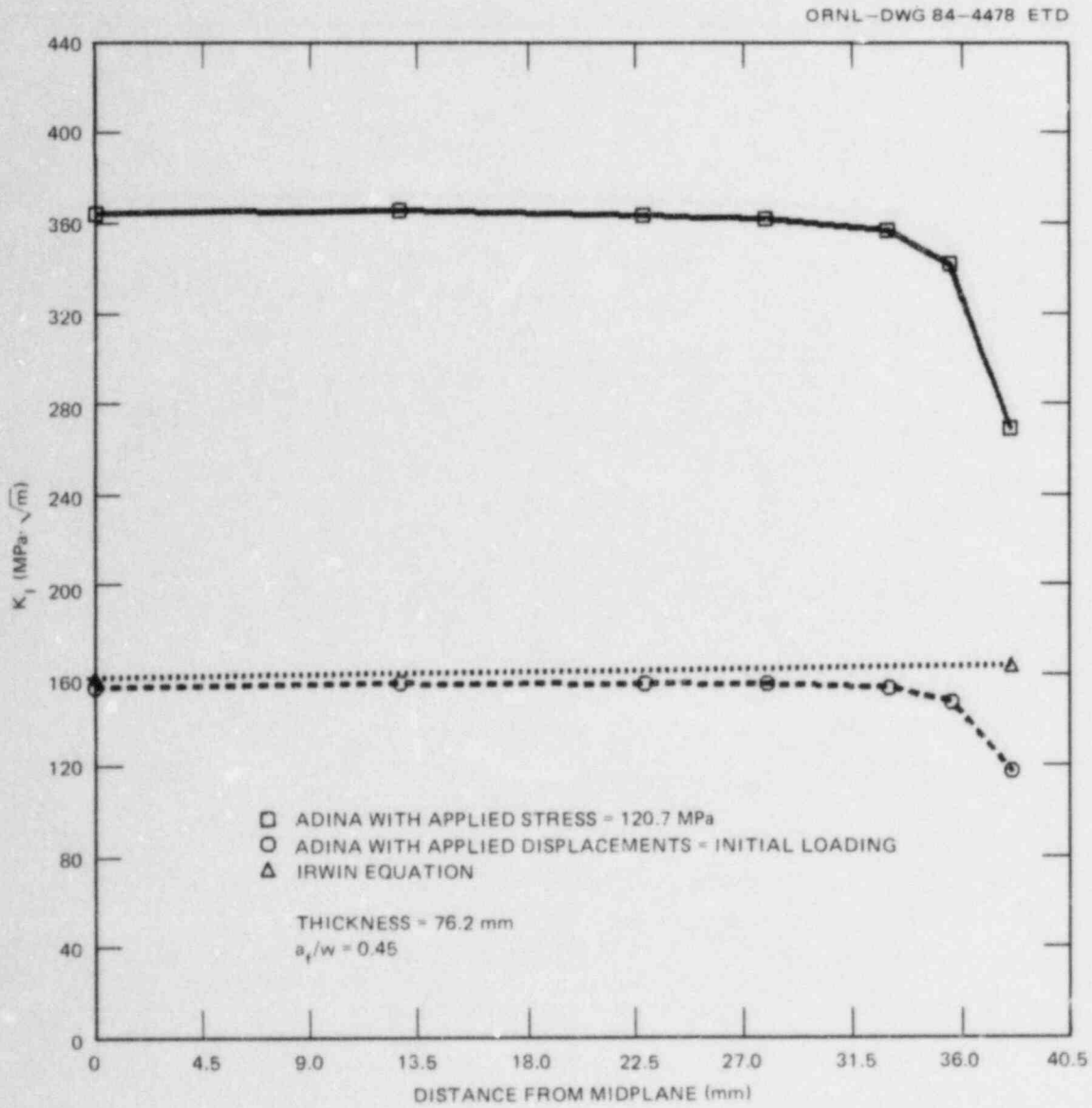

Fig. 5.3. Through-the-thickness variation of K_I for arrested crack-depth ratio a_f/w = 0.45.

the axial deflections computed for the stress loading plane of the linear model of $a_o/w = 0.2$ were applied to the model of $a_f/w = 0.45$. In Fig. 5.3, these results are compared with an empirical relation for K_I suggested by Irwin[1]

$$K_I = \sigma \left[\pi a_f \sec \left(\frac{\pi a_f}{2w}\right)\right]^{1/2} . \tag{5.4}$$

The results of Fig. 5.3 yield estimates of the K-reduction that would result because of dynamic effects for a rapid crack approaching crack arrest.

To aid in scoping the NBS test system for application to the wide-plate tests, K_I approximations were made using Eq. (5.2), the Irwin formula [Eq. (5.4)], and the following equations: Japanese ESSO,[3]

$$K_I = \sigma \left[2w \tan \left(\frac{\pi a_f}{2w}\right)\right]^{1/2} ; \tag{5.5}$$

Rolfe and Barsom,[4]

$$K_I = \sigma[\pi a_f]^{1/2} F(a_f/w) ; \tag{5.6}$$

and modified Rolfe,

$$K_I = \sigma[\pi a_f]^{1/2} F(a_o/w) , \tag{5.7}$$

where F(a/w) is given by Eq. (5.3). For an arrested crack-depth ratio $a_f/w = 0.45$, Fig. 5.4 depicts the relation between K_Q, which is calculated from Eq. (5.2), and the arrest values K_{Ia} from the Irwin relation [Eq. (5.4)] for initial crack-depth ratios ranging from 0.029 to 0.20. These curves are used to estimate the arrest value K_{Ia} that could be expected for a given initial crack-depth ratio a_o/w and applied K_Q value. The P = 6000 curve denotes the maximum K_{Ia} value (~360 MPa$\cdot\sqrt{m}$), associated with arrest ratio $a_f/w = 0.45$ that can be achieved at the maximum load capacity [26.7 MN (6000 kips)] of the NBS test system. The RLS = 70 denotes the K_{Ia} values (~295 MPa$\cdot\sqrt{m}$) associated with an average net ligament stress equal to the flow stress of 484 MPa (70 ksi). Figure 5.5 depicts this upper bound in K_{Ia} as a function of arrest depth ratio a_f/w over the interval 0.4 to 0.6. As the figure indicates, the maximum K_{Ia} curve is independent of the initial depth ratio a_o/w. Figure 5.6 gives an estimate of the reduction in K_I values caused by dynamic effects for a fast crack approaching arrest. The Rolfe curve indicates the variation of static K_I values with arrest depth ratio a_f/w; while the ESSO, Irwin, and modified Rolfe approximate the reduced dynamic values. These results are presented for a far-field stress of $\sigma = 120.7$ MPa.

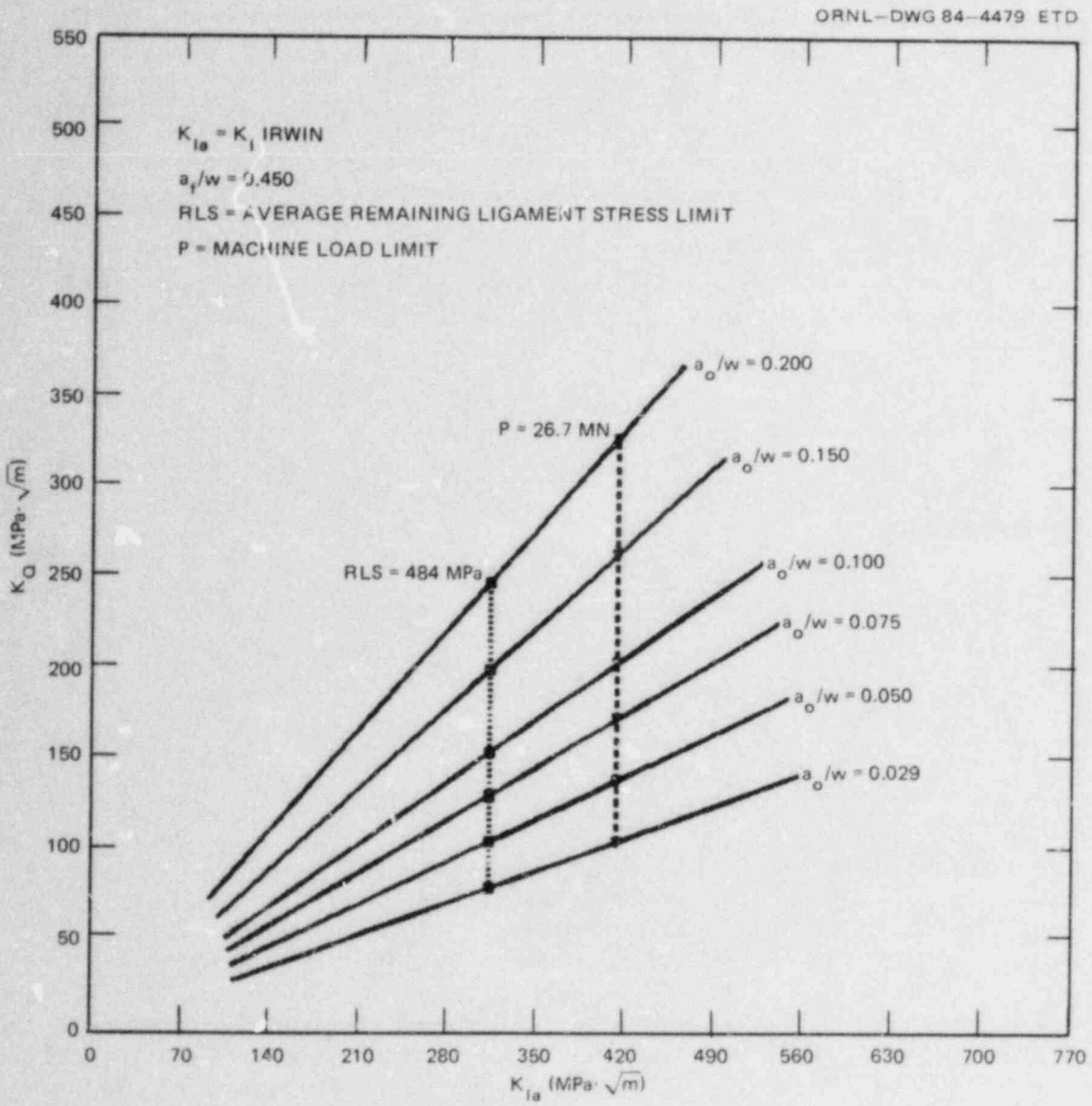

Fig. 5.4. Initiation vs arrest stress-intensity values for crack arrest at a/w = 0.45, and for various initial crack depths.

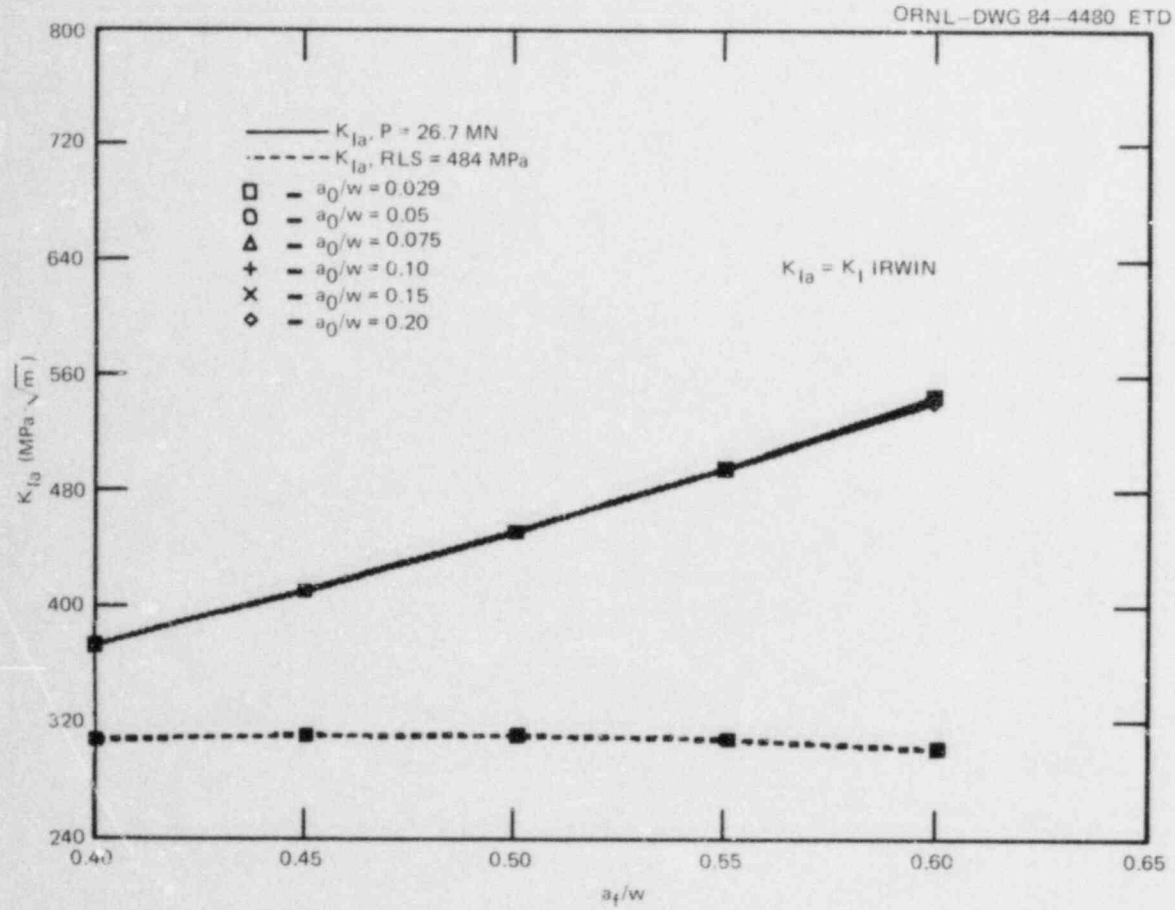

Fig. 5.5. Maximum crack-arrest values vs final crack depth based on load capacity of NBS machine (P = 6000 kips = 26.7 MN) and on average remaining ligament stress equal to 484 MPa (70 ksi).

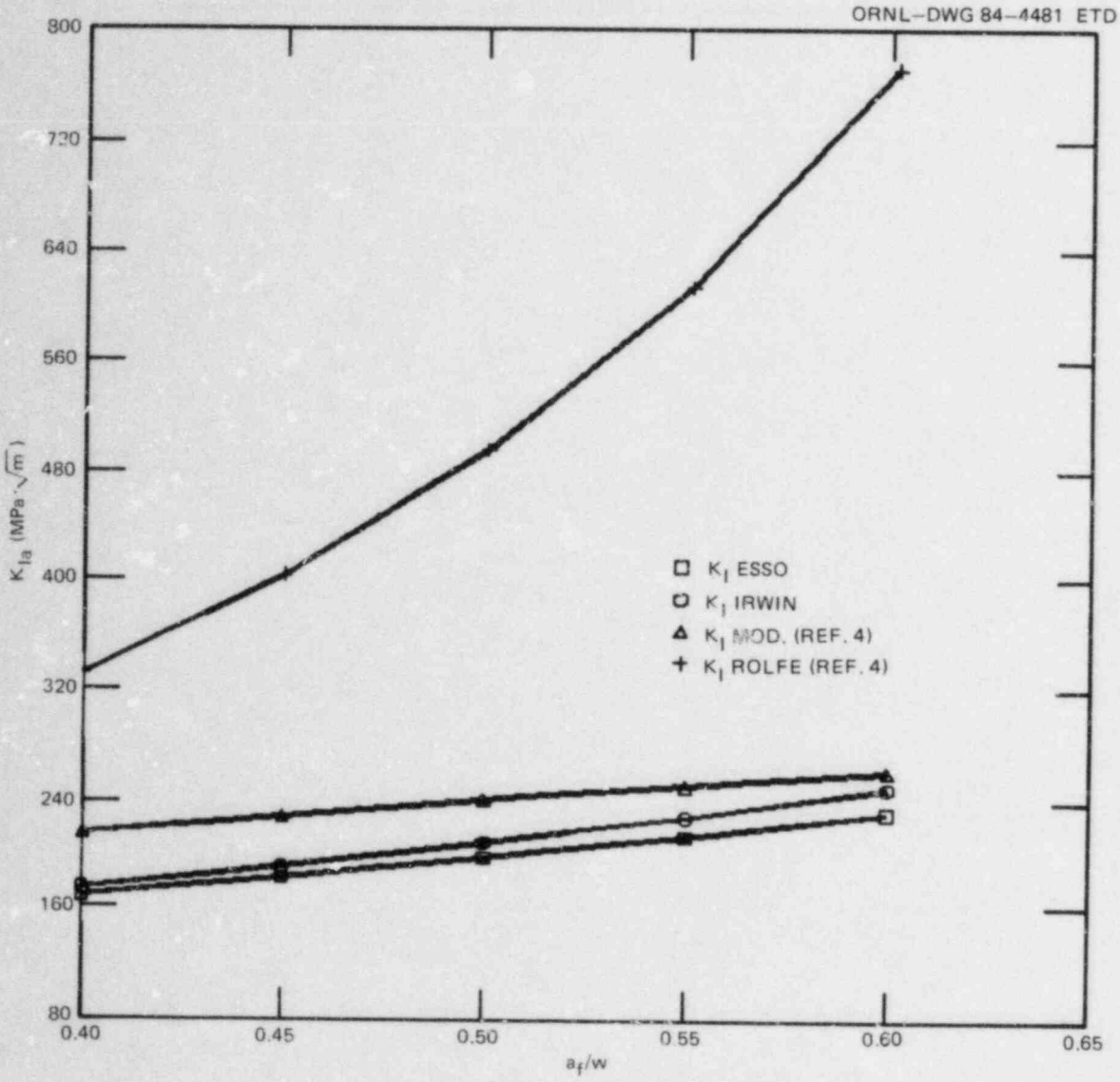

Fig. 5.6. Crack-arrest toughness values vs arrested crack depth calculated by various empirical equations for far-field stress of 121 MPa and initial $a_o/w = 0.20$.

5.2 Crack-Arrest Studies at The University of Maryland*

W. L. Fourney† G. R. Irwin†
R. Chona†

5.2.1 Analysis and experiments in support of wide-plate tests

Two experiments were conducted with compact tension (CT) specimens fabricated from 7075 aluminum in which strain gages were placed 12.7 and 25.4 mm ahead of the starter notch and 12.7 mm above the crack line. The outputs from these gages were recorded on Nicolet digital oscilloscopes as the crack initiated and propagated across the specimen. Figure 5.7 shows the strain gage outputs from the two gages for one experiment. Sharp peaks in the y-directional strain (ε_{yy}) can clearly be seen as the crack ran past the gages. Further study is planned to correlate such strain gage outputs with crack-tip location and crack-tip stress intensity. This will be done with hybrid analysis techniques utilizing high-speed photography, dynamic photoelasticity, and computations with SMACR, a dynamic fracture computer code.

---

*Work sponsored by HSST Program under UCC-ND Subcontract 7778 between UCC-ND and the University of Maryland.

†Department of Mechanical Engineering, University of Maryland, College Park, Maryland.

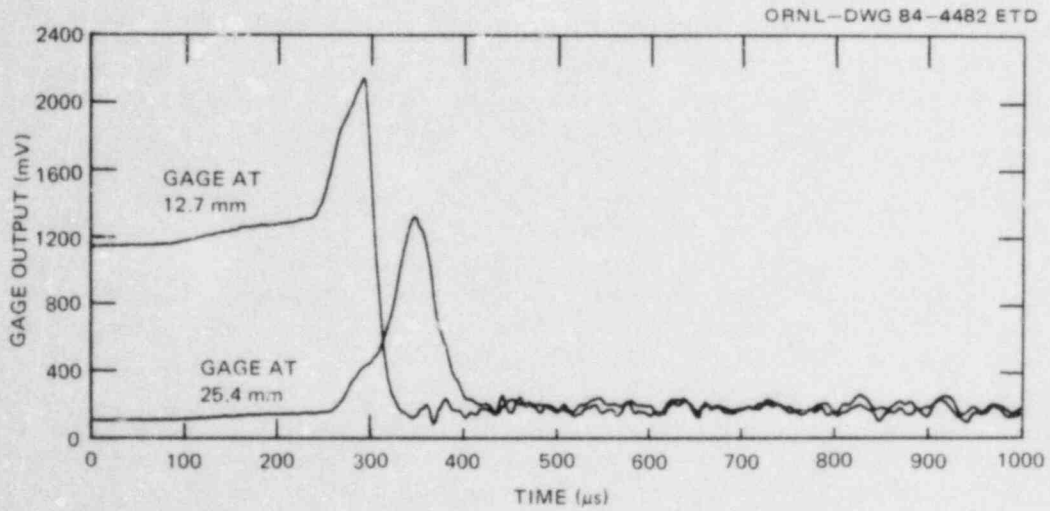

Fig. 5.7. Strain gage outputs recorded as functions of time at locations 12.7 and 25.4 ahead of notch tip, 12.7 mm above crack line, in CT specimen (W = 152 mm).

5.2.2 ASTM round robin on K_{Ia} testing

A round-robin testing program is being conducted under the auspices of American Society for Testing and Materials (ASTM) Task Group E24.01.06 on Crack Arrest to verify the validity of a proposed test method for determining the crack-arrest fracture toughness of ferritic materials. The method utilizes a crack-line-wedge-loaded compact specimen and measurements of the crack length and crack opening displacement at arrest to calculate the arrest toughness using a static analysis. The proposed method actually provides an estimate of the true value of K_{Ia}, which is a measure of the ability of a material to arrest a fast-running crack.

The specimen geometry, testing procedure, and type of data analysis were decided upon following the experience gained in a Cooperative Test Program[5] that was completed by 1980. Unlike the Coop Program, the round robin places a heavier emphasis on independent use of the test procedure by the participants. Loading fixtures and specimens are to be prepared by the participants, with only specimen blanks being provided.

In the round robin, each participant will test 12 specimens. Six specimens are of A533B reactor pressure vessel (RPV) steel and are to be tested at two specified temperatures. The other six specimens are of two bridge steels (A514 and A588) with three specimens of each tested at a specified temperature. Upon completion of the testing, the results are to be forwarded to the program administrators, who will then be responsible for preparation of a final report prior to consideration of the test method by the membership of ASTM Committee E-24 for possible adoption as an ASTM standard.

The round-robin program is being supported by the ORNL/HSST Program, Electric Power Research Institute (EPRI), and Federal Highway Authority (FHWA). The RPV steel has been provided by ORNL, and the cutting and packaging costs for the RPV steel and the bridge steels are being paid by EPRI and FHWA, respectively. The overall management of the program is carried out by the Department of Mechanical Engineering at the University of Maryland, under ORNL support. Twenty-five laboratories have volunteered to participate in the program, with nine laboratories located in the United States.

Specimen blanks of all three steels were prepared during the current reporting period and shipped to the participants in early February. This was somewhat later than originally planned, but the delay allowed both the bridge and RPV steels to be shipped at the same time, resulting in a substantial savings in shipping costs. Some of the participants have indicated that specimen preparation is under way.

The Task Group E24.01.06 met in Pittsburgh in November to discuss the choice of test temperatures for the different steels. Data obtained from R. Roberts (Lehigh University) on material properties, impact tests, RT_{NDT}, and crack-arrest toughness measurements for the A514 and A588 bridge steels were circulated to the members. The consensus was that both bridge steels could pose problems in testing due to their tendency to delaminate and display various degrees of splitting normal to the main fracture surface. In addition, the data were unclear as to a precise testing temperature for the A514 material, and there were indications that testing of the A588 material would require sequential load-unload cycling. It

was therefore decided to recommend a test temperature of −30°C (−13°F) for both the A588 and A514 specimens, since this temperature would still be within the range of practical interest of FHWA. It was also decided that the A514 and A588 specimens be tested first and that the participants should be alerted to potential problems that could occur during testing. A short writeup has been prepared by G. R. Irwin and is being circulated to the round-robin participants.

ORNL agreed to perform some preliminary tests on the A533B material to establish appropriate test temperatures. (It is desirable to test at temperatures that would provide data as far into the transition range as possible, without jeopardizing the probability of successful testing.) Problems encountered with preparation of the brittle-weld crack-starter notches have delayed a decision on the test temperatures to be used for the RPV steel. However, the preliminary tests have served to highlight a potential problem that could have caught the participants unaware. P. N. Mincer and C. W. Marschall [Battelle Columbus Laboratories (BCL)] have prepared a set of guidelines for notch embrittlement, based on their extensive experience in crack-arrest testing. It is anticipated that the test temperatures will be selected very soon.

5.3 Crack-Arrest Studies at BCL*

A. R. Rosenfield† C. W. Marschall†
P. N. Mincer† S. W. Rust†

5.3.1 Overcooling experiment support

The objective of this task is to provide crack-arrest characterization data in support of overcooling experiments carried out at ORNL. During this reporting period, experiments were completed on the PTSE-1 material and a section from the low-upper-shelf-energy weld of vessel V-8A.

Concerning PTSE-1 steel, results from brittle-weld specimens were given in the previous report,[6] and the data were for temperatures from 25 to 93°C. Attempts to initiate rapid cracks at higher temperatures were unsuccessful, even when inverted split pins were used. Because the goal was to provide K_a values up to a temperature of 150°C and/or a K_{Ia} value of 150 MPa$\cdot\sqrt{m}$, duplex specimens were fabricated. Some of these specimens were provided with contoured side grooves. However, even use of duplex specimens with contoured side grooves and inverted split pins resulted in some cracks arresting at the interface between the starter section and the test section. In those cases, data were obtained by reinitiating the arrested cracks.

The new results are shown in Table 5.1, for which the notations are defined in Table 5.2. Unstable fracture and crack arrest were obtained successfully up to 150°C. This temperature is slightly above the onset

---

*Work sponsored by HSST Program under UCC-ND Subcontract 85X-17624C between UCC-ND and BCL.

†Battelle Columbus Laboratories, Columbus, Ohio.

Table 5.1. Crack-arrest toughness of steel from PTSE-1 material[a]

Sample ID	Sample type[b]	Temperature (°C)	K_a (MPa·√m)	K_a/K_{IR}	Yield strength (MPa)	Comments
P1OR-1	1	79.0	78.0	1.974	609.0	
P1OR-1a	12	67.0	149.0[c]	4.049	612.0	
P1OR-2	1	93.0	73.0	1.661	606.0	
P1OR-2a	12	51.0	33.0	0.963	616.0	
P1OR-3	1	51.0	53.0	1.546	616.0	
P1OR-3a	12	25.0	46.0[c]	1.442	622.0	
P1OR-4	1	79.0	89.0	2.253	609.0	
P1OR-4a	12	52.0	47.0[c]	1.366	616.0	
P1OR-8a	13	67.0	147.0[c]	3.995	612.0	
P1OR-5	1	66.0	53.0	1.448	613.0	
P1OR-5a	12	29.0	39.0[c]	1.213	621.0	
P1OR-10	9	150.0	140.0[c]	1.494	593.0	
P1OR-11	14	53.0	70.0[c]	2.026	616.0	
P1OR-12	9	107.0	90.0[c]	1.787	603.0	
P1OR-15	11	66.0	92.0	2.513	613.0	*d*
P1OR-16	9	121.0	106.0[c]	1.779	559.0	
P1OR-17	11	81.0	117.0	2.921	610.0	*d, e*
P1OR-18	14	68.0	73.0[c]	1.973	612.0	*d*
P1OR-13	9	122.0	117.0[c]	1.937	599.0	
P1OR-6	10	137.0	128.0[c]	1.701	596.0	
P1OR-7	14	137.0	88.0	1.170	596.0	

[a]A complete printout of the raw data and subsidiary calculations is available from the authors upon request.

[b]See Table 5.2 for key to notation.

[c]Dimensions are too small to satisfy the tentative ASTM requirements.

[d]Crack ran badly out of side grooves.

[e]Very irregular crack front.

of the Charpy upper shelf (~140°C), consistent with past experience[7] that the upper-shelf-onset temperature is about the limit for obtaining crack-arrest data using current BCL procedures. However, despite the Charpy specimen behavior, low-power fractographic examination (30×) revealed that the compact-specimen crack-jump mechanism at 150°C was cleavage.

It also should be pointed out that the 150°C specimen does not satisfy the tentative ASTM size requirements. The main concerns are the length of the remaining ligament, which is only 70% of the minimum allowed value, and the thickness, which is only 80% of the minimum allowed value.

Table 5.2. Sample types

Type No.	Specimen geometry[a]	Starter notch[b]	Split-pin geometry[c]	Initiation[d]	Other
1	Compact	BW	N	O	
2	Contoured DCB	F			Machine loaded
3	Cylinder	H			Thermal shock
4	DCB	D			
5	Compact	D	N	O	Test after 1/1/80
6	ESSO				
7	Compact	BW	I	O	
8	Compact	D	N	O	Tested after 12/31/79
9	Compact	D	I	O	
10	Compact	D	I	O	Contoured side grooves
11	Compact	D	N	R	
12	Compact	BW	N	R	
13	Compact	BW	I	R	
14	Compact	D	I	R	Contoured side grooves
15	Compact	F			Machine loaded

[a] DCB = double-cantilever beam

[b] BW = brittle weld
D = duplex specimen
H = hydrogen-charged brittle weld
F = fatigue precrack

[c] N = normal (shoulder up)

[d] O = initial crack jump
R = reinitiation

Based on evidence that departures of this magnitude do not affect the reported arrest toughness,[8] the K_{Ia} value at 150°C is considered representative of large-specimen behavior. The same conclusion holds true for all of the other Table 5.1 specimens that apparently were of insufficient size.

The complete PTSE-1 crack-arrest data are plotted in Fig. 5.8. The bulk of the points are a fair fit to a straight line (correlation coefficient, R = 0.85):

$$K_{Ia} = 21.9 + 0.712T \ , \qquad (5.8)$$

where the units are MPa·$\sqrt{m}$ and degrees celsius. Note that Eq. (5.8) does not include the two very high points for specimens that exhibited very irregular crack geometries and that are considered nonrepresentative (discussed further in Sect. 5.3.4 on crack-arrest data base). Figure 5.8 also compares the PTSE-1 data with the ASME K_{IR} curve (for RT_{NDT} = 70°C).* This curve is seen to provide a useful lower bound to the compact-specimen

*A determination of RT_{NDT} is reported in Chap. 10 as 91.3°C.

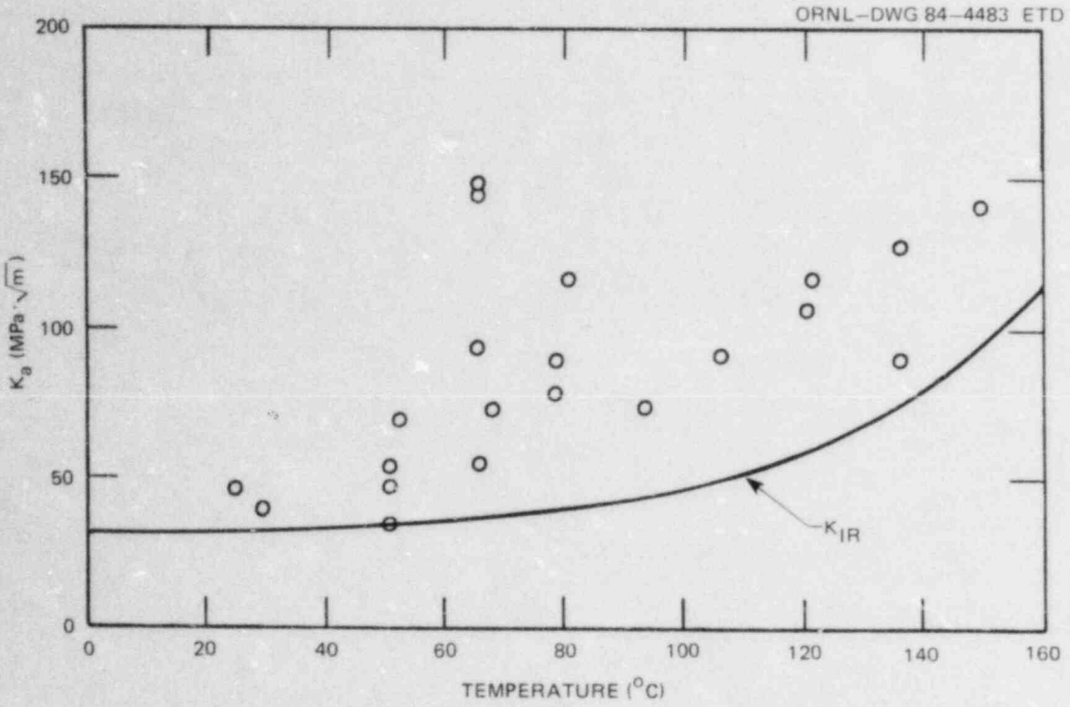

Fig. 5.8. Crack-arrest toughness of steel from PTSE-1 material.

data. However, the K_a data appear to be represented by K_{IR} at the upper and lower ends of the temperature scale.

5.3.2 Low-upper-shelf-energy weld from vessel V-8A

A low-upper-shelf-energy ITV-84 weld from ITV-8A has been included to gain experience in testing a material of this type in preparation for future PTS tests.

Because the amount of weld metal available for specimens in piece V-8A-D was appreciably less than was originally thought, only eight compact crack-arrest specimens were fabricated. Specimens numbered 17, 18, and 19 were for testing at temperatures near RT_{NDT} (estimated to be ~25°C), and they were ~100 mm square by 10 mm thick. Specimens 12–16 were fabricated for testing at somewhat higher temperatures, and they were ~150 mm square by 35 mm thick. In each specimen, the crack plane coincided with the plane of the weld, and the crack extended in the thickness direction from top to bottom.[9] All were duplex specimens in which a hardened AISI 4340 steel crack-starter was electron-beam welded to the test section. The duplex design was selected for the larger specimens to ensure initiation of an unstable fracture at the higher test temperatures. It was selected also for the smaller specimens to conserve the scarce test material and permit several more specimens to be fabricated than would be possible if brittle-weld specimens were used.

In the past, fabrication of duplex specimens from weld metal samples has proven difficult because of gas evolution in the molten zone of the electron-beam weld, resulting in porosity.[10] As was noted in earlier reports,[6,9] trial electron-beam welds made on blanks cut from the characterization weld of vessel V-872 revealed that oscillating the electron beam parallel to the weld path reduced the porosity significantly. Based on those trials, all duplex specimens fabricated in this task employed the beam-oscillation procedure.

At the time of this report, testing of all specimens fabricated from piece V-8A-D had been completed, with the exception of specimen 13, which contained obvious cracks in the electron-beam weld. The highest test temperature investigated (66°C) was only about 40°C greater than the estimated RT_{NDT}. Although it was planned originally to test at temperatures somewhat higher than 66°C, this was not done because of difficulties encountered in getting the crack to penetrate into the test section even at temperatures as low as 42°C.

Results of the crack-arrest experiments are given in Table 5.3 and Fig. 5.9. In only one of the seven specimens tested (specimen 19) did the rapid crack, which was initiated in the hardened starter section, penetrate into the test section prior to arrest. As was reported previously,[6]

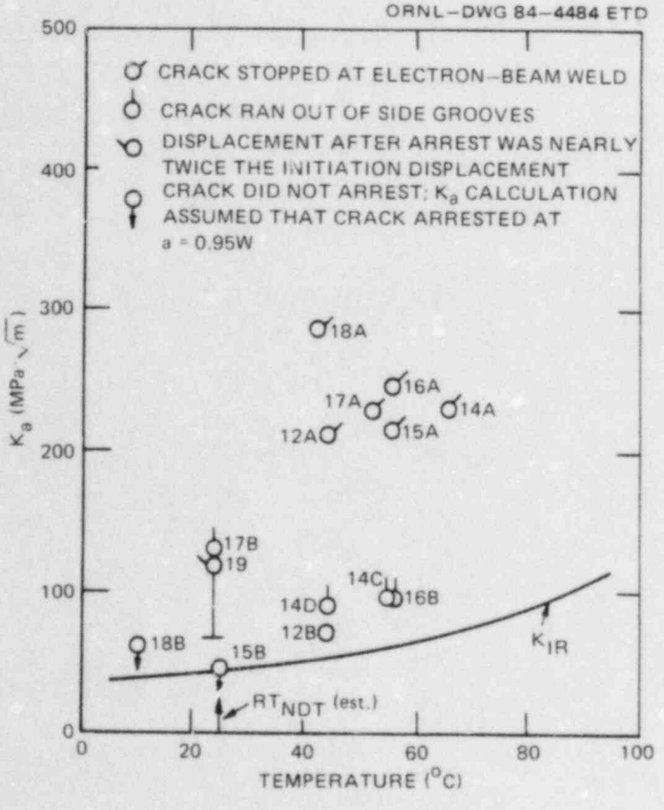

Fig. 5.9. Results of crack-arrest tests on submerged-arc weld from vessel V-8A.

Table 5.3. Crack-arrest tests of duplex compact specimens fabricated from piece V-dA-D, low-toughness weld

Specimen No.	Test temperature (°C)	Specimen dimensions (mm)			Displacement (mm)		Crack length (mm)		Stress intensity (MPa·√m)	
		W	B	B_N	Initiation	Arrest	Initiation	Arrest	Initiation, K_o	Arrest, K_a
19	24	84.6	18.5	13.7	1.21	2.26	25.7	76.5	266	120[a]
17A	52	84.6	18.5	13.7	1.16	1.39	25.9	41.1[b]	254	226[b]
17B[c]	24	84.6	18.5	13.7	1.78	1.96	41.1	72.4	289	130[d]
12A	44	127	34.9	25.4	1.43	1.52	40.6	59.7[b]	252	210[b]
12B[c]	44	127	34.9	25.4	1.28	1.77	59.7	116.8	177	70
13[e]		127.0	34.9	25.4						
14A	66	124.6	34.2	20.4[f]	1.42	1.50	41.1	58.4[b]	275	231[b]
14B[c]	66	124.6	34.2	20.4	[g]	[g]	[g]	[g]	[g]	[g]
14C[c]	55	124.6	34.2	20.4	1.22[h]	1.24[h]	58.4	98.0	188[h]	95[d,h]
14D[c]	44	124.6	34.2	20.4	1.43[h]	1.44[h]	98.0	105.7	110[h]	90[d,h]
15A	56	127.0	34.2	25.6	1.46	1.55	43.2	58.4[b]	246	215[b]
15B[c]	25	127.0	34.2	25.6	1.38	~1.51[i,j]	58.4	>120.7[i,k]	191	<45.5[l]
16A	56	125.3	34.1	20.6[f]	1.50	1.61	41.5	58.4[b]	287	247[b]
16B[c]	56	125.3	34.1	20.6	1.35[h]	1.29[h]	58.4	99.8	207[h]	96[d,h]
18A	42	84.6	18.5	13.7	1.42	1.67	~25.9	~38.9[b]	~311[i]	~285[b]
18B[c]	10	84.6	18.5	13.7	1.52	1.68[i,j]	38.9	>80.4[i,k]	258[m]	<62[m,l]

[a]The test was unusual in that the displacement after arrest was nearly twice the initiation displacement; when the latter was used to calculate K_a, the result was 64 MPa·√m.

[b]Crack stopped at electron-beam weld.

[c]Reinitiation of arrested crack.

[d]Crack ran out of the side grooves and had large unbroken ligaments at the specimen surfaces.

[e]Not tested because of cracks detected in the electron-beam weld.

[f]The side groove was contoured from a depth of 25% at the notch tip to 40% at and beyond the electron-beam weld.

[g]Unstable crack growth was not initiated.

[h]Corrected for plasticity by the use of Fig. 1 in Ref. 6.

[i]Crack did not arrest.

[j]Displacement shown is 1.1 times the initiation displacement.

[k]Crack length shown is 0.95 W.

[l]Estimated upper bound of K_a, assuming that the crack arrested at a = 0.95 W.

[m]Not corrected for pronounced plasticity that was observed during the test.

specimen 19 exhibited unusual behavior; namely, the displacement after arrest was nearly twice that at initiation rather than 5 to 10% greater as is usually observed. In the six remaining specimens, tested at 42 to 66°C, the rapid fracture arrested at the electron-beam weld at K-levels greater than 200 MPa$\cdot\sqrt{m}$. Contoured side grooves, which have had some previous success in promoting crack penetration through the electron-beam weld,[7] were used without success on specimens 14 and 16. The results for the six specimens in which the crack arrested at the electron-beam weld are shown in Fig. 5.9 for information purposes only; they are not believed to be representative of the crack-arrest toughness of the submerged-arc weld. Each K_a value for specimens that exhibited arrest at the electron-beam weld was more than 1.5 K_{IR}; as discussed below, statistical analysis of data in Battelle's crack-arrest data bank (see Sect. 5.3.4) suggests that K_a values in excess of 2.5 K_{IR} are unrepresentative.

Each of the six specimens that displayed arrest at the electron-beam weld line was retested at the same or a lower temperature. In two instances, specimens 15B and 18B, the rapid crack either did not arrest or it arrested ~0.99W, thus precluding calculation of K_a. An estimate of an upper-bound K_a value was obtained by assuming that the crack had arrested at 0.95W and that the arrest displacement was 10% greater than that at initiation. Notice in Fig. 5.9 that the K_a value calculated in this manner for specimen 15B falls on the ASME K_{IR} curve.

The results (Fig. 5.9) suggest that K_a values for this submerged-arc weldment lie only slightly above the K_{IR} curve at temperatures above RT_{NDT} and may lie below the K_{IR} curve at lower temperatures. Several of the values shown were for specimens in which the crack ran out of the plane of the side grooves (specimens 14C, 14D, 16B, and 17B); this condition usually causes some elevation of the apparent K_a value. The results obtained for piece V-8A-D will be compared with results obtained on other submerged-arc weldments in the next progress report.

With respect to future crack-arrest testing of submerged-arc welds, the work performed in the task reported here has been helpful from several standpoints. First it suggests that brittle-weld crack starters may be preferable to duplex specimens at temperatures near and somewhat above RT_{NDT}. Second, at higher temperatures where rapid crack initiation becomes difficult in brittle-weld specimens, merely switching to duplex specimens may not suffice, owing both to porosity problems from electron-beam welding and to difficulties in penetrating the electron-beam weld line with the rapid crack. Third, the porosity problem encountered in passing an electron-beam through submerged-arc weld metal can be reduced greatly by oscillating the beam along the weld path. Fourth, contouring the side grooves from 25% depth at the notch tip to 40% at the electron-beam weld line to achieve a greater K value at the latter location may not be sufficient to achieve crack penetration of the test section; additional deepening of the side grooves at the electron-beam weld line may be necessary. Finally, cracks that arrest at the electron-beam weld line often can be reinitiated by testing at the same or a lower temperature. When retesting is done, appreciable plastic deformation may occur prior to reinitiation because the crack tip is adjacent to the lower strength test material. A suitable method of accounting for this plastic deformation is required to avoid overestimation of K_a values. Use of sequential load-unload cycles,[11,12] measurement of displacement at two locations,[13] or

estimating the plastic component of displacement from Fig. 1 in Ref. 11 appears to be satisfactory.

5.3.3 Crack-arrest test refinement

An objective of this task is to examine alternative methods for instrumenting crack-arrest test specimens in order to answer unresolved questions concerning plasticity and dynamic effects. During this period, preliminary experiments on both topics were performed.

Plasticity. A problem with crack-arrest testing is that the load must be inferred from the displacement. Two experiments were undertaken to estimate arrest loads from direct postarrest measurements. Conventional weld-embrittled specimens (150 × 150 × 25 or 37 mm) were provided with two added loading holes positioned as for crack-initiation compact specimens. The specimens were first wedge-loaded in the manner prescribed by the draft ASTM Crack-Arrest Standard[12] using the cyclic technique.[11] Residual displacements due to plasticity were recorded. Following rapid crack propagation and arrest, the specimens were unloaded and some reverse displacements occurred. Pin-loading fixtures were then attached, and the specimens were reloaded until the total displacements reached those attained prior to the unloading but subsequent to crack arrest.

The arrest loads had been inferred previously from Ripling's compliance relation[14] using both the elastic displacement on the final wedge-loading cycle and the total displacement (elastic plus plastic) just after crack arrest. A comparison of the different arrest-load calculations is shown in Table 5.4. As was anticipated, the estimated arrest load was lower when only elastic displacements were used in the calculations than when plasticity was included. However, the direct-reload values are inconsistent, one being higher and the other lower than both displacement-based values.

5.4. Estimation of crack-arrest load

Specimen No.	Test temperature (°C)	K_a^c (MPa·√m)	Arrest load, KN (lb)		
			Estimated from elastic displacement on final cycle	Estimated from total displacement	Estimated from reload experiment
7-OR-6[a]	38	66	7.1 (1600)	8.0 (1860)	12.1 (2720)
P1-OR-9[b]	79	64	18.6 (4170)	20.5 (4620)	14.6 (3280)

[a] Steel from TSE-7; earlier crack-arrest data were reported in Ref. 1.

[b] Steel from PTSE-1; additional crack-arrest data reported in Table 1.

[c] Calculated using elastic displacement at arrest on final loading cycle.

Insight into the sources of the problem was obtained from closer examination of the reload-displacement curves. As shown in Fig. 5.10, these curves were nonlinear and exhibited hysteresis and lack of closure. (Subsequent reloadings to the same displacement still resulted in open curves; however, peak loads were slightly lower, and there was no residual displacement at zero load). In addition to load data, an additional clip gage had been located at the 0.30W location to provide effective crack-length data.[13] Figure 5.11 shows the results from these experiments. Although the two specimens behaved differently, both results indicated that the effective crack length was less than the actual crack length. The most likely explanation of such a discrepancy would be the presence of unbroken ligaments generated during the run-arrest event. In support of this suggestion, a lack of closure due to the presence of ligaments is consistent with the fracture-topography studies of Kobayashi et al.[15]

These results, pointing to a significant contribution of ligaments to the experimental record, clearly present a problem in evaluating the plasticity contribution. Experimentally, it will be difficult to separate ligament and plasticity effects. Furthermore, any analytical model would have to be extremely complex, given the three-dimensional nature of ligamented cracks.[16] Finally, such questions as predicting the size and location of ligaments have not been resolved. Further experimental techniques will be needed, and several are under evaluation.

Dynamics. It is important to determine the extent to which dynamic effects influence both the test specimen record and the behavior of a crack in a vessel undergoing a thermal transient. A review of the literature reveals several points.

1. Predictions of crack-jump length obtained from fully dynamic analyses of thermally shocked cylinders differ only slightly from those obtained from static analyses.[17,18]

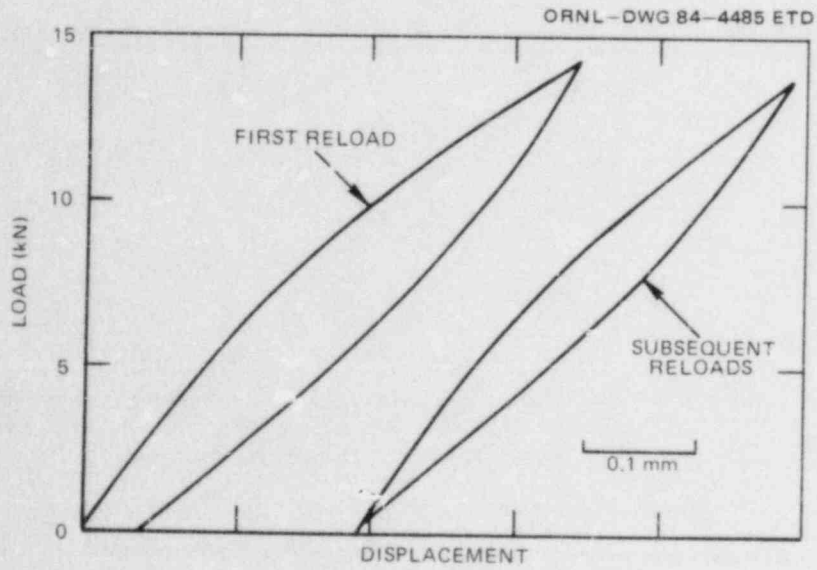

Fig. 5.10. Load-displacement record associated with reloading arrested-cleavage crack.

2. Although dynamic effects may be significant in the early stages of crack propagation in a wedge-loaded compact specimen, they do not play an important role in crack deceleration and arrest.[19,20]

3. Statically calculated stress intensities at arrest in compact specimens provide good, conservative estimates of the results of thermal-shock experiments at ORNL.[21]

From all of these considerations, we can conclude that dynamic effects should be minimized in crack-arrest property testing. The best way

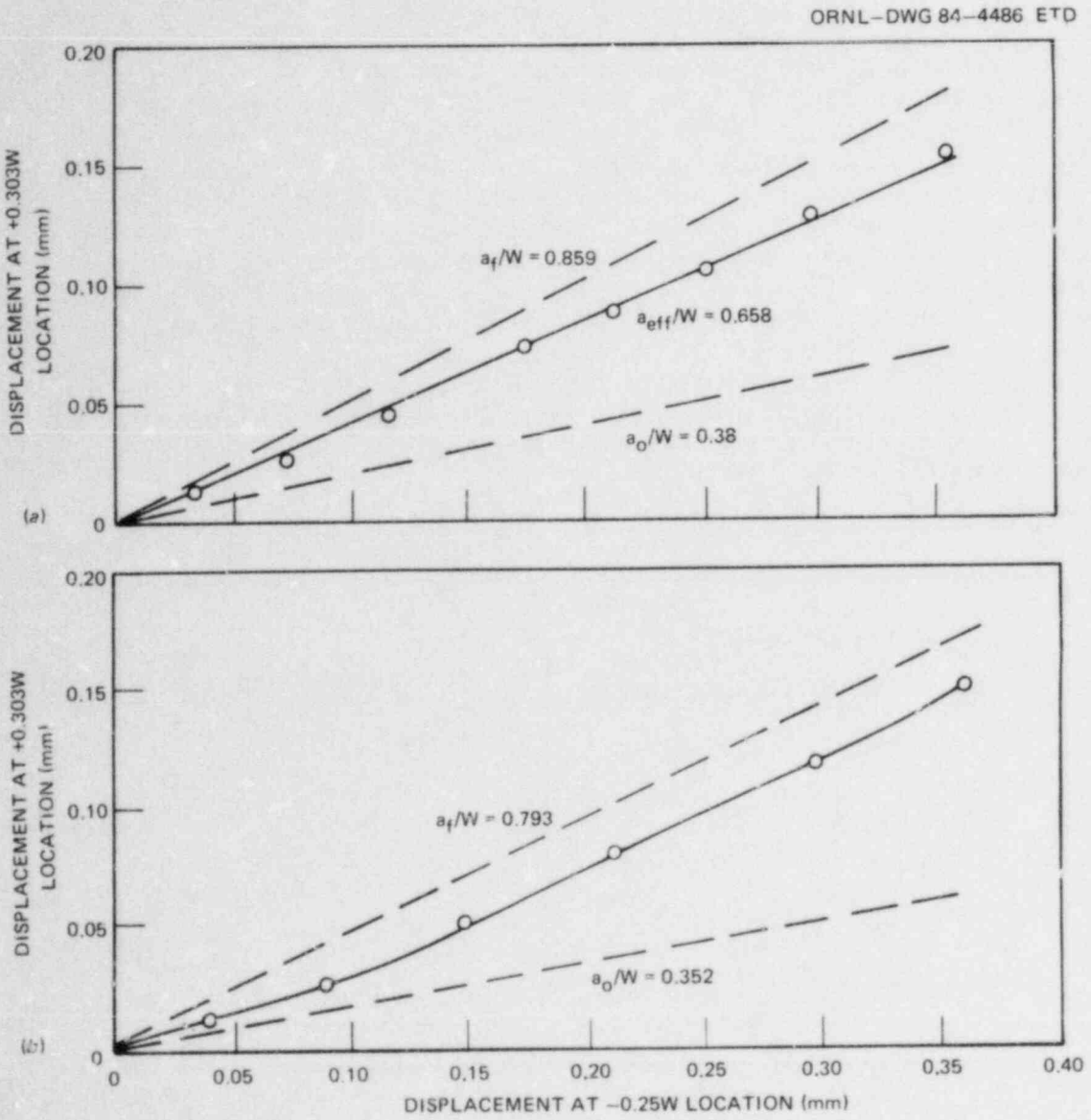

Fig. 5.11. Double-displacement records of reloading specimens that contained arrested cracks. Dashed lines show theoretical curves associated with initial crack length (a_o/w) and arrested-crack length (a_f/w). (*a*) Reload of specimen 7-OR.6 and (*b*) reload of specimen P1-OR.9.

to accomplish this is to adhere as closely as possible to fixed-grip conditions.

Dynamic effects may be introduced into the compact specimen, particularly when inverted split pins are used to facilitate rapid crack initiation at relatively high test temperature.[22] These effects probably are minimized by the formation and rupture of ligaments, which have been shown to effectively damp specimen vibrations.[22] Nevertheless the question of the influence of dynamic effects on crack-arrest toughness measurements still needs to be investigated.

Experiments are planned in which arm motion and crack length will both be measured as functions of time during propagation and up to a few milliseconds after arrest. Crack position will be monitored by strain gages bonded to the specimen surface and oriented normal to the crack plane.

A calibration experiment was carried out to determine the optimum gage locations. Gages were located at various distances from the specimen centerline, and their responses to a given displacement were measured. The starting notch was then extended by sawing, and the response was remeasured. The procedure was repeated until the saw cut extended 90% of the specimen width. Figure 5.12 shows one such record. Note that the peak strain response is reached before the sawcut reached the gage and that the curve is asymmetric: the falloff after peak strain response was sharper than the rise before it.

It was found that the height of the strain-response peak was influenced surprisingly by the side grooves. From elastic analysis, the strain response would be expected to decrease sharply with increasing separation of the strain gage from the centerline. Figure 5.13 shows that the side grooves perturb this response so that the maximum response being recorded by the gages located 19 mm from the centerline. At the same time, the falloff in strain as the crack approached and passed the strain gage was sharper the closer the gage was to the centerline. Despite this observation, it has been decided to use the maximum response location in the dynamic experiments, because the less severe falloff will allow fewer gages to be used and still obtain useful information on the region between gages.

Finally, note that the gages can provide semiquantitative information about crack-tip stress intensities and may be helpful in sorting out the ligament-plasticity question.

5.3.4 Data base

The objectives of this task are to maintain and expand the computerized data base and to issue an FY 84 inventory report. During the reporting period, 231 crack-arrest (K_{Ia}) points have been added, making a total of 344 points. Currently all of the data are for unirradiated base plate.

Crack arrest. Table 5.5 summarizes the data base contents. About one-half of the specimens were tested in reasonable conformance with procedures being considered by the ASTM Task Group on Crack Arrest. Slightly over one-half (198) were tested at BCL.

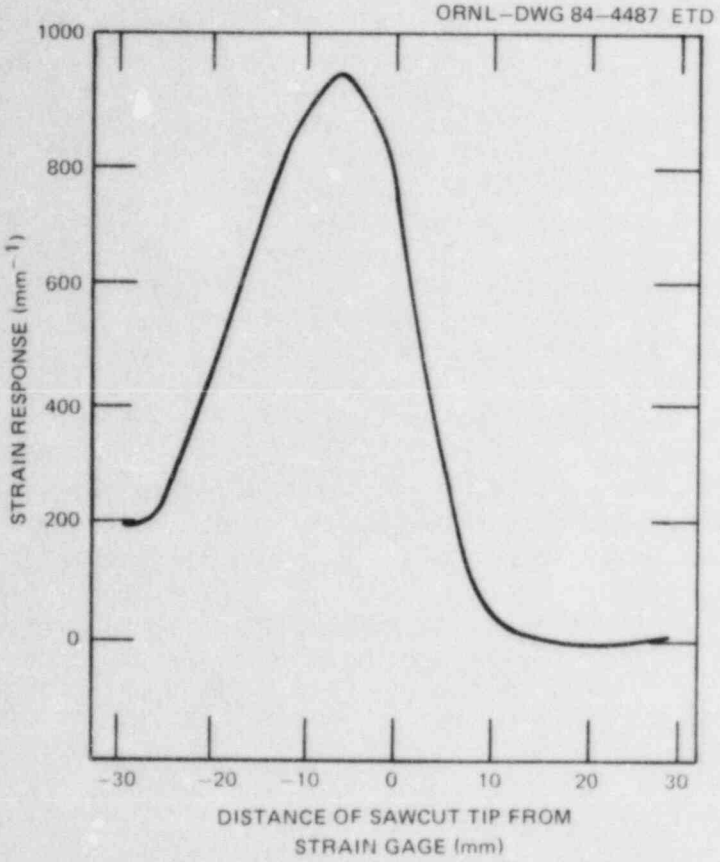

Fig. 5.12. Trace of strain gage response derived from calibration experiment. Saw-cut was made from left to right. Gage was positioned 12.7 mm from specimen centerline.

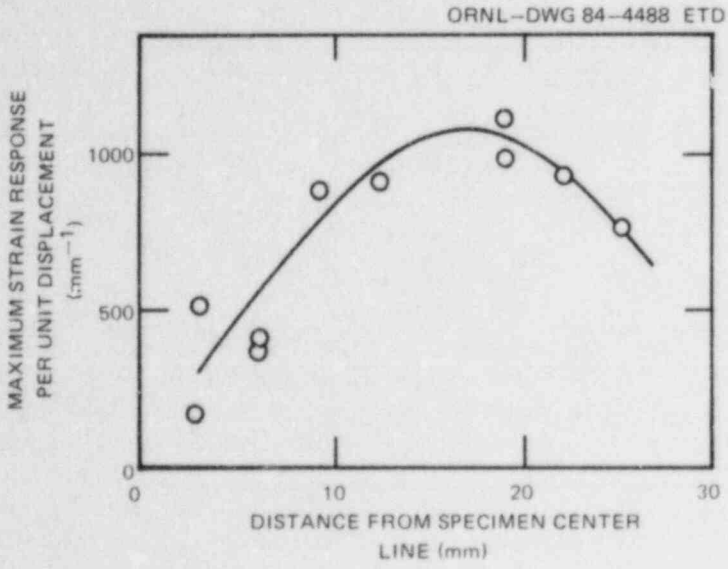

Fig. 5.13. Maximum strain gage response as a function of gage response.

Table 5.5. Classification of data-base contents

Specimen design	Number of specimens	Laboratories
Wedge loaded		
Compact	204 (170)[a]	BCL, MRL, Kawasaki
Double-cantilever beam	35	BCL
Machine loaded		
Compact	29	Westinghouse
Contoured double-cantilever beam	46	MRL
ESSO	17	Kawasaki, Mitsubishi
Thermal shock		
Cylinder	13[b]	ORNL, Framatome
Total	344 (170)[a]	

[a]The numbers in parentheses indicate the specimens for which raw data are available and for which results were computer-calculated at BCL.

[b]The number listed is the total number of jumps from five cylinders.

The statistical analysis was performed by assuming that the ratio K_{Ia}/K_{IR} obeys a temperature-dependent Weibull distribution,[6] where K_{IR} is the ASME Boiler and Pressure-Vessel Code Sect. XI lower-bound toughness curve. Fifteen points (4.4% of the data) fell below K_{IR}, but most of these points fell within 5% of K_{IR}, were tested at temperatures below RT_{NDT}, or both. This observation is consistent with past estimates;[16,23] although K_{IR} represents a small, but finite, cumulative probability level, it can be considered an acceptable lower-bound estimate. There were no points for K_{Ia}/K_{IR} values between 2.5 and 3.0, but nine points (2.6%) were above 3.0. While these very high values are suspect, they were included in the analysis because their effect on the final result was minimal. The median value of K_{Ia} was found to be well represented by the equation

$$K_{Ia} = 30.0 + 48.176 \exp (0.0146\ \Delta T) , \qquad (5.9)$$

where ΔT is $T - RT_{NDT}$ and the units are $MPa\cdot\sqrt{m}$ and degrees celsius. The spread of the data increases with increasing temperature so that the coefficient of variation (standard-deviation/mean) is approximately constant, varying between 0.26 and 0.31. This observation, which means that the K_{Ia}/K_{IR} ratio is essentially temperature independent over the range

considered, has been used in the analysis of crack initiation that follows.

Crack initiation. A simplified statistical analysis was applied to the Battelle crack-initiation data and to the literature thermal-shock data with two objectives: (1) judging how well methods using compact specimens represent large-specimen data, and (2) developing a preliminary K_{Ic} distribution function.

The analysis used the assumption that the quantity K_{Ic}/K_o ($K_o \equiv$ the ASME Boiler and Pressure Vessel Code K_{Ic} curve) forms a temperature-independent population. To calculate the individual points, the following equation was fitted to the ASME plot:

$$K_o = 29.43 + 31.50 \exp[0.0321\Delta T] , \qquad (5.10)$$

where ΔT = test temperature minus reference temperature and the units are MPa$\cdot\sqrt{m}$ and degrees celsius. The data were obtained from large thermally shocked cylinders,[24-26] compact specimens in which arrested cracks were reinitiated,[6,7,9,13] and conventional compact specimens.[27-30] The last group was corrected for plasticity using the available energy technique.[28,30] The reinitiation data were separated into cleavage-precrack and ductile-precrack subsets, with the ductile-precrack data being eliminated to provide a set of points with equivalent crack-tip morphologies. As shown in Fig. 5.14, the remaining data were fitted to Weibull distribution of slope equal to four. This procedure resulted in fairly good descriptions of the two methods of analyzing fatigue-precracked compact specimens but was not adequate for either the reinitiation or the cylinder data. However, the agreement between these latter two sets suggests that they are members of the same population. Accordingly, both sets were combined and replotted as shown in Figure 5.15. The combined distribution is satisfactorily described by a Weibull plot of slope equal to three.

The characteristics of the Weibull distributions from Figs. 5.14 and 5.15 are listed in Table 5.6. Because the values of m are in a range where the Weibull distribution is very close to the Gaussian distribution, the means and standard deviations in the table can be used with a Gaussian distribution. Whichever distribution is used, it is recommended that the combined cylinder-reinitiation data be used in any evaluation that requires lower-bound toughness values. Also, the data are limited to temperatures less than (RT_{NDT} + 30°C). Above this temperature, the distribution may not apply.

The most interesting point of the analysis concerns the agreement between reinitiation and thermal-shock data. The common points between the specimens in those two types of experiments are that neither employs a fatigue precrack and neither experiences stable crack growth prior to cleavage. To the extent that the BCL data are representative of the behavior of steel within the ductile-brittle transition region in general, it appears that fatigue does not provide the sharpest possible crack tip, contrary to the underlying assumption of ASTM E399. In contrast to the reinitiation data, the fatigue-precrack results were significantly higher than the cylinder values, even when adjusted for plasticity prior to cleavage initiation. However, there was sufficient overlap between the adjusted fatigue-precrack data and the cylinder data to confirm the proven

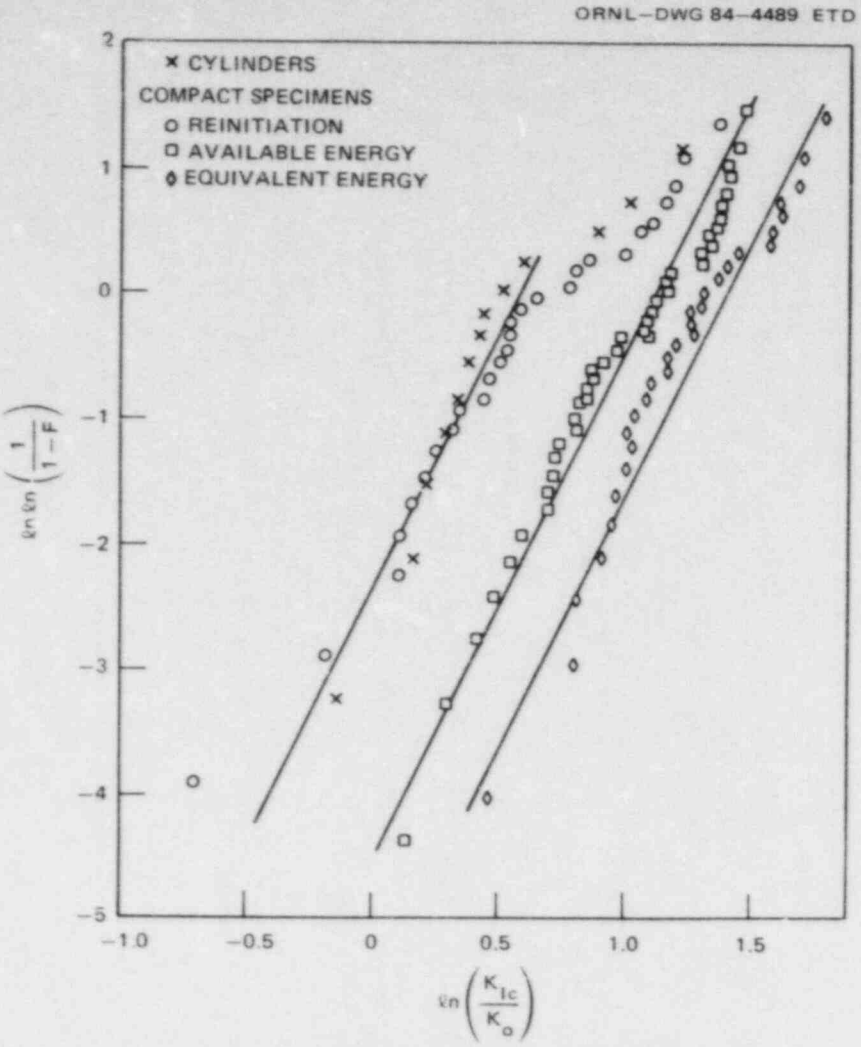

Fig. 5.14. Weibull plots of K_{Ic} obtained using various test techniques.

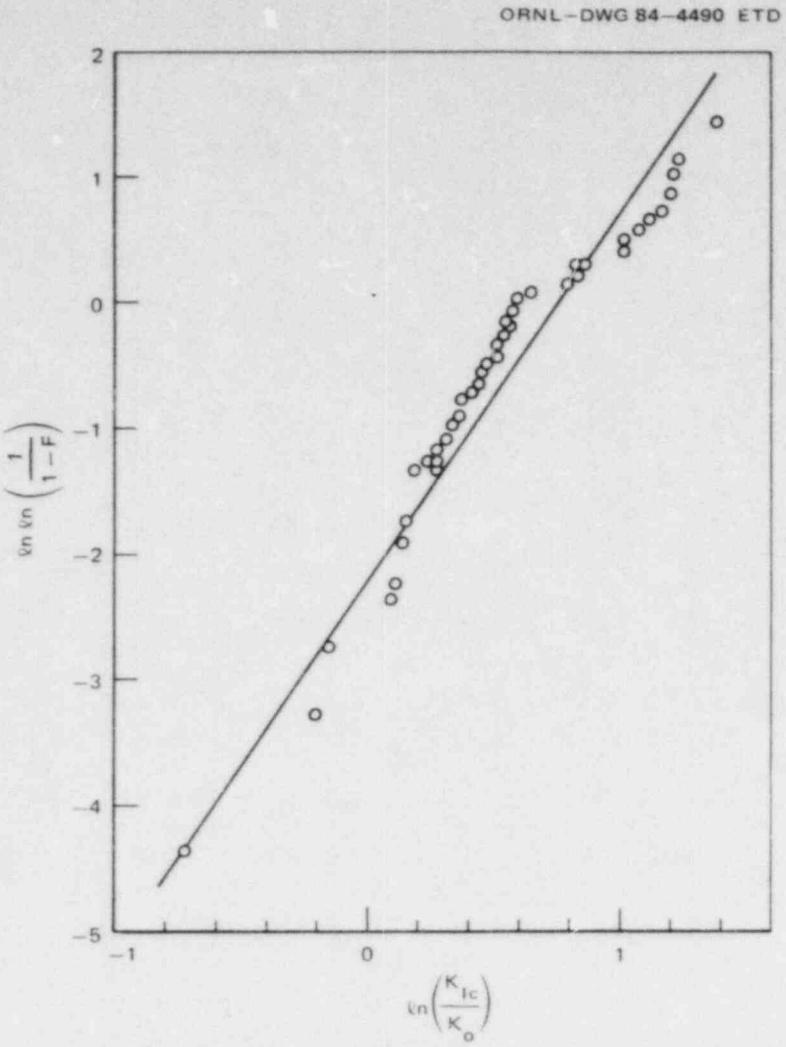

Fig. 5.15. Weibull plot of combined thermal-shock and reinitiation K_{Ic} values.

Table 5.6. Distribution functions for K_{Ic}

Test method	Number of specimens	Weibull[a] parameters		K_{Ic}/K_o	
		A	m	Mean	Standard deviation
Thermally shocked cylinders	13	2.15	3	1.92	0.70
Compact specimens					
Reinitiation of an arrested cleavage crack	27				
Fatigue precrack[b]	41	3.06	4	2.77	0.78
Fatigue precrack[c]	30	4.06	4	3.68	1.03

[a]The cumulative Weibull distribution is

$$F = 1 - \exp[-(K_{Ic}/AK_o)^m].$$

[b]Available energy.

[c]Equivalent energy.

success of the available energy method (and the Merkle β_c correction).[31] Thus, these latter procedures are considered acceptable, albeit less efficient, predictors of cylinder behavior.

References

1. G. R. Irwin, "Notes on Testing Arrangements for Crack Arrest Tests Using an SEN Specimen and a Temperature Gradient," University of Maryland, College Park, October 1983.

2. H. Tada, P. C. Paris, and G. R. Irwin, *The Stress Analysis of Cracks Handbook*, Del Research Corp., Hellertown, Pa., 1973.

3. Japan Welding Council, *Structural Integrity of Very Thick Steel Plate for Nuclear Reactor Pressure Vessels*, JWES-AE-7806, 1977 (in Japanese).

4. S. T. Rolfe and J. M. Barsom, *Fracture and Fatigue Control in Structures*, Prentice-Hall, Inc., Englewood Cliffs, N.J., 1977.

5. P. B. Crosley et al., *Cooperative Test Program on Crack Arrest Toughness Measurement*, University of Maryland, College Park, NUREG/CR-3261, April 1983.

6. A. R. Rosenfield et al., "BCL HSST Support Program," in *Heavy-Section Steel Technology Program Quart. Prog. Rep. January–March 1983*, NUREG/CR-3334, Vol. 3 (ORNL/TM-8787/V3), Union Carbide Corp. Nuclear Div., Oak Ridge Natl. Lab., September 1983.

7. A. R. Rosenfield et al., "BCL HSST Support Program," in *Heavy-Section Steel Technology Program Quart. Prog. Rep. January–March 1983*, NUREG/CR-3334, Vol. 1 (ORNL/TM-8787/V1), Union Carbide Corp. Nuclear Div., Oak Ridge Natl. Lab.

8. A. R. Rosenfield et al., "Recent Advances in Crack-Arrest Technology," in *Fracture Mechanics: Fifteenth Symposium, STM STP 833*, American Society for Testing and Materials, Philadelphia, Pa. (in press).

9. A. R. Rosenfield et al., "BCL HSST Support Program," in *Heavy-Section Steel Technology Program Quart. Prog. Rep. January–March 1983*, NUREG/CR-3334, Vol. 2 (ORNL/TM-8787/V2), Union Carbide Corp. Nuclear Div., Oak Ridge Natl. Lab.

10. C. W. Marschall and A. R. Rosenfield, "Crack-Arrest Tests of Irradiated High-Copper ASTM A508 Submerged-Arc Weld Metal," pp. 2467–75 in *Advances in Fracture Research*, Vol. 5, ed. D. Francois, Pergamon Press, Oxford, 1981.

11. C. W. Marschall, P. N. Mincer, and A. R. Rosenfield, "Subsize Specimens for Crack Arrest Testing," pp. II-295–II-319 in *Fracture Mechanics: Fourteenth Symposium-Volume II: Testing and Applications, ASTM STP 791*, American Society for Testing and Materials, Philadelphia, Pa., 1983.

12. W. L. Fourney, "Proposed ASTM Test Method for Crack Arrest Fracture Toughness of Ferritic Materials," informal ASTM committee document, September 1983.

13. A. R. Rosenfield and P. N. Mincer, "Reinitiation of Arrested Cleavage Crack," *Eng. Fract. Mech.* 18, 1125–29 (1983).

14. E. J. Ripling and P. B. Crosley, unpublished manuscript entitled "Contribution to the ORNL Heavy-Section Steel Technology Program Quarterly Report for the Period Ending November 30, 1979."

15. T. Kobayashi, G. R. Irwin, and X.-J. Zhang, "Topographic Examination of Fracture Surfaces in Fibrous-Cleavage Transition Behavior," presented at ASTM Symposium on *Fractography in Failure Analysis of Ceramics and Metals*, 1982.

16. G. T. Hahn et al., "Fast Fracture Toughness and Crack Arrest Toughness of Reactor Pressure Vessel Steel," pp. 289–320 in *Crack Arrest Methodology and Applications, ASTM STP 711*, American Society for Testing and Materials, Philadelphia, Pa., 1980.

17. A. R. Rosenfield et al., "BCL HSST Support Program" in *Heavy-Section Steel Technology Program Quart. Prog. Rep. January–March 1981*, NUREG/CR-2141/V1 (ORNL/TM-7822), Union Carbide Corp. Nuclear Div., Oak Ridge Natl. Lab.

18. A. R. Rosenfield et al., "BCL HSST Support Program," in *Heavy-Section Steel Technology Program Quart. Prog. Rep. July–September 1981*, NUREG/CR-2141/V3 (ORNL/TM-8145), Union Carbide Corp. Nuclear Div., Oak Ridge Natl. Lab.

19. L. Dahlberg, F. Nilsson, and B. Brickstad, "Influence of Specimen Geometry on Crack Propagation and Arrest Toughness," pp. 89–108 in *Crack Arrest Methodology and Applications, ASTM STP 711*, 1980.

20. A. Shulka, "Comparison of Static and Dynamic Energy Release Rates for Different Fracture Specimens," *Eng. Fract. Mech.* 18, 725–30 (1983).

21. A. R. Rosenfield, "Validation of Compact-Specimen Crack-Arrest Data," ASME Paper JEMT-36-82 (1983).

22. K. Rahka, "Vibrations in Compact Specimens During Crack-Arrest Testing," *J. Test. Eval.* 8, 318–23 (1980).

23. A. R. Rosenfield et al., *Critical Experiments, Measurements, and Analyses to Establish a Crack Arrest Methodology for Nuclear Pressure Vessel Steels*, NUREG/CR-1887 (BMI-2071), Battelle-Columbus Laboratory (1981).

24. R. D. Cheverton et al., "Application of Crack Arrest Theory to a Thermal Shock Experiment," pp. 392–421 in *Crack Arrest Methodology and Applications, ASTM STP 711*, 1980.

25. R. D. Cheverton et al., "Fracture Mechanics Data Deduced from Thermal-Shock and Related Experiments with LWR Pressure Vessel Material," *J. Press. Vess. Tech., Trans. ASME* 105, 102–10 (1983).

26. A. Pellisier-Tanon et al., "Crack Initiation and Arrest in a SA508 Cl 3 Cylinder Under Liquid Nitrogen Thermal Shock Experiment," *SMIRT-7 Proc.*, Paper G/F 1/8 (1983).

27. A. R. Rosenfield et al., "BCL HSST Support Program," in *Heavy Section Steel Technology Program Quart. Prog. Rep. April–June 1982*, NUREG/CR-2751/V2 (ORNL TM-8369/V2), Union Carbide Corp. Nuclear Div., Oak Ridge Natl. Lab.

28. A. R. Rosenfield and D. K. Shetty, "Lower-Bound Fracture Toughness of a Reactor-Pressure-Vessel Steel," *Eng. Fract. Mech.* 14, 833–42 (1981).

29. A. R. Rosenfield and D. K. Shetty, "Cleavage Fracture of Steel in the Upper Ductile-Brittle Transition Region," *Eng. Fract. Mech.* 17, 461–70 (1983).

30. A. R. Rosenfield and D. K. Shetty, "Cleavage Fracture of Steel in the Ductile-Brittle Transition Region," presented at ASTM Symposium on *Users Experience With Elastic Plastic Toughess Test Methods*, Louisville, 1983.

31. J. G. Merkle, "An Approximate Method of Elastic-Plastic Fracture Analysis for Nozzle-Corner Cracks," pp. 674–702 in *Elastic Plastic Fracture*, *ASTM STP 668*, 1979.

6. IRRADIATION EFFECTS STUDIES

R. K. Nanstad

6.1 Third HSST Irradiation Series

J. J. McGowan R. G. Berggren
T. N. Jones R. K. Nanstad

The third 4TCS irradiation experiment contained miniature tensile specimens of four low-upper-shelf weldments. The irradiation conditions were reported in Ref. 1, and the results from Charpy V-notch (CVN) specimens tested in this series have been reported in Ref. 2. The chemical composition of these submerged-arc welds is shown in Table 6.1. The final item to be completed in this series was the tensile testing, which has now been completed and is reported below.

The two types of miniature tensile specimens used in this study are shown in Fig. 6.1. The sizes were selected because of the space available in the irradiation capsule. The diameters of both long and short specimens were 4.52 mm with the total lengths of the long and the short specimen being 5.5 and 5.0 cm, respectively. The tensile strength properties of the welds are summarized in Tables 6.2 and 6.3 for the unirradiated and irradiated condition, respectively. The unirradiated strengths of the welds are similar with weld 66W showing slightly higher (10% to 15%) values than the other three welds. Irradiation at 252 to 290°C to a fluence in the range of 2 to 10 × 10^{22} neutrons/m^2 (E > 1 MeV) produced a significant increase in the strength of the four welds. (Figure 6.2 shows the behavior of weld 65W.) The yield strength of all four welds was more sensitive (10%) to irradiation than the ultimate strength as shown in Table 6.4. The strength of welds 64W and 67W was generally more sensitive (10%) to irradiation than welds 65W and 66W.

The elongation properties of the welds are listed in Tables 6.2 and 6.3 for the unirradiated and irradiated condition, respectively. The total elongation changed up to 2% with irradiation as shown in Table 6.5.

6.2 Fourth HSST Irradiation Series

J. J. McGowan R. G. Berggren
T. N. Jones R. K. Nanstad
R. L. Swain

The fourth capsule of the Fourth HSST Irradiation Series contained materials supplied by the Federal Republic of Germany (FRG). The CVN impact tests were completed on both irradiated and unirradiated specimens, and posttest measurements are in progress. The cooperative testing program[3] on specimens from the first three capsules of the Fourth HSST Irradiation Series is continuing. Tensile testing has been completed. Testing of all unirradiated 1TCS specimens has been completed, and the scoping tests of the irradiated 1TCS specimens have been initiated. The

Table 6.1. Chemical composition of submerged-arc welds for Third HSST Irradiation Series

Material	Average[a] composition (wt %)									
	C	Mn	P	S	Si	Cr	Ni	Mo	Cu	V
64W	0.085	1.59	0.014	0.015	0.520	0.092	0.660	0.420	0.350	0.007
	0.070 / 0.10	1.54 / 1.64	0.012 / 0.017	0.014 / 0.016	0.445 / 0.600	0.074 / 0.110	0.600 / 0.720	0.410 / 0.430	0.310 / 0.390	0.006 / 0.008
65W	0.080	1.45	0.015	0.015	0.480	0.088	0.597	0.385	0.215	0.006
	0.070 / 0.090	1.42 / 1.49	0.014 / 0.017	0.013 / 0.017	0.450 / 0.610	0.076 / 0.100	0.585 / 0.610	0.370 / 0.400	0.180 / 0.250	0.005 / 0.008
66W	0.092	1.63	0.018	0.009	0.540	0.105	0.595	0.400	0.420	0.009
	0.075 / 0.110	1.59 / 1.67	0.017 / 0.020	0.009 / 0.010	0.480 / 0.600	0.090 / 0.120	0.580 / 0.610	0.380 / 0.420	0.350 / 0.490	0.007 / 0.012
67W	0.082	1.44	0.011	0.012	0.500	0.089	0.590	0.390	0.265	0.007
	0.070 / 0.095	1.40 / 1.48	0.010 / 0.013	0.012 / 0.013	0.410 / 0.590	0.067 / 0.110	0.580 / 0.600	0.370 / 0.410	0.220 / 0.310	0.005 / 0.010

[a]Numbers shown below each entry indicate range of composition measurements.

Table 6.2. Tensile properties of unirradiated welds
Third HSST Irradiation Series

Specimen No.	Test temperature (°C)	Yield strength (MPa)	Ultimate strength (MPa)	Uniform strain (%)	Reduction in area (%)	Total[a] elongation (%)
64W10[b]	27	467	583	9.9	65.8	19.5
11[b]	27	469	581	9.6	64.5	18.8
12[b]	151	426	539	9.0	65.5	17.2
13	151	418	533	9.9	67.4	18.9
14[b]	286	398	547	8.4	60.0	16.0
15[b]	288	398	549	9.6	52.7	15.8
16[b]	27	458	575	10.1	64.1	18.4
17[b]	151	407	519	9.0	66.7	17.4
18[b]	286	398	533	8.6	51.5	14.4
65W10[b]	27	461	572	10.1	63.9	19.6
11[b]	27	460	571	9.5	64.4	17.2
12[b]	151	425	535	7.7	62.9	15.4
13[b]	150	428	538	8.0	63.6	15.2
14[b]	288	423	550	7.5	55.5	13.3
15[b]	288	414	548	7.8	57.3	14.3
16[b]	27	451	571	9.5	67.2	17.6
17[b]	150	416	526	7.4	66.0	15.2
18[b]	288	398	550	9.3	61.1	16.9
66W1	27	533	639	8.4	63.3	17.1
2	150	507	599	7.2	64.9	14.7
6	287	496	610	6.8	46.3	12.7
7	27	534	639	6.8	63.4	14.8
8	149	506	595	6.2	63.5	13.5
10	288	500	607	6.4	47.0	11.7
67W1	27	445	569	8.2	65.8	16.2
2	27	461	581	8.5	67.7	17.2
3	150	424	538	6.5	67.9	14.3
5	149	429	543	6.5	63.9	13.7
6	288	431	565	7.3	61.0	13.9
7	288	433	567	7.7	55.1	13.8
8	27	479	600	11.4	66.1	20.2
10	148	433	544	7.3	64.6	15.0
11	288	427	554	7.3	57.7	12.8

[a]Elongation for 31.75-mm gage length.

[b]Short specimens, all others are long specimens.

Table 6.3. Tensile properties of irradiated welds
Third HSST Irradiation Series

Specimen No.	Fluence (10^{22} neutrons/m^2)	Irradiation temperature (°C)	Test temperature (°C)	Yield strength (MPa)	Ultimate strength (MPa)	Uniform strain (%)	Reduction in area (%)	Total[a] elongation (%)
64W1	4.5	273	288	519	640	7.5	39.0	11.9
4[b]	6.7	281	33	610	709	10.0	58.4	17.1
5[b]	6.7	282	288	527	656	8.3	40.4	14.0
6[b]	2.4	289	33	594	688	10.9	56.5	17.1
7[b]	2.4	290	289	525	658	7.2	52.1	12.2
8[b]	6.4	273	149	524	626	7.5	56.5	14.8
65W3	3.8	281	151	476	612	9.3	61.3	16.6
4[b]	7.6	279	28	582	676	11.2	63.0	20.2
5[b]	7.6	284	287	507	644	9.3	53.6	16.7
6[b]	2.0	288	288	504	627	8.2	62.1	14.7
7[b]	2.0	287	28	562	662	10.6	57.7	18.6
8[b]	6.0	268	150	493	592	9.1	62.4	17.1
9[b]	6.0	270	288	475	601	8.0	49.5	15.0
66W3	6.4	284	149	599	684	6.7	67.4	13.4
4	5.6	279	149	603	692	6.8	52.4	13.3
5	5.2	279	287	573	683	7.1	50.8	12.8
9	4.0	282	34	635	715	6.8	59.3	14.8
11[b]	8.7	281	290	580	683	6.0	42.2	11.2
12[b]	8.7	286	34	671	746	8.0	60.8	18.2
67W4	5.4	282	149	566	645	6.7	66.3	13.5
9	4.2	282	149	553	655	7.5	60.8	13.9
15[b]	9.5	261	288	519	632	7.1	60.7	13.0
16[b]	9.5	252	288	511	627	7.1	52.7	12.8
17[b]	1.8	284	34	613	691	8.6	61.4	15.4
18[b]	1.8	286	288	529	655	8.0	59.7	13.3

[a]Elongation for 31.75-mm gage length.

[b]Short specimens, all others long specimens.

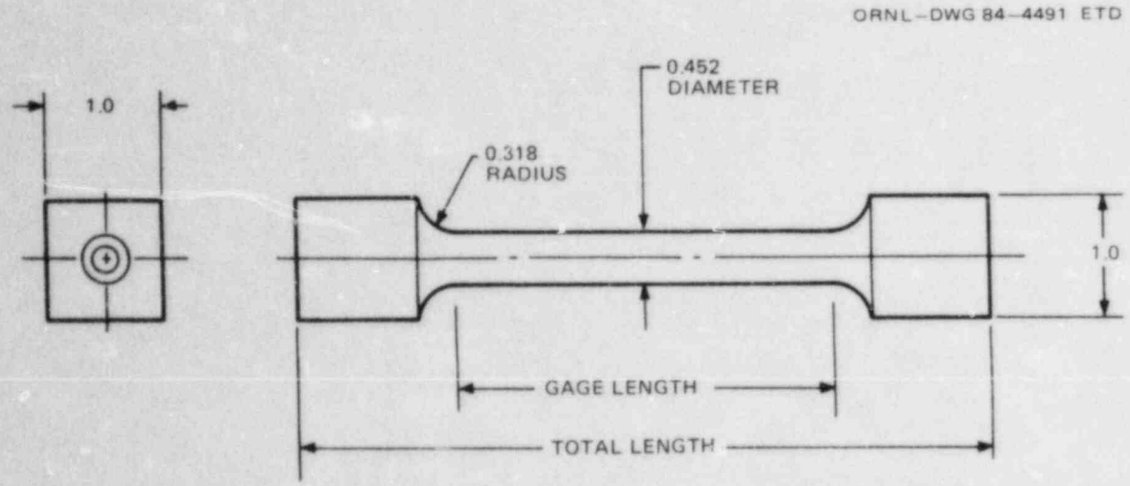

	GAGE LENGTH (cm)	TOTAL LENGTH (cm)
LONG SPECIMEN	3.175	5.5
SHORT SPECIMEN	2.924	5.0

Fig. 6.1. Tensile specimen configurations.

Table 6.4. Average tensile strength
Third HSST Irradiation Series[a]

Material	$\sigma_{Y,U}$ (MPa)	$\sigma_{Y,I}$ (MPa)	$\frac{\sigma_{Y,I}-\sigma_{Y,U}}{\sigma_{Y,U}}$ (%)	$\sigma_{U,U}$ (MPa)	$\sigma_{U,I}$ (MPa)	$\frac{\sigma_{U,I}-\sigma_{U,U}}{\sigma_{U,U}}$ (%)
64W	422	537	27	541	644	19
65W	427	501	18	542	590	9
66W	509	608	19	606	695	15
67W	434	561	29	552	655	19

[a]where

$\sigma_{Y,U}$ = average unirradiated yield strength from 22 to 288°C

$\sigma_{Y,I}$ = average irradiated yield strength from 22 to 288°C

$\sigma_{U,U}$ = average unirradiated ultimate strength from 22 to 288°C

$\sigma_{U,I}$ = average irradiated ultimate strength from 22 to 288°C

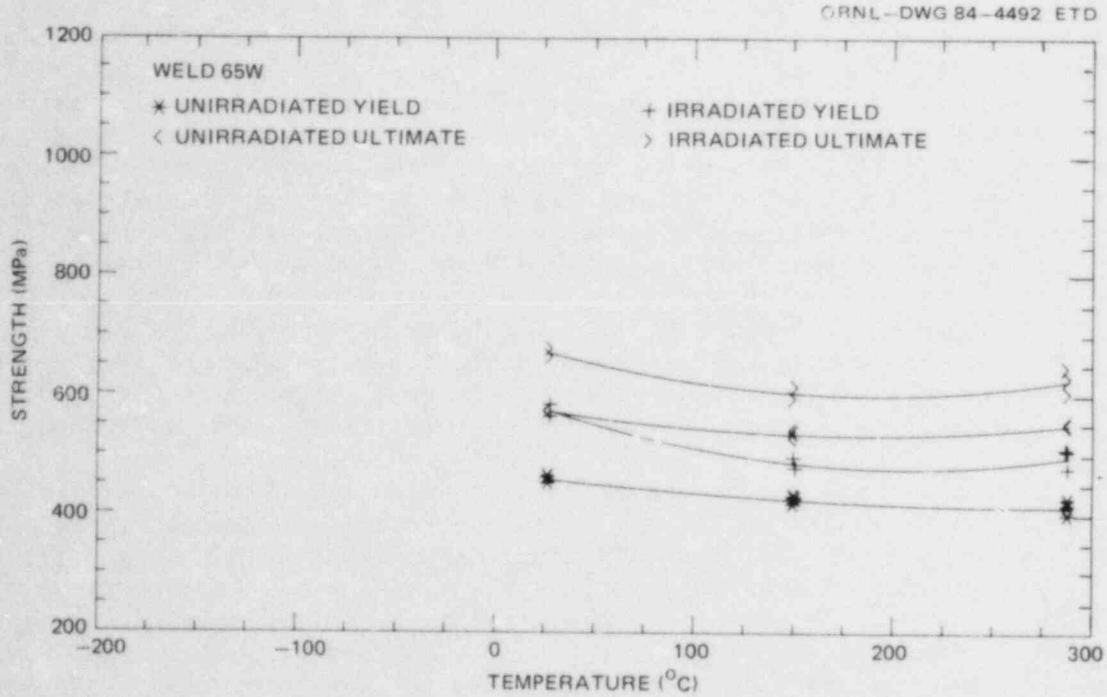

Fig. 6.2. Tensile strength of irradiated and unirradiated weld 65W.

Table 6.5. Average total elongation
Third HSST Irradiation Series[a]

Material	$\varepsilon_{T,U}$ (%)	$\varepsilon_{T,I}$ (%)	$\varepsilon_{T,I} - \varepsilon_{T,U}$ (%)
64W	17	15	-2
65W	16	17	1
66W	14	14	0
67W	15	14	-1

[a]where

$\varepsilon_{T,U}$ = average unirradiated total elongation from 22 to 288°C

$\varepsilon_{T,I}$ = average irradiated total elongation from 22 to 288°C

CVN results for the first three capsules have been reported previously in Ref. 4. A summary of the CVN results is shown in Table 6.6. Plate 02 was the most sensitive to irradiation, whereas welds 68W and 71W were the least sensitive. The chemical composition of these materials is shown in Table 6.7.

The long-type miniature tensile specimen shown in Fig. 6.1 was used in this study. The diameter was 4.52 mm, and the overall length was 5.5 cm. The tensile strength properties of the materials are summarized in Tables 6.8 and 6.9 for the unirradiated and irradiated condition, respectively. The unirradiated strengths differ considerably with weld 69W being the strongest; welds 70W and 71W were the weakest. Irradiation at 288°C to a fluence of 11 to 23 $\times 10^{22}$ neutrons/m^2 (E > 1 MeV) produced varied responses in the materials. The behavior of welds 70W and 71W is shown in Figs. 6.3 and 6.4, respectively. The yield strength was generally affected more than the ultimate strength as shown in Table 6.10. The strength of plate 02 was more affected by irradiation (10%) than the welds.

The elongation properties of the materials are listed in Tables 6.8 and 6.9 for the unirradiated and irradiated condition, respectively. The total elongation changed ±1% with irradiation as shown in Table 6.11.

All testing of unirradiated 1TCS specimens at Oak Ridge National Laboratory (ORNL) has been completed, and only limited testing of unirradiated 1TCS specimens remains at Materials Engineering Associates (MEA). Some preliminary tests of irradiated 1TCS specimens have been performed at ORNL. Both laboratories used unloading compliance to measure crack length, and all specimens had razor blades mounted at the load line. The ORNL testing system used an HP-9836 microcomputer to control the test and acquire data; as a result, the crack length could be determined within 0.02 mm during each unloading. The specimen was loaded under load-line displacement control at a rate of 0.2 mm/min. A 1-min hold at constant load-line displacement was performed prior to each unloading to minimize hysteresis problems. Smooth-sided specimens were used in the transition region, whereas 20% side-grooved specimens were used in the upper-shelf region. When applicable, K_{Ic} according to ASTM E399 (Ref. 5) was determined; otherwise, the Modified-Ernst J-Integral[6] was used to infer $K_J = \sqrt{EJ_c}$ where E(GPa) = 207.2 − 0.57 T(°C). If there was no significant crack growth (the J_I vs Δa curve did not intersect the 0.15-mm exclusion line), J to maximum load was used to determine K_J. If there was significant crack growth (the J_I vs Δa curve did intersect the 0.15-mm exclusion line), J_{Ic} was used to determine K_J. A typical J-R curve is shown in Fig. 6.5. Note that J_{Ic} is determined both with the power law and ASTM E813 (Ref. 7) procedure. A summary of results from all the unirradiated tests with nonsignificant crack growth is shown in Tables 6.12 and 6.13 for ORNL and MEA, respectively. A summary for all unirradiated tests with significant crack growth is shown in Tables 6.14 and 6.15 for ORNL and MEA, respectively. A summary for all ORNL irradiated tests with nonsignificant crack growth is shown in Table 6.16. A summary for all ORNL irradiated tests with significant crack growth is shown in Table 6.17. A comparison of the fracture-toughness data for the two laboratories is shown in Figs. 6.6–6.10. Note that there is no significant variation between the two laboratories. The welds show substantially more scatter in the fracture toughness (±50 MPa$\cdot\sqrt{m}$) because of their relative

Table 6.6. Charpy property degradation of low-copper welds and plate produced by irradiation to 2.0×10^{23} neutrons/m^2 (288°C)

Material	Content (wt %)		Observed transition temperature shift (°C)	Observed upper-shelf energy change (%)
	Cu	Ni		
Plate 02	0.14	0.67	78 ± 4	−14 ± 2
Weld 68W	0.040	0.13	14 ± 3	−3 ± 4
Weld 69W	0.120	0.10	51 ± 4	0 ± 6
Weld 70W	0.056	0.63	37 ± 6	+0.5 ± 3
Weld 71W	0.046	0.063	15 ± 7	+12 ± 4

Table 6.7. Chemical composition of plate 02 and submerged-arc welds for Fourth HSST Irradiation Series

Material	Average composition (wt %)									
	C	Mn	P	S	Si	Cr	Ni	Mo	Cu	V
Plate 02	0.23	1.55	0.009	0.014	0.20	0.04	0.67	0.53	0.14	0.003
Weld 68W	0.15	1.38	0.008	0.009	0.16	0.04	0.13	0.60	0.04	0.007
Weld 69W	0.14	1.19	0.010	0.009	0.19	0.09	0.10	0.54	0.12	0.005
Weld 70W	0.10	1.48	0.011	0.011	0.44	0.13	0.63	0.47	0.056	0.004
Weld 71W	0.124	1.58	0.011	0.011	0.54	0.12	0.63	0.45	0.046	0.005

Table 6.8. Tensile properties of unirradiated welds and plates
Fourth HSST Irradiation Series

Specimen No.	Test temperature (°C)	Yield strength (MPa)	Ultimate strength (MPa)	Uniform strain (%)	Reduction in area (%)	Total elongation (%)
68W1	-140	772	821	9.3	69.0	18.9
4	-140	816	847	11.6	67.0	20.3
8	-40	588	693	9.7	72.7	20.5
12	124	519	599	3.5	73.1	13.6
13	287	497	624	7.4	73.1	15.9
14	287	493	618	6.9	72.8	15.2
69W1	-140	873	927	12.4	65.8	21.5
2	-90	737	838	10.1	66.2	20.8
3	-40	678	780	9.2	69.9	17.3
4	27	642	723	7.6	68.3	16.2
5	123	600	688	6.5	68.0	13.9
7	204	571	696	7.3	67.4	14.8
8	287	572	714	9.1	59.2	16.3
10	-140	849	920	9.8	67.2	18.3
11	-40	679	779	8.4	67.9	16.8
16	27	635	721	6.8	71.1	15.4
19	122	601	681	5.9	70.5	13.6
20	287	582	708	6.8	60.5	13.4
70W1	-140	686	809	18.4	57.1	26.0
2	-90	574	715	11.8	64.2	23.3
3	-40	524	658	11.5	68.0	22.4
4	27	480	593	10.3	68.1	19.8
5	122	453	558	8.3	68.8	16.1
6	203	436	561	7.3	66.7	15.8
9	287	436	578	8.1	65.5	15.4
11	-140	664	784	12.7	62.7	22.9
12	-40	525	655	12.0	67.2	21.2
15	27	476	594	9.1	69.4	18.2
17	124	452	556	8.3	67.8	16.9
18	288	429	573	8.4	64.1	16.3
71W1	-140	669	795	13.7	60.8	21.9
2	-91	566	718	13.4	62.1	22.2
4	-40	506	659	12.5	64.2	20.9
5	27	469	600	9.3	67.3	18.2
7	122	447	557	8.7	66.1	16.0
8	203	429	557	8.3	64.2	15.9
10	289	430	581	8.2	59.6	14.6
12	-140	681	806	13.9	58.7	23.5
13	-40	511	658	12.4	65.2	20.5
14	27	469	598	10.0	68.3	19.4
16	122	442	558	8.7	64.9	16.0
18	289	428	568	8.7	60.9	15.1
02GA510	28	466	621	9.1	68.2	17.8
511	28	468	623	9.1	69.4	18.9
514	-40	517	687	12.2	67.2	20.0
515	-40	505	683	11.1	68.1	19.9
516	-90	559	746	11.8	62.6	20.7
517	-90	569	755	12.2	55.8	18.8
518	122	448	569	7.5	68.1	15.2
519	123	441	584	7.3	65.7	15.2
520	203	426	586	7.9	66.9	15.5
521	203	423	582	7.7	65.5	15.3
523	289	433	622	9.6	56.8	18.0
524	-140	684	836	12.9	58.3	23.4
525	-140	678	846	12.8	55.4	20.1
532	289	432	621	9.0	59.5	16.5

Table 6.9. Tensile properties of irradiated welds and plates
Fourth HSST Irradiation Series

Specimen No.	Fluence (10^{22} neutrons/m^2)	Irradiation temperature (°C)	Test temperature (°C)	Yield strength (MPa)	Ultimate strength (MPa)	Uniform strain (%)	Reduction in area (%)	Total elongation (%)
68W2	7.5	288	36	555	634	6.1	72.5	15.0
6	13.0	288	122	537	612	5.7	77.0	14.0
7	14.6	288	36	573	656	6.9	69.6	16.0
9	16.9	288	287	575	641	6.3	76.9	16.1
15	12.8	288	289	521	633	6.8	70.2	15.3
69W6	8.0	288	35	704	776	8.4	65.0	17.4
12	13.6	288	121	674	747	7.0	66.8	14.4
14	16.6	288	288	652	755	7.4	59.2	14.2
15	15.8	288	122	675	749	6.5	68.9	14.1
17	13.8	288	34	717	792	7.1	65.7	15.3
18	10.5	288	287	653	756	6.8	59.5	14.0
70W7	10.4	288	288	467	615	9.1	62.0	16.9
8	16.5	288	28	534	649	10.3	64.6	19.0
10	19.8	288	121	499	607	9.1	60.8	17.1
13	21.1	288	288	472	615	9.2	48.8	15.7
16	14.0	288	122	495	597	10.1	68.7	18.0
71W3	10.2	288	288	461	592	7.9	60.1	14.5
9	19.5	288	122	498	604	10.1	60.3	18.0
11	20.8	288	288	470	608	8.3	48.5	13.6
15	18.6	288	29	539	649	10.3	62.2	18.8
17	13.7	288	121	487	592	9.2	63.8	17.0
02GA503	17.6	288	34	609	749	10.4	61.1	18.1
504	22.5	288	288	533	706	8.5	50.3	14.7
505	22.0	288	121	581	712	8.2	54.4	14.4
506	21.4	288	31	617	753	9.4	52.9	16.8
508	13.9	288	121	566	699	9.5	62.5	16.1
509	13.6	288	288	519	696	9.3	61.3	15.3

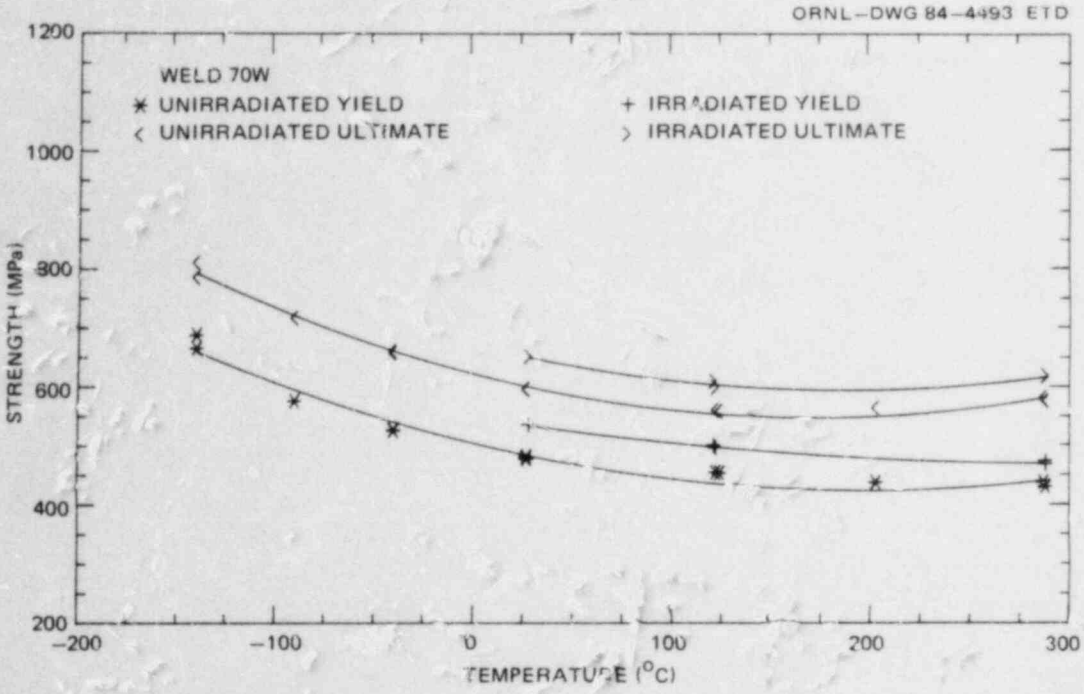

Fig. 6.3. Tensile strength of irradiated and unirradiated weld 70W.

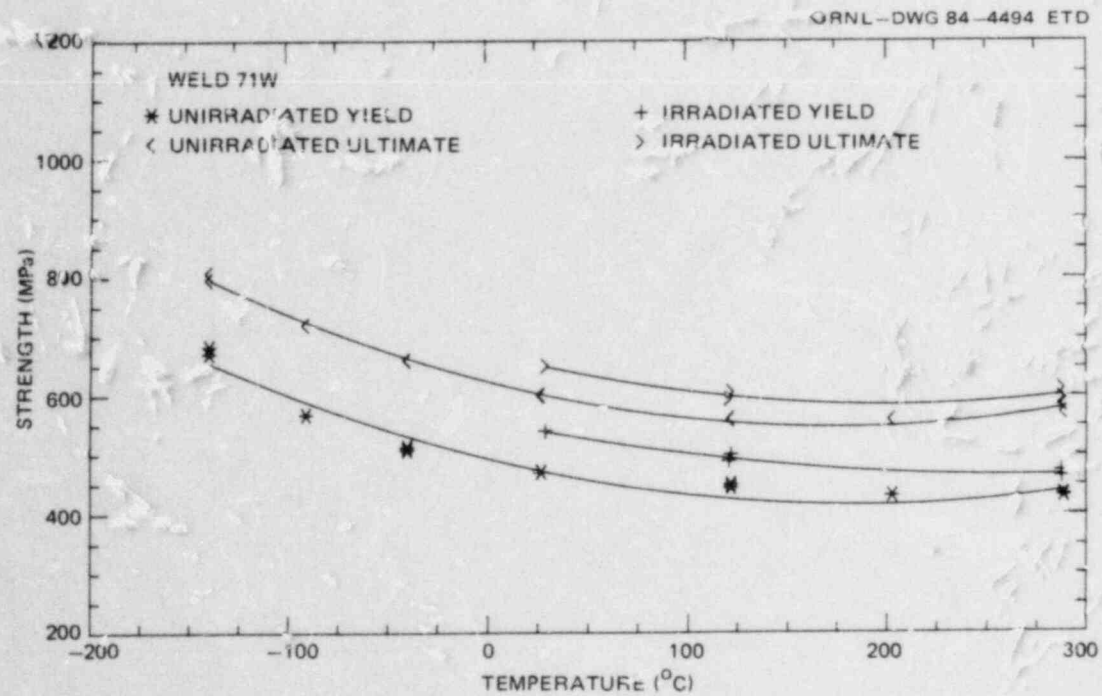

Fig. 6.4. Tensile strength of irradiated and unirradiated weld 71W.

Table 6.10. Average tensile strength
Fourth HSST Irradiation Series[a]

Material	$\sigma_{Y,U}$ (MPa)	$\sigma_{Y,I}$ (MPa)	$\frac{\sigma_{Y,I}-\sigma_{Y,U}}{\sigma_{Y,U}}$ (%)	$\sigma_{U,U}$ (MPa)	$\sigma_{U,I}$ (MPa)	$\frac{\sigma_{U,I}-\sigma_{U,U}}{\sigma_{U,U}}$ (%)
Plate 02	432	564	31	590	707	20
Weld 68W	496	590	19	604	620	3
Weld 69W	584	672	15	692	752	9
Weld 70W	440	493	12	562	608	8
Weld 71W	430	489	14	563	602	7

[a]where

$\sigma_{Y,U}$ = average unirradiated yield strength from 22 to 288°C

$\sigma_{Y,I}$ = average irradiated yield strength from 22 to 288°C

$\sigma_{U,U}$ = average unirradiated ultimate strength from 22 to 288°C

$\sigma_{U,I}$ = average irradiated ultimate strength from 22 to 288°C

Table 6.11. Average total elongation
Fourth HSST Irradiation Series[a]

Material	$\varepsilon_{T,U}$ (%)	$\varepsilon_{T,I}$ (%)	$\varepsilon_{T,I}-\varepsilon_{T,U}$ (%)
Plate 02	15	16	+1
Weld 68W	16	15	−1
Weld 69W	15	15	0
Weld 70W	17	17	0
Weld 71W	16	17	+1

[a]where

$\varepsilon_{T,U}$ = average unirradiated total elongation from 22 to 288°C

$\varepsilon_{T,I}$ = average irradiated total elongation from 22 to 288°C

Table 6.12. ORNL transition region test data summary unirradiated 1TCS specimens

Specimen No.	Test temperature (°C)	$(a/W)_i$	J_{max} (kJ/m^2)	K_J (MPa·$\sqrt{m}$)	K_{Ic} (MPa·$\sqrt{m}$)	$K_{\beta c}$ (MPa·$\sqrt{m}$)	Yield stress (MPa)
02GA283	-95	0.619			57.3		593.1
02GA296	-40	0.617	22.81	69.1		59.6	529.4
02GA30[illegible]	-40	0.621	26.60	74.7		62.6	529.4
02GA312	-95	0.612			42.0		593.1
02GA350	-80	0.622	13.36	53.2		50.1	574.3
02GA367	0	0.622	75.50	125.1		79.5	492.0
02GA415	-100	0.614			44.4		599.6
02GA417	0	0.606	76.04	125.5		79.6	492.0
68WCB	-80	0.601			59.5		683.7
68WDD	-30	0.616	216.82	212.8		113.4	614.7
68WEB	-135	0.597			40.2		775.6
68WKD	-80	0.604	70.87	122.5		92.9	683.7
69W103	-100	0.595			42.4		778.8
69W109	-100	0.597			40.7		778.8
69W124	-20	0.605	58.31	110.2		87.4	679.9
69W128	-5	0.599	44.31	95.9		79.7	664.8
69W136	-60	0.596			60.8		725.5
69W140	-60	0.587			56.1		725.5
69W151	20	0.600	118.25	156.1		101.6	642.0
70W103	-135	0.550			35.9		652.1
70W120	-40	0.552	59.23	111.4		78.9	540.0
70W127	-135	0.549			47.3		652.1
70W143	-65	0.546	58.12	110.7		80.5	565.8
71W105	-90	0.547			47.8		587.0
71W107	-50	0.544	35.07	85.8		68.6	540.7
71W114	-10	0.553	61.02	112.6		76.4	501.6

Table 6.13. MEA transition region test data summary
unirradiated 1TCS specimens

Specimen No.	Test temperature (°C)	$(a/w)_i$	J_{max} (kJ/m^2)	K_{Jc} (MPa·$\sqrt{m}$)	K_{Ic} (MPa·$\sqrt{m}$)	$K_{\beta c}$ (MPa·$\sqrt{m}$)	Yield stress (MPa)
02G-292	–95	0.617	8.8	43.2	44.4	42.1	593
02G-300	–95	0.623	15.6	57.6	58.7	53.8	593
02G-308	–95	0.620	9.1	44.1	45.2	42.8	593
02G-297	–5	0.619	74.2	124.1		79.5	496
02G-304	–5	0.619	90.6	137.2		83.2	496
02G-313	–5	0.619	81.8	130.3		81.3	496
68W-JE	–125	0.603	29.4	79.4		72.9	757
68W-HA	–120	0.599	16.2	58.9	59.8	56.9	749
68W-JC	–95	0.597	40.2	92.5		79.6	707
68W-HE	–80	0.608	107.3	150.8		103.3	684
69W-135	–100	0.592	9.6	45.1	46.6	44.6	779
69W-104	–60	0.597	30.6	80.3		72.7	725
69W-111	–5	0.604	39.4	90.5		76.8	665
69W-158	–5	0.600	84.4	132.4		95.5	665
70W-102	–115	0.544	21.5	67.8		61.7	625
70W-109	–115	0.546	8.3	42.0	44.1	41.2	625
70W-121	–65	0.546	32.8	83.2		68.6	566
70W-122	–65	0.548	73.0	124.1		85.2	566
70W-141	–35	0.566	89.5	136.9		86.7	525
71W-132	–95	0.550	16.8	59.8		55.4	593
71W-113	–95	0.548	17.7	61.4		56.5	593

Table 6.14. ORNL upper-shelf J-R curve data summary, unirradiated lTCS specimens

Specimen No.	Test temperature (°C)	Side groove (%)	$(a/W)_i$	Δa_m (mm)	$\Delta a_p - \Delta a_m$ (mm)	J_{Ic}		K_{Jc}		T_{avg}		Flow stress (MPa)	J=8.8T (kJ/m²)	E813 Validity
						Power law (kJ/m²)	ASTM (kJ/m²)	Power law (MPa·√m)	ASTM (MPa·√m)	Power law	ASTM			
02GA299	50	20	0.620	3.091	0.086	244.1	247.2	223.4	224.7	132.7	129.4	531.2	2148.1	Valid
02GA303	121	20	0.620	3.063	-0.215	182.?	187.2	191.0	193.6	142.2	135.6	500.3	1251.4	Valid
02GA321	204	20	0.626	3.089	0.166	158.9	154.1	176.3	173.6	110.2	112.9	498.5	969.8	Valid
02GA325	121	24	0.622	4.107	0.155	145.7	138.6	170.8	166.6	146.7	139.7	500.3	1291.0	Valid
02GA326	204	20	0.623	5.728	0.042	139.7	137.7	165.3	164.1	102.7	103.6	498.5	903.8	Valid
02GA327	288	20	0.632	6.007	-0.140	141.7	140.3	164.4	163.6	65.3	68.9	534.0	574.6	Valid
02GA357	288	20	0.627	3.729	-0.082	137.4	136.0	161.9	161.1	93.9	95.3	534.0	826.3	Valid
68WAA	288	20	0.598	3.205	-0.610	268.5	256.8	226.3	221.3	122.6	128.3	561.6	1078.9	
68WHB	121	20	0.607	3.124	-0.233	234.2	178.6	216.6	189.1	203.4	221.2	542.5	1789.9	Valid
68WKA	23	20	0.604	2.784	0.292	213.9	146.7	209.9	173.8	211.6	226.7	600.1	1862.1	Valid
69W117	121	20	0.598	3.178	0.297	172.9	169.4	186.1	184.2	85.8	85.0	630.5	755.0	Valid
69W125	50	20	0.591	2.715	0.318	175.8	168.5	189.6	185.6	74.6	77.3	664.1	656.5	Valid
69W141	121	20	0.595	3.200	0.400	180.1	188.6	189.9	194.4	82.2	79.5	630.5	723.4	Valid
69W145	204	20	0.603	3.658	0.255	144.9	144.5	168.3	168.1	59.7	62.1	623.1	525.4	Valid
69W154	288	20	0.598	3.307	-0.069	126.3	123.5	155.2	153.5	49.9	51.6	650.9	439.1	Valid
69W161	288	20	0.598	3.929	-0.058	148.8	148.0	168.5	168.0	50.3	52.4	650.9	442.6	Valid
69W169	204	20	0.609	2.891	0.437	102.3	103.1	141.5	142.0	62.0	62.6	623.1	545.6	
70W114	121	20	0.552	3.274	0.251	130.4	116.4	161.6	152.7	151.2	156.1	494.4	1330.6	Valid
70W116	288	20	0.553	3.800	0.017	121.4	118.8	152.2	150.6	83.5	86.2	511.2	734.8	Valid
70W135	121	20	0.548	2.977	0.319	114.3	90.4	151.3	134.5	171.0	179.4	494.4	1504.8	Valid
70W144	204	20	0.553	2.809	0.230	147.1	126.5	169.6	157.3	124.9	135.2	486.6	1089.1	Valid
70W147	204	20	0.553	3.010	0.271	126.5	125.4	157.3	156.6	108.0	108.4	486.6	950.4	Valid
70W150	50	20	0.543	2.995	0.330	146.5	115.4	173.0	153.6	168.1	179.8	526.2	1479.3	Valid
70W152	288	20	0.545	3.053	0.033	117.7	112.4	149.8	146.5	92.1	95.4	511.2	810.5	Valid
71W103	121	20	0.556	3.330	0.252	112.5	108.8	150.1	147.6	117.7	118.1	4?9.3	1035.8	Valid
71W124	50	20	0.556	3.012	0.338	98.2	78.6	141.7	126.8	160.2	162.8	52?.5	1409.8	Valid
71W125	204	20	0.553	3.190	-0.288	113.6	113.2	149.1	148.8	86.6	88.0	482.1	762.1	Valid
71W127	288	20	0.553	3.868	0.058	72.9	73.4	117.9	118.3	65.0	64.6	508.2	572.0	Valid
02GA293	23	0	0.619	1.059	-0.240	208.9	166.4	207.4	185.1	164.7	194.5	549.9	1473.1	
02GA309	23	0	0.617	0.559	-0.165	258.1		230.5		124.6		549.9	1096.5	
02GA374	40	0	0.623	3.838	-0.945	259.6	192.2	230.7	198.5	251.1	274.7	537.7	2209.7	
69W132	22	0	0.592	0.942	-0.228	95.0	47.0	139.9	98.3	101.0	120.8	684.4	888.8	
71W130	30	0	0.547	3.686	-0.315	95.0	56.4	139.7	107.7	204.2	203.6	534.8	1797.0	
71W135	-10	0	0.551	0.455	-0.074	160.5		182.6		146.8		567.3	1291.8	

Table 6.15. MEA upper-shelf J-R curve data summary, unirradiated ITCS specimens

Specimen No.	Test temperature (°C)	Side groove (%)	$(a/w)_i$	Δa_m (mm)	$\Delta a_p - \Delta a_m$ (mm)	J_{Ic} Power law (kJ/m²)	J_{Ic} ASTM (kJ/m²)	K_{Jc} Power law (MPa·√m)	K_{Jc} ASTM (MPa·√m)	T_{avg} Power law	T_{avg} ASTM	Flow stress (MPa)	J = 8.8T (kJ/m²)	E813 Validity
02G-294	121	20	0.623	8.95	−0.254	164.3	141.6	181.4	168.4	168	178	500	752.6	V
02G-302	121	20	0.618	6.01	−0.528	170.2	167.0	184.6	182.9	149	147	500	746.3	V
02G-310	121	20	0.622	6.00	−0.102	183.3	173.9	191.6	186.6	127	133	500	696.0	V
02G-306	204	20	0.620	10.31	−0.447	145.1	139.8	168.4	165.3	117	118	498	558.4	V
02G-315	204	20	0.623	10.40	−0.263	156.3	148.5	174.8	170.4	104	113	498	459.0	V
02G-320	204	20	0.623	10.96	−0.492	150.5	147.3	171.5	169.7	113	115	498	535.6	V
02G-319	288	20	0.622	8.73	−0.316	128.6	121.3	156.6	152.1	73	81	534	431.1	V
02G-324	288	20	0.622	8.50	−0.280	135.1	128.0	160.5	156.3	87	92	534	509.7	V
02G-333	288	20	0.626	5.84	−0.126	121.1	121.6	152.0	152.3	76	73	534	475.4	V
68W-MC	121	20	0.606	8.01	−0.217	177.5	156.1	188.5	176.8	203	204	542	1054.8	V
68W-HD	200	20	0.606	4.07	−0.229	242.3	236.1	217.8	215.0	106	111	533	575.9	V
68W-JD	288	20	0.604	7.09	−0.157	161.3	131.5	175.4	158.4	117	132	561	651.0	V
69W-110	121	20	0.603	9.98	−0.136	147.4	147.3	171.8	171.8	82	82	630	466.9	V
69W-162	121	20	0.598	9.72	−0.080	152.9	144.2	175	169.9	85	89	630	493.2	V
69W-150	200	20	0.602	4.69	+0.318	187.6	184.3	191.6	190	50	54	623	323.1	V
69W-168	204	20	0.607	9.98	−0.121	126.1	124.0	157.0	124.0	61	61	623	343	V
69W-127	288	20	0.601	10.50	−0.101	101.5	102.0	139.2	139.5	51	49	651	299.7	V
69W-180	288	20	0.605	10.80	−0.122	106.4	97.2	142.4	136.2	50	56	651	296.3	V
70W-105	121	20	0.547	10.59	−0.130	148.4	135.4	172.4	164.7	140	148	494	684.5	V
70W-146	204	20	0.548	9.95	−0.011	115.6	109.3	150.3	146.2	105	108	486	480.1	V
70W-151	288	20	0.552	9.98	−0.087	94.6	95.5	134.4	135	80	79	381	380.7	V
71W-152	121	20	0.553	10.08	−0.099	131.6	114.4	162.4	151.4	143	153	489	705.5	V
71W-136	121	20	0.554	11.94	−0.228	144.4	135.2	170.1	164.6	151	155	489	750.8	V
71W-129	204	20	0.555	10.96	−0.043	95.5	89.7	136.7	132.4	82	87	482	355.5	V
71W-106	204	20	0.544	10.48	+0.052	81.0	82.1	125.8	126.7	68	66	482	291.3	V
71W-148	288	20	0.545	11.05	−0.020	81.1	83.8	124.4	126.5	74	71	508	347.2	V
71W-104	288	20	0.565	10.11	−0.005	77.5	69.9	121.6	115.5	65	72	508	296.9	V
68W-AE	−40	0	0.600	0.53		262.3		234.4				664		IV
71W-137	−5	0	0.556	3.13	−0.820	188.3	155.3	197.7	179.5	165	170	563		IV
71W-145	−10	0	0.555	1.43	−0.370	168.9	101.7	187.3	145.3	162	201	567		IV

Table 6.16. ORNL transition region test data summary
irradiated 1TCS specimens (preliminary data)

Specimen No.	Test temperature (°C)	Fluence 10^{22} (neutrons/m^2)	Irradiated temperature (°C)	$(a/W)_1$	J_{max} (kJ/m^2)	K_{Jc} (MPa·$\sqrt{m}$)	K_{Ic} (MPa·$\sqrt{m}$)	$K_{\beta c}$ (MPa·$\sqrt{m}$)	Yield stress (MPa)
02GA288	79	20.4	288	0.615	83.10	129.8		89.1	590.8
02GA407	50	20.5	288	0.606	18.12	60.9		56.4	604.3
69W113	29	12.4	288	0.599	51.80	103.2		85.7	713.9
69W142	-36	13.4	288	0.597			52.0		752.7
71W122	-13	20.5	288	0.535	56.11	108.0		79.6	567.3
71W143	-73	19.4	288	0.527			34.4		616.1

Table 6.17. ORNL upper-shelf J-R curve data summary
irradiated lTCS specimens (preliminary data)

Specimen No.	Test temperature (°C)	Fluence 10^{22} (neutrons/m^2)	Side groove (%)	Irradiation temperature (°C)	$(a/W)_i$	Δa_p (mm)	J_c		$K_{J_{Ic}}$		T_{avg}		Flow stress (MPa)	J=8.8T (kJ/m^2)
							Power law (kJ/m^2)	ASTM (kJ/m^2)	Power law (MPa·$\sqrt{m}$)	ASTM (MPa·$\sqrt{m}$)	Power law	ASTM		
69W116	52	14.0	0	288	0.588	1.124	80.31	57.6	128.1	108.4	61.9	69.3	738.5	544.7
71W140	16	21.2	0	288	0.535	0.392	140.5		170.2		81.6		603.3	718.1

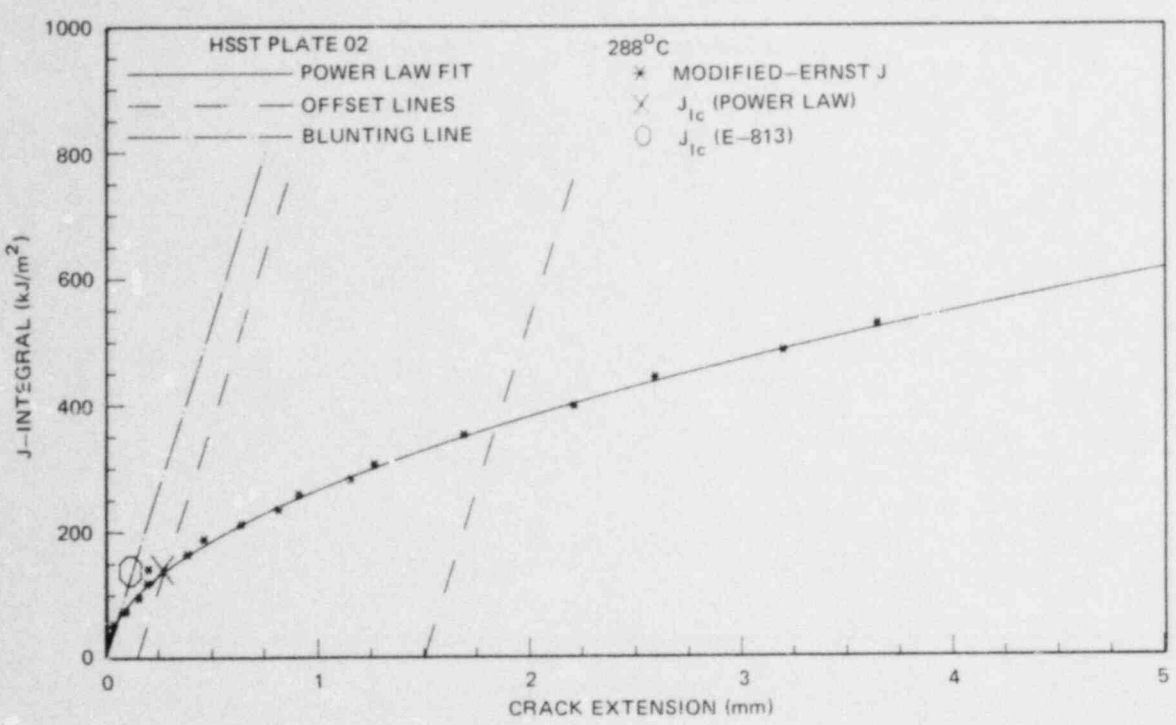

Fig. 6.5. Typical J-R curve from ORNL microcomputer testing system.

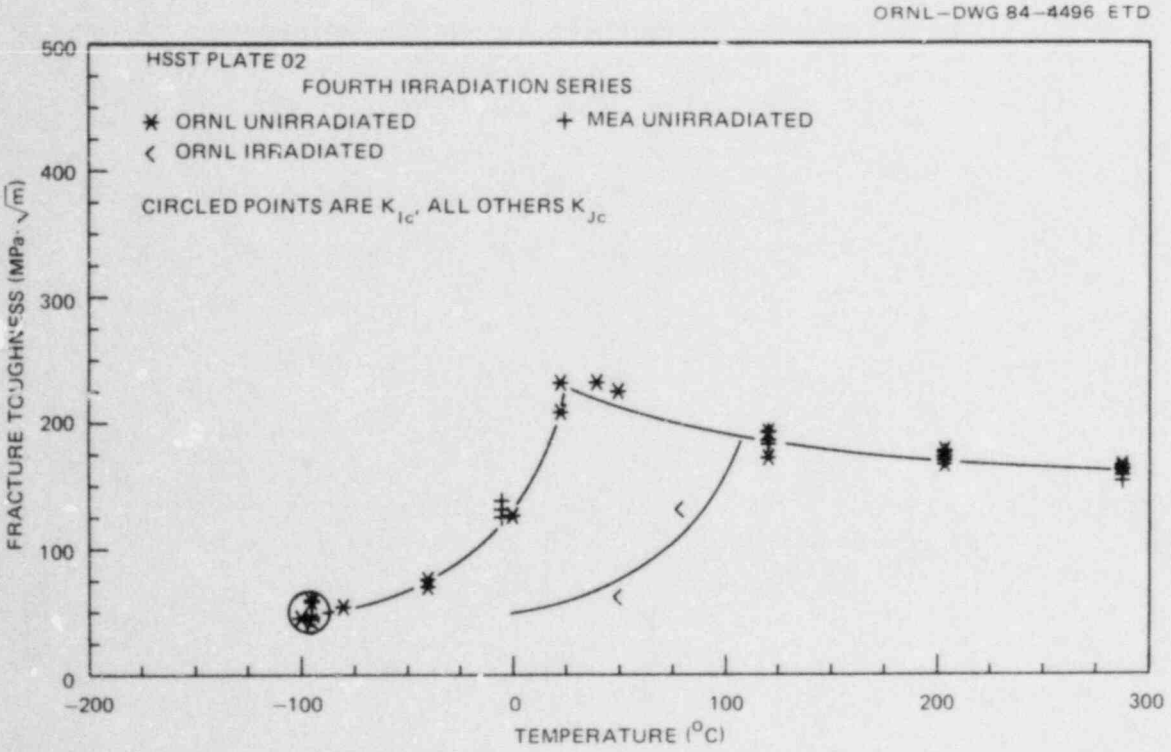

Fig. 6.6. Fracture toughness of irradiated and unirradiated plate 0.2.

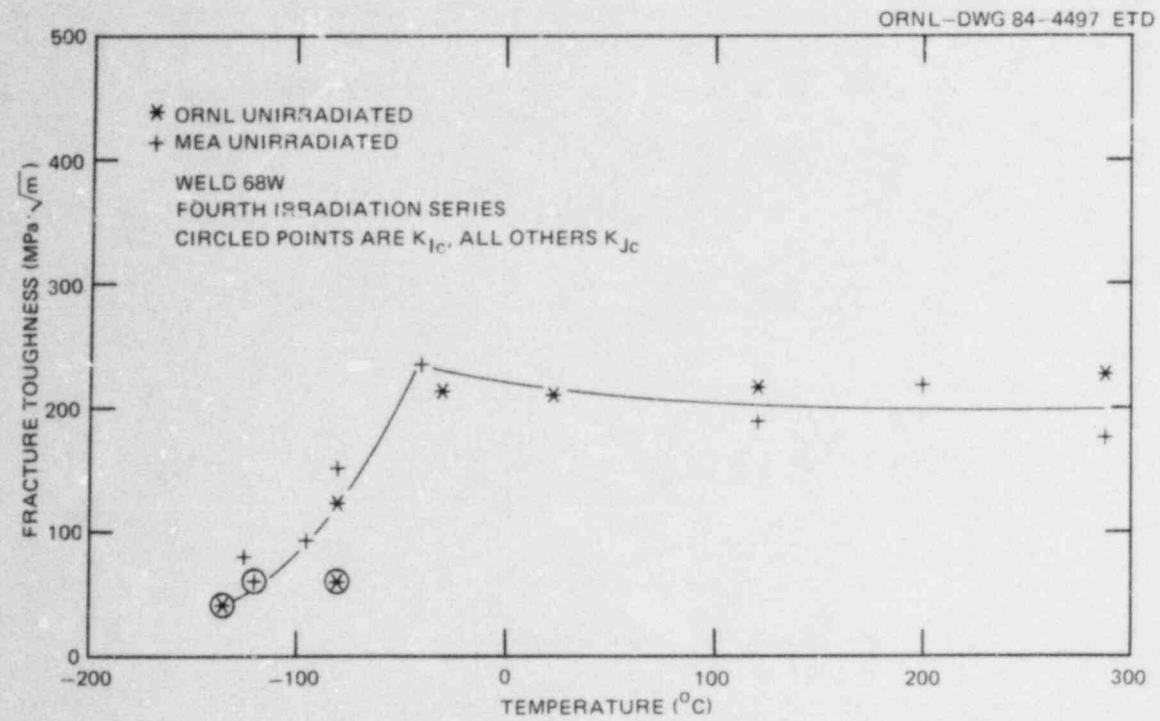

Fig. 6.7. Fracture toughness of unirradiated weld 68W.

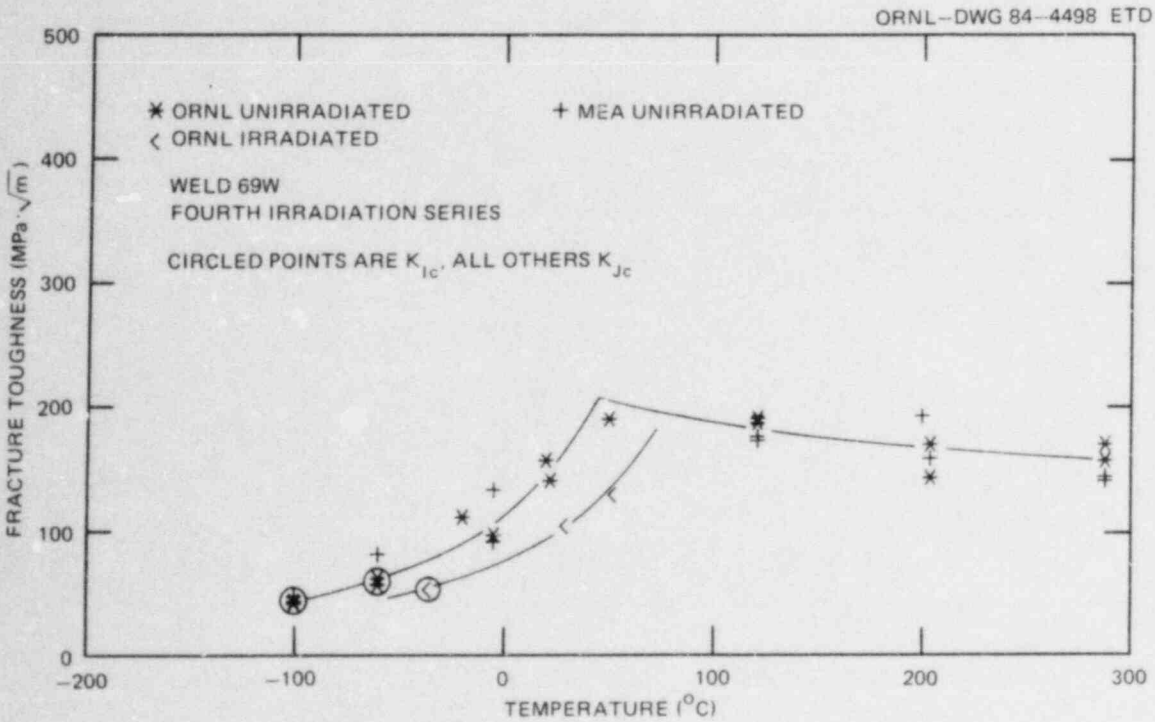

Fig. 6.8. Fracture toughness of irradiated and unirradiated weld 69W.

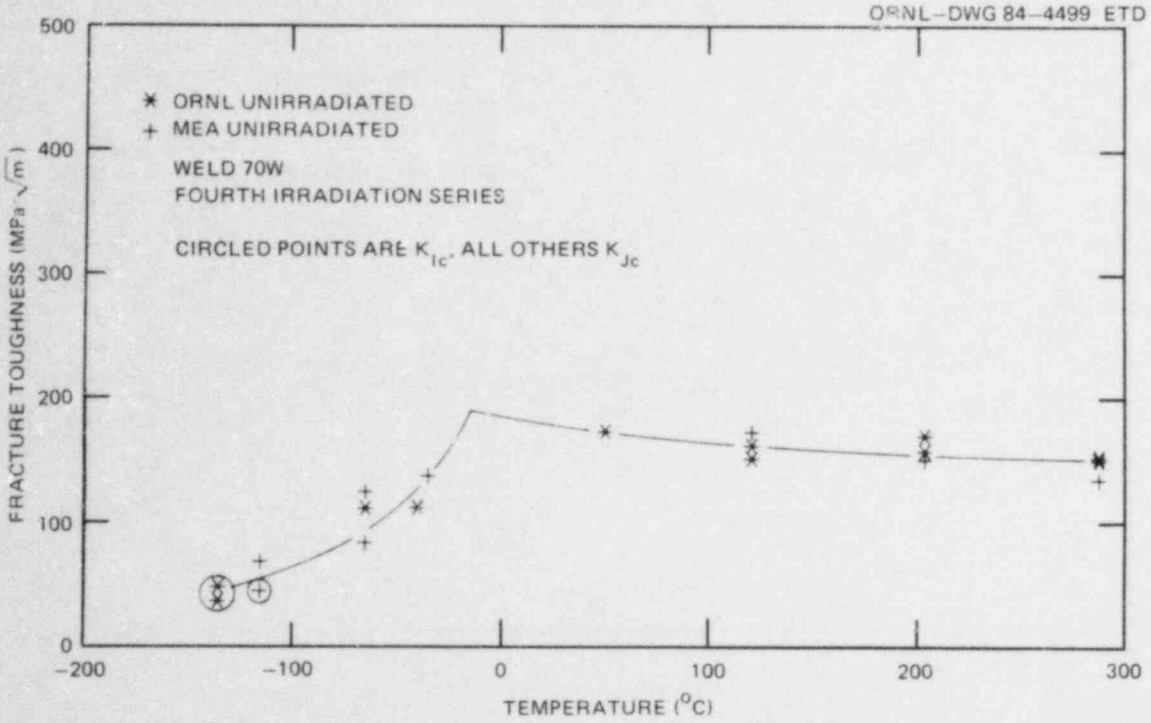

Fig. 6.9. Fracture toughness of unirradiated weld 70W.

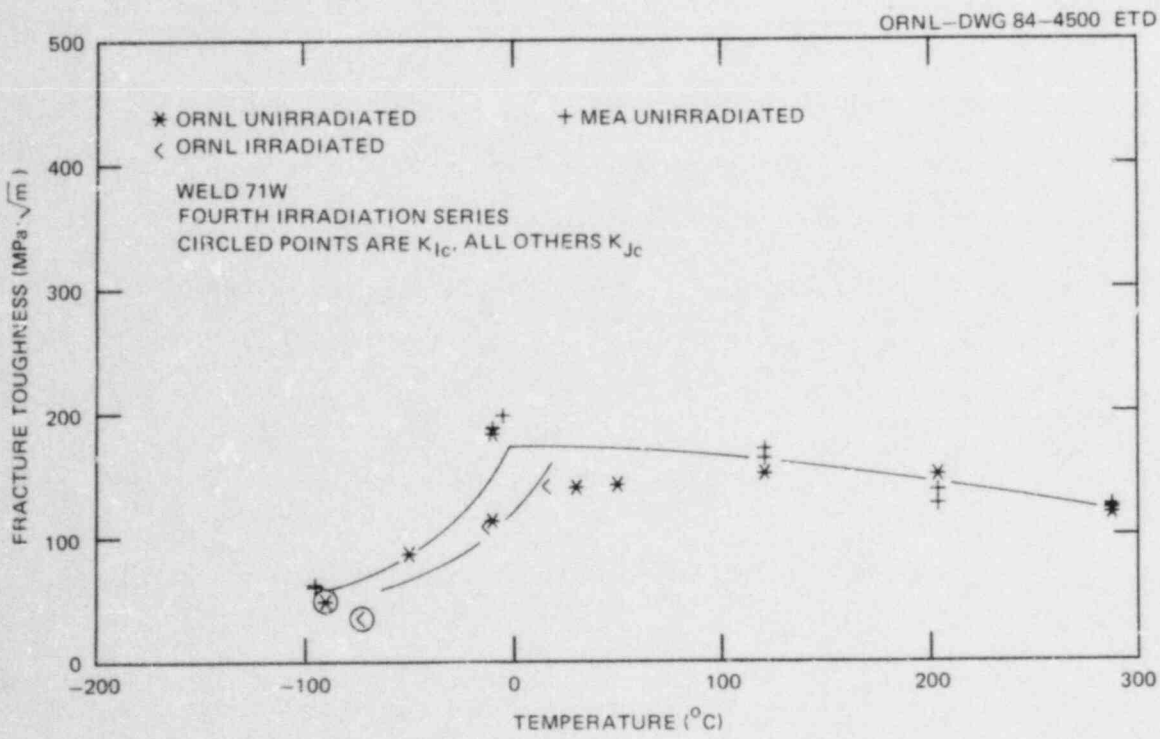

Fig. 6.10. Fracture toughness of irradiated and unirradiated weld 71W.

inhomogeneity. The $K_{\beta c}$ values were calculated using the Merkle method[8] to estimate lower-bound fracture toughness in the transition region.

A summary of the fracture-toughness parameters for the five materials is shown in Table 6.18. Weld 68 had the lowest transition temperature, and weld 69W had the highest. The estimated irradiation-induced transition temperature shift is within 15°C of that predicted from CVN results (Table 6.6). Weld 68W had the highest upper-shelf toughness, whereas weld 71W had the lowest. Testing should be completed shortly with the final draft report being completed in the next 6 months.

Table 6.18. Fracture toughness parameters summary
Fourth HSST Irradiation Series[a]

Material	$T_{T,U}$ (°C)	$T_{T,I}$ (°C)	ΔT_T (°C)	$K_{I,US}$ (MPa·$\sqrt{m}$)
Plate 02	-10	80	90	171
Weld 68W	-75	NA	NA	205
Weld 69W	10	50	40	166
Weld 70W	-45	NA	NA	155
Weld 71W	-15	10	25	140

[a]where

$T_{T,U}$ = estimated unirradiated 125 MPa·$\sqrt{m}$ transition temperature

$T_{T,I}$ = estimated irradiated 125 MPa·$\sqrt{m}$ transition temperature

ΔT_T = estimated transition temperature shift, $T_{T,I} - T_{T,U}$

$K_{I,US}$ = estimated average upper-shelf toughness from 121 to 288°C

NA = not available

6.3 Irradiation-Induced K_{Ic} Curve Shift

R. G. Berggren K. R. Thoms
R. K. Nanstad F. B. Kam

This study (Fifth HSST Irradiation Series) has been described in previous reports.[9,10] Eight of the twelve required 1.22-m-long (4-ft) weldments of the lower copper (Cu) composition (HSST 72W; 0.25% Cu) and four of the twelve required 1.22-m-long weldments of the higher copper composition (HSST 73W; 0.35% Cu) have been received from Combustion Engineering,

Inc. (CE, Inc.), Chattanooga, Tennessee. Fabrication of the remaining weldments is in progress.

The base plate for these weldments is a 220-mm-thick plate of SA533 grade B class 2 steel. The welding wires are from two special heats of AWS A5.23, type EF-2, with copper added to the melts to achieve two levels of copper content. One lot of Linde 124 flux is used for all the welds. The submerged-arc welding is done with a tandem-arc, alternating current procedure using a 0° bevel (constant-width) weld groove. The width of the completed welds ranges from 28 to 32 mm. Postweld heat treatment is performed at 607°C for 40 h. A cross section of one of these welds is shown in Fig. 6.11.

Chemical compositions are being determined for each drum of welding wire, weld test coupons, weld runouts from each weldment, and cross sections from the weldments. Table 6.19 lists chemical analysis results for the plate materials, weld wires, weld test coupons, and weld metal from the runout tabs for the weldments received to date. All values are averages of a number of determinations. Compositions for the sections taken from the main weldments are not yet available. The compositional variations in this table are those usually found as a result of segregation in the ingot and dilution in the weld nugget. The two weldments are of nearly the same composition with the exception of the desired difference of copper content. The copper contents, 0.23% for HSST 72W and 0.32% for HSST 73W, are close to our desired 0.10% Cu difference.

Mechanical properties tests were conducted by CE, Inc., and results from the weld test coupons are presented in Table 6.20. Both welds meet our specifications. We have also conducted CVN impact tests on specimens from a 1.22-m weldment of HSST 73W, and our results agree with the CE, Inc. results.

Fabrication of specimens from the weldments now on hand is in progress. Specimens for the first two irradiation capsules are being assembled in the capsules. These first two capsules will each contain 2 4TCS specimens and 12 CVN specimens of the higher copper composition (HSST 73W). Design of the capsules for 4TCS specimens was completed; capsule designs for 1TCS and 2TCS specimens are nearing completion.

6.4 Irradiated Crack-Arrest Studies

W. R. Corwin R. K. Nanstad

Weldment materials for this future irradiation study (Sixth HSST Irradiation Series) will be from the same weldments being fabricated for the Fifth HSST Irradiation Series. The irradiations are tentatively scheduled to begin near the beginning of FY 1986.

Preparations for this study involve participation in the ASTM Crack-Arrest Round Robin and continuing involvement in the development of an optimum crack-arrest-toughness specimen and test procedures.

M&C PHOTO Y-195691

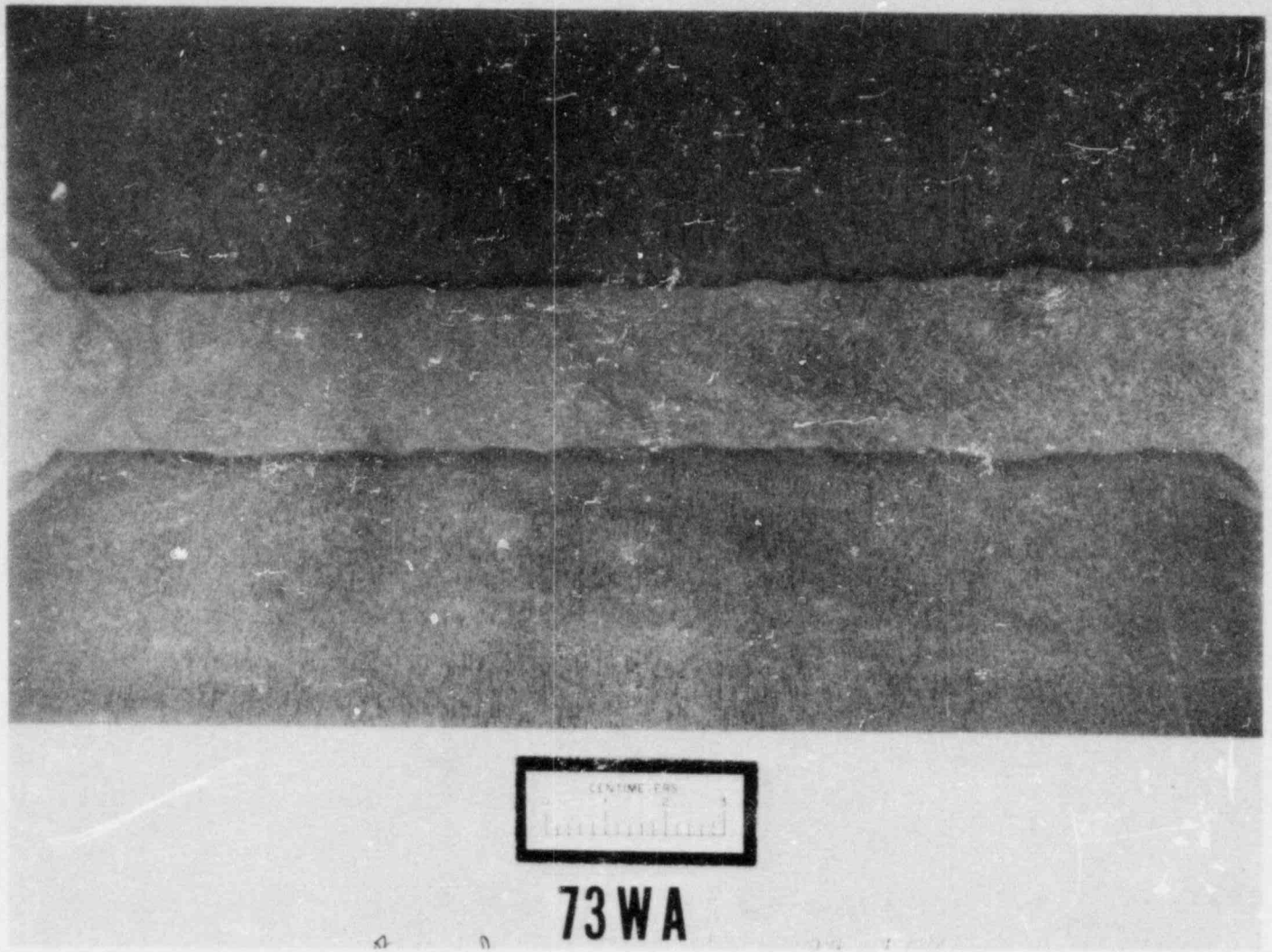

Fig. 6.11. Macroetched cross section of weldment HSST-73W.

Table 6.19. Average chemical compositions of materials for the Fifth HSST Irradiation Series

	Composition[a] (wt %)													
	C	Mn	P	S	Si	Ni	Cr	Mo	V	Co	Cu	Al	As	Sn
Base metal for test welds and runout tabs														
	0.21	1.41	0.007	0.004	0.21	0.62	0.04	0.50	0.002	0.014	0.04	0.020	0.016	0.003
Base plate for main welds (midthickness)														
Ingot top end	0.19	1.22	0.008	0.004	0.23	0.65	0.12	0.53	0.003	0.015	0.11	0.042	0.007	0.008
Ingot bottom end	0.24	1.26	0.008	0.003	0.23	0.68	0.12	0.56	0.003	0.015	0.12	0.038	0.007	0.009
HSST-72W (low copper)														
Weld wire	0.11	2.15	0.004	0.002	0.06	0.64	0.31	0.57	0.003	0.032	0.25	0.002	0.002	0.003
Test weld coupon	0.083	1.52	0.006	0.006	0.48	0.62	0.28	0.58	0.004	0.032	0.24	0.006	0.002	0.003
Runout tabs (weld metal)	0.085	1.53	0.006	0.005	0.45	0.60	0.26	0.56	0.003	0.030	0.23	0.006	0.002	0.003
HSST-73W (high copper)														
Weld wire	0.12	2.03	0.004	0.002	0.07	0.62	0.28	0.56	0.003	0.032	0.35	0.005	0.004	0.002
Test weld coupon	0.097	1.46	0.006	0.005	0.38	0.61	0.23	0.55	0.003	0.030	0.30	0.006	0.004	0.002
Runout tabs (weld metal)	0.089	1.50	0.006	0.005	0.43	0.61	0.25	0.56	0.003	0.030	0.32	0.006	0.002	0.003

[a]For all materials, the following additional elements were determined: Cb/Ta < 0.01, Ti < 0.01, B < 0.001, W < 0.01, and Zr < 0.001.

Table 6.20. Mechanical properties of HSST welds 72W and 73W

(Weld test coupons)

	72W	73W
Yield strength (MPa)	517	500
Tensile strength (MPa)	624	607
Elongation in 50 mm (%)	24.5	26.0
Reduction of area (%)	65.4	65.8
Drop-weight NDT (°C)	−50	−50
Charpy-V transition temperature (41 J), (°C)	−30	−45
Charpy-V upper-shelf energy (J)	133	142

6.5 Irradiated Stainless Steel Cladding

W. R. Corwin R. G. Berggren
R. K. Nanstad

6.5.1 Introduction

It has been proposed that the existence of a tough surface layer of weld-deposited stainless steel cladding has potential to keep a short surface flaw from becoming long either by impeding the initiation of extension of a static flaw and/or by arresting a running flaw. To obtain preliminary material properties typical of those needed to make such an evaluation, a program has been established to obtain data on the degradation (or lack thereof) on the fracture properties of stainless steel weld overlay cladding. A recent review of the literature[11] has indicated the possibility for significant degradation of fracture properties of stainless steel weld metal under irradiation conditions relevant to light-water reactors (LWRs). To evaluate this potential degradation, tensile, CVN, and precracked Charpy specimens of stainless steel weld overlay cladding were irradiated to ~2 × 10^{23} neutrons/m^2 (E > 1 MeV) at 288°C. The results of the tensile and CVN tests will be reported here and compared with data from unirradiated specimens. Previous quarterly reports[12-14] provide additional details in this area.

6.5.2 Materials

The specimens were all taken from a single laboratory weldment[15] fabricated using the single-wire oscillating submerged-arc procedure for a companion program investigating structural effects of stainless steel cladding on composite specimens. The weldment consisted of a lower layer of type 309 stainless steel deposited on A533 grade B class 1 plate, followed by two upper layers of type 308 stainless steel cladding. This was done to provide adequate cladding thickness to obtain specimens. Subsequent metallographic examination[16] showed that the upper two layers appeared typical of LWR stainless steel clad overlay, whereas the lower layer had incurred excessive dilution of base metal during welding. Two sets of specimens were carefully fabricated to be contained as fully as possible within either the upper two layers (nominally type 308 specimens) or the lower layer (nominally type 309 specimens). The specimens from the lower layer with excess base metal dilution are more typical of examples of cladding that have been shown to exist in LWRs,[17,18] where off-normal welding conditions occurred.

All specimens were fabricated such that the specimen axis was parallel to the welding direction. The notch of the Charpy specimens was parallel to the plate surface in all cases.

6.5.3 Irradiation history

The specimens were irradiated by MEA in the core of the 2-MW pool reactor (UBR) at the Nuclear Science and Technology Facility, Buffalo, New York. Two separate capsules were used, one each for the types 308 and 309 specimens, respectively. The capsules were instrumented with thermocouples and dosimeters and were rotated 180° once during the irradiation for fluence balancing. Capsule UBR 51-A, containing the type 308 specimens, reached a fluence of 2.09×10^{23} neutrons/m^2 ($E > 1$ MeV) ±10% during 679 h of irradiation. Capsule UBR 51-B, containing the type 309 specimens, reached a fluence of 2.02×10^{23} neutrons/m^2 ($E > 1$ MeV) ±5% in 508 h. Temperatures were maintained at 288 ± 14°C except for the initial week of irradiation. During that time, temperatures as low as 263°C were recorded for the type 308 specimens.

6.5.4 Results and discussion

Tensile testing was conducted at room temperature, 149, and 288°C. Irradiation increased the yield strength of the type 309 specimens by 30% to 40%, whereas the increase of the type 308 specimens was only 5% to 25%. Surprisingly, the total elongation and reduction of areas of both materials tended to increase following irradiation (see Table 6.21).

While transition type behavior was observed in the Charpy impact properties of both materials, the effect of irradiation on the type 308 weld metal microstructurally typical of good practice weld overlay cladding was minimal (Fig. 6.12). Only a very slight shift in transition temperature and drop in upper shelf were observed. Fracture surfaces of selected specimens were examined in the lower-transition and upper-shelf regions. Macrographs of the irradiated type 308 specimens tested

Table 6.21. Tensile properties of stainless steel cladding before and after irradiation

Specimen No.	Material type[a]	Fluence, E > 1 MeV (neutrons/m^2 × 10^{23})	Temperature (°C)		Strength (MPa)		Total elongation[c] (%)	Reduction of area (%)
			Irradiation[b]	Test	Yield	Ultimate		
CPL-80	309	0		27	299	593	28.4	30.6
CPL-83	309	0		27	273	586	49.5	55.5
CPC-72	308	0		27	268	589	40.0	55.0
CPC-73	308	0		27	276	568	42.4	58.0
CPL-81	309	2.0	288	29	388	606	39.4	48.0
CPL-85	309	2.0	288	29	364	624	45.4	58.0
CPC-70	308	2.1	288	29	289	605	51.5	62.3
CPC-75	308	2.1	288	29	300	589	60.1	67.1
CPL-86	309	0		149	213	448	31.9	55.5
CPL-89	309	0		149	236	450	30.4	63.4
CPC-77	308	0		149	221	445	31.3	44.0
CPC-78	308	0		149	213	444	32.4	52.0
CPL-82	309	2.0	288	149	297	508	57.2	57.9
CPL-87	309	2.0	288	149	345	526	48.6	60.4
CPC-71	308	2.1	288	149	290	501	56.3	59.3
CPC-76	308	2.1	288	149	262	485	53.8	58.1
CPL-90	309	0		288	195	429	31.7	51.5
CPL-91	309	0		288	207	423	32.4	52.2
CPC-79	308	0		288	205	393	28.5	51.4
CPC-80	308	0		288	205	402	27.6	53.3
CPL-84	309	2.0	288	288	277	475	52.9	56.6
CPL-88	309	2.0	288	288	290	501	56.3	59.3
CPC-74	308	2.1	288	288	198	422	51.9	55.0
CPC-81	308	2.1	288	288	232	427	49.5	59.8

[a]Type 309 consists primarily of the first metal pass, type 308 primarily the third (last pass).

[b]±14°C.

[c]Gage length/diameter = 7.

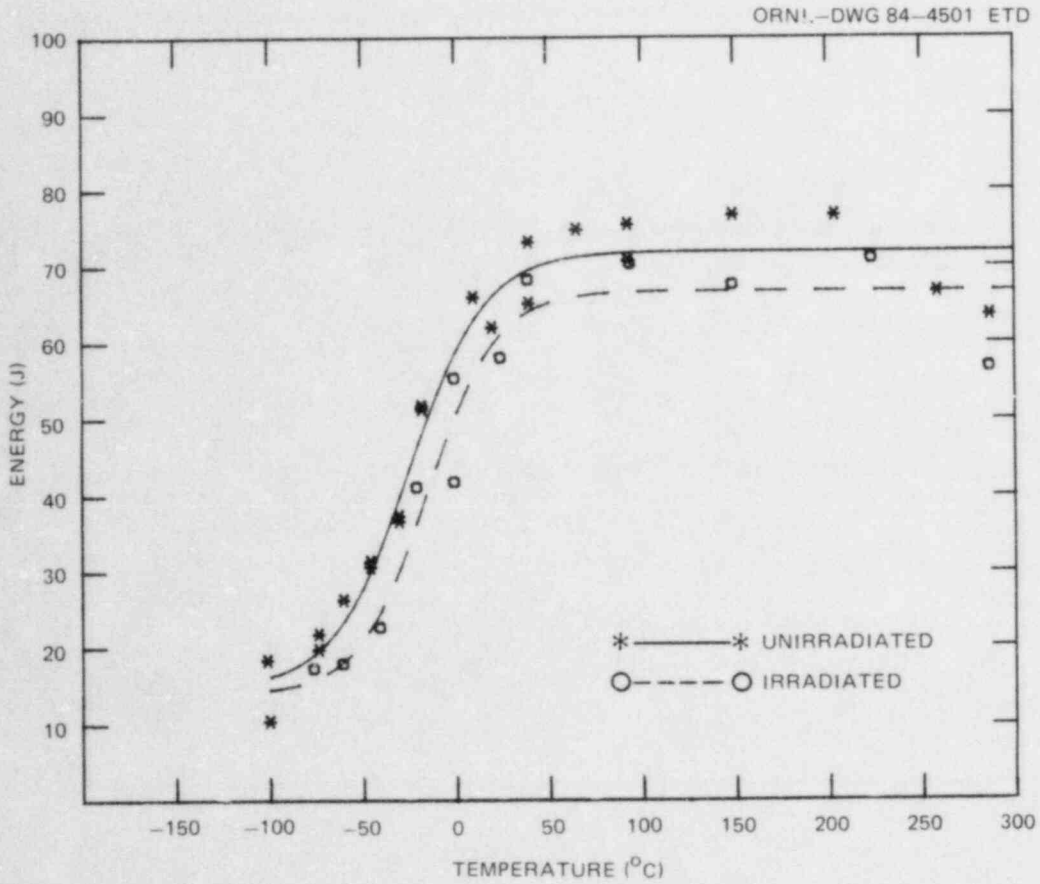

Fig. 6.12. Effect of irradiation on Charpy impact energy of type 308 stainless steel cladding.

at temperatures low in the transition show flat fracture with clear definition of some of the large grains produced during welding (Fig. 6.13). By comparison, specimens at upper-shelf temperatures produced fracture surfaces more typical of wrought stainless with deep shear lips and a dull appearance. Scanning electron microscopy (SEM) of unirradiated specimens tested in the lower-transition and upper-shelf regions clearly show the transition from a cleavage to a fibrous-fracture mode (Fig. 6.14).

By comparison, the interpretation of the type 309 specimens is more complicated. Since the type 309 weld pass was not thick enough to obtain specimens composed entirely of type 309 weld metal, a portion of all the specimens nominally called type 309 is indeed type 308. Macrographs of the irradiated specimen fracture surfaces show that over the range of the full Charpy curve, the portion made up of type 309 weld metal remains bright and faceted (Fig. 6.15). The remainder of the fracture surface, composed of upper cladding layers of type 308 weld metal, exhibits the same behavior seen in the fully type 308 specimens.

Examining a lower-transition range unirradiated specimen in the SEM (Fig. 6.16) illustrates the very different fracture morphology of the type

ORNL–PHOTO 2206–84

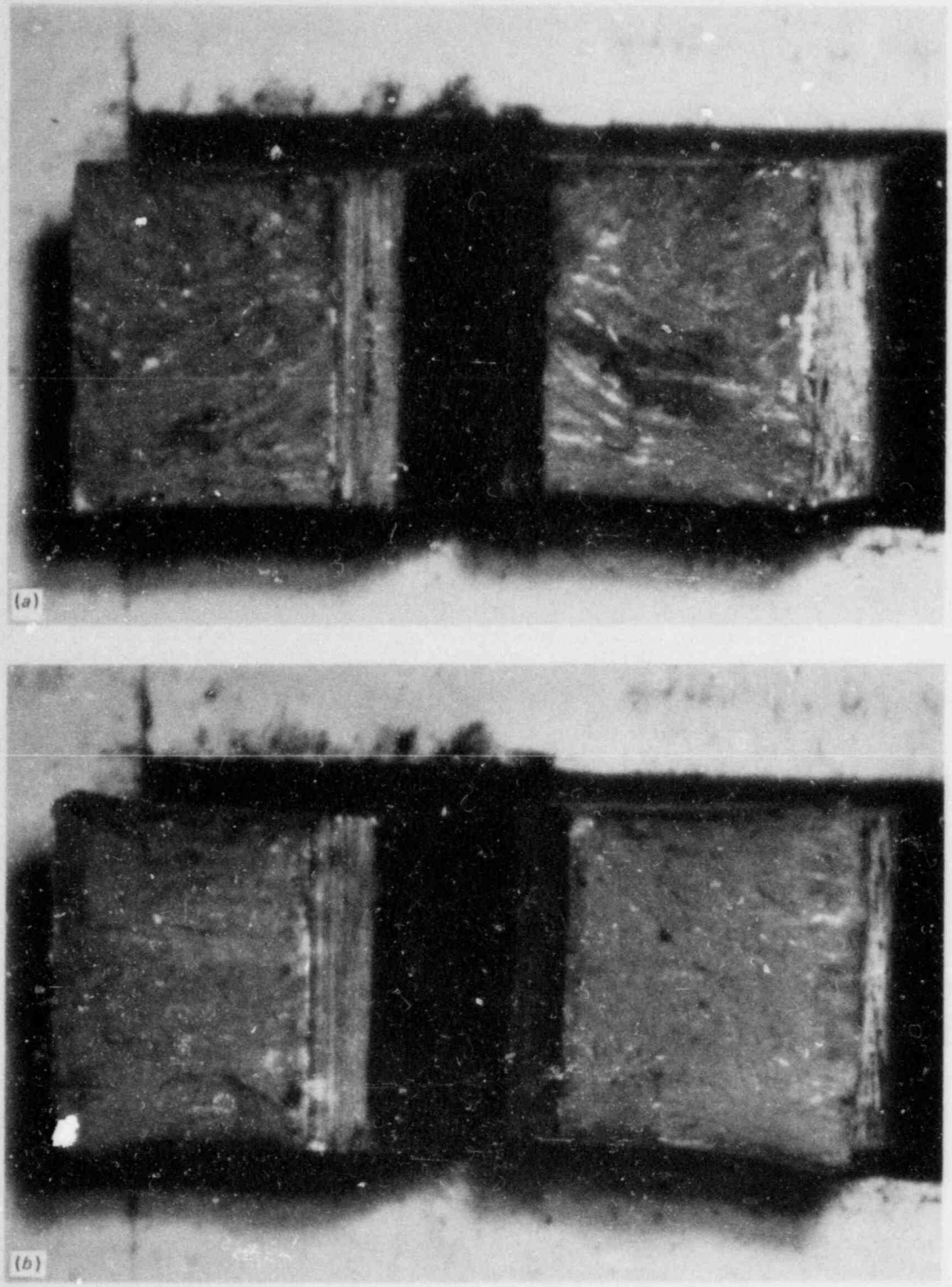

Fig. 6.13. Fracture surfaces of irradiated type 308 stainless steel cladding Charpy impact specimens. (*a*) Specimen CPC-304 tested at –60°C in very low-transition range and (*b*) specimen CPC-290 tested at 150°C on upper shelf.

ORNL–PHOTO 2207–84

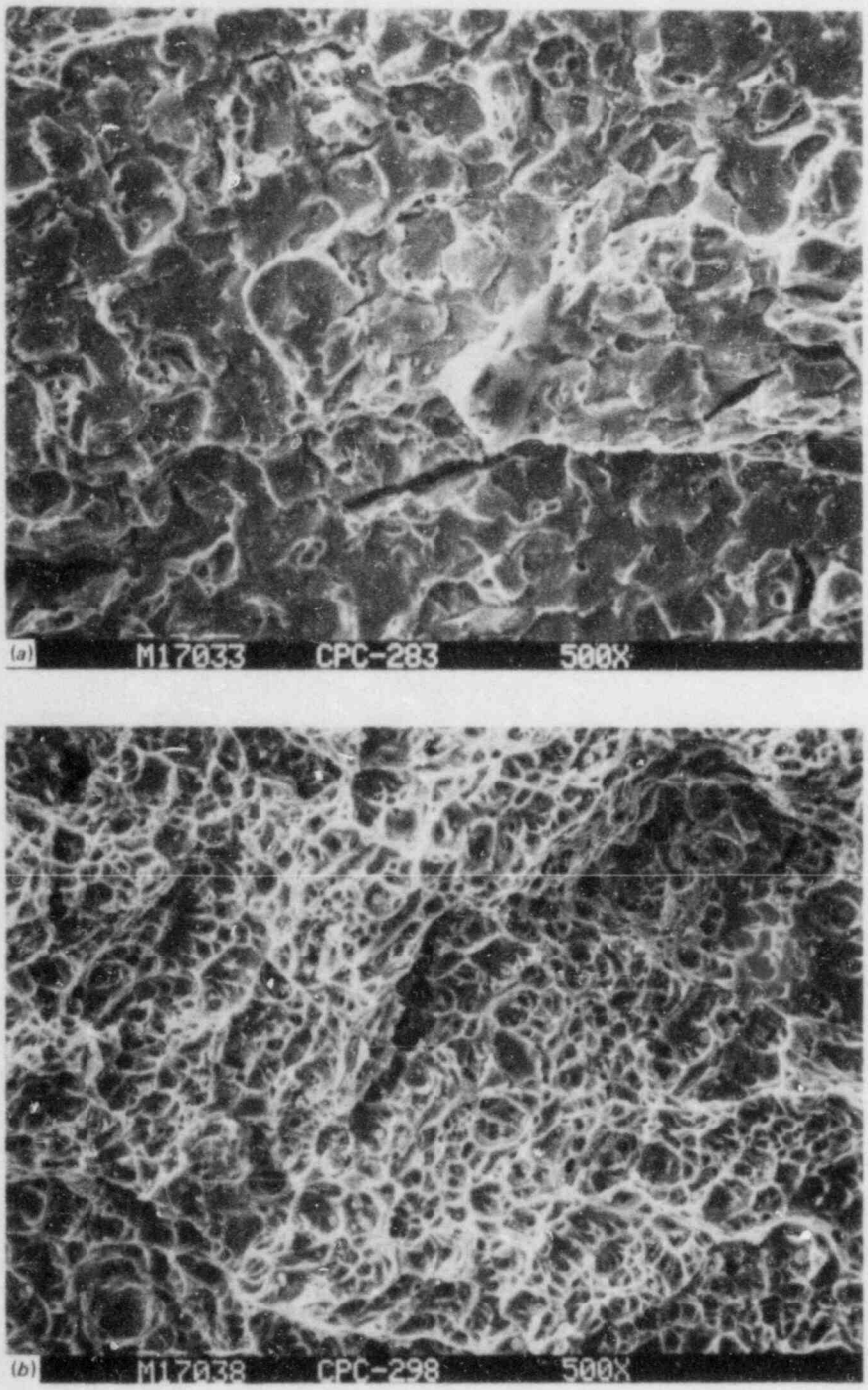

Fig. 6.14. SEMs of fracture surfaces of nonirradiated type 308 stainless steel cladding Charpy impact specimens. (*a*) Specimen CPC-283 tested at −100°C on lower shelf showing brittle fracture (500×) and (*b*) specimen CPC-298 tested at 150°C on upper shelf showing fibrous fracture (500×).

ORNL–PHOTO 2208–84

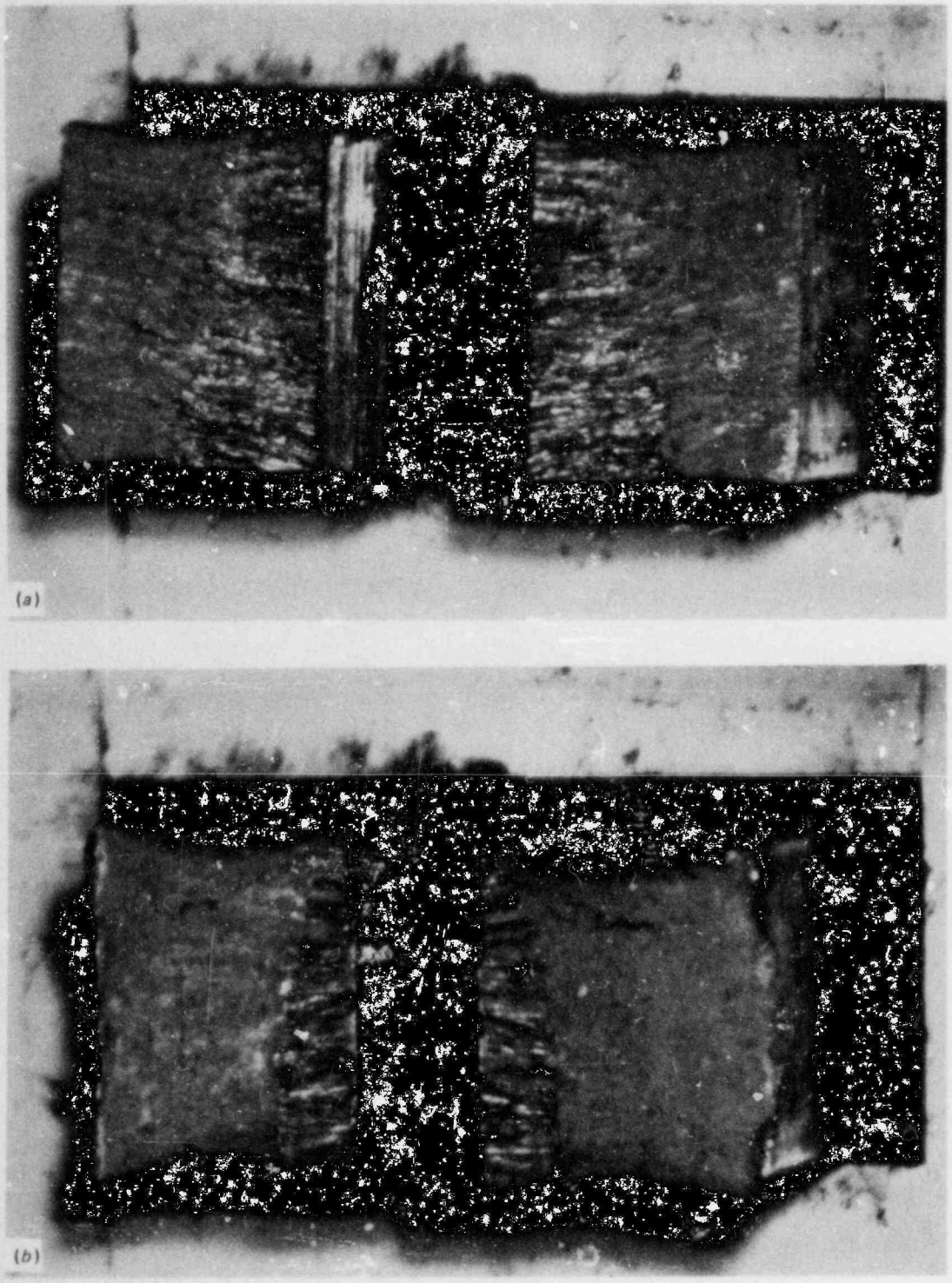

Fig. 6.15. Fracture surfaces of irradiated stainless steel cladding Charpy impact specimens (nominally type 309) clearly showing bright, faceted type 309 weld metal pass directly below notch and duller type 308 weld metal comprising rest of specimen. (*a*) Specimen CPL-515 tested at 0°C in very low-transition region and (*b*) specimen CPL-518 tested at 250°C on upper shelf.

ORNL–PHOTO 2209–84

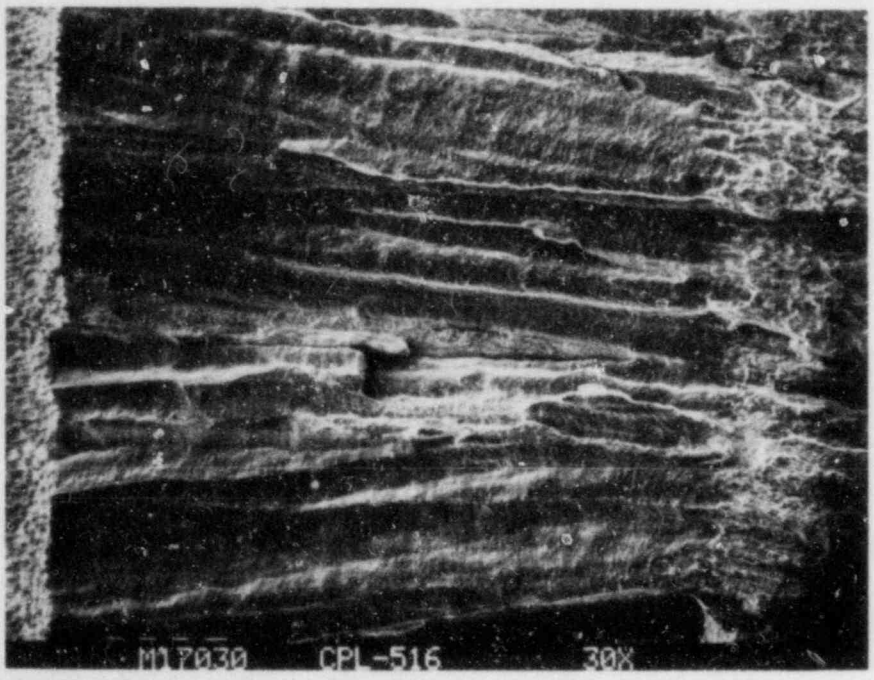

Fig. 6.16. SEM of fracture face of unirradiated Charpy specimen CPL-516 (nominally type 309) tested at −32°C in transition region. Dimpled area at left is specimen notch, central flat portion is type 309 weld metal, and rough portion at right is first type 308 weld pass (30×).

309 weld metal just below the notch and rest of the fracture surface composed of type 308 weld metal. The type 309 is very flat and formed predominately by cleavage (Fig. 6.17) at a temperature (−32°C) at which the type 308 weld metal is still mixed mode (Fig. 6.18). Although the type 309 and 308 weld metals can still be distinguished in the SEM at upper-shelf temperatures, both fail in a fibrous manner (Fig. 6.19).

In the nominally type 309 specimens, interpreting the Charpy impact curves demands that the dual fracture properties of the type 308 and 309 portions of the material be taken into consideration. Examining the impact data reveals a bimodal population depending on the amount of the tougher type 308 weld metal present in the sample. The compilation of the unirradiated and irradiated impact data in Tables 6.22 and 6.23, respectively, includes the percentage of type 308 weld metal measured visually on each fracture surface. Using this percentage as a yardstick, the impact data were divided into low- and high-energy populations. The most appropriate criterion for separating the low-energy populations appeared to be less than 70% and 80% type 308 weld metal for the unirradiated and irradiated data sets, respectively (Figs. 6.20 and 6.21).

Once these populations were established, the effect of irradiation was seen to be quite appreciable (Fig. 6.22), with both populations experiencing large drops in upper-shelf energy and shifts in transition temperature.

ORNL PHOTO 2210–84

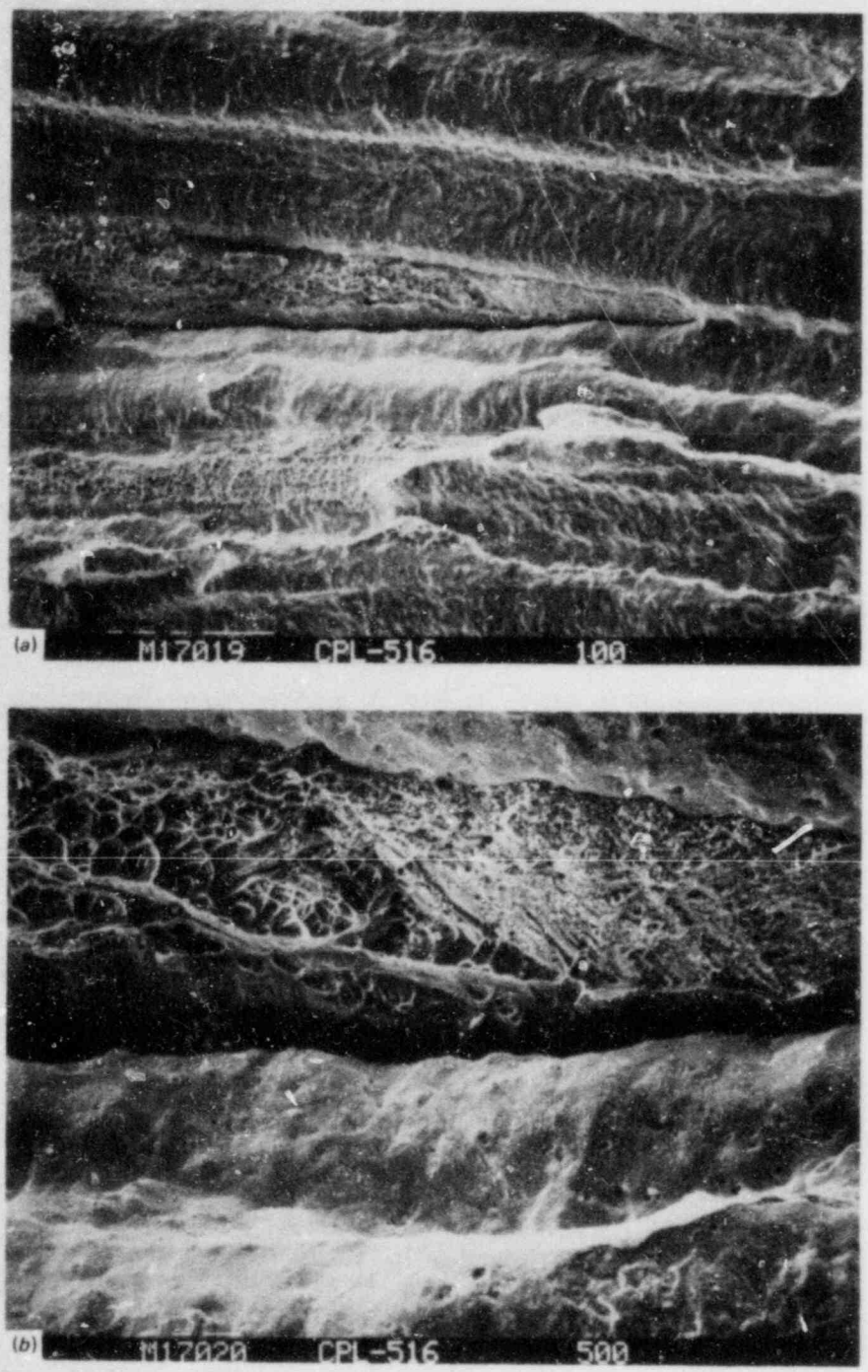

Fig. 6.17. Detailed views of type 309 weld metal fracture surface of specimen CPL-516 showing predominantly flat fracture with islands of fibrous tearing. (*a*) 100× and (*b*) 500×.

ORNL PHOTO 2211–84

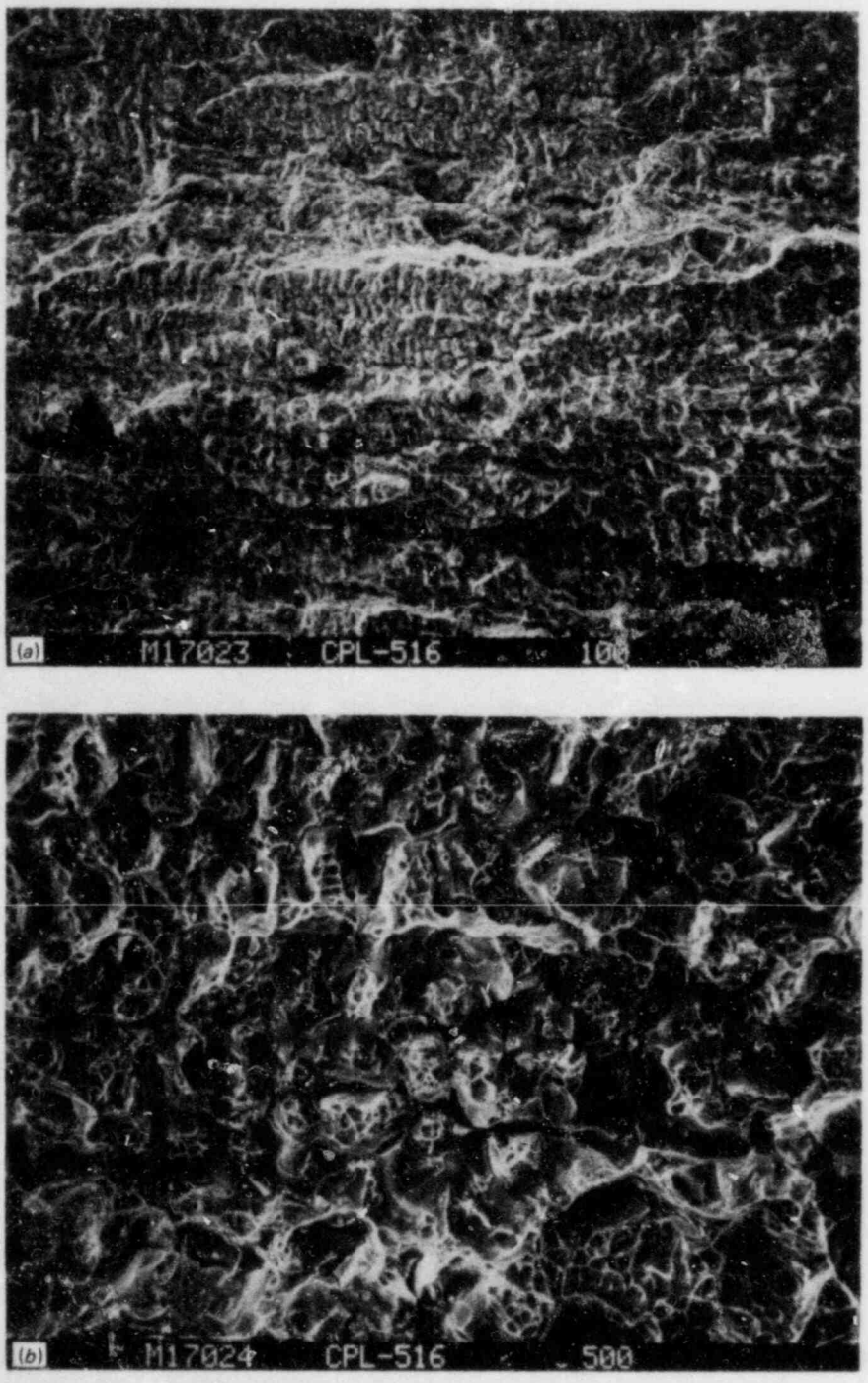

Fig. 6.18. Detailed views of type 308 weld metal fracture surface of specimen CPL-516 showing mixed mode fracture. (*a*) 100× and (*b*) 500×.

ORNL PHOTO 2212-84

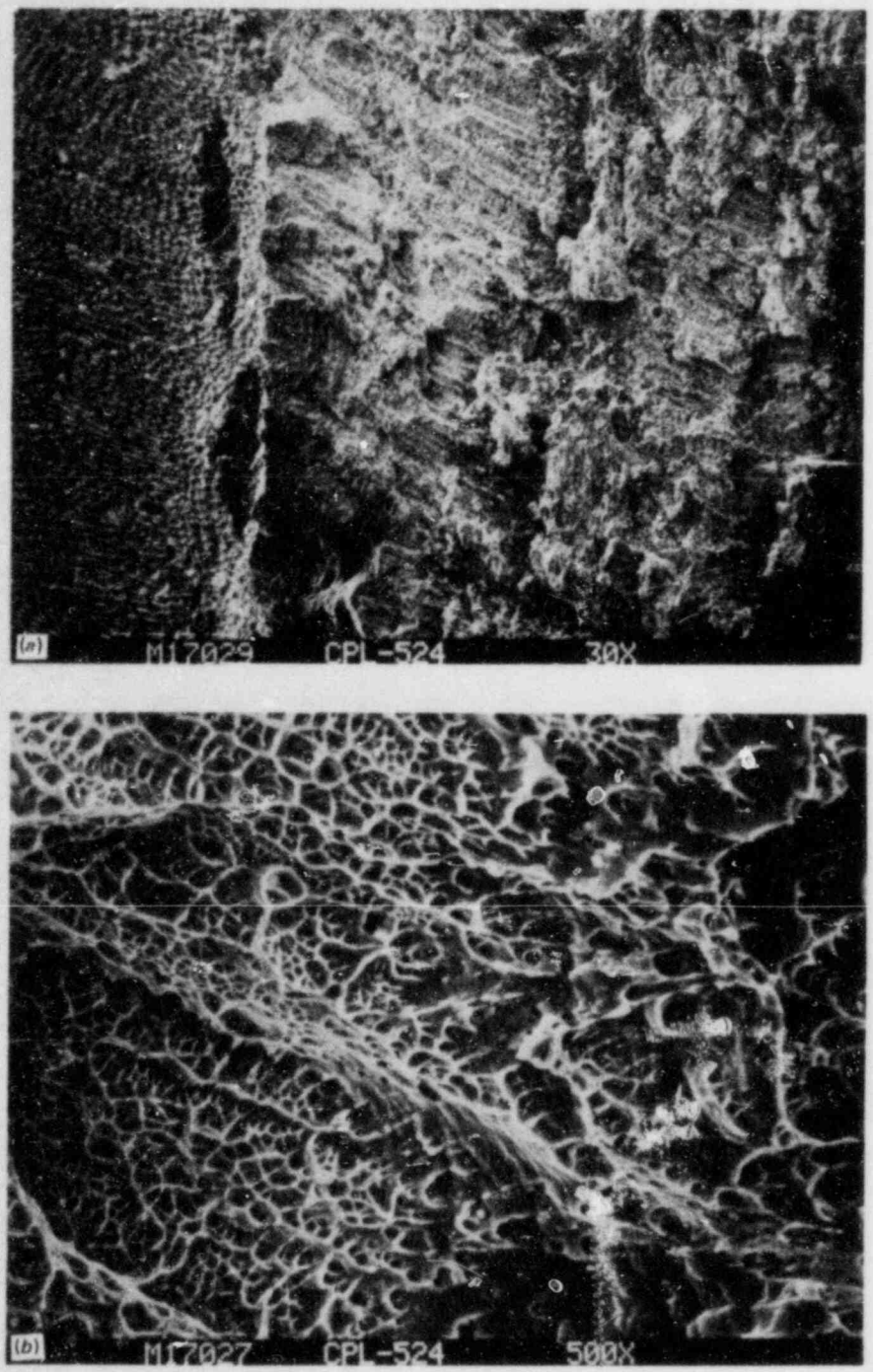

Fig. 6.19. SEM of fracture surface of unirradiated nominally type 309 Charpy specimen CPL-524 tested at 177°C on upper shelf. (*a*) Low-magnification view of notch, type 309 weld layer, and type 308 weld layer each comprising roughly one-third of micrograph from left to right, respectively (30×); and (*b*) detail of type 309 weld layer showing fibrous fracture.

Table 6.22. Charpy impact energy of unirradiated nominally type 309 stainless steel cladding

Specimen No.	Test temperature (°C)	Impact energy (J)	Amount of type 308 weld metal[a] (%)
Low-energy population[b]			
CPL-516	−32	9.5	65
CPL-530	−30	12.7	65
CPL-534	10	33.4	60
CPL-514	20	28.5	65
CPL-545	50	36.2	60
CPL-542	66	34.6	55
CPL-517	93	67.1	60
CPL-524	177	80.3	60
CPL-522	260	72.3	40
High-energy population[c]			
CPL-519	−100	5.4	85
CPL-539	−73	6.9	75
CPL-520	−40	12.9	75
CPL-540	−30	11.5	75
CPL-529	−4	44.7	95
CPL-532	−4	54.2	95
CPL-547	−4	30.5	70
CPL-544	10	65.1	100
CPL-527	20	63.0	80
CPL-535	50	83.9	80
CPL-525	66	69.2	80
CPL-537	150	93.3	70
CPL-549	150	94.9	70

[a]As measured on the fracture surface.

[b]Less than 70% type 308 weld metal.

[c]Greater than or equal to 70% type 308 weld metal.

Table 6.23. Charpy impact energy of nominally type 309 stainless steel cladding irradiated to 2×10^{23} neutrons/m^2 (E > 1 MeV) at 288°C

Specimen No.	Test temperature (°C)	Impact energy (J)	Amount of type 308 weld metal[a] (%)
Low-energy population[b]			
CPL-515	0	10.8	60
CPL-543	40	17.0	75
CPL-541	65	25.1	65
CPL-548	85	15.6	40
CPL-521	100	25.1	60
CPL-523	150	40.7	65
CPL-518	250	42.7	70
CPL-528	288	36.6	75
High-energy population[c]			
CPL-533	–20	12.0	80
CPL-538	0	21.7	90
CPL-526	28	40.7	100
CPL-531	80	54.2	95
CPL-546	120	51.5	80
CPL-536	130	56.9	85

[a]As measured on the fracture surface.

[b]Less than 80% type 308 weld metal.

[c]Greater than or equal to 80% type 308 weld metal.

The extensive degradation seen in the type 309 material as compared with very little degradation in the type 308 is probably a result of the higher fraction of ferritic phases in the type 309 resulting from the excessive base metal dilution.[16]

6.5.5 Conclusions and recommendations for future work

On the basis of irradiation of one weldment of stainless steel overlay under conditions similar to those at end-of-life for an LWR, it seems that very little degradation of good quality cladding would occur. It must be stressed, however, that this is only a single case and that no

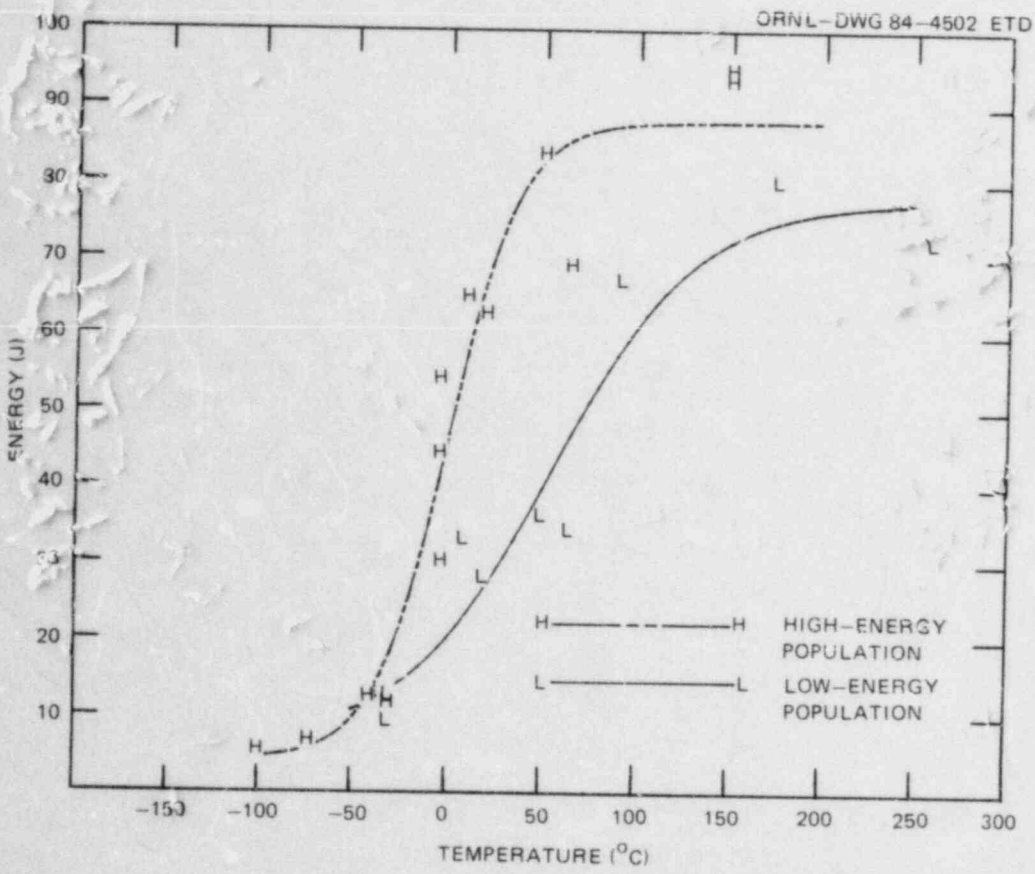

Fig. 6.20. Charpy impact energy of unirradiated nominally type 309 cladding divided into low- and high-energy populations based on fraction of type 308 weld metal composing specimen ligament.

conclusions, positive or negative, can be drawn regarding welding procedures or material chemistries producing material appreciably different than that studied here.

It would be very valuable to repeat this type of experiment on clad overlay produced in a manner similar to existing cladding in LWR reactor pressure vessels (e.g., multiple wire or strip cladding).

Results from the highly diluted type 309 weld metal do show appreciable radiation-induced degradation. In the few cases where out-of-specification welding has produced cladding with excessive dilution, this may be cause for concern.

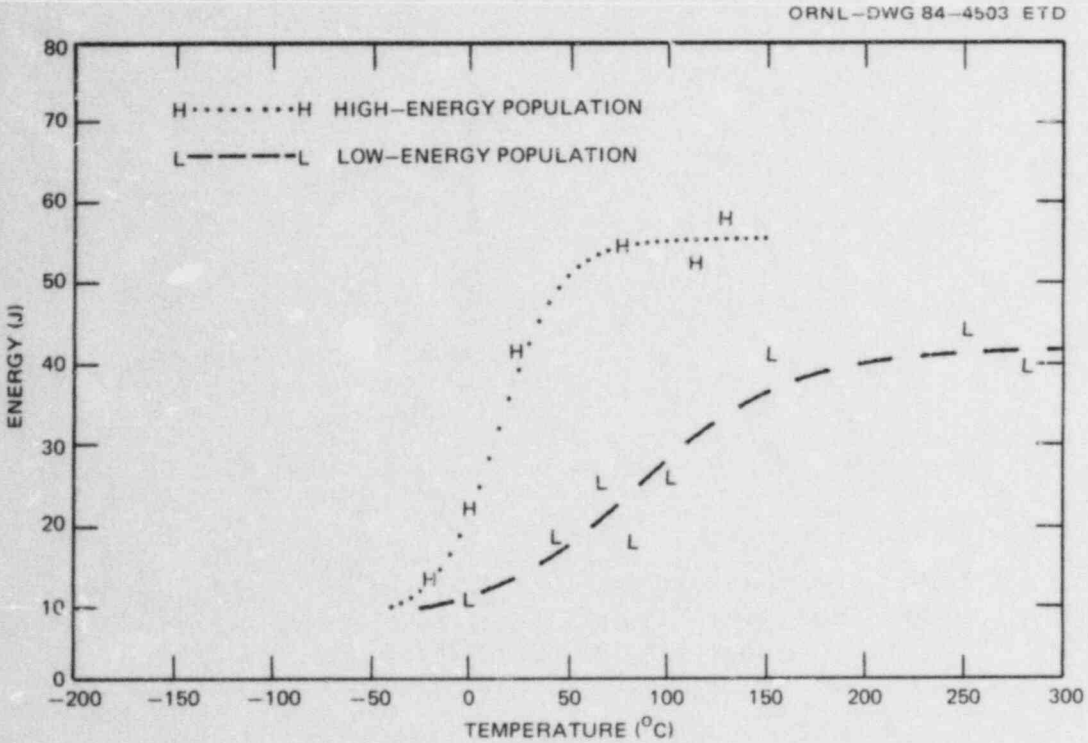

Fig. 6.21. Charpy impact energy of irradiated nominally type 309 cladding divided into low- and high-energy populations based on fraction of type 308 weld metal composing the specimen ligament.

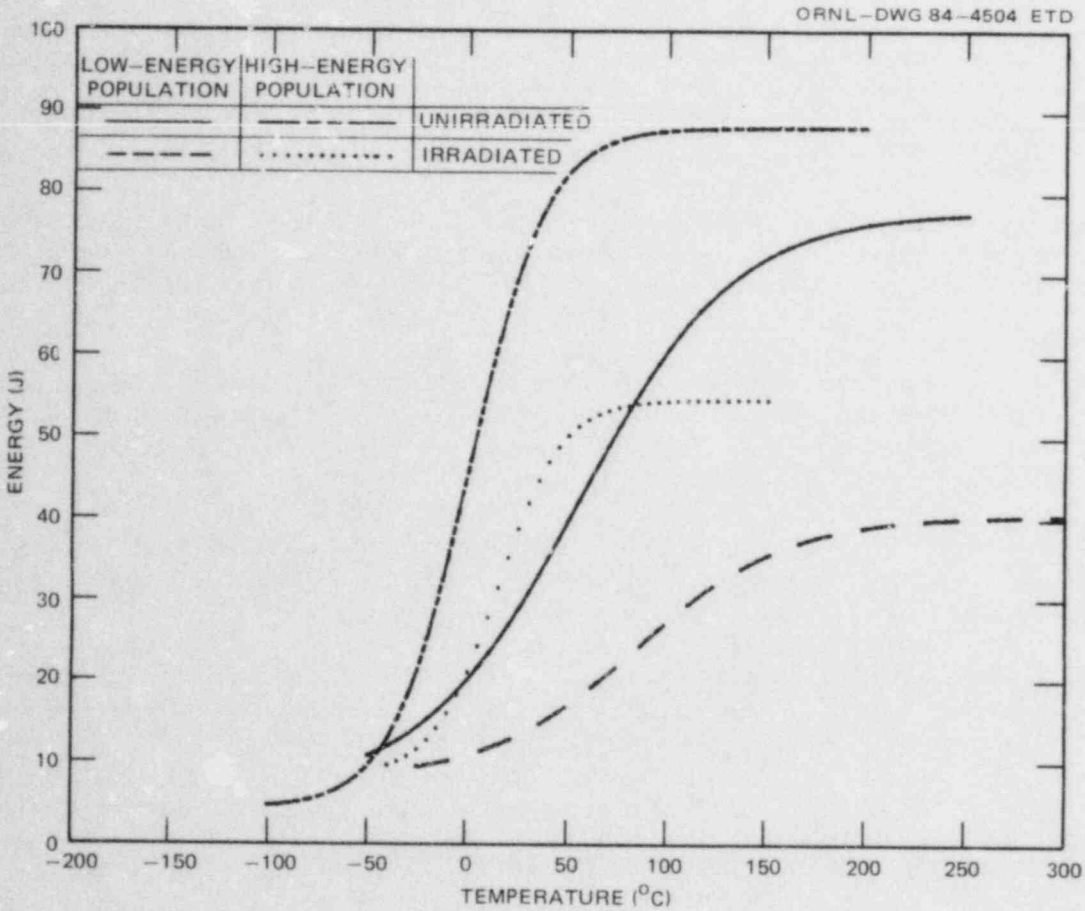

Fig. 6.22. Effect of irradiation on Charpy impact energy of high- and low-energy populations of nominal type 309 cladding specimens.

References

1. R. G. Berggren et al., "Toughness Investigations of Irradiated Materials," in *Heavy-Section Steel Technology Program Quart. Prog. Rep. July–September 1979*, NUREG/CR-1197 (ORNL/NUREG/TM-370), Union Carbide Corp. Nuclear Div., Oak Ridge Natl. Lab.

2. R. G. Berggren, R. K. Nanstad, and F. W. Stallman, "Second and Third 4T-CS Irradiation Study," in *Heavy-Section Steel Technology Program Quart. Prog. Rep. April–June 1982*, NUREG/CR-2751, Vol. 2 (ORNL/TM-8369/V2), Union Carbide Corp. Nuclear Div., Oak Ridge Natl. Lab.

3. R. G. Berggren, T. N. Jones, and R. K. Nanstad, "Fourth HSST Irradiation Studies," in *Heavy-Section Steel Technology Program Quart. Prog. Rep. October–December 1982*, NUREG/CR-2751, Vol. 4 (ORNL/TM-8369/V4), Union Carbide Corp. Nuclear Div., Oak Ridge Natl. Lab.

4. R. G. Berggren, T. N. Jones, and R. K. Nanstad, "Fourth HSST Irradiation Studies," in *Heavy-Section Steel Technology Program Quart. Prog. Rep. April–June 1983*, Vol. 2 (ORNL/TM-8787/V2), Union Carbide Corp. Nuclear Div., Oak Ridge Natl. Lab.

5. American Society for Testing and Materials, *Standard Test Method for Plane-Strain Fracture Toughness of Metallic Materials*, E-399-81, Philadelphia, 1981.

6. H. A. Ernst, *Material Resistance and Instability Beyond J-Controlled Growth*, Research Report 81-1D7-JINTF-P6, Westinghouse Research and Development Center, Pittsburgh, December 3, 1981.

7. American Society for Testing and Materials, "J_{Ic}, A Measure of Fracture Toughness, ASTM Designation: E-813," *1983 Annual Book of ASTM Standards*, Sect. 3, Vol. 03.01.

8. J. G. Merkle, "A New Method for Analysing Small Scale Fracture Specimen Data in the Transition Zone," pp. 307–15 in *Proc. U.S. Nuclear Regulatory Commission 10th Water Reactor Safety Research Information Meeting*, NUREG/CP-0041, Vol. 4, 1982.

9. R. G. Berggren and R. K. Nanstad, "Irradiation-Induced K_{Ic} Curve Shift," in *Heavy-Section Steel Technology Program Quart. Prog. Rep. April–June 1982*, NUREG/CR-2751, Vol. 2 (ORNL/TM-8369/V2), Union Carbide Corp. Nuclear Div., Oak Ridge Natl. Lab.

10. R. G. Berggren and R. K. Nanstad, "Irradiation-Induced K_{Ic} Curve Shift," in *Heavy-Section Steel Technology Program Quart. Prog. Rep. October–December 1982*, NUREG/CR-2751, Vol. 4 (ORNL/TM-8369/V4), Union Carbide Corp. Nuclear Div., Oak Ridge Natl. Lab.

11. W. R. Corwin, *Assessment of Radiation Effects Relating to Reactor Pressure Vessel Cladding*, NUREG/CR-3671 (ORNL-6047), to be published at Oak Ridge National Laboratory.

12. R. G. Berggren, R. K. Nanstad, and W. R. Corwin, "Irradiated Stainless Steel Cladding," in *Heavy-Section Steel Technology Program Quart. Prog. Rep. October–December 1982*, NUREG/CR-2751, Vol. 4 (ORNL/TM-8369/V4), Union Carbide Corp. Nuclear Div., Oak Ridge Natl. Lab.

13. R. G. Berggren, R. K. Nanstad, and W. R. Corwin, "Irradiated Stainless Steel Cladding," in *Heavy-Section Steel Technology Program Quart. Prog. Rep. January–March 1983*, NUREG/CR-3334, Vol. 1 (ORNL/TM-8787/V1), Union Carbide Corp. Nuclear Div., Oak Ridge Natl. Lab.

14. R. G. Berggren, R. K. Nanstad, and W. R. Corwin, "Irradiated Stainless Steel Cladding," in *Heavy-Section Steel Technology Program Quart. Prog. Rep. July–September 1983*, NUREG/CR-3334, Vol. 3 (ORNL/TM-8787/V3), Union Carbide Corp. Nuclear Div., Oak Ridge Natl. Lab.

15. R. K. Nanstad et al., "Weld Cladding and Material Characterization," in *Heavy-Section Steel Technology Program Quart. Prog. Rep. January–March 1982*, NUREG/CR-2751, Vol. 1 (ORNL/TM-8369/V1), Union Carbide Corp. Nuclear Div., Oak Ridge Natl. Lab.

16. W. R. Corwin et al., "Stainless Steel Cladding Investigations," in *Heavy-Section Steel Technology Program Quart. Prog. Rep. January–March 1983*, NUREG/CR-3334, Vol. 1 (ORNL/TM-8787/V1), Union Carbide Corp. Nuclear Div., Oak Ridge Natl. lab.

17. E. B. Norris, D. R. Ireland, and C. E. Lautzenheiser, *The Second Inspection of the Elk River Pressure Vessel After Operation*, SWRI 122 8P9-13, Southwest Research Institute, San Antonio, Texas, July 21, 1967.

18. T. Kondo, H. Nakajima, and R. Nagasaki, "Metallographic Investigation of the Cladding Failure in the Pressure Vessel of a BWR," *Nucl. Eng. Design* 16, 205–22 (1971).

7. CLADDING EVALUATIONS

The FY 1984 program plan deferred work in this task until data are available on the effects of irradiation on the fracture properties of stainless steel cladding. However, a subcontract is in place with Combustion Engineering to provide three-wire series-arc clad plates for future studies, and delivery is now expected in the second half of FY 1984.

8. INTERMEDIATE VESSEL TESTS AND ANALYSES

During this reporting period, as had been planned, no significant work was done on this task. In the next reporting period, the posttest evaluation and reporting on V-8A will be performed.

9. THERMAL-SHOCK TECHNOLOGY

R. D. Cheverton

9.1 Summary

Preliminary exploratory fracture-mechanics (FM) calculations were conducted for the proposed thermal-shock experiment TSE-8, an objective of which is to investigate crack behavior in the upper-transition and upper-shelf temperature regimes. It appears that the present liquid-nitrogen test facility and associated experimental technique will not be adequate; however, use of a higher initial temperature (~300°C), a long axial initially blunted flaw, "instantaneous" sharpening of the flaw during the transient, and spray application of liquid nitrogen (LN_2) to induce the thermal shock will result in satisfactory test conditions.

Modifications were made to our deterministic-probabilistic FM computer code, OCA-P,[1] to include crack arrest on the upper shelf, multiple flaw zones, importance sampling, error analysis, and an increase in the number of flaw depths simulated. The latter modification was made after conducting a detailed study to determine the effect of the number and relative values of the flaw depths simulated.

Stress-intensity factor influence coefficients, which had previously been calculated for 6/1 and 1.8-m-long semielliptical inner-surface flaws in the absence of cladding, were calculated for the cladding effect for the same two flaw geometries and were then added to OCA-P and OCA-II.[2]

The probabilistic FM study for the Oconee-I vessel for the Integrated Pressurized-Thermal-Shock (IPTS) program was completed, and a preliminary feasibility study associated with the possibility of conducting thermal-shock experiments with the German HDR facility was begun.

9.2 Thermal-Shock Experiment TSE-8

R. D. Cheverton Keith Reading

The objective of TSE-8, a proposed thermal-shock experiment, is to investigate crack-arrest behavior in a rising K_I field at temperatures corresponding to the upper-transition and upper-shelf portions of the fracture-toughness curve. Temperatures for arrest events in previous thermal-shock experiments have been limited to midtransition; proposed wide-plate tests that have the same objective as TSE-8 may lack adequate crack-tip restraint; and the HSST pressurized-thermal-shock (PTS) experiment, which also has the capability for investigating crack arrest at elevated temperatures, tends to be more expensive and introduces the risk of through-wall cracking.

The present thermal-shock facility, which uses a liquid nitrogen heat sink, a rubber-cement coating on the inner surface of the test cylinder to enhance heat transfer, and a maximum initial test cylinder temperature of ~100°C, does not have the capability of achieving the TSE-8 objective because of the limitation on initial temperature.

The maximum permissible temperature in the present thermal-shock facility is limited by the properties of the rubber-cement coating. It is possible that higher-temperature coatings could be developed. However, an attractive alternative is to spray the liquid nitrogen against the surface, allowing liquid droplets to penetrate the vapor barrier and continuously strike the surface. In principle, this technique will result in an effectively higher heat transfer coefficient and thus a more severe thermal transient than achieved with the surface coating of rubber cement in combination with complete submergence of the test cylinder in LN_2. Development of the spray technique is scheduled for the immediate future.

An exploratory FM analysis for TSE-8 indicates that a combination of frangible crack initiation, long crack jump, and arrest (?) at elevated temperatures can be achieved by using the LN_2 spray technique in combination with an initial temperature of ~300°C and an initially blunted, long, axial flaw to postpone initiation until late in the transient. A parametric study indicates that combinations of temperature, K_I, and the depth at which specific pairs of these values occur can be controlled over a reasonably wide range by proper selection of time of induced-crack initiation, initial temperature, heat transfer coefficient, wall thickness, and RT_{NDT}. A set of critical-crack-depth curves for a typical combination of conditions is illustrated in Fig. 9.1; the corresponding test conditions are given in Table 9.1, and a conceptual schematic of the test

Table 9.1. TSE-8 test conditions corresponding to Fig. 9.1

Test parameter	Specification
Cylinder dimensions, mm	
Outside diameter	991
Wall thickness	152
Material	
Type	A508 Class 2
RT_{NDT}, °C	−18
Flaw	
Type	Long, axial, blunted
Method of generation	Machined
Depth, mm	~8
Thermal shock	
Quench medium	LN_2
Application technique	Spray
Heat-transfer coefficient, $W/m^2 \cdot °C$	5700[a]

[a]Assumed for analysis.

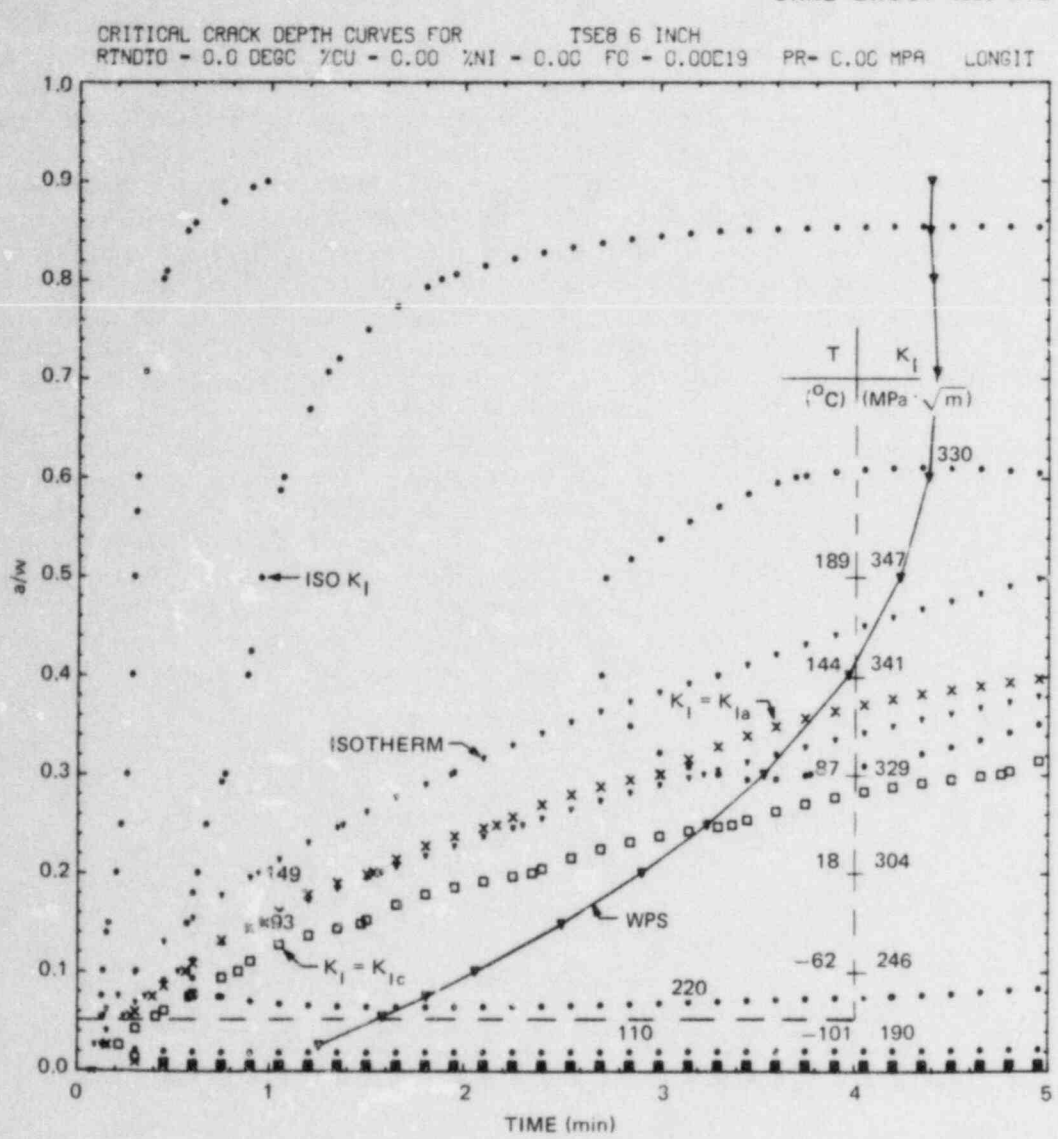

Fig. 9.1. Critical-crack-depth curves for TSE-8 indicating flow path using blunted flaw.

facility is shown in Fig. 9.2. Note that fully tempered material can be used.

As indicated in Fig. 9.1, the specified time for crack initiation and an initial flaw depth of 8 mm results in (1) a very low temperature (−100°C) and a high value of K_I (190 MPa·$\sqrt{m}$) for the crack-initiation event and (2) K_I values up to 350 MPa·$\sqrt{m}$ and temperatures above the onset of upper-shelf temperature for crack arrest.

The specified time for initiating the flaw is well past the time of warm prestressing (WPS). The delay is made possible by using a blunted

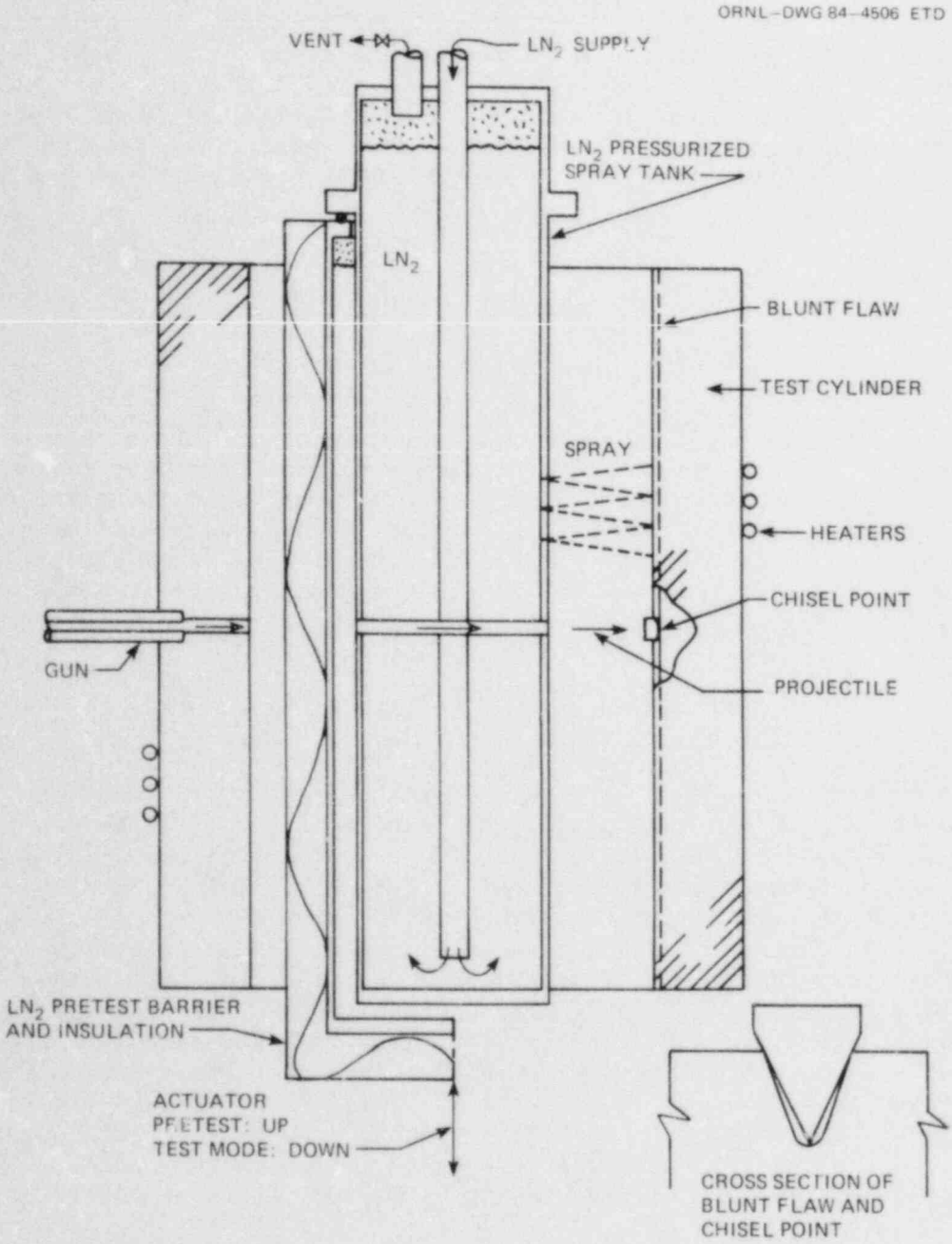

Fig. 9.2. Conceptual schematic of LN_2-spray thermal-shock test facility.

flaw. It is believed that this flaw can be made to propagate at a specified time by suddenly and locally sharpening the tip mechanically, extending the sharpened tip beyond the compressive plastic zone, thus overcoming WPS. This crack sharpening operation would be done near midlength of the flaw and presumably would be accompanied by axial as well as radial extension of the flaw, with axial extension being confined to the path defined by the initial full-length blunted flaw. The mechanical

sharpening of the flaw might be accomplished by firing a projectile at a chisel point located in the crack opening as shown in Fig. 9.2. Also, because at the specified time $K_I/K_{Ic} \gg 1$, the plastic zone size is very small and the temperature is very low at the tip of the flaw, a machining process such as milling or broaching might be used to sharpen the blunted flaw. A development effort will soon be under way to explore these possibilities.

9.3 Modifications to OCA-P

R. D. Cheverton D. G. Ball

OCA-P is a deterministic-probabilistic FM code designed specifically for analysis of PWR reactor pressure vessels under transient thermal and pressure loadings.[1] The code is under development at ORNL under the auspices of the Heavy-Section Steel Technology (HSST) and (IPTS) programs and has been operational since May 1983. Since OCA-P is rather new and complex, it is undergoing almost continuous change. Recent modifications to OCA-P and features that have not been discussed in previous progress reports are discussed in the following paragraphs.

9.3.1 Crack arrest on the upper shelf

A provision is made in OCA-P for limiting K_{Ia} to some maximum value, $(K_{Ia})_{max}$. One way to select a value of $(K_{Ia})_{max}$ is to use a K_J value corresponding to the upper portion of an appropriate J vs Δa curve (J-resistance curve), as illustrated in Fig. 9.3. This figure shows the radial distribution of fracture toughness through the wall of the vessel at some time during a typical postulated overcooling accident (OCA). At temperatures less than T_D, it is assumed that the flaw will behave in a frangible manner, and above T_D only ductile tearing will take place. In accordance with this model, it is not likely that the load line will intersect the steeply rising portion of the J vs Δa curve. Thus, it is sufficient to extend $(K_{Ia})_{max}$ across the T_D line as shown. It is then possible in the analysis for crack arrest to take place on the upper shelf, if the load line rises steeply enough to miss the knee of the K_{Ia} curve and then drops back down again, as it does for some of the postulated OCAs.

A particular J vs Δa curve of interest corresponds to a specific low-upper-shelf weld [referred to as 61W (Ref. 3)], which was irradiated to a fluence of $\sim 1.2 \times 10^{19}$ neutrons/cm^2 at a temperature of ~290°C and was tested at ~200°C. The upper portion of the curve is essentially horizontal and equivalent to a K_J value of ~220 MPa$\cdot\sqrt{m}$. This value has been used for $(K_{Ia})_{max}$ in the OCA studies, but the user may specify a different value.

9.3.2 Consideration of multiple flaw zones

If the results of OCA-P are used in an absolute sense, the flaw density must be estimated. It is also necessary to estimate the fraction of

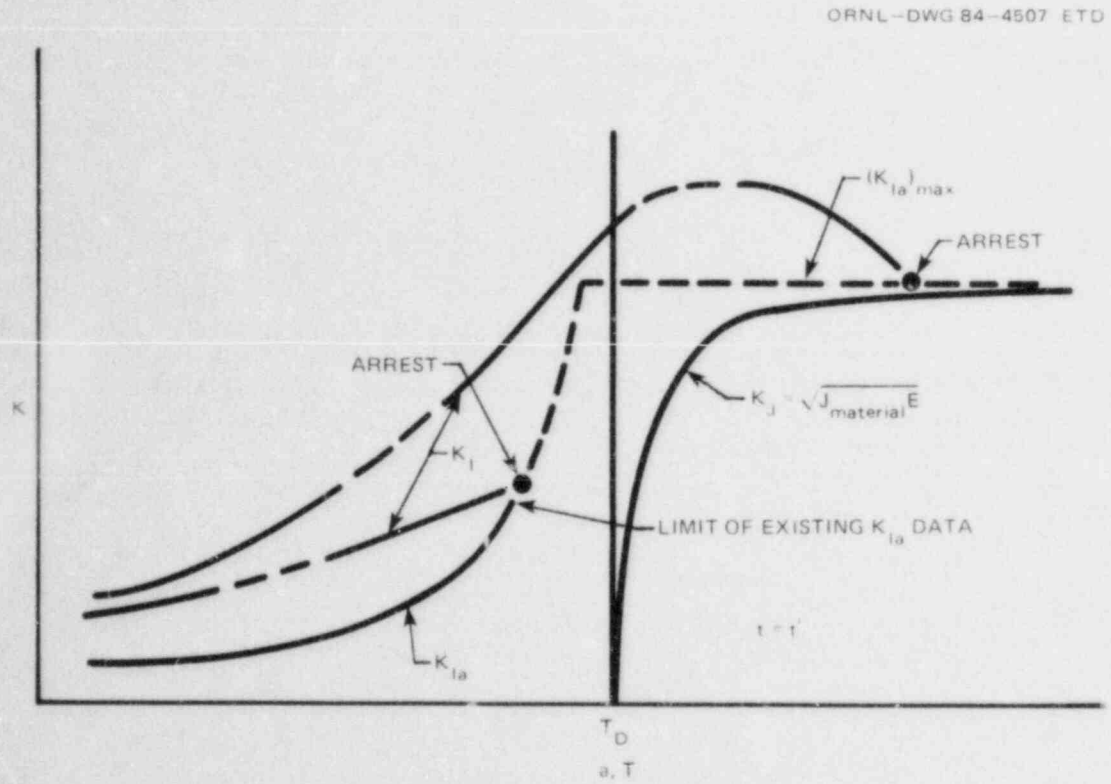

Fig. 9.3. Illustration of method of selecting $(K_{Ia})_{max}$.

vessels that have no flaws whatsoever, since these vessels are not accounted for in the flaw-depth density function. The number of flaws in a vessel at the time the vessel goes into service is

$$NV \int_0^W f(a)B(a)da \ , \tag{9.1}$$

where

a = flaw depth,
N = flaw density,
V = volume of vessel area of concern,
w = wall thickness,
f(a) = flaw-depth density function prior to final preservice inspection and repair,
B(a) = probability of nondetection of flaws during final preservice inspection.

If this number [Eq. (9.1)] is less than unity, more than one vessel must be generated to have a vessel with a flaw; if each vessel that has a flaw has only one flaw, then

$$\frac{\text{number of vessels with flaws}}{\text{total number of vessels}} = NV \int_0^W f(a)B(a)da \ . \tag{9.2}$$

OCA-P calculates (number of failures)/(number of vessels with flaws). Therefore, if the number of flaws per vessel is less than one,

$$P(F|E) = \left(\frac{\text{number of failures}}{\text{number of vessels with flaws}}\right) \times \left(\frac{\text{number of vessels with flaws}}{\text{total number of vessels}}\right) , \quad (9.3)$$

where $P(F|E)$ is the conditional probability of vessel failure.

If there is more than one unique zone* of concern in a vessel and if it is assumed that there is fewer than one flaw per zone, then $P(F|E)$ can be obtained as follows.

Let the flaw density be uniform throughout all areas of concern. Then

$$N_{vj} = \frac{V_j}{\sum_j V_j} \sum_j N_{vj} , \quad (9.4)$$

and

$$P(F|E) = \frac{\sum_j N_{fj}}{\sum_j N_{vj}} N \sum_j V_j \int_0^W f(a)B(a)da , \quad (9.5)$$

where

N_{vj} = number of vessels simulated with a flaw in the jth zone,
V_j = volume of the jth zone,
N_{fj} = number of vessels that fail as the result of a flaw in the jth zone.

The actual values of N_{vj} used in the analysis often do not satisfy Eq. (9.4). However, they can be included in Eq. (9.5) as follows:

$$P(F|E) = \frac{\sum_j C_j N'_{fj}}{\sum_j C_j N'_{vj}} N \sum_j V_j \int_0^W f(a)B(a)da , \quad (9.6)$$

---

*Uniqueness defined in terms of chemistry, initial reference temperature, and fluence.

where

N'_{fj} = actual number of failures calculated for vessels with a flaw in the jth zone,

N'_{vj} = actual number of vessels simulated that contain a flaw in the jth zone.

$$C_j = \frac{V_j}{V_1} \frac{N'_{v1}}{N'_{vj}} . \tag{9.7}$$

Equation (9.7) is obtained from Eq. (9.4) as follows:

$$\frac{N_{v1}}{N_{vj}} = \frac{V_1}{V_j} = \frac{N'_{v1}}{C_j N'_{vj}} . \tag{9.8}$$

Substituting Eq. (9.7) into (9.6) yields

$$P(F|E) = \sum_j \frac{N'_{fj}}{N'_{vj}} V_j N \int_0^w f(a)B(a)da . \tag{9.9}$$

Each term in Eq. (9.9) represents the probability of a flaw in the jth zone resulting in vessel failure.

9.3.3 Methods for accelerating the convergence of P(F|E)

When P(F|E) is very small, the value of N'_{vj} required to achieve reasonable accuracy (see Sect. 9.3.4) becomes quite large. Under some circumstances, the value of N'_{vj} can be reduced by using importance sampling of one or more of the parameters simulated. Two provisions of this type are included in OCA-P as optional methods for calculating P(F|E), and both deal only with the simulation of flaw depth.

In many cases, particularly those that do not include cladding or flaws in the cladding, the shallowest simulated flaw (3.2-mm depth) does not contribute much to failure; however, ~70% of the flaws normally simulated have this depth. If simulated vessels containing the 3.2-mm flaw are counted but not calculated, the number of simulated vessels actually calculated can be reduced significantly.

The other option makes use of a stratified sampling technique[4] in which a uniform distribution of flaw depths is assumed when simulating flaw depths. The results of the subsequent analysis are then weighted

by the actual flaw-depth density to obtain

$$P(F|E) = \sum_j \sum_i \frac{N'_{fij}}{N'_{vij}} \left[\frac{\int_{\Delta a_i} f(a)B(a)da}{\int_0^W f(a)B(a)da} \right] NV_j \int_0^W f(a)B(a)da \ , \quad (9.10)$$

where

N'_{fij} = number of vessels that fail with a flaw in the jth zone with depth in Δa_i,

N'_{vij} = number of vessels simulated with a flaw in the jth zone with depth in Δa_i.

The stratified sampling procedure is useful for low-probability transients that are characterized by high pressure and mild thermal shock.

9.3.4 Error analysis

When the number of vessels simulated is quite large, the central limit theorem[4] can be used to estimate the uncertainty in calculated values of the conditional probability of vessel failure as a function of the number of vessels simulated. Using this approach and specifying a 95% confidence level yields

$$P(F|E)_j = \hat{P}_j \, NV_j \int_0^W f(a)B(a)da \pm 1.96 \, \sigma_j \ , \quad (9.11)$$

where

$P(F|E)_j$ = true value of the conditional probability of vessel failure for those vessels having flaws in the jth zone only,

σ_j = one standard deviation,

$$\hat{P}_j = \frac{N'_{fj}}{N'_{vj}} \ .$$

For the direct approach (no importance sampling),

$$\sigma_j = \left[\frac{\hat{P}_j(1 - \hat{P}_j)}{N'_{vj}} \right]^{1/2} NV_j \int_0^W f(a)B(a)da \ . \quad (9.12)$$

When stratified sampling is used,

$$\sigma_j = \left\{ \sum_i \left[\frac{\int_{\Delta a_i} f(a)B(a)da}{\int_0^W f(a)B(a)da} \right]^2 \left[\frac{\hat{P}_{ij}(1 - \hat{P}_{ij})}{N'_{vij}} \right] \right\}^{1/2}$$

$$\times NV_j \int_0^W f(a)B(a)da \ , \quad (9.13)$$

where

$$\hat{P}_{ij} = \frac{N'_{fij}}{N'_{vij}} \ .$$

The values of σ corresponding to all of the vessels simulated, including those without flaws, is

$$\sigma_{P(F|E)} = \sqrt{\sum_j \sigma_j^2} \ , \quad (9.14)$$

and the error ε_j associated with the jth zone is

$$\varepsilon_j = \frac{1.96\ \sigma_j}{\hat{P}_j\ NV_j \int_0^W f(a)B(a)da} \ . \quad (9.15)$$

The total error ε, considering all zones of interest, is

$$\varepsilon = \frac{1.96\ \sigma_{P(F|E)}}{\sum_j \hat{P}_j\ NV_j \int_0^W f(a)B(a)da} \ . \quad (9.16)$$

Two criteria are used in OCA-P for limiting the value of N'_{vj}. One is to just achieve a user-specified value of ε_j in Eq. (9.15), and the other is simply a user-specified maximum value of N'_{vj}. This latter criterion is included because the former can result in an exorbitant value of N'_{vj}.

9.3.5 Simulation of the flaw depth

When simulating flaw depth in OCA-P, it is necessary to consider ranges of flaw depths and then use the averages of these ranges for the deterministic analysis. Thus, there is a question regarding the number and sizes of the ranges that must be used to accurately represent flaw behavior. For instance, the first increment, which extends from zero crack depth upward, contains a range of subcritical crack depths. However, if the average crack depth for that increment is critical, all flaws in the first increment are considered critical.

The original version of OCA-P included seven crack-depth increments with averages of 3.2, 6.3, 12.7, 19.0, 25.4, 38.1, and 50.8 mm, extending from the inner surface outward. Recently, comparative studies were conducted with 7, 9, 11, and 13 increments; for each of these four configurations, the size of the first increment was the same (0–4.3 mm), and the deepest increment had an extreme of 57.2 mm. The size of each increment, other than the first, was established on the basis of a geometric progression.

The relative values of $P(I|E)$* for the above four cases are dependent to some extent on the severity of the transient. Thus, the comparative studies were conducted for several transients characterized by an exponential decay of the coolant temperature and a constant pressure of 15 MPa. The initial temperature of the coolant and vessel was 288°C, the exponential decay constant was 0.15 min^{-1}, and the heat transfer coefficient was ~6000 $W/m^2 \cdot °C$. The asymptotic coolant temperature, T_f, was changed to vary the severity of the transient; values considered ranged from 66 to 149°C.

Results of the comparative study are presented in Table 9.2, which shows the effect on $P(I|E)$ of changing the number of crack-depth increments for four different transients. In terms of estimating the probability of vessel failure, the differences in $P(I|E)$ were considered small, and it was concluded that nine increments would be sufficient.

*The comparisons were made using the conditional probability of crack initiation, $P(I|E)$, rather than $P(F|E)$.

Table 9.2. Influence of number of simulated crack depths on $P(I|E)$

Number of increments	$P(I\|E)$ at T_f (°C)			
	66	93	121	149
7	(2.7 ± 0.1)E-1	(7.3 ± 0.3)E-2	(6.1 ± 0.4)E-3	(9 ± 2)E-5
9	(2.6 ± 0.1)E-1	(7.1 ± 0.3)E-2	(6.0 ± 0.4)E-3	(9 ± 2)E-5
11	(2.7 ± 0.1)E-1	(6.9 ± 0.3)E-2	(5.9 ± 0.4)E-3	(8 ± 2)E-5
13	(2.7 ± 0.1)E-1	(6.9 ± 0.3)E-2	(5.9 ± 0.4)E-3	(8 ± 2)E-5

The size of the first increment tends to have a particularly large effect on P(I|E) because small flaws are more abundant and because, as mentioned above, the shallower flaws in the first increment are subcritical. To investigate the effect of the size of the first increment, calculations were made for the most severe of the above transients and also for a large-break loss-of-coolant accident (LBLOCA), using nine increments and a range of sizes for the first increment. For the exponential transient, the size of the first increment had to be reduced from 4.3 to 2.5 mm to effectively eliminate initiations in the first increment. For the LBLOCA, the range was reduced from 4.3 to 1.8 mm to effectively eliminate initiations in the first increment. The corresponding reductions in P(I|E) were 20% and 44%, respectively. As expected, the effect is greater for the more severe transients.

It was concluded that a Δa of 4.3 mm for the first increment and a total of nine increments would be satisfactory for transients of interest to the IPTS program.

9.4 Influence Coefficients for Cladding

R. D. Cheverton D. G. Ball

As discussed in Refs. 2, 5, and 6, stress-intensity-factor influence coefficients can be used in conjunction with superposition techniques to accurately calculate, at reasonable cost, stress-intensity factors for both two- and three-dimensional (2- and 3-D) surface flaws in pressure vessel walls containing arbitrary stress distributions. The coefficients are calculated for specific sets of vessel dimensions, using a finite-element analysis.[7,8] This cost is relatively high, but once the coefficients are available, they can be used for any stress distributions; thus, the coefficients are particularly suitable for transient and parametric analyses.

Reference 2 describes the general method for calculating and applying 2-D flaw coefficients for a cylinder wall with or without cladding, whereas Ref. 6 provides similar information for semielliptical surface flaws without cladding. When using coefficients for 3-D flaws, it is necessary to represent the stress distribution in the uncracked cylinder with a third-order polynomial, and thus the discontinuity in the thermal stress at the cladding-base material interface presents a problem. However, this problem is overcome by calculating influence coefficients for the cladding stresses alone and then in effect superposing the corresponding K_I value on the K_I value caused by stresses in the base material. As indicated in Fig. 9.4, this is accomplished by first calculating a K_I value for a continuous-function stress distribution obtained by a linear extrapolation of the stress distribution in the base material into the cladding. Then a K_I value is calculated for a stress distribution in the cladding which is obtained by subtracting the extrapolated distribution from the actual distribution in the cladding, which is also assumed to be linear. The total K_I value is simply the sum of the two. Since the stress distribution in the cladding is essentially linear, only a first-order polynomial is used for the cladding coefficients.

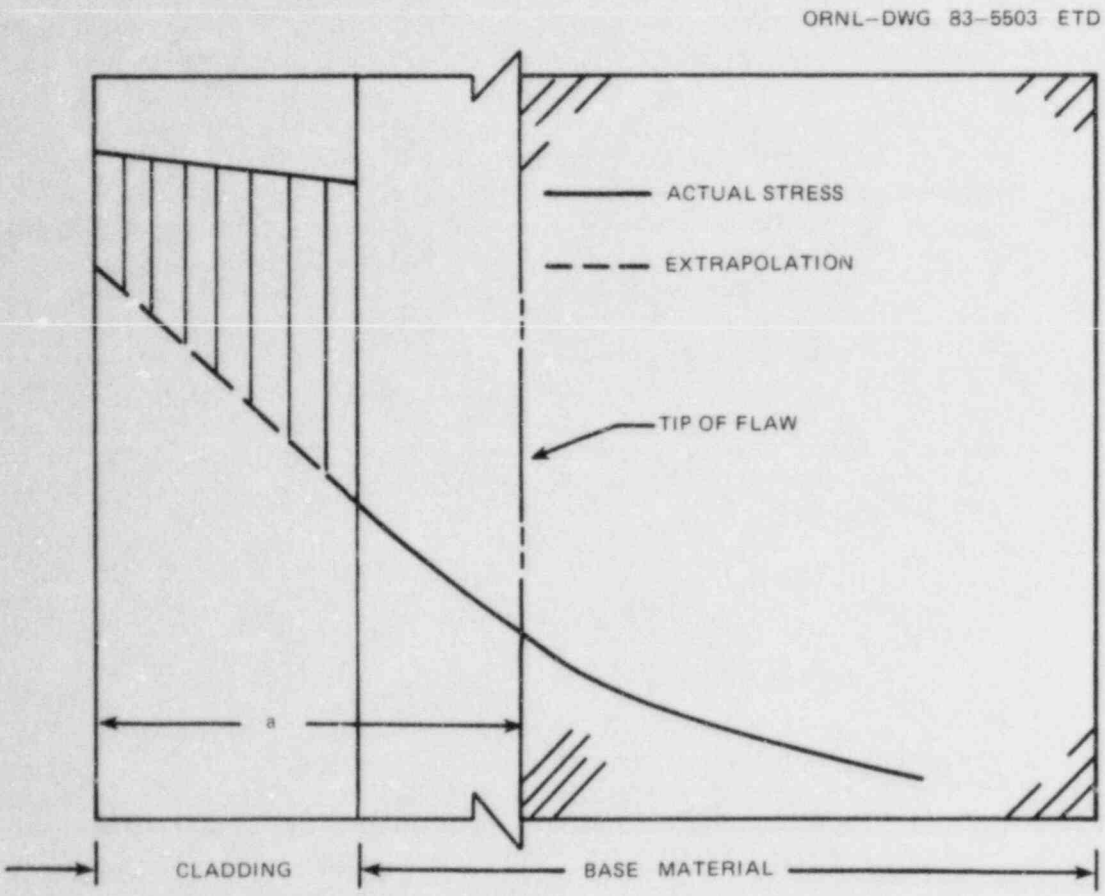

Fig. 9.4. Stress distributions used in superposition technique for including effect of cladding on K_I.

Cladding coefficients were recently calculated for 1.8-m-long inner-surface semielliptical flaws with depths ranging from 20% to 90% of the wall thickness of a clad cylinder that has an inner radius of 2184 mm, a wall thickness of 216 mm, and a cladding thickness of 5.4 mm. These coefficients and the previously obtained coefficients have been incorporated in the PWR pressure-vessel FM computer codes OCA-II[2] and OCA-P.[1]

9.5 Integrated Pressurized-Thermal-Shock Program Studies

R. D. Cheverton D. G. Ball

The general purpose of the IPTS program is to estimate the frequency of failure of specific PWR pressure vessels during overcooling accidents that are postulated for the specific plant. The effort includes defining transients, estimating the frequency of these transients, calculating the corresponding primary-system pressure and downcomer coolant-temperature

transients, and finally a probabilistic FM analysis of the pressure vessel. In addition, sensitivity and uncertainty analyses are performed, and the effects of proposed remedial measures are investigated. Studies of this type were recently completed for the Oconee-I nuclear plant and are under way for the Calvert Cliffs and H. B. Robinson plants. FM aspects of these studies have been reported previously[9,10] and are updated in the following paragraphs.

9.5.1 Contribution to P(F|E) of flaws in the circumferential welds and the base material

Flaws anywhere in the beltline region of the reactor vessel will contribute to the conditional probability of vessel failure, P(F|E). However, aside from the effect of flaw depth, some contribute more than others because of differences in orientation, length, local chemistry of the material, and local fluence. Axial flaws have the highest values of K_I, and in Oconee-I the axial welds have higher concentrations of copper than the circumferential welds and the base material.

Because the difference in copper concentration between the axial welds and base material is rather large in terms of radiation damage, the extended surface length of an axial flaw in a weld tends to be limited to the height of a shell course. For deep flaws, this limit on surface length results in significantly lower K_I values than for much longer flaws. The surface length of extended flaws in the circumferential welds and in the base material are not limited by this mechanism, although the lengths of these flaws may be limited by gradients in fluence and coolant temperature.

Thus far our FM model has not been sophisticated to the point of being able to consider gradients in fluence and coolant temperature along the specified surface flaw path. In lieu of considering this sort of detail, all flaws in the circumferential welds and in the base material were assumed to be 2-D. It was believed that even under these conservative conditions, flaws in the circumferential welds and in the base material would not be dominant in terms of the calculated probability of vessel failure.

To be certain that the above assumption was reasonable, a few comparison calculations were made for circumferential flaws in the circumferential welds, for axial flaws in the base material, and for axial flaws in the axial welds. The flaw density was assumed to be the same for the three categories of flaws considered, and since the volume of the base material is much greater than that of the welds, the base material contributed many more flaws than the welds.

In an attempt to account for the azimuthal variation in fluence in the base plate without dividing the plate region into several zones, each with a different fluence, an average fluence was used. Also, the initial values of RT_{NDT} for the base material were reduced by 14°C to account for a lower radiation damage rate in the base material than in the welds.[11] The radiation-damage trend curve [$\Delta RT_{NDT} = f(F, Cu, Ni)$] in the FM model corresponds to weld material only.

The comparison calculations were made for transient 44 and for 32 effective full-power years (EFPY). The results indicate that the circumferential flaws add ~5% to P(F|E) and the base material ~30%. Since the

contributions were small, flaws in the base material and the circumferential welds were not included in the remainder of the studies.

9.5.2 Sensitivity analysis

A sensitivity analysis was conducted by determining the change in $P(F|E)$ corresponding to a change in the mean value of each of several parameters. The mean value of only one parameter was changed at a time, while all other parameters retained their original mean values. The parameters changed were K_{Ic}, K_{Ia}, RT_{NDT}, Cu, F, fluid-film heat-transfer coefficient, downcomer coolant temperature, primary-system pressure, and flaw density. The amount of the change for each parameter was one standard deviation; and for some parameters, both plus and minus changes were made because of a suspected strong nonlinearity.

The values of σ used in the sensitivity analysis for K_{Ic}, K_{Ia}, RT_{NDT}, Cu, and F are listed in Table 9.3, and the values of the flaw density N, corresponding to the application of $\pm 1\sigma$ were 10^2 and 10^{-2} times the original mean value. The 1σ change in the downcomer coolant temperature constituted a linear change in temperature from zero at time zero to 28°C at a time corresponding to the minimum point in the temperature vs time curve. From that point on in time the change in temperature was a constant value of 28°C. The 1σ change in the heat-transfer coefficient h was 0.25 h, and for the pressure it was 0.34 MPa.

Table 9.3. Parameters simulated in OCA-P

Parameter	Standard deviation[a] (σ)	Truncation
Fluence (F)	$0.3\ \mu(F)$	$F = 0$
Copper	0.025%	
Nickel	0.0	
RT_{NDT_o}	9°C[b]	[b]
ΔRT_{NDT}	13°C[b]	[b]
K_{Ic}	$0.15\ \mu(K_{Ic})$	$\pm 3\sigma$
K_{Ia}	$0.10\ \mu(K_{Ia})$	$\pm 3\sigma$

[a] Normal distribution used for each parameter.

[b] $\sigma_{(RT_{NDT})} = \left[\sigma^2_{(RT_{NDT_o})} + \sigma^2_{(\Delta RT_{NDT})}\right]^{1/2}$, truncated at $\pm 3\sigma$.

9.5.3 Summary of results for Oconee-I

A complete summary of results for the Oconee-I studies is beyond the scope of this report. Furthermore, the full significance of the FM results cannot be appreciated without combining these results with estimated frequencies of occurrence of the postulated transients, which is also beyond the scope of this report. However, a few points of particular interest will be discussed below.

Although a million or so end points of event trees were considered, only 18 postulated transients were actually subjected to a probabilistic FM analysis. For most of the others, it was apparent that either the frequency or the conditional probability of vessel failure $P(F|E)$ was insignificant, or that some transients were very similar to others. A detailed description of the transients calculated is included in Ref. 12.

Values of $P(F|E)$ were calculated as a function of EFPY for the 18 transients, and the results are presented in Fig. 9.5. Note that at 32 EFPY (normal end of plant life), $P(F|E)$ ranges from $\sim 10^{-6}$ to $\sim 10^{-2}$. Transients with $P(F|E) < 10^{-6}$ were not included in the detailed FM studies; and generally speaking, the transients with the higher values of $P(F|E)$ had the lower frequencies of occurrence.

Results of the sensitivity study indicate that aside from the sensitivity to N, $P(F|E)$ is most sensitive by far to the reduction in downcomer coolant temperature and is about a factor of 6 less sensitive to a reduction in K_{Ic} and an increase in RT_{NDT}. The probability of failure is least sensitive to variations in the heat transfer coefficient and the primary-system pressure.

For most of the Oconee-I postulated transients, WPS could be a factor because the calculations indicate that K_I does not become equal to K_{Ic} until after the time of WPS ($\dot{K}_I = 0$). The effects of WPS were not included in the calculation of $P(F|E)$ because in most cases the K_I vs t curves for the shallow flaws were very flat, making it difficult to determine where the maximum was located. Furthermore, unforeseen perturbations in pressure and coolant temperature might exist and defeat WPS. Even so, it is of interest to see what the effect is for the idealized transients. The results of this study are presented in Table 9.4. As indicated, WPS reduces $P(F|E)$ substantially for most of the transients.

9.6 Thermal-Shock Investigations Related to HDR Reactor Vessel

R. D. Cheverton

Some consideration has been given to the idea of conducting pressurized thermal-shock experiments with the reactor pressure vessel at the German HDR facility. Presumably, this would be a cooperative effort between ORNL-HSST and Staatliche Materialprüfungsanstalt (MPA).

A number of thermal-hydraulic tests and nozzle-corner cyclic thermal-shock experiments have already been conducted with the HDR vessel. Presumably, the particular experiment of interest now would involve an inner

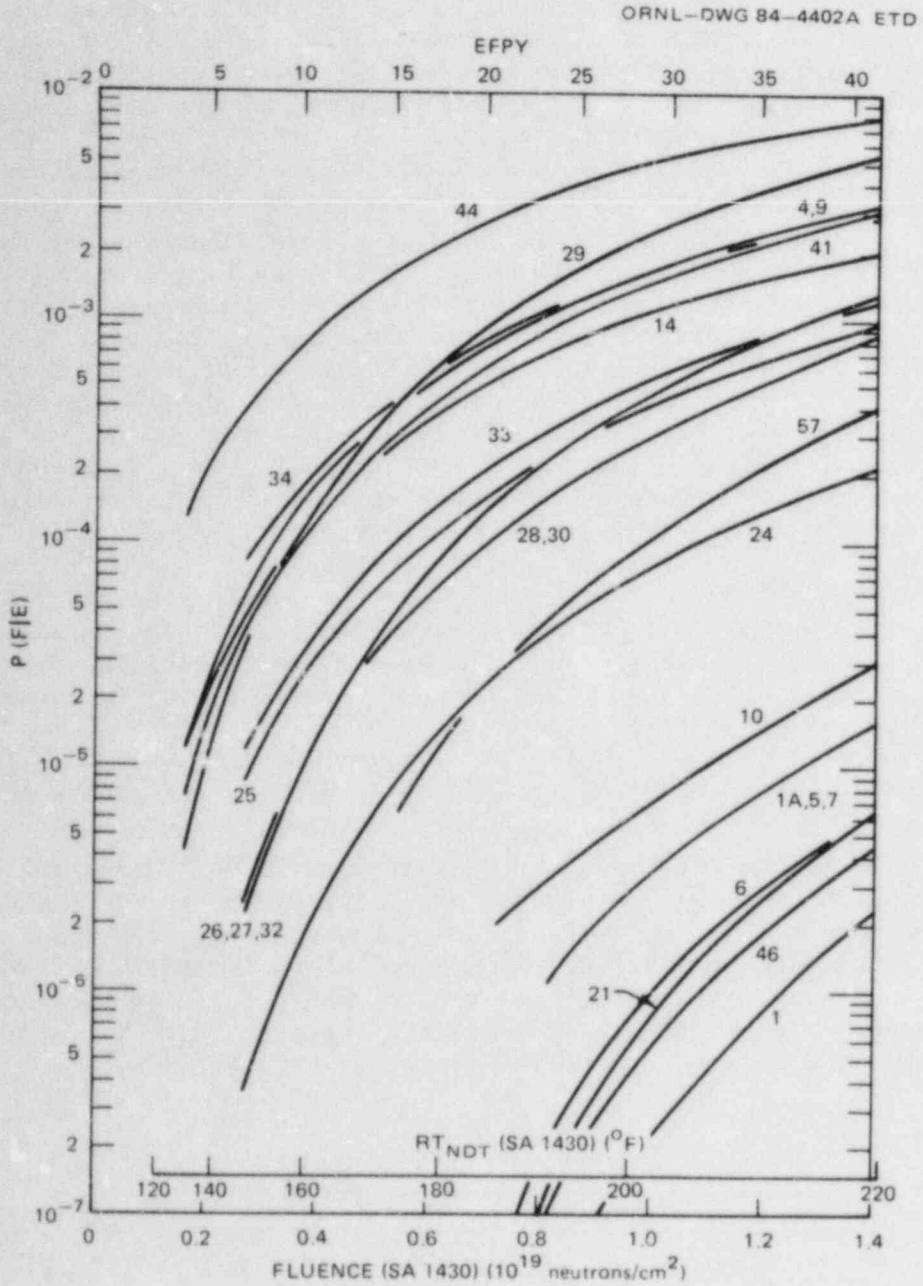

Fig. 9.5. P(F|E) vs EFPY for Oconee-I postulated OCAs.

Table 9.4. Effect of including WPS in calculation of $P(F|E)$ at 32 EFPY

Transient	$P(F|E)$ without WPS	Time of WPS (min)	$P(F|E)$ with WPS
1	3×10^{-7}	27	$<10^{-7}$
1A, 5, 7	5.2×10^{-6}	18	
4, 9	2.0×10^{-3}	22	$<10^{-6}$
6	1.7×10^{-6}	28	$<10^{-7}$
10	9.8×10^{-6}	28	$<10^{-7}$
14	1.3×10^{-3}	36	$<10^{-6}$
21	9×10^{-7}	40	$<10^{-7}$
24	1.0×10^{-4}	18	9×10^{-7}
25	5.2×10^{-4}	17	3×10^{-5}
26, 27, 32	6.2×10^{-4}	28	3×10^{-4}
28, 30	4.0×10^{-4}	18	4×10^{-5}
29	3.0×10^{-3}	20	$<2 \times 10^{-6}$
33	6.5×10^{-4}	18	3×10^{-6}
34	1.8×10^{-3}	18	5×10^{-5}
41	1.8×10^{-3}	30	$<10^{-6}$
44	5.4×10^{-3}	22	$<10^{-6}$
46	1.0×10^{-6}	20	$<10^{-7}$
57	1.5×10^{-4}	20	1×10^{-5}

surface axial flaw in the beltline region and a thermal shock similar to that used in the HSST program.

The dimensions of the HDR vessel (1510-mm inner radius, 112-mm wall thickness) and the thermal-shock capability of the HDR facility are such that thermal-shock experiments of interest to the U.S. PWR safety studies may not be practical.

For the purpose of conducting a preliminary FM analysis, it was assumed that an initial temperature of the vessel of 288°C, a pressure of 10.3 MPa, a coolant temperature of 21°C, and a fluid-film heat transfer coefficient of 5700 $W/m^2 \cdot °C$ could be achieved. To account for the thermal effect of the cladding, the inner surface heat-transfer coefficient was reduced from 5700 to 1700 $W/m^2 \cdot °C$. The stress effect of the cladding, which will enhance K_I, was neglected.

Assuming RT_{NDT} = −18, 66, and 93°C and using the ASME Sect. XI toughness curves,[13] the calculations indicated that WPS would prevent crack initiation. Even if WPS were ignored, the minimum critical crack depth for RT_{NDT} = −18°C was 45% of the wall thickness, indicating that pressure stresses were controlling. For RT_{NDT} = 66 and 93°C, shallow flaws would initiate, if it were not for WPS.

To delay the time of WPS, various pressure ramps were used; however, the delays were not long enough to permit crack initiation. Further studies will be required to see if a more severe thermal shock will be of benefit.

References

1. R. D. Cheverton and D. G. Ball, *OCA-P, A Deterministic and Probabilistic Fracture-Mechanics Code for Application to Pressure Vessels*, NUREG/CR-3618 (ORNL-5991), Union Carbide Corp. Nuclear Div., Oak Ridge Natl. Lab. (in preparation).

2. D. G. Ball et al., *OCA-II, A Code for Calculating the Behavior of 2-D and 3-D Surface Flaws in a Pressure Vessel Subjected to Temperature and Pressure Transients*, NUREG/CR-3491 (ORNL-5934), Union Carbide Corp. Nuclear Div., Oak Ridge Natl. Lab., February 1984.

3. Letter from F. J. Loss, Naval Research Laboratory, to R. H. Bryan, Oak Ridge National Laboratory, March 31, 1981.

4. R. Y. Rubinstein, *Simulation and the Monte Carlo Method*, Israel Institute of Technology, John Wiley & Sons, New York, 1981, pp. 115–17.

5. S. K. Iskander, R. D. Cheverton, and D. G. Ball, *OCA-I, A Code for Calculating the Behavior of Flaws on the Inner Surface of a Pressure Vessel Subjected to Temperature and Pressure Transients*, NUREG/CR-2113 (ORNL/NUREG-84), Union Carbide Corp. Nuclear Div., Oak Ridge Natl. Lab., August 1981.

6. R. D. Cheverton and D. G. Ball, "Thermal-Shock Investigations," pp. 77–83 in *Heavy-Section Steel Technology Program Quart. Prog. Rep. January–March 1983*, NUREG/CR-3334, Vol 1 (ORNL/TM-8787/V1), Union Carbide Corp. Nuclear Div., Oak Ridge Natl. Lab., September 1983.

7. S. K. Iskander, *Two Finite Element Techniques for Computing Mode I Stress Intensity Factors in Two- and Three-Dimensional Problems*, NUREG/CR-1499 (ORNL/NUREG/CSD/TM-14), Computer Sciences Division, Union Carbide Corp. Nuclear Div., Oak Ridge Natl. Lab., February 1981.

8. B. R. Bass and J. W. Bryson, *ORVIRT: A Finite Element Program for Energy Release Rate Calculations for 2-Dimensional and 3-Dimensional Crack Models*, NUREG/CR-2997, Vol. 2 (ORNL/TM-8527/V2), Union Carbide Corp. Nuclear Div., Oak Ridge Natl. Lab., February 1983.

9. R. D. Cheverton and D. G. Ball, "Thermal-Shock Investigations," pp. 82–88 in *Heavy-Section Steel Technology Program Quart. Prog. Rep. April–June 1983*, NUREG/CR-3334, Vol 2 (ORNL/TM-8787/V2), Union Carbide Corp. Nuclear Div., Oak Ridge Natl. Lab., December 1983.

10. R. D. Cheverton and D. G. Ball, "Thermal-Shock Investigations," in *Heavy-Section Steel Technology Program Quart. Prog. Rep. July–September 1983*, NUREG/CR-3334, Vol 3 (ORNL/TM-8787/V3), Union Carbide Corp. Nuclear Div., Oak Ridge Natl. Lab.

11. P. N. Randall, U.S. Nuclear Regulatory Commission, personal communication to R. D. Cheverton, Oak Ridge National Laboratory.

12. J. D. White et al., *OCA-II: A Code for Calculating Behavior of 2-D and 3-D Surface Flaws in a Pressure Vessel Subjected to Temperature and Pressure Transients*, NUREG/CR-3491 (ORNL-5934), Union Carbide Corp. Nuclear Div., Oak Ridge Natl. Lab., January 31, 1984.

13. T. U. Marston, *Flaw Evaluation Procedures: ASME Section XI*, EPRI NP-719-SR, August 1978.

10. PRESSURIZED-THERMAL-SHOCK TECHNOLOGY

R. H. Bryan

During this reporting period, the first pressurized-thermal-shock (PTS) test, PTSE-1, of a pressure vessel was performed. The objectives of the test were to investigate (1) the effects of warm prestressing (WPS) on initiation of propagation of an existing crack and (2) to determine the nature of arrest of a rapidly propagating crack at temperatures on the ductile upper shelf. The intended conditions were produced in PTSE-1, and a preliminary study of the information collected in the experiment indicates that the desired objectives were attained. Two crack initiations and arrests occurred after a succession of WPS episodes. Preliminary analyses imply that the initiations occurred at stress-intensity factor K_I values of 157 and 221 MPa$\cdot\sqrt{m}$ at temperatures T of 100 and 120°C, respectively. The corresponding arrest values were K_I = 177 and 265 MPa$\cdot\sqrt{m}$ at T = 157 and 168°C, respectively.

During the reporting period, modifications to the test facility were completed; characterization tests were completed; the preliminary test series, PTSE-0, was performed; extensive fracture analyses based on characterization data were performed; and the PTSE-1 vessel was flawed, instrumented, and tested.

10.1 Experimental Planning

R. H. Bryan G. D. Whitman

PTSE-1 was planned to be conducted in two phases, as discussed in detail in an earlier progress report.[1] The objective of the first phase was to initiate the propagation of a shallow crack in the cleavage mode and to achieve arrest in the transitional toughness regime prior to the onset of WPS. During the WPS interlude, the stress-intensity factor of the arrested crack would attain the critical value, K_{Ic}, but the crack would not propagate because of WPS. In the second phase of the test, the crack would be forced to propagate again (by increasing the pressure loading) with the objective of causing the crack to propagate into material in the upper-shelf toughness regime. The conditions of the test were selected to favor the arrest of the crack prior to penetration of the wall of the vessel.

Definition of a suitable transient for PTSE-1 involved the evaluation of a large number of parameters that generally fall into two categories:

1. characteristics of the test vessel —
   - flaw size (length, depth)
   - fracture toughness (K_{Ic}, K_{Ia}, J_R vs T)
   - ductile-brittle transition temperature (T_D)
   - yield strength
   - thermoelastic properties

2. facility-related characteristics of transients —
   pressure vs time (t)
   convective heat transfer coefficient, h vs t
   initial vessel temperature, T_o
   coolant temperature, T_c vs t

Preliminary fracture analyses of the type now being performed by the OCA/USA program[2] were the basis for designing the test vessel and the facility. Early material characterization data confirmed that the designed characteristics were probably satisfactory. The selection of test transients depended on the actual characteristics of the vessel and the facility as determined by preliminary tests. Material properties, except for K_{Ia}, were determined by the Babcock & Wilcox Company,[3] and K_{Ia} determinations were made by Battelle Columbus Laboratories, as presented elsewhere in this report. The principal results of these two investigations are shown in Figs. 10.1 and 10.2. OCA/USA and ADINA-ORVIRT analyses performed prior to the first test were based on the vessel and material characteristics given in Table 10.1 and Figs. 10.1–10.3.

The basic three-dimensional (3-D) analyses for the vessel with closed ends and a flaw of finite length were performed by the ADINA-ORVIRT system of programs. These analyses included the consideration of plasticity. ADINA-ORVIRT was used to calculate the 3-D influence coefficients for the OCA/USA code. Parameter studies were performed with the OCA/USA program by which variations of many of the parameters identified in Table 10.1 were considered. These studies defined flaw depths to be considered for the PTSE-1 vessel and transients to be investigated experimentally in the PTSE-0 series of tests. The initial flaw depth was selected prior to the performance of thermal transient tests to maintain a reasonable schedule for preparing the PTSE-1 vessel for testing in January 1984.

The ideal plan for PTSE-1 is illustrated in Fig. 10.4, which shows the evolution of crack-tip conditions. K_I and K_{Ic} vs time curves are shown for three crack depths: a_0, the initial crack depth; a_1, an intermediate depth; and a_2, the final depth. In the phase $t < t_1$, the initial crack is subcritical and should not propagate. If it does not propagate at t_1, it may still propagate at some time prior to t_2, at which time the initial crack would become warm prestressed. In the interval $t_1 < t < t_2$, K_I/K_{Ic} for the initial crack may become much greater than unity, but the loading rate $\dot{K}_I$ diminishes. A crack propagating at $t = t_1$ would arrest at a depth a_1, for which $K_I = K_{Ia}$ (point B). K_I for the intermediate crack would continue to rise until $t = t_3$, at which time the intermediate crack would be warm prestressed (point C). The crack would again become critical at $t = t_4$ (point D), but it would not propagate immediately because of its warm prestressed state. When $t_5 < t < t_7$ (after point E), the nominal WPS condition ($\dot{K}_I < 0$) no longer obtains; and, since $K_I > K_{Ic}$, the crack should again propagate, for example, at point F. This running crack should again arrest at a depth a_2 for which $K_I = K_{Ia}$ (point G).

In any persistent transient, there is generally a time t_I beyond which an arrested crack in the upper-shelf regime would not be stable, either because of a tearing instability or a net ligament tensile instability. Since it is essential to the interpretation of the experiment to preserve evidence of the arrested crack geometry, it is necessary that t_I be predictable and that the transient be terminated at some time $t_7 < t_I$ (point H).

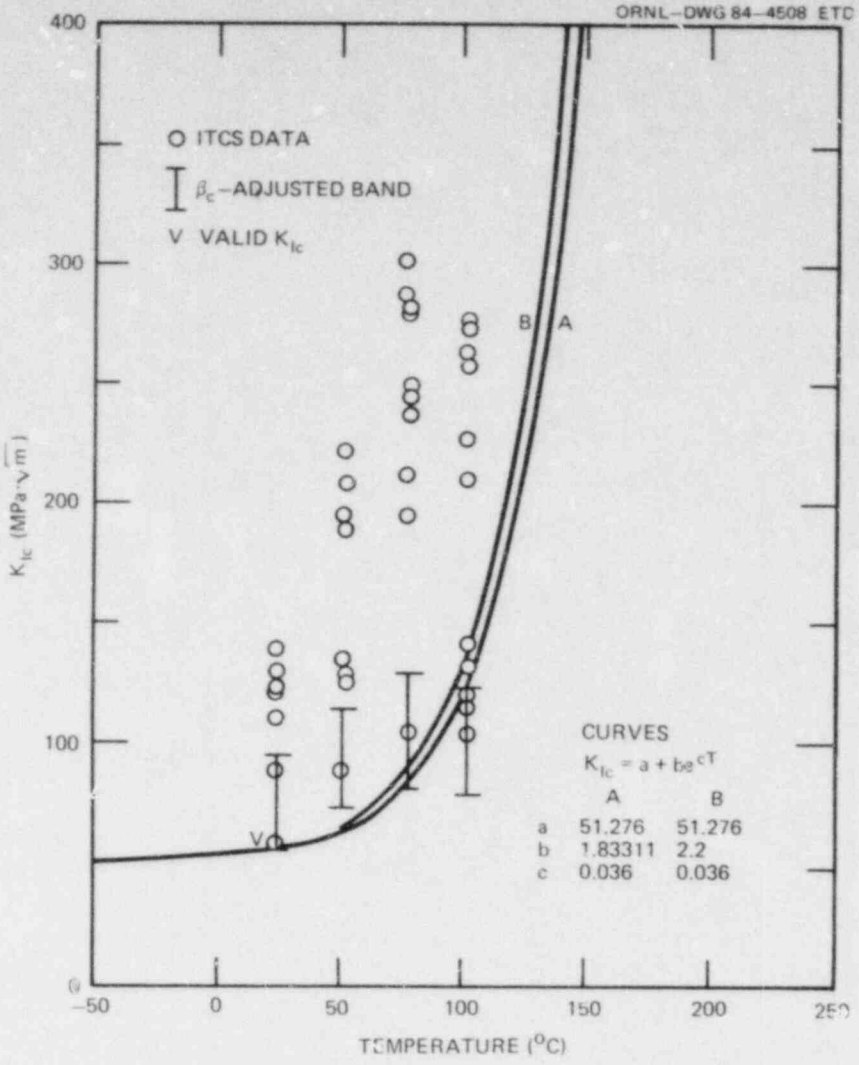

Fig. 10.1. K_{Ic} data for PTSE-1 vessel. Curves represent functions in OCA/USA analysis.

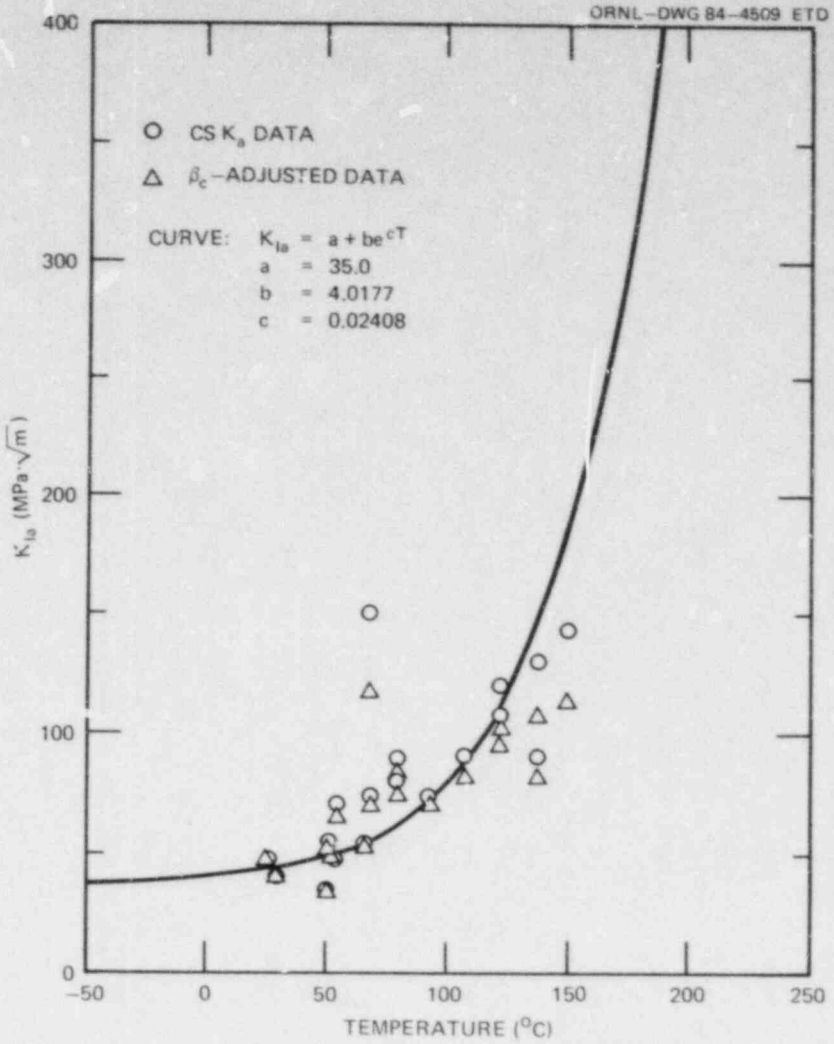

Fig. 10.2. K_{Ia} data for PTSE-1 vessel. Curve represents function in OCA/USA analysis.

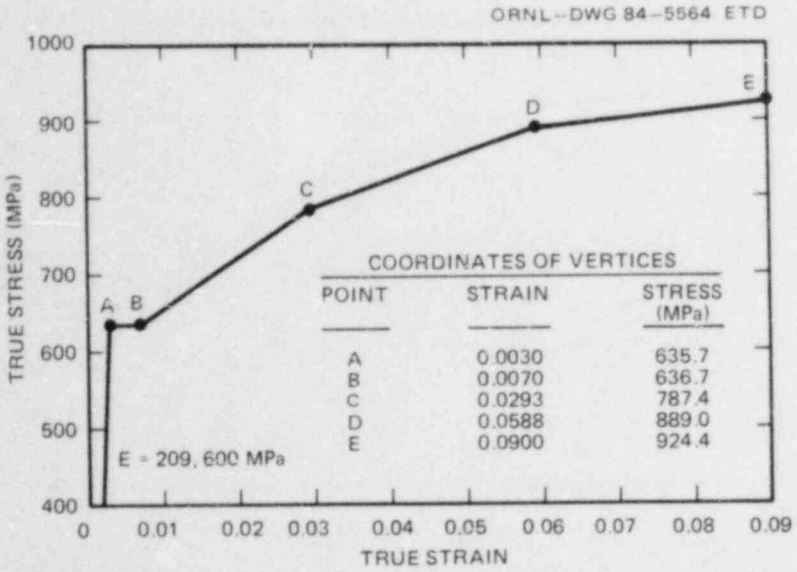

Fig. 10.3. Piecewise linear stress-strain relationship assumed for ADINA-ORVIRT pretest analysis of PTSE-1.

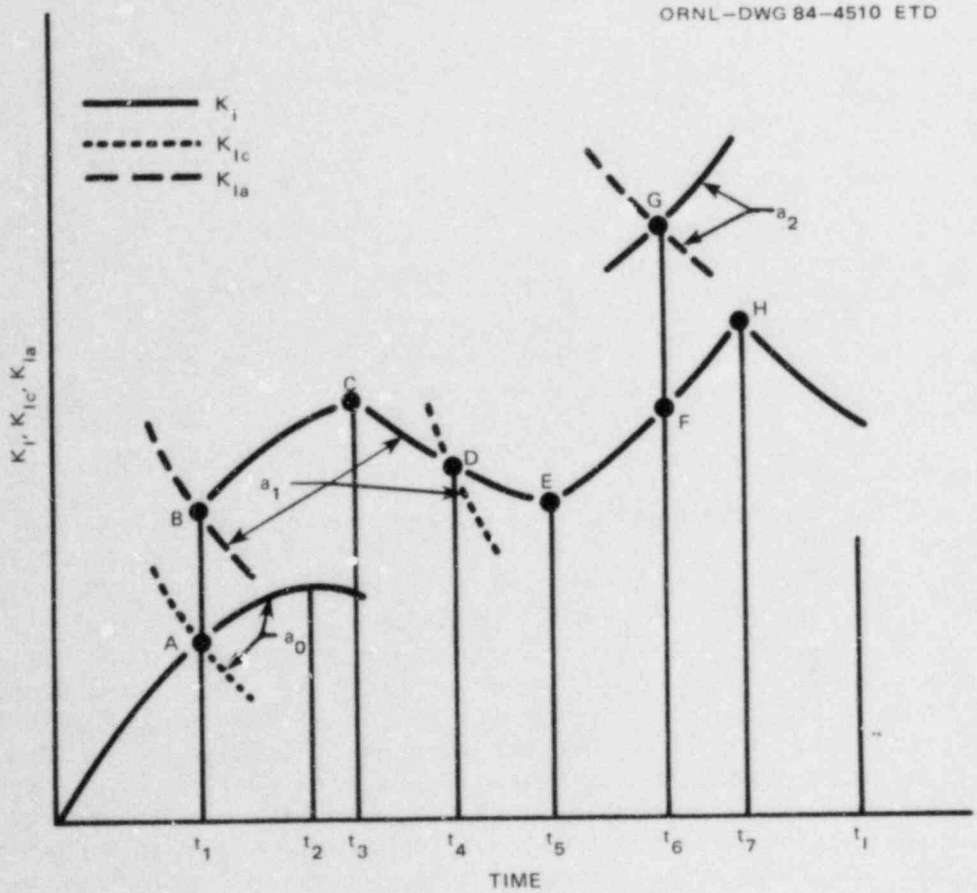

Fig. 10.4. Plan for PTSE-1, the evolution of K_I and crack-tip K_{Ic} and K_{Ia} values for ideal experiment.

Table 10.1. Characteristics of the PTSE-1 vessel used in OCA/USA pretest analysis

Parameter	Value
Toughness	
K_{Ic}	Curve A, Fig. 10.1
K_{Ia}	Curve, Fig. 10.2
Upper-shelf threshold temperature TD, °C	175
J_R parameters[a]	
c	2.60
n	0.359
Elastic-plastic parameters	
Yield strength, σ_y, for OCA/USA, MPa	600
Stress-strain relationship for ADINA-ORVIRT	Fig. 10.3
Thermoelastic parameters	
Young's modulus E, MPa	209,600
Coefficient of thermal expansion, α (K^{-1})	1.445×10^{-5}
Poisson's ratio, ν	0.3
Conductivity k, $W \cdot m^{-1} \cdot K^{-1}$	41.54
Heat capacity C, $J \cdot kg^{-1} \cdot K^{-1}$	502.4
Density ρ, kg/m^3	7833
Geometry of vessel	
Inside radius r_i, mm	343
Wall thickness w, mm	147.6
Flaw length 2b, mm	1000
Flaw depth a, mm	Various

[a] $J_R = c(\Delta a)^n$; J_R in MJ/m^2, Δa in m.

After the PTSE-0 tests were completed, it was recognized that a single thermal shock might not be the best means of attaining the PTSE-1 objective. It was decided, therefore, to plan three tests (PTSE-1A, -1B, and -1C), the first of which would be designed to provide the best opportunities to be a complete test. For this to be the case, an initial crack propagation would have to occur promptly (when $K_I \approx K_{Ic}$), and arrest would have to take place at an optimum depth for initiation in the second phase of the transient. If the objectives were not fulfilled by the PTSE-1A test, then one or two additional transients (starting with high initial temperatures) would be conducted. The strategy for the B and C tests was to produce conditions in the B test that would have a high probability of causing the crack to propagate to an intermediate depth and in the C test to produce conditions that would drive the intermediate crack to the upper shelf.

10.2 PTSE Test Facility and Vessel Preparation

R. H. Bryan S. E. Bolt
G. C. Robinson

Most of the construction and modification activities were completed, and the PTSE-0 series of tests was initiated during the preceding reporting period.[4] In the current period all modifications were completed, and the facility tests above ambient temperature were performed with the unflawed PTSE-0 vessel. Four thermal transient tests, designated PTSE-0A, -0B, -0C, and -0D, were performed under conditions specified in Table 10.2. In addition to the thermal transients, many pressurization tests were conducted while the vessel was at high, nearly isothermal temperature.

Operating characteristics of the heating, refrigeration, pressurization, and main coolant systems were determined. Several problems were

Table 10.2. PTSE-0 test conditions

Parameter	Test			
	A	B	C	D
Date	11/2/83	11/8/83	11/16/83	11/17/83
Initial vessel temperature, nominal, °C	285	278	283	284
Initial coolant temperature, °C	7.5	7.5	7.5	7.5
Flow control valve openings, %				
Main loop	100	28.6	28.6	34.2
Bypass loop	100	100	100	100
Main loop flow, nominal, m^3/s	0.1100	0.0685	0.0661	0.0880
Heat transfer coefficient[a] nominal, $W \cdot m^{-2} \cdot K^{-1}$	10,000	6,700	6,000	6,500
Pressure transient nominal				
P_o, MPa	1	20	0.4	0.7
P_{max}, MPa		25		20, 49[b]
$\dot{P}$, MPa/s				0.43

[a] These values were calculated on the basis of indirectly estimated bulk coolant temperature and are, therefore, considered imprecise.

[b] Transient consisted of two positive pressure ramps, each followed by a depressurization.

experienced, some of which limit operating ranges that are currently practicable: high compliance of the test vessel ballast; asymmetric temperatures during heatup, evidently associated with the large access nozzle at the beltline of the outer test vessel; and instability of the main flow control valve near the 35% position.

A crack 1000 mm long and 11.4 mm deep was placed in a radial-axial plane of the vessel in the plug of specially tempered material, as illustrated in Fig. 10.5. This flaw was generated by the electron-beam welding, hydrogen-charging technique used in flawing many other HSST test vessels and cylinders.[5]

The PTSE-1 test vessel was instrumented to measure transient temperature profiles in the wall of the vessel, surface strain, crack-mouth-opening displacement (CMOD), and internal pressure (Fig. 10.6). A data acquisition system samples and records the output of sensors at the rate of 10,000 points/s. Values of pressure, temperatures, and CMOD are displayed in the control room during the PTSE transients by digital and graphic displays to permit proper coordination of the thermal and pressure transients.

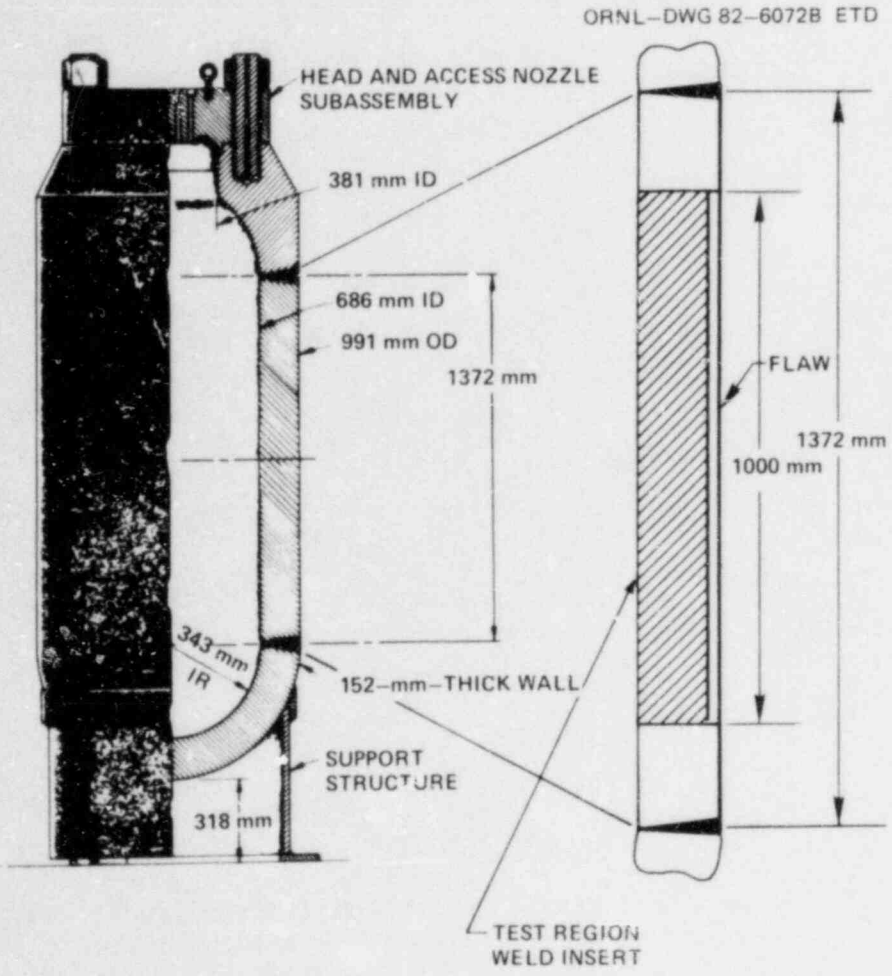

Fig. 10.5. PTSE-1 test vessel geometry.

ORNL-PHOTO 8172-83

Fig. 10.6. PTSE-1 test vessel after instrumentation was applied. Ends of two thermocouple thimbles directly facing the camera (~16-mm diam) are visible. About 250 mm to right of thimbles is vertical array of CMOD gages crossing 1-m-long flaw.

10.3 Analysis of PTSE-1

R. H. Bryan B. R. Bass
J. W. Bryson J. G. Merkle
D. A. Steinert

The final pretest analysis of PTSE-1 was based on the results of the PTSE-0 series in conjunction with the known vessel characteristics. The initial flaw depth of 11.4 mm had been measured ultrasonically, and all material characterization tests had been completed. Upon consideration of the operating characteristics observed in PTSE-0, the PTSE-0B (thimble 3) thermal transient was selected as the prototype for PTSE-1.

The PTSE-0B temperature vs time and position data were used in OCA/USA analyses directly. This was accomplished by means of a series of data processing programs developed to facilitate the evaluation of performance of instrumentation and equipment and to produce data sets of experimental temperature profiles for OCA/USA input.

Each thermocouple thimble contains 12 thermocouples distributed at various depths in the outer 100 mm of the 147.6-mm-thick vessel wall.[6] Transient tests of individual thimbles showed that thimble temperatures deviate significantly from wall temperatures late in a transient.[7] Accordingly, a mapping procedure was used to extend the domain of the temperature profiles from the depth of the thimbles to the full thickness of the vessel wall.

In the OCA/USA analyses discussed in this report, the K_I values have been adjusted for a plastic zone size based on σ_y = 600 MPa (Table 10.1). K_I values were computed from both two-dimensional (2-D) and 3-D influence coefficients; values presented are 3-D, center-of-crack values unless it is specified otherwise. Generally for $a/w < 0.1$, OCA/USA calculates K_I only from 2-D influence coefficents. This approximation is convenient and acceptable, since full 3-D ADINA/ORVIRT analyses have shown that for $a/w = 0.1$, OCA/USA 2-D K_I values are very close to the 3-D K_I values at the center of a long flaw.[2]

10.3.1 PTSE-1A pretest analysis by OCA/USA

The first test, PTSE-1A, was planned as a complete experiment, consisting of a thermal shock with two phases of increasing pressure (curve A, Fig. 10.7). The input for the OCA/USA analysis is defined in Table 10.1 and Fig. 10.7, and the results are presented in Figs. 10.8 and 10.9. According to this analysis, crack propagation and arrest would have occurred twice during the first pressurization phase with a third initiation during the anti-WPS phase of the test.

In addition to this particular analysis, other analyses were performed to show the effects of deviations of the vessel and transient from the assumed characteristics. An analysis of the type required by Sect. XI of the *ASME Boiler and Pressure Vessel Code* was also performed. The drop-weight and Charpy V-notch impact test results indicated that the material in which the flaw resides has an RT_{NDT} = 91.3°C. On that basis, an OCA/USA analysis of the proposed PTSE-1A transient implied that the

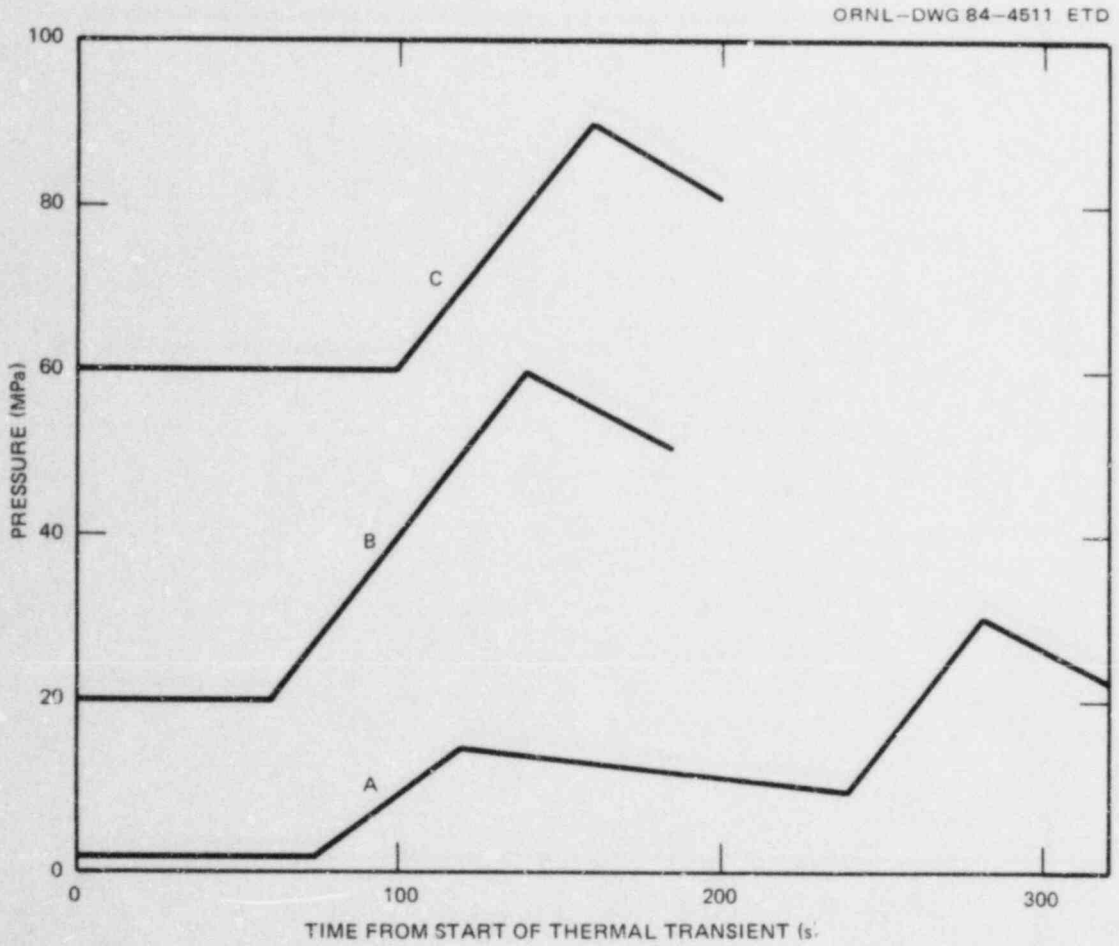

Fig. 10.7. Pressure transients planned for PTSE-1A, -1B, and -1C.

crack would penetrate the wall of the vessel at ~100 s in the transient, which is a time at which the pressure is low.

10.3.2 Crack-depth analyses for the PTSE-1 test series

In preparation for the PTSE-1A, -1B, and -1C series, extensive pretest analyses were performed with the ORMGEN/ADINA/ORVIRT fracture-mechanics system and the CYBER 205 computer of CYBERNET Services. Results from these analyses were used to correlate incremental changes in crack depth with measured changes in CMOD during a PTS transient. This was accomplished by employing a superposition technique that combines midplane CMOD values for pressure loading with those values for thermal effects over a range of crack-depth ratios and selected times in the transient.

For test PTSE-1A, 3-D finite-element analyses were conducted for a series of crack depths in the test vessel subjected to unit internal pressure loading only. Each finite-element model in this series consisted of

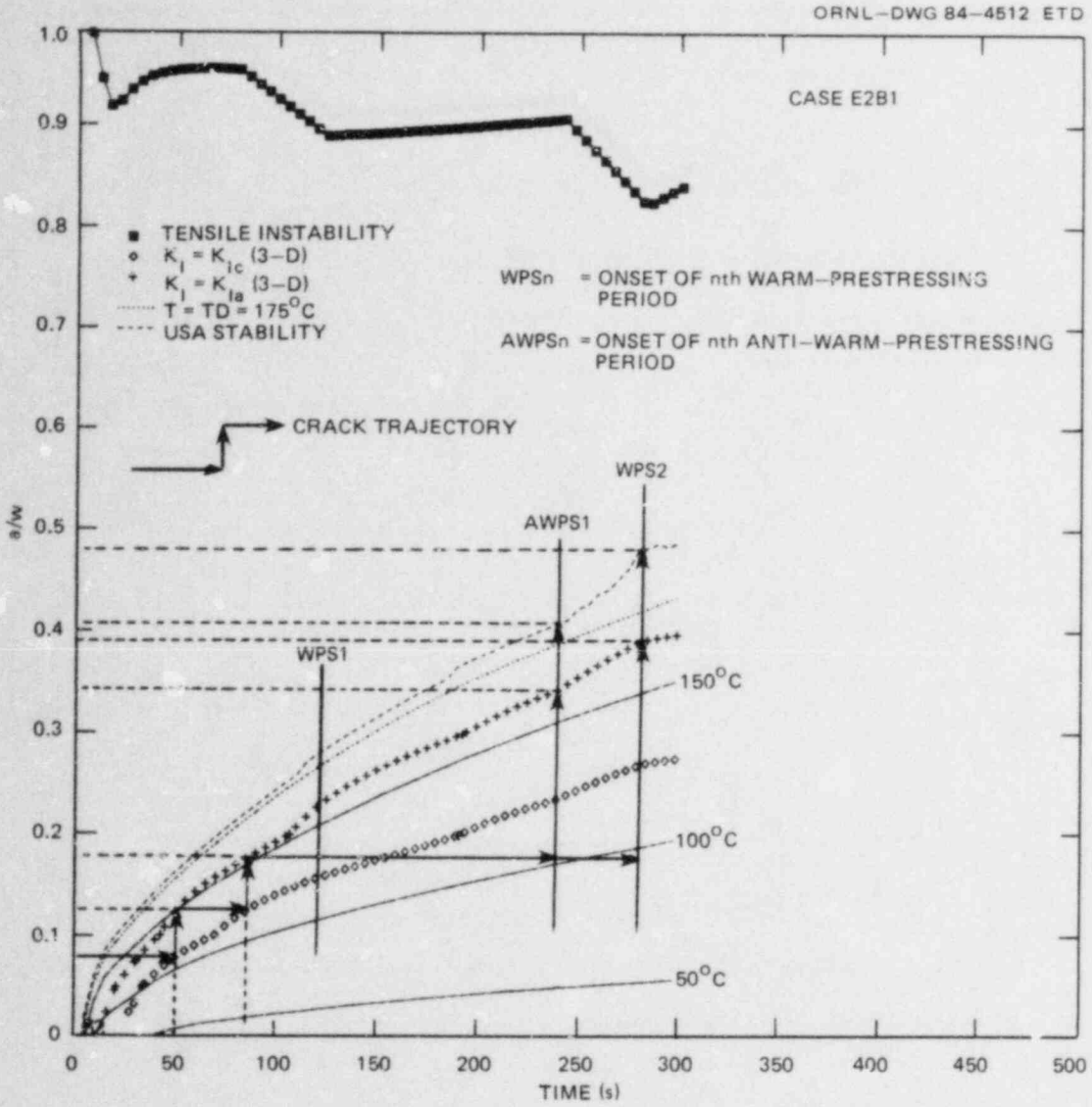

Fig. 10.8. Critical-crack-depth loci from the PTSE-1A pretest analysis. Initiation and arrest loci are computed from 3-D influence coefficients.

3496 nodes and 688 isoparametric elements. Material properties were taken to be Young's modulus $E = 2.00 \times 10^5$ MPa, Poisson's ratio $\nu = 0.3$, and thermal expansion coefficient $\alpha = 13.0 \times 10^{-6}$ K^{-1}. The selected crack depths (all 1 m in length) and the midplane CMOD corresponding to internal pressure, p = 1 MPa, are given in Table 10.3. For the same series of finite-element models, a second set of 3-D analyses was performed with the vessel subjected only to thermal loading. The temperature distributions for these computations were selected from the PTSE-0B test data (thermocouple thimble 3) at times in the transient given in Table 10.4. The selected time intervals $55 \leq t \leq 155$ and $240 \leq t \leq 280$ define the periods in which crack initiation events were anticipated in

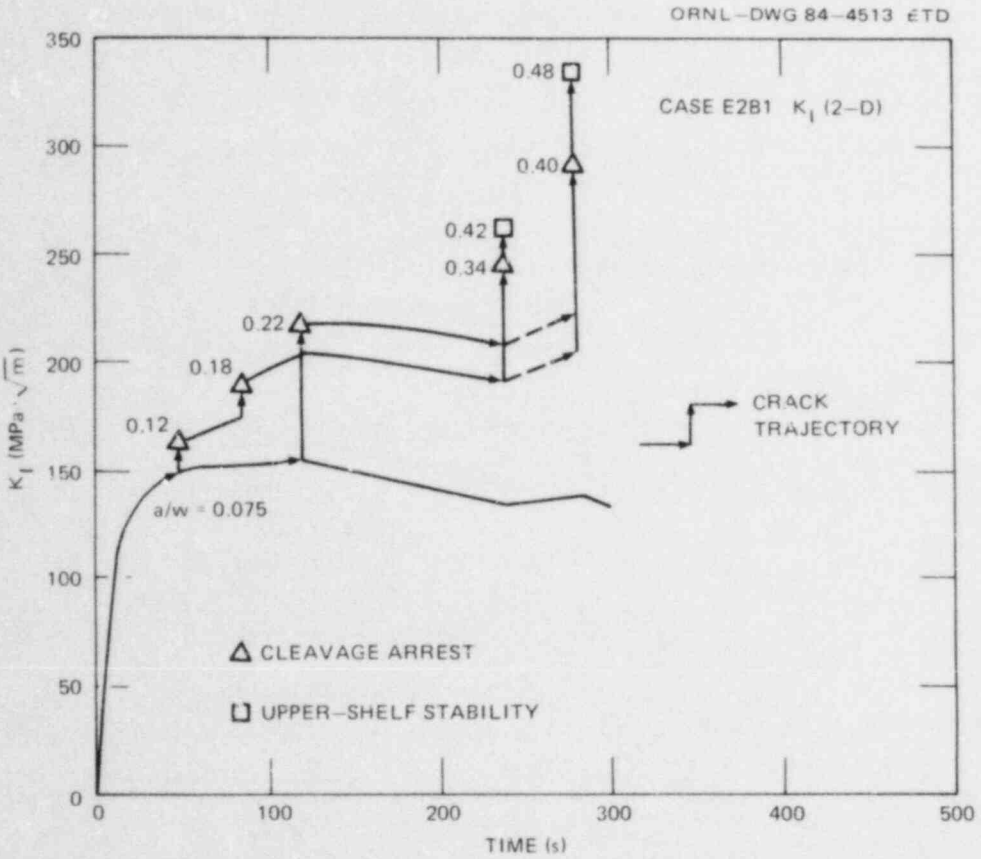

Fig. 10.9. K_I vs time and a/w from the PTSE-1A pretest analysis, based on 2-D analysis.

Table 10.3. Calculated midplane CMOD for selected crack-depth ratios a/w in test vessel PTSE-1 (internal pressure p = 1 MPa)

a/w	CMOD (mm)
0.08	0.0592×10^{-2}
0.10	0.0761×10^{-2}
0.15	0.1213×10^{-2}
0.20	0.1726×10^{-2}
0.30	0.3022×10^{-2}
0.50	0.7308×10^{-2}
0.60	1.0690×10^{-2}

Table 10.4. Calculated midplane CMOD for selected crack-depth ratios a/w and times t in test transient PTSE-0B (internal pressure p = 0)

a/w	Time (s)					
	55	85	115	240	260	280
0.08	0.242	0.233	0.218			
0.10				0.236	0.231	0.225
0.20	0.544	0.549	0.537			
0.30	0.779	0.814	0.812	0.755	0.741	0.726
0.50				1.395	1.374	1.352
0.60				1.763	1.738	1.713

test PTSE-1A. Included in the same table are the calculated midplane CMOD values for thermal-only loading.

A computer program was then developed that utilized the prescribed pressure transient of the test and the unit pressure CMOD values of Table 10.3 to estimate CMOD because of pressure only during prescribed time intervals. These results were superimposed with thermal CMOD values from Table 10.4 to produce CMOD estimates for a range of crack-depth ratios and prescribed time intervals. These estimates of crack-depth ratio as a function of CMOD are displayed in Fig. 10.10 for time interval $55 \leq t \leq 115$ and the prescribed PTSE-1A pressure transient of Fig. 10.7.

For test PTSE-1A, the initial crack-depth ratio was assumed to be a/w = 0.08. To correlate measured changes in CMOD with arrested crack-depth values during the proposed PTSE-1A transient, the curves of Fig. 10.10 were offset by the CMOD values for a/w = 0.08. These offset curves, displayed in Fig. 10.11, express a/w as a function of ΔCMOD with time t as a parameter. Because crack initiation was not achieved in the PTSE-1A test, no estimates of arrested a/w were made with these curves.

For test PTSE-1B, the above procedure for estimating a/w as a function of ΔCMOD and t was repeated, but revised thermal loading calculations were performed to replace those of Table 10.4. This revision was necessary because of changes in the nominal heat transfer coefficient h on the vessel outer surface. The shift in h resulted from a change of the bulk coolant fluid from water to methanol to permit a lower initial coolant temperature and, consequently, a more severe thermal shock. Because measured temperature data were not available for the new bulk coolant, it was necessary to repeat the thermal calculation using a range of values for h, of which two are given in Table 10.5. The h values of Table 10.5 were used in OCA/USA calculations to estimate the thermal gradient as a function of time. The computed thermal gradients at times t = 50 s and t = 130 s (which define the interval of anticipated crack

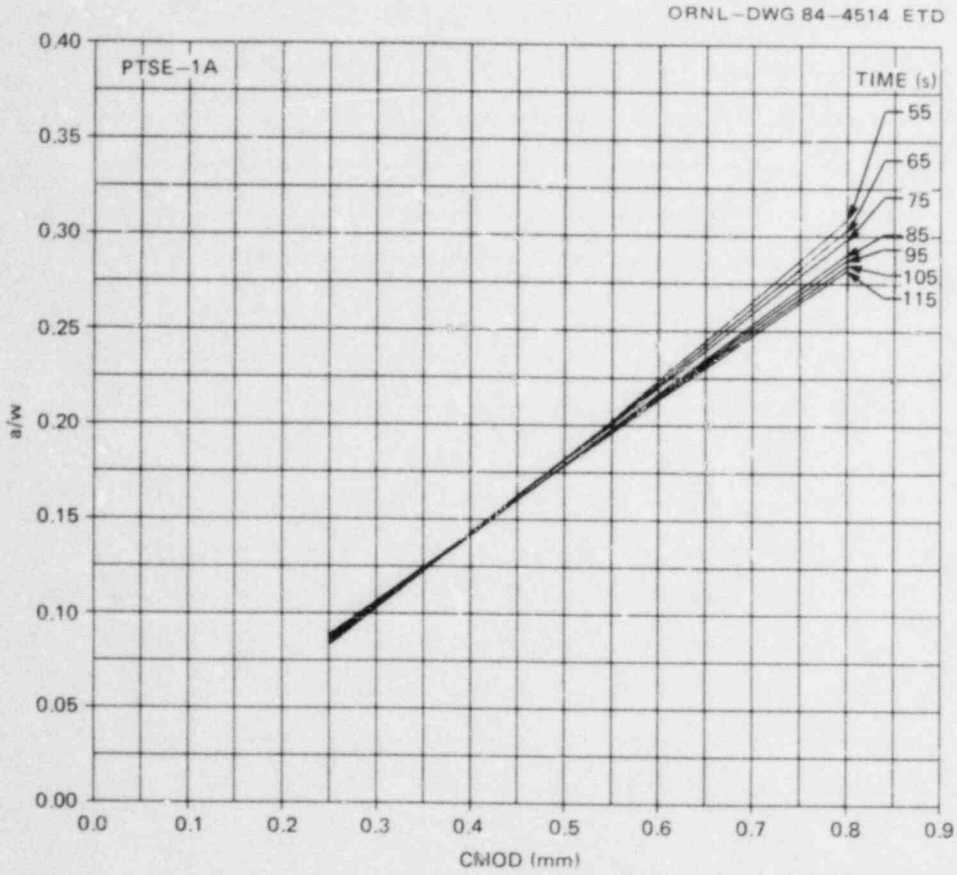

Fig. 10.10. a/w vs CMOD for proposed PTSE-1A transient, $55 \leq t \leq 115$ s.

Table 10.5. Calculated CMOD for crack-depth ratios a/w = 0.08 and 0.30 in two proposed PTSE-1B test transients

Time (s)	Heat transfer coefficient ($W \cdot m^{-2} \cdot K^{-1}$)	a/w	
		0.08	0.30
50	4545	0.225	0.726
50	6250	0.244	0.779
130	4545	0.211	0.799
130	6250	0.220	0.835

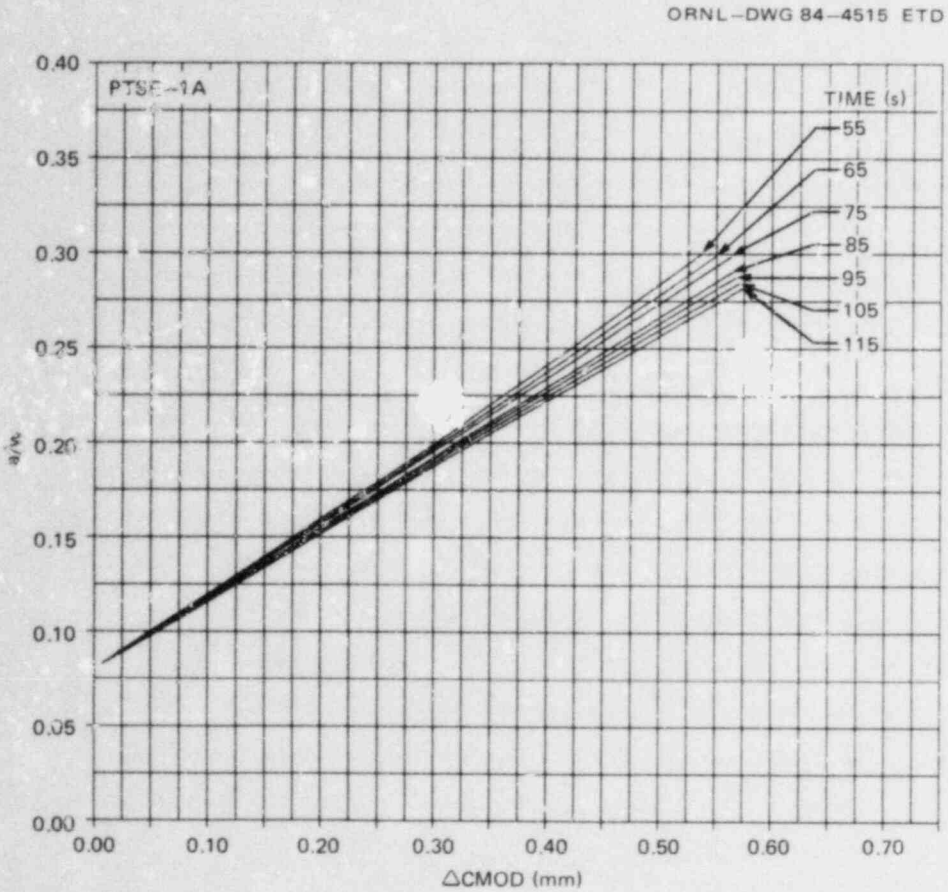

Fig. 10.11. a/w vs ΔCMOD for proposed PTSE-1A transient, 55 ≤ t ≤ 115 s, offset by CMOD for a/w = 0.08.

initiation) were employed in the ORMGEN/ADINA analyses to produce the CMOD values of Table 10.5. Figure 10.12 depicts the variation of a/w with ΔCMOD and time obtained from superposition of values from Tables 10.3 and 10.5 (for h = 6250 $W \cdot m^{-2} \cdot K^{-1}$), again offset by CMOD values for a/w = 0.08. Included in the figure is the measured change Δ = 0.175 mm that accompanied crack initiation at ~67 s in the PTSE-1B transient. The graphical result from Fig. 10.12 indicates that crack arrest occurred at a crack-depth ratio of a/w ≈ 0.144. The high h curves are used here because it was observed from measured temperature data early in the transient that the higher h value more accurately reflected surface conditions for the vessel.

For PTSE-1C, the superposition procedure was repeated using values from Table 10.3 for pressure loading, the proposed pressure transient of Fig. 10.7, and values from Table 10.5 (h = 6250 $W \cdot m^{-2} \cdot K^{-1}$) for thermal loading. The resultant curves of Fig. 10.13 are offset by CMOD values for a/w = 0.15, the approximate arrested depth ratio of test PTSE-1B. In PTSE-1C, crack initiation was achieved at t = 124 s in the transient with a measured change in CMOD of 0.353 mm. This implies crack arrest at a depth ratio of a/w ≈ 0.25, as indicated in Fig. 10.13.

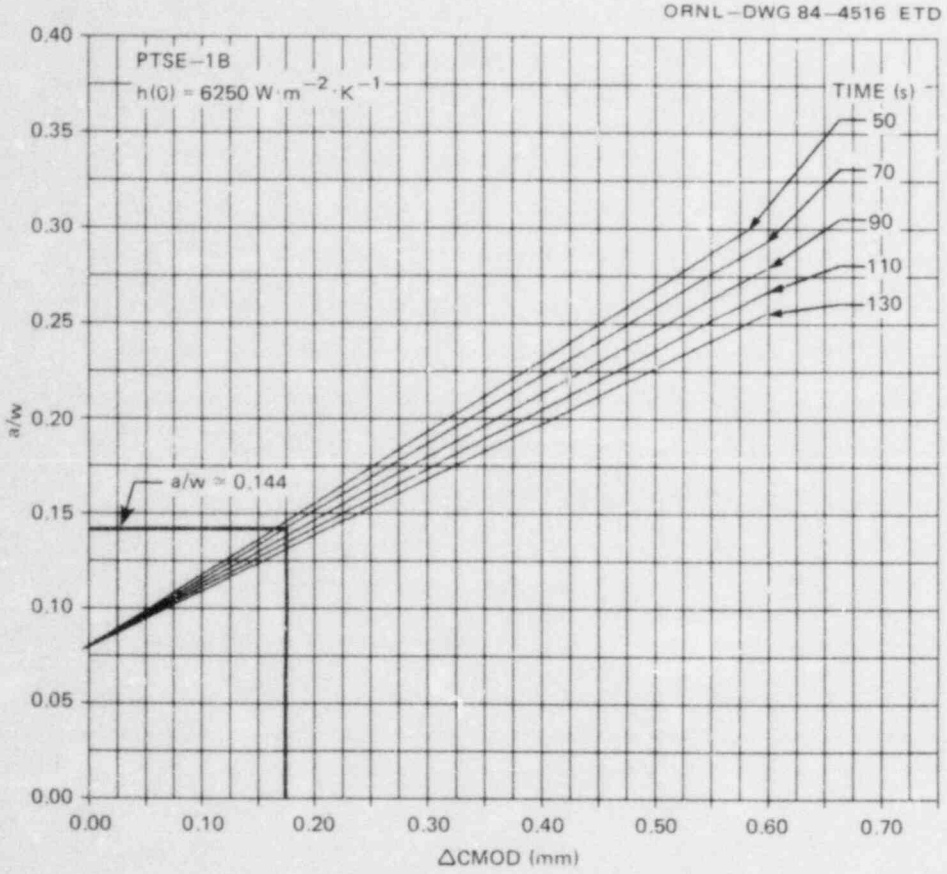

Fig. 10.12. a/w vs ΔCMOD for PTSE-1B transient, $50 \leq t \leq 130$ s, $h = 6250\ W \cdot m^{-2} \cdot K^{-1}$, offset by CMOD for a/w = 0.08.

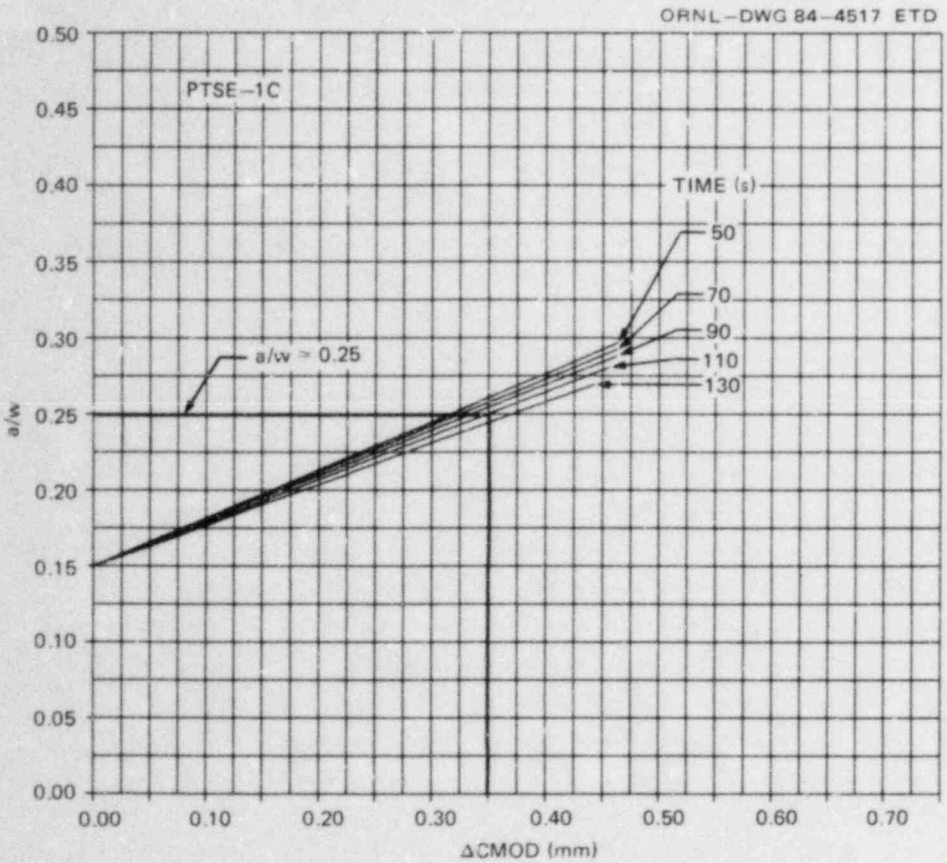

Fig. 10.13. a/w vs ΔCMOD for PTSE-1C transient, $50 \leq t \leq 130$ s, offset by CMOD for a/w = 0.15.

10.4 Results and Analyses of PTSE-1

R. H. Bryan B. R. Bass
S. E. Bolt J. W. Bryson
J. G. Merkle G. C. Robinson
G. D. Whitman

Results reported are tentative at this time because quantitative information from the test is still being evaluated, adjusted from calibration data, and analyzed.

10.4.1 Results of PTSE-1A

The conditions actually experienced in the test are presented in Figs. 10.14–10.16. The crack did not propagate. Figure 10.15 indicates that the crack was in a warm prestressed state in the time intervals 54 s < t < 71 s and 111 s < t < 235 s. The first period of WPS was inadvertent.

Tentatively, the PTSE-1A results imply the following.

1. The assumed toughness relationship (curve A, Fig. 10.1) is too low at the crack temperature at the time of initial WPS (t ≈ 54 s). Accordingly, the K_{Ic} expression used for the posttest OCA/USA analysis and for subsequent pretest analyses was adjusted (as in curve B, Fig. 10.1) to make $K_I = K_{Ic} = 133$ MPa·$\sqrt{m}$ at t = 54 s and T = 100.4°C.

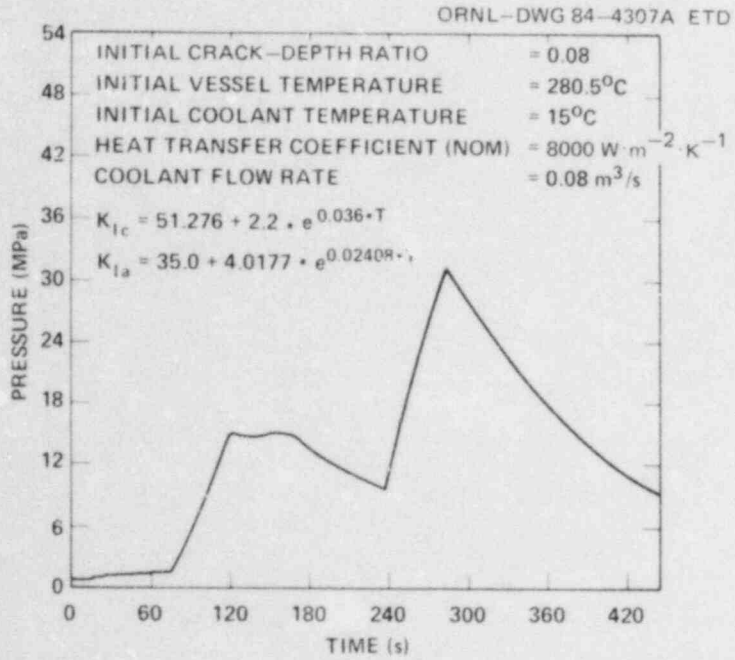

Fig. 10.14. Actual PTSE-1A pressure transient and other test parameters.

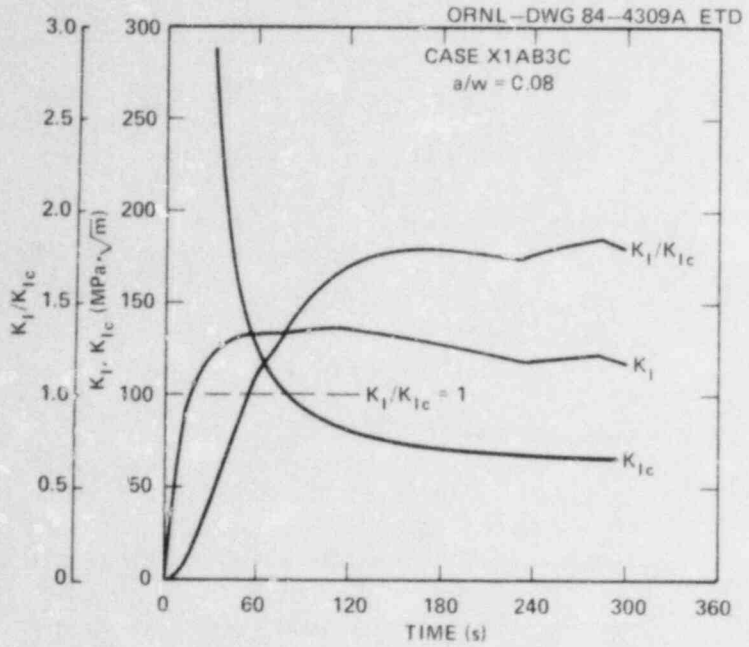

Fig. 10.15. Results (parameters vs time) of posttest OCA/USA analysis of PTSE-1A. Values are computed from measured temperatures (thimble 5) and pressures. K_I values are based on 2-D calculations.

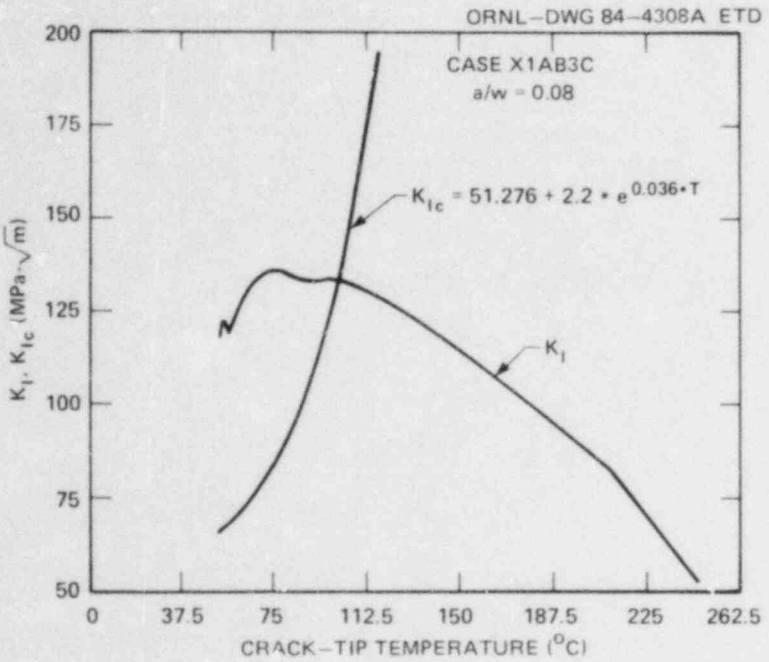

Fig. 10.16. Results (parameters vs T) of posttest OCA/USA analysis of PTSE-1A. K_I values are 2-D.

2. During the initial period of WPS the ratio K_I/K_{Ic} reached a value of ~1.24.

3. During the first anti-WPS period, 71 s < t < 111 s, K_I increased to ~136 MPa·$\sqrt{m}$ and K_I/K_{Ic} to ~1.65.

4. During the last anti-WPS period, 235 s < t < 280 s, K_I reached a peak of ~122 MPa·$\sqrt{m}$ and K_I/K_{Ic} of ~1.85.

Since the crack did not propagate in PTSE-1A, the methods of analysis and the parameters used in the OCA/USA and ADINA-ORVIRT calculations were reevaluated. Consequently, the values for E and α were reduced from the values shown in Table 10.1 to 200,000 MPa and 1.3×10^{-5} K^{-1}, respectively. This adjustment of parameters reduces all parameters proportional to K_I by ~14%. All OCA/USA analyses performed subsequent to the PTSE-1A test used the lower values of E and α as well as the revised K_{Ic} expression in Curve B of Fig. 10.1.

10.4.2 Test PTSE-1B

The initial flaw having been warm prestressed at a K_I level of ~136 MPa·$\sqrt{m}$, it was necessary to plan the PTSE-1B test so as to exceed that level. Also, to keep the predicted initiation event in a temperature range for which the K_{Ic} curve is credible, the coolant temperature had to be decreased.

The strategy for tests PTSE-1B and -1C was to produce conditions in the B test that would have a high probability of causing the crack to propagate to an intermediate depth and in the C test that would drive the intermediate crack to the upper shelf. Contingency plans were made for the B test to add a secondary pressure transient, if during the test it appeared that conditions would be conducive to attaining the upper-shelf crack depth.

The coolant was changed to a methanol-water mixture so that temperatures at the crack tip would be generally lower without diminishing the attainable K_I level. The pressure transient planned for the test is shown in Fig. 10.7 (curve B). Since a preliminary thermal-hydraulic test was not feasible, the pretest analysis was based entirely on estimated heat transfer parameters, shown in Table 10.6. The effects of variations from the nominal performances were considered in selecting the transient and in making contingency plans for a secondary pressure transient.

The pretest predictions for the nominal h(t) case (see Table 10.6) are shown in Figs. 10.17 and 10.18. Two successive crack jumps to a/w ≈ 0.14 and 0.20 were predicted. The actual thermal transient was more severe than in the nominal pretest case, the actual value of h being possibly 40% higher. In any case, the crack propagated in PTSE-1B to a depth of 22.1 mm (a/w = 0.15), estimated by 3-D analysis from the measured CMOD. The results of posttest analysis, based on measured temperatures and pressures, are shown in Figs. 10.19–10.22. The fracture mechanics parameters in the posttest analysis are identical to the pretest parameters. K_I values at initiation and arrest were ~157 and 177 MPa·$\sqrt{m}$, respectively. Before the end of the transient, the K_I of the arrested crack reached ~215 MPa·$\sqrt{m}$. The values for a/w > 0.1 were calculated from the OCA/USA 3-D influence coefficients.

Table 10.6. Basis for planned transients for PTSE-1A, -1B, and -1C and pretest analyses

	Test		
	PTSE-1A	PTSE-1B	PTSE-1C
Thermal transient	T data from thimble 3, PTSE-0B		T data from thimble 5, PTSE-1B
Equivalent parameters			
Initial vessel temperature, °C	284	290	293.3
Coolant temperature T(t), °C	10 to 34	−25 to −1	−22 to 0
h(t), $W \cdot m^{-2} \cdot K^{-1}$	8000 to 6000	4550 to 3700	5500 to 6500
Pressure transient (planned)	Curve A, Fig. 10.7	Curve B, Fig. 10.7	Curve C, Fig. 10.7
Material properties			
K_{Ic}	Curve A, Fig. 10.1	Curve B, Fig. 10.1	Curve B, Fig. 10.1
K_{Ia}	Curve, Fig. 10.2	Curve, Fig. 10.2	Curve, Fig. 10.2
Upper-shelf temperature T_D, °C	175	175	175
c, n (note *a*)	2.60, 0.359	2.60, 0.359	2.60, 0.359
σ_y (MPa)	600	600	600
E (MPa)	209,600	200,000	200,000
α (K^{-1})	14.45×10^{-6}	13×10^{-6}	13×10^{-6}
Initial flaw depth			
a, mm	11.4	11.4	22.1
a/w	0.077	0.077	0.15

[a] $J_R = c(\Delta a)^n$, where J_R is in MJ/m^2 and Δa is in m.

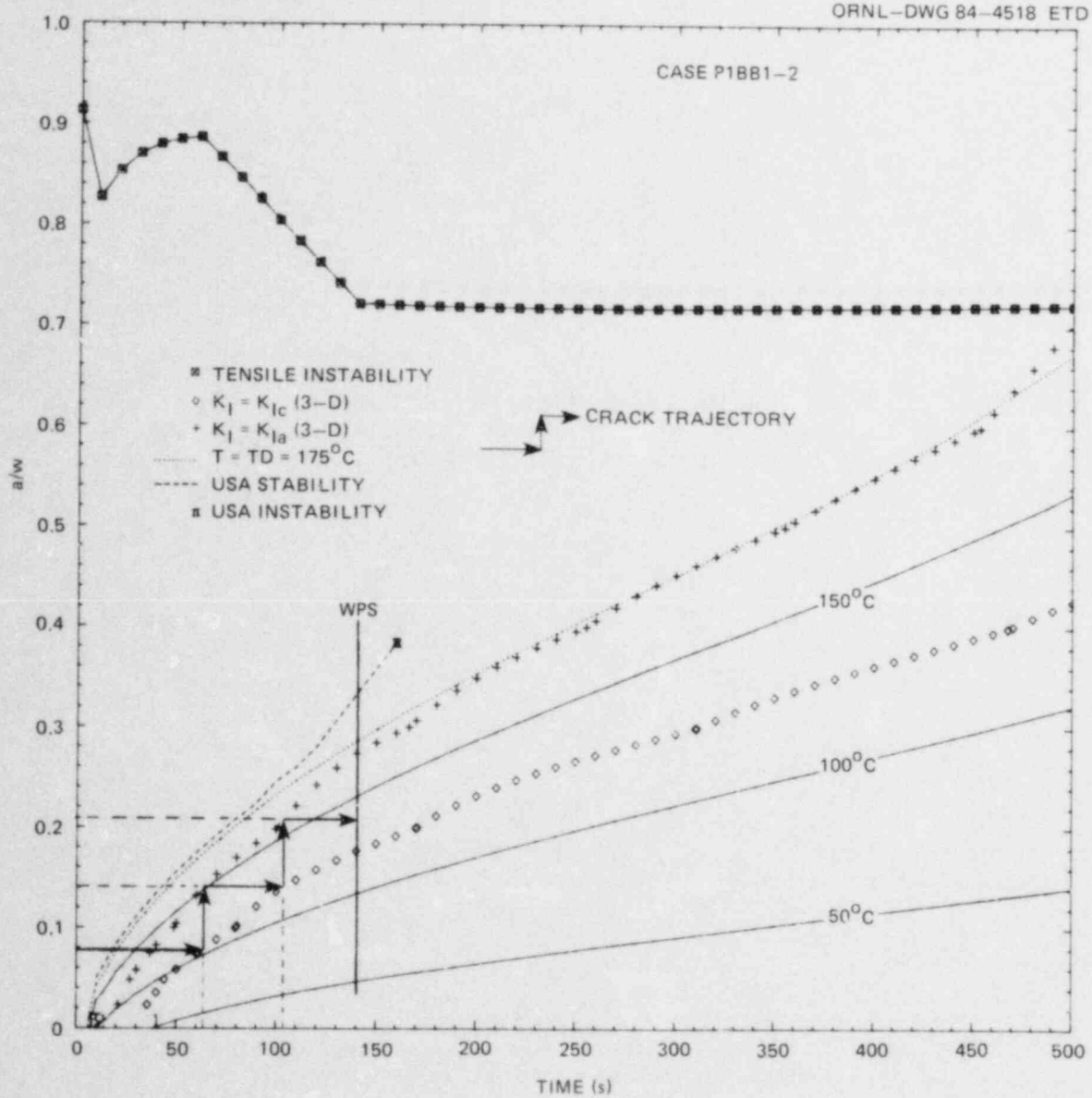

Fig. 10.17. Critical-crack-depth loci from PTSE-1B pretest analysis. Initiation and arrest loci are computed from 3-D influence coefficients. Note that two crack jumps were predicted.

In a posttest analysis of PTSE-1B, 3-D finite-element analyses were performed for crack-depth ratios a/w = 0.08 and 0.143 for the measured pressure and temperatures at the time of the initiation-arrest event. The crack length was held constant at 1 m, and a semielliptical shape was assumed. The computed ΔCMOD for these two analyses is plotted in Fig. 10.23 as a function of the axial position along the crack. Also included in the figure are measured ΔCMOD values. The distribution of these measured values suggests an asymmetric configuration for the shape of the arrested crack.

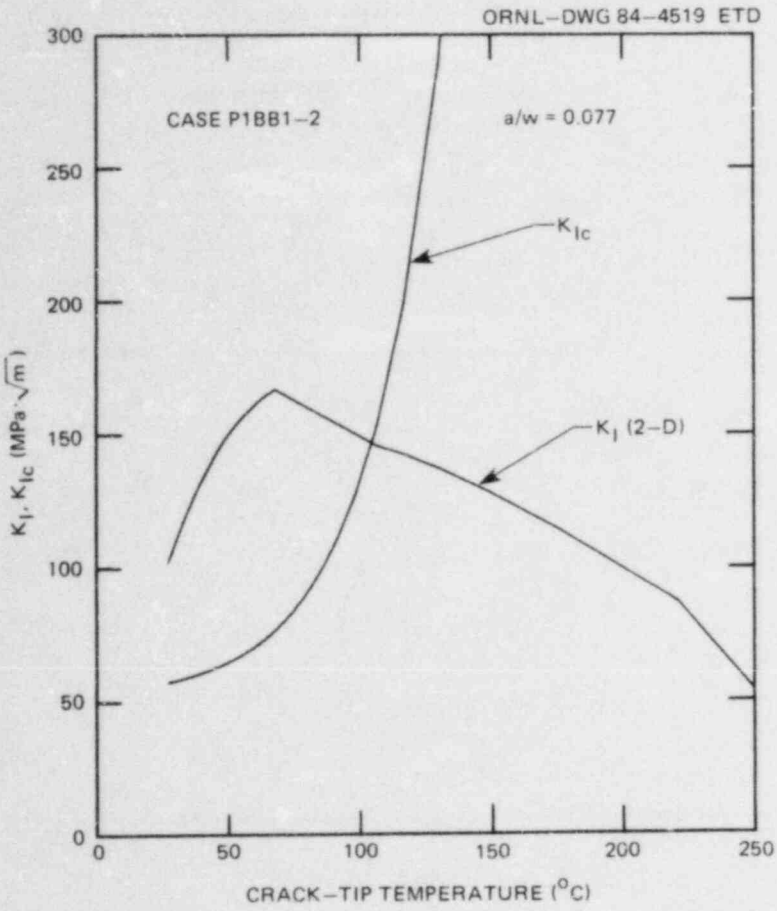

Fig. 10.18. K_I and K_{Ic} vs T for a/w = 0.077 from PTSE-1B pretest analysis.

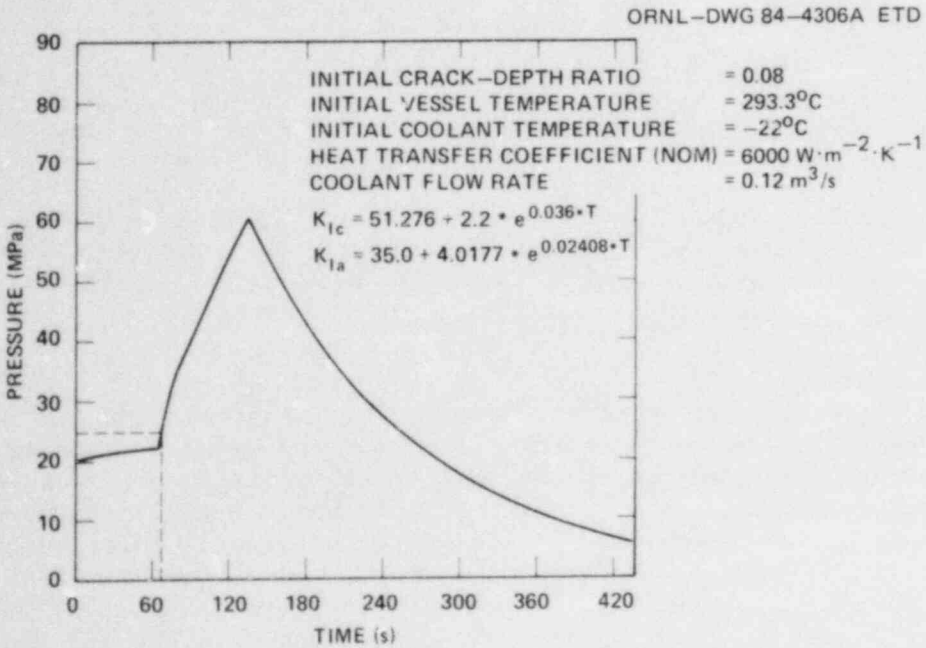

Fig. 10.19. Actual PTSE-1B pressure transient and other test parameters.

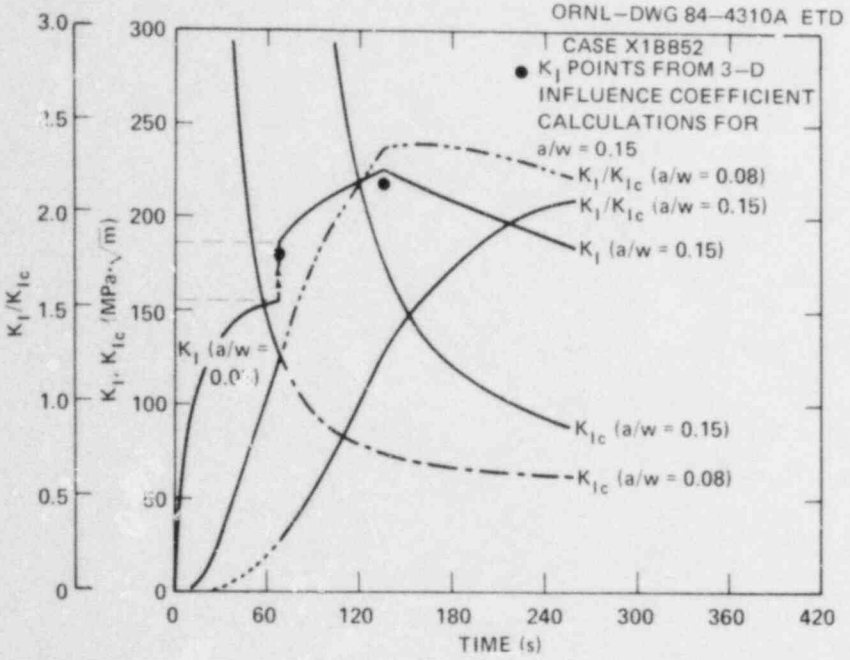

Fig. 10.20. Results (parameters vs time) of the posttest OCA/USA analysis of PTSE-1B. Values are computed from measured temperatures (thimble 5) and pressures. K_I and K_I/K_{Ic} curves are based on 2-D calculations.

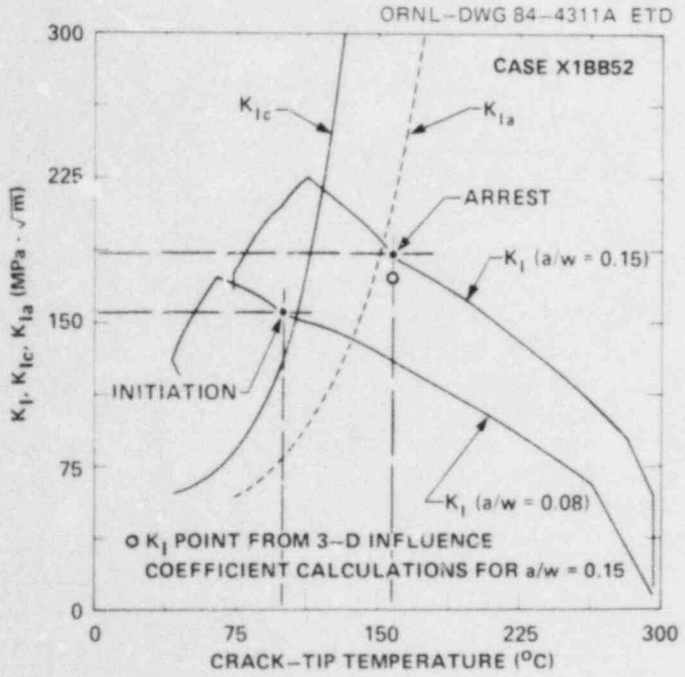

Fig. 10.21. Results (parameters vs T) of posttest OCA/USA analysis of PTSE-1B. K_I curves are 2-D.

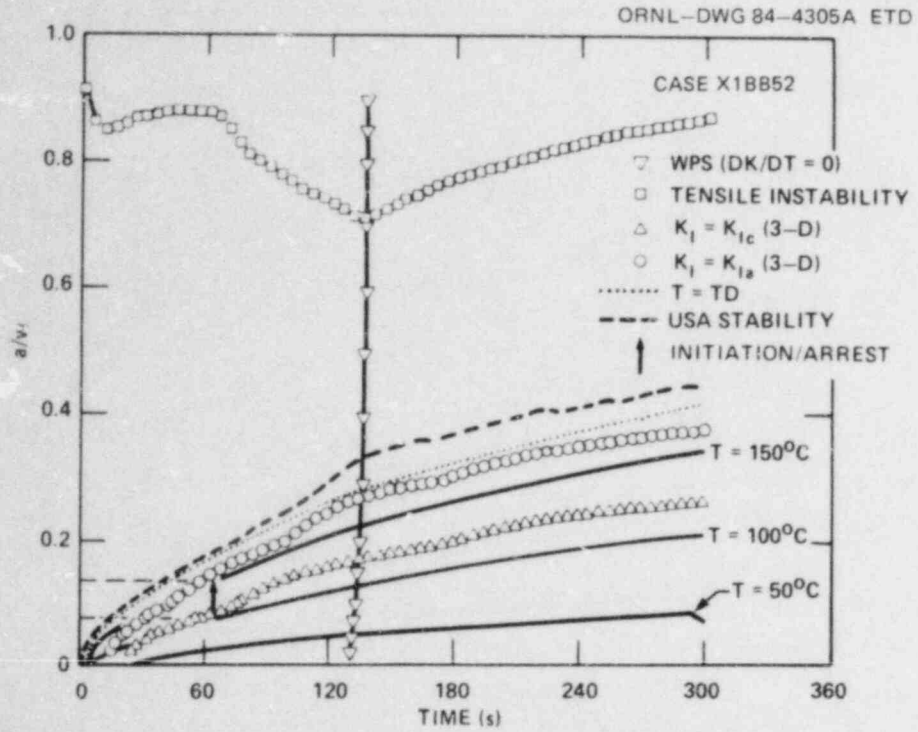

Fig. 10.22. Results (critical-crack-depth loci) of posttest OCA/USA analysis of PTSE-1B. Initiation and arrest loci are computed from 3-D influence coefficients. Note that an arrested crack with a/w = 0.15 should have reinitiated by a small margin, but crack-tip temperature is high in transition (~120°C when $K_I = K_{Ic}$).

10.4.3 Test PTSE-1C

The plans for PTSE-1C were made on the basis of heat transfer performance demonstrated in PTSE-1B. The thermal transient in the B test was satisfactory for promoting crack propagation in the C test to the upper-shelf temperature range (T > 150°C). However, the intermediate crack was warm prestressed to a K_I level of ~215 MPa·$\sqrt{m}$, which necessitated that a higher value be attainable in PTSE-1C. Accordingly, a pressure transient to 90 MPa (~1.3 × design pressure) was planned (Fig. 10.7, curve C). As indicated in Fig. 10.24, the pretest analysis predicted a single crack jump to an a/w ≈ 0.23 at t ≈ 105 s.

Results of the actual transient are shown in Figs. 10.25–10.28. The crack jumped at t = 125 s to a depth of 36.9 mm (a/w = 0.25). K_I values at initiation and arrest were ~221 and 265 MPa·$\sqrt{m}$, respectively. The crack-tip temperature at the time of arrest was 168°C, which is ~20 K above the onset of the Charpy upper shelf as indicated by 100% shear fracture appearance.

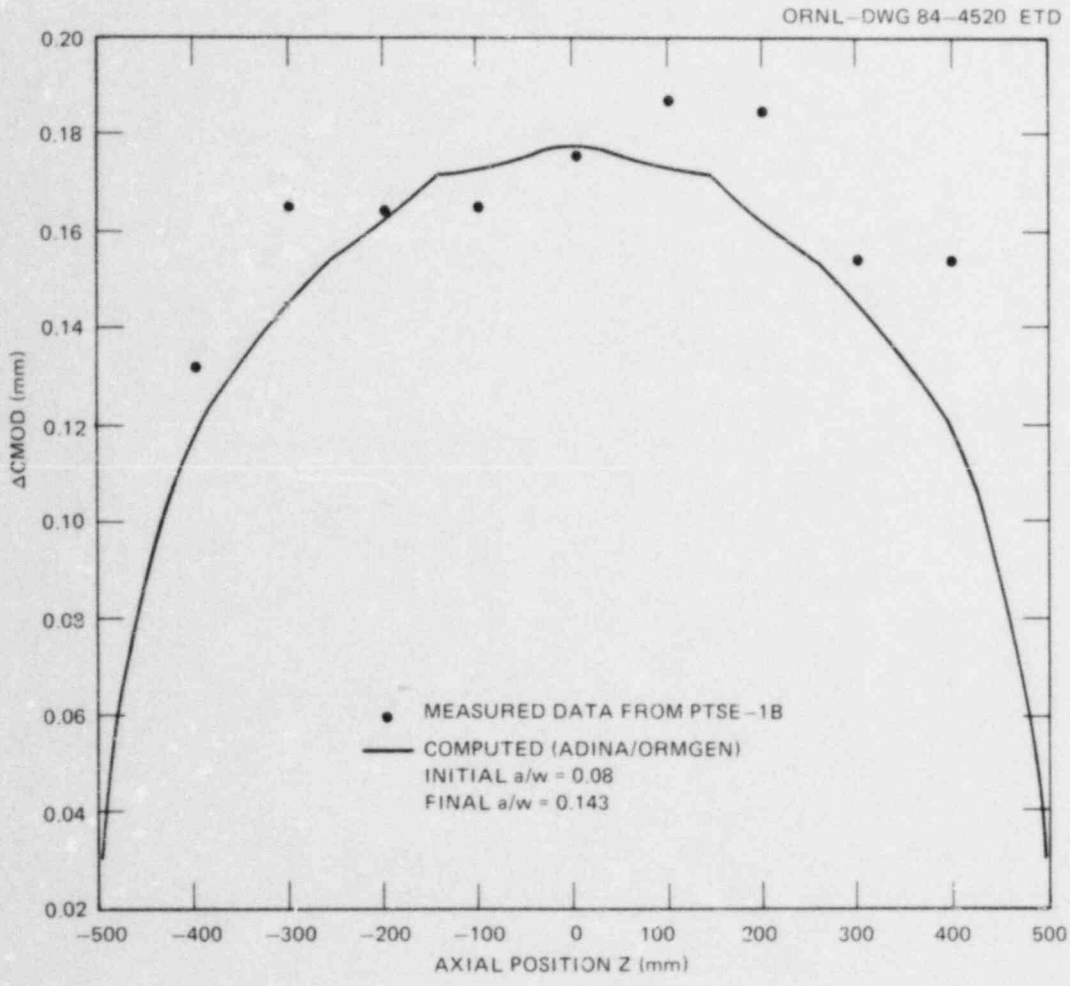

Fig. 10.23. ΔCMOD vs axial position along crack front at time of crack initiation in test PTSE-1B. Z = 0 at center of initial flaw.

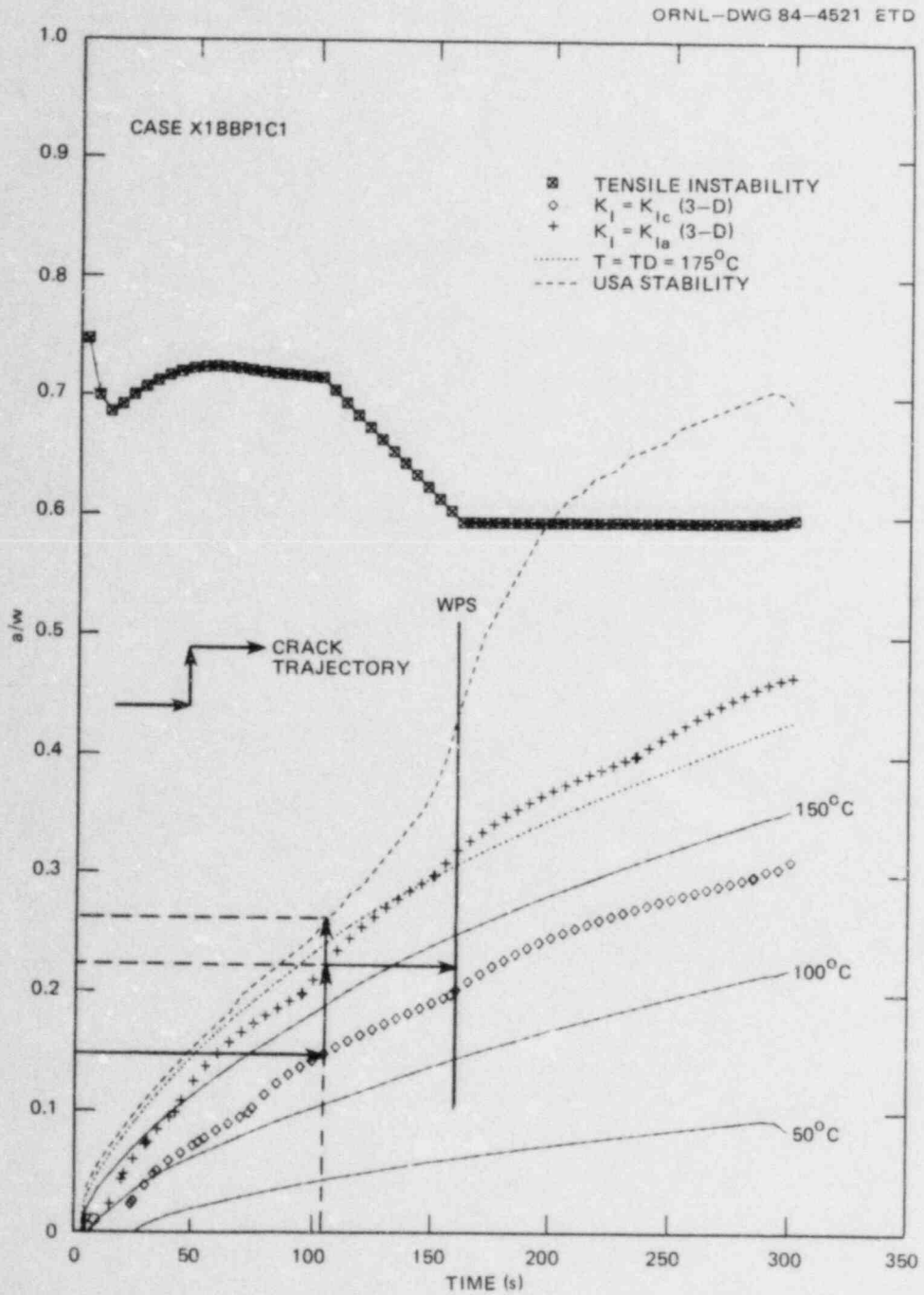

Fig. 10.24. Critical-crack-depth loci from PTSE-1C pretest analysis. Initiation, arrest, and upper-shelf stability loci are computed from 3-D influence coefficients.

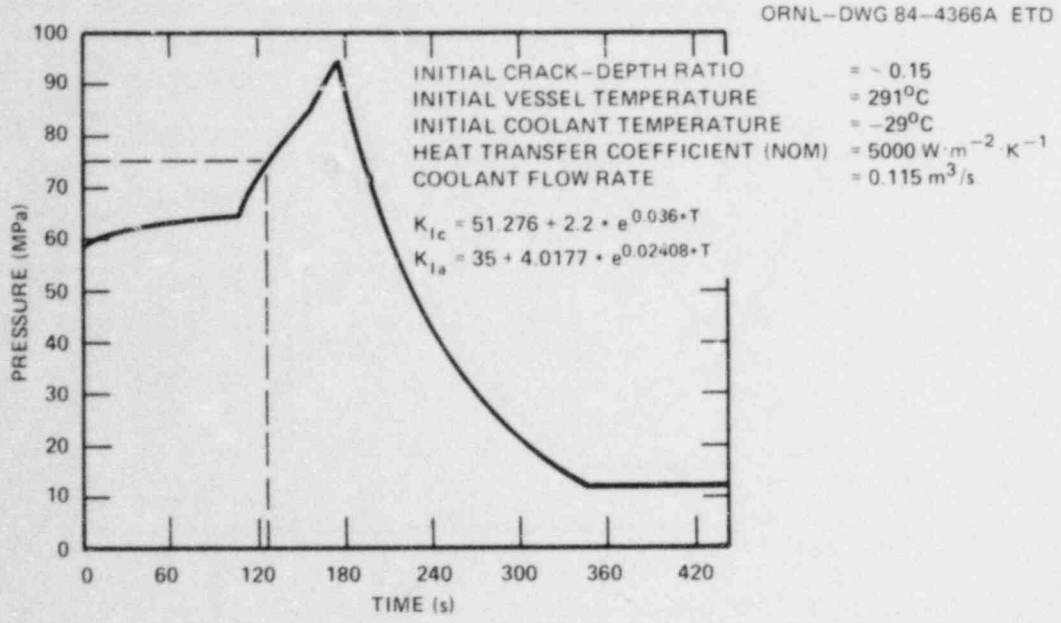

Fig. 10.25. Actual PTSE-1C pressure transient and other test parameters.

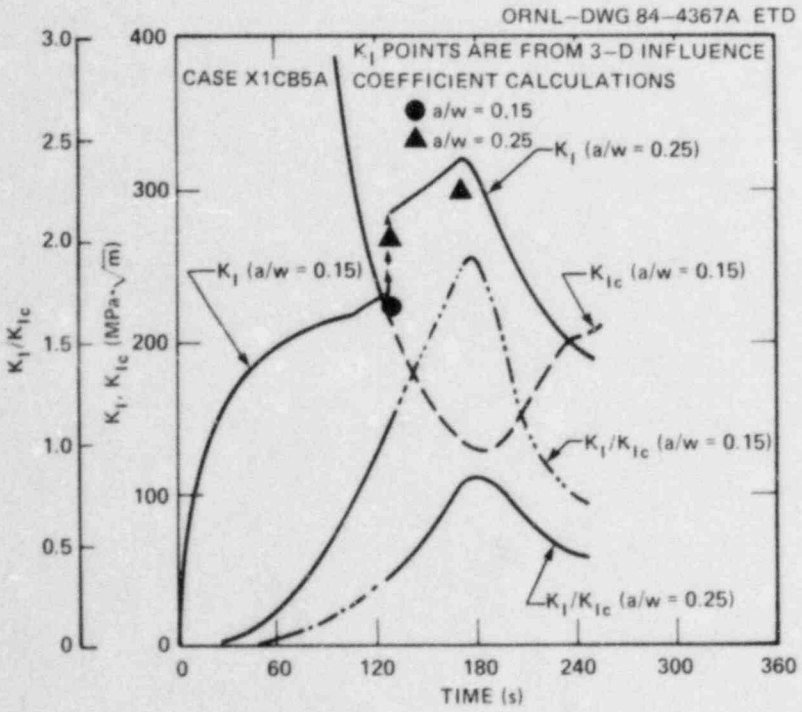

Fig. 10.26. Results (parameters vs time) of the posttest OCA/USA analysis of PTSE-1C. Values are computed from measured temperatures (thimble 5) and pressures. K_I and K_I/K_{Ic} curves are based on 2-D calculations.

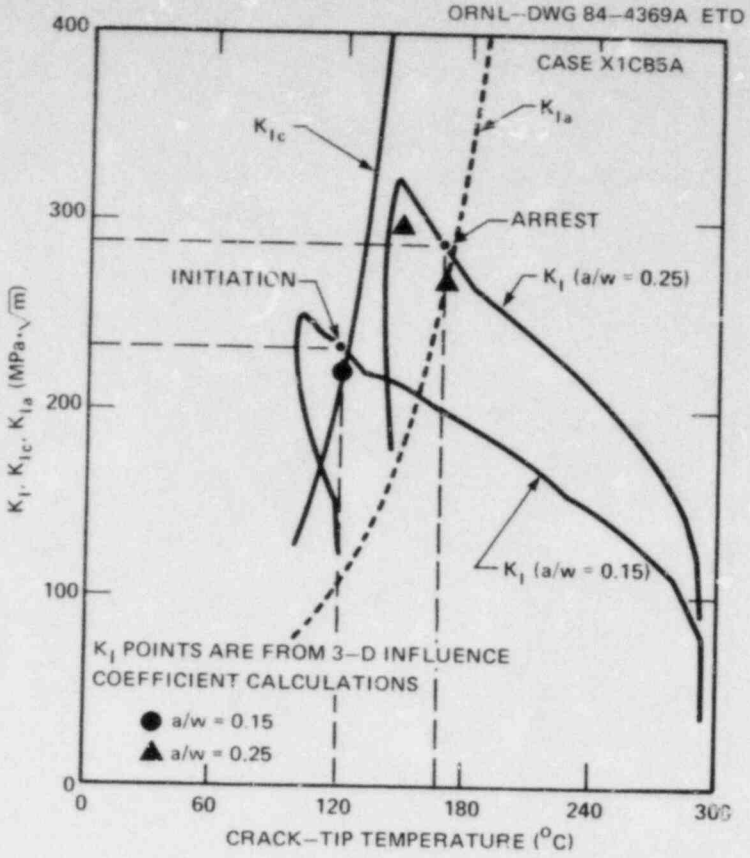

Fig. 10.27. Results (parameters vs T) of posttest OCA/USA analysis of PTSE-1C. K_I curves are 2-D.

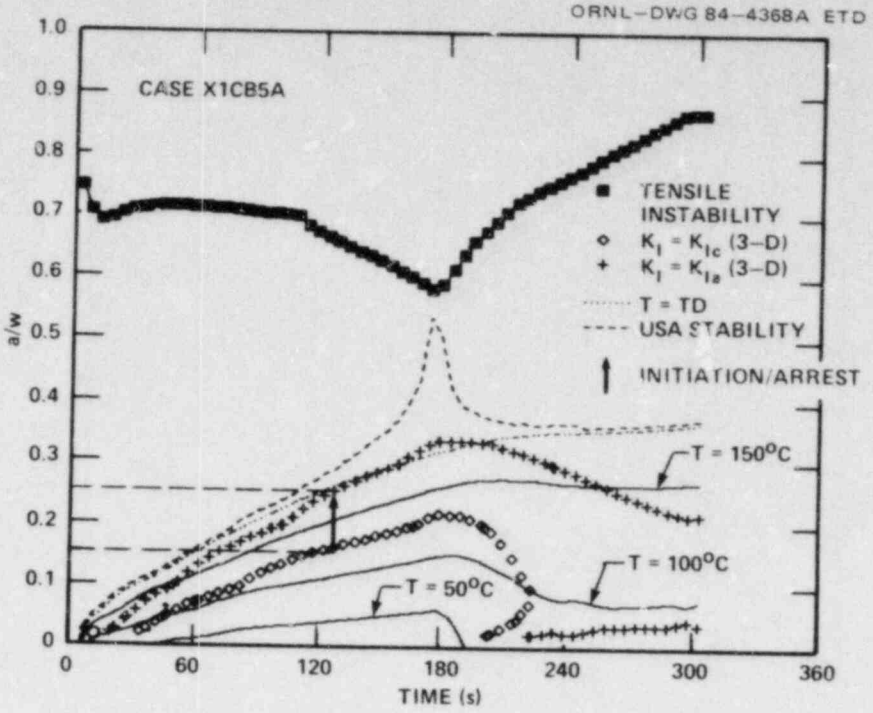

Fig. 10.28. Results (critical-crack-depth loci) of posttest OCA/USA analysis of PTSE-1C. Initiation, arrest, and upper-shelf stability loci are computed from 3-D influence coefficients.

10.5 Conclusions

Three PTS sequences were imposed on the flawed PTSE-1 vessel. In the first, PTSE-1A, the 1-m-long initial crack experienced three periods of WPS (in the sense that $\dot{K}_I < 0$) and two periods of anti-WPS ($\dot{K}_I > 0$), whereas K_I was greater than K_{Ic}. In the subsequent sequence (PTSE-1B), before the crack propagated, the K_I level was raised about 13% above the maximum K_I attained previously. This seems to imply that, after WPS has occurred, the conditions $K_I > K_{Ic}$ and $\dot{K}_I > 0$ are not sufficient to initiate cleavage crack propagation.

PTSE-1B and -1C produced two pairs of K_{Ic} and K_{Ia} values. Both arrest events occurred in a positive K_I gradient. The values appear to be reasonably close to K_{Ic} and K_{Ia} curves based on small specimen data; however, the values indicated in this report are subject to adjustments for sensor calibrations, 3-D analysis, and actual crack depth.

An arrest in the Charpy upper-shelf temperature range — one of the principal objectives of the test — was achieved. If posttest examination of the fracture surface confirms the final arrested crack depth inferred from test data, the determination of K_{Ia} from this event would be a rare measurement of crack-arrest toughness, perhaps the only one at a Charpy upper-shelf temperature.

The K_{Ic} and K_{Ia} values inferred from PTSE-1 are summarized in Fig. 10.29 and compared with the curves from Figs. 10.1 and 10.2 based on small specimen data and with the *ASME Code* Sect. XI values. Although K_I at the time of crack arrest in PTSE-1B was below the Sect. XI limit (220 MPa$\cdot\sqrt{m}$), the crack arrested in PTSE-1C at ~265 MPa$\cdot\sqrt{m}$.

The Sect. XI curves are for an RT_{NDT} = 91.3°C, which is the value determined from the PTSE-1 Charpy and drop-weight data in accordance with a strict interpretation of Sect. III of the Code.

Visual inspection of the vessel shows that the initial flaw grew axially at each end by ~120 mm. The extension near the hemispherical head of the vessel was bifurcated at the end of the initial flaw. Test data show that all axial extensions were concurrent with the crack jump in the PTSE-1B test. A posttest ultrasonic scan of the flaw indicates that the flaw is 30 to 40 mm deep over ~80% of the length and shallower (~20 mm) nearest the hemispherical head. The flaw is being excised for fractographic examination.

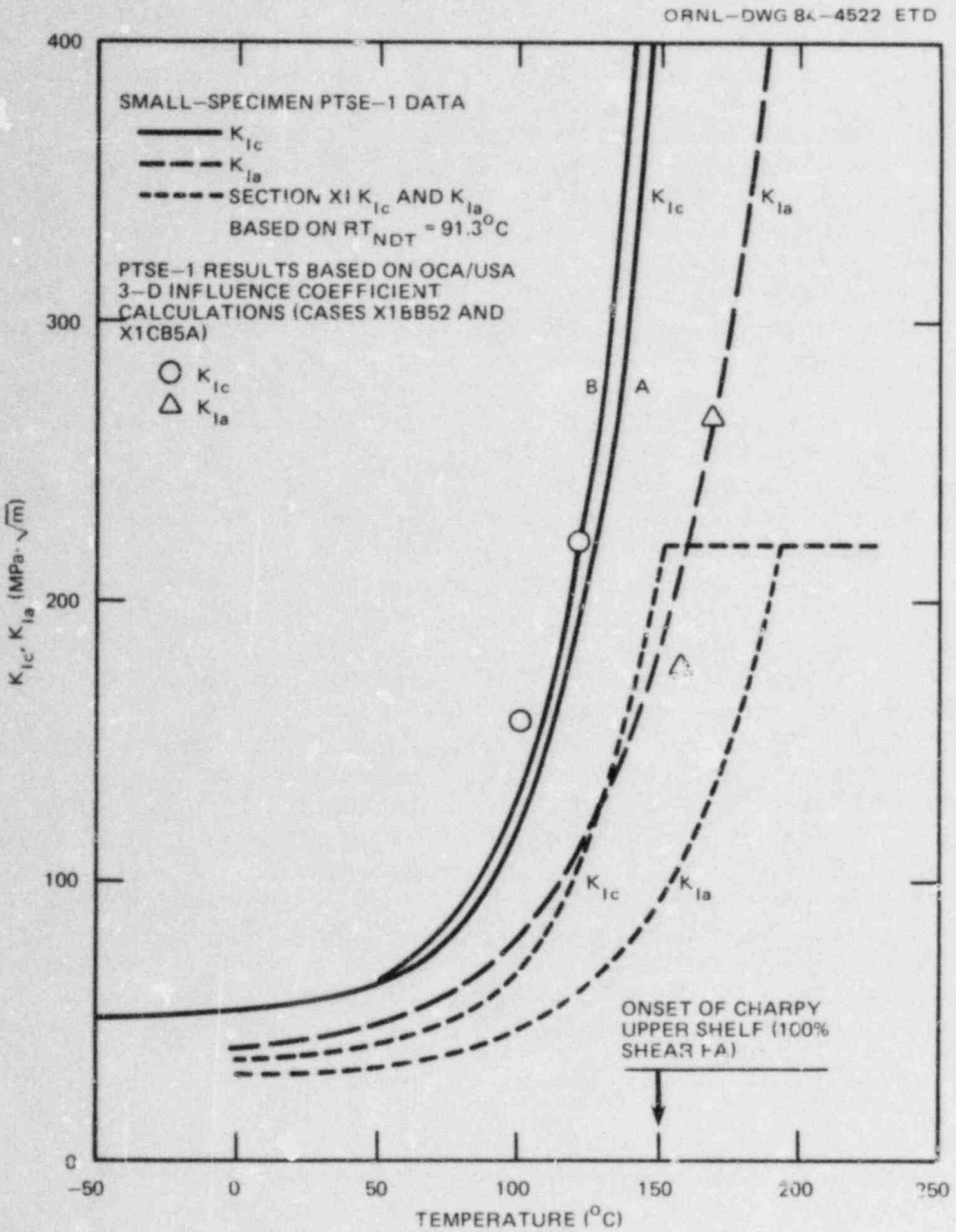

Fig. 10.29. Comparison of curves representing small-specimen K_{Ic} and K_{Ia} data with Sect. XI curves and results of PTSE-1 experiment. The 3-D values are generally lower than 2-D values shown elsewhere.

References

1. R. H. Bryan and R. W. McCulloch, "Pressurized-Thermal-Shock Studies, "*Heavy-Section Steel Technology Program Quart. Prog. Rep. October–December 1982,* NUREG/CR-2751, Vol. 4 (ORNL/TM-8369/V4), Union Carbide Corp. Nuclear Div., Oak Ridge Natl. Lab.

2. B. R. Bass, R. H. Bryan, and J. W. Bryson, "The OCA/USA Program for Analysis of PTS Experiments," *Heavy-Section Steel Technology Program Quart. Prog. Rep. July–September 1983,* NUREG/CR-3334, Vol. 3 (ORNL/TM-8787/V3), Union Carbide Corp. Nuclear Div., Oak Ridge Natl. Lab.

3. H. A. Domian, *Vessel V-7 and V-8 Repair and Characterization of Insert Material,* Research and Development Division of the Babcock & Wilcox Company, Alliance, Ohio (to be published).

4. R. H. Bryan, S. E. Bolt and G. C. Robinson, "Preparation for PTSE-1," *Heavy-Section Steel Technology Program Quart. Prog. Rep. July–September 1983,* NUREG/CR-3334, Vol. 3 (ORNL/TM-8787/V3), Union Carbide Corp. Nuclear Div., Oak Ridge Natl. Lab.

5. P. P. Holz, *Flaw Preparations for HSST Program Vessel Fracture Mechanics Testing: Mechanical Cyclic Pumping and Electron-Beam Weld-Hydrogen-Charge Cracking Schemes,* NUREG/CR-1274 (ORNL/NUREG/TM-369), Union Carbide Corp. Nuclear Div., Oak Ridge Natl. Lab., May 1980.

6. R. W. McCulloch, "PTS Test Facility Construction," *Heavy-Section Steel Technology Program Quart. Prog. Rep. April–June 1983,* NUREG/CR-3334, Vol. 2 (ORNL/TM-8787/V2), Union Carbide Corp. Nuclear Div., Oak Ridge Natl. Lab.

7. R. W. McCulloch, "PTSE Vessel Instrumentation," *Heavy-Section Steel Technology Program Quart. Prog. Rep. July–September 1983,* NUREG/CR-3334, Vol. 3 (ORNL/TM-8787/V3), Union Carbide Corp. Nuclear Div., Oak Ridge Natl. Lab.

CONVERSION FACTORS[a]

SI unit	English unit	Factor
mm	in.	0.0393701
cm	in.	0.393701
m	ft	3.28084
m/s	ft/s	3.28084
kN	lb_f	224.809
kPa	psi	0.145038
MPa	ksi	0.145038
$MPa \cdot \sqrt{m}$	$ksi \cdot \sqrt{in.}$	0.910048
J	ft·lb	0.737562
K	°F or °R	1.8
kJ/m^2	$in.\text{-}lb/in.^2$	5.71015
$W \cdot m^{-2} \cdot K^{-1}$	$Btu/h\text{-}ft^2\text{-}°F$	0.176110
kg	lb	2.20462
kg/m^3	$lb/in.^3$	3.61273×10^{-5}
mm/N	$in./lb_f$	0.175127
$T(°F) = 1.8\ T(°C) + 32$		

[a]Multipiy SI quantity by given factor to obtain English quantity.

NUREG/CR-3744
Volume 1
ORNL/TM-9154/V1
Dist. Category RF

Internal Distribution

1. D. G. Ball
2. B. R. Bass
3. R. G. Berggren
4. S. E. Bolt
5. R. H. Bryan
6. J. W. Bryson
7. R. D. Cheverton
8. J. M. Corum
9. W. R. Corwin
10. D. P. Edmonds
11. D. M. Eissenberg
12-13. D. S. Griffith
14. R. C. Gwaltney
15. S. K. Iskander
16. K. K. Klindt
17. A. P. Malinauskas
18. S. S. Manson
19. R. W. McCulloch
20. J. J. McGowan
21. J. G. Merkle
22-23. R. K. Nanstad
24. D. J. Naus
25-28. C. E. Pugh
29. G. C. Robinson
30. J. W. Roddy
31. G. M. Slaughter
32. J. E. Smith
33. R. W. Swindeman
34. K. R. Thoms
35. H. E. Trammell
36. C. D. West
37-40. G. D. Whitman
41. G. T. Yahr
42. ORNL Patent Office
43. Central Research Library
44. Document Reference Section
45-46. Laboratory Records Department
47. Laboratory Records (RC)

External Distribution

48. C. Z. Serpan, Division of Engineering Technology, Nuclear Regulatory Commission, Washington, DC 20555
49. M. Vagins, Division of Engineering Technology, Nuclear Regulatory Commission, Washington, DC 20555
50. Office of Assistant Manager for Energy Research and Development, DOE, ORO, Oak Ridge, TN 37831
51-52. Technical Information Center, DOE, Oak Ridge, TN 37831
53-327. Given distribution as shown in category RF (NTIS – 10)

NRC FORM 335 (11-81)

U.S. NUCLEAR REGULATORY COMMISSION

BIBLIOGRAPHIC DATA SHEET

1. REPORT NUMBER *(Assigned by DDC)*
NUREG/CR-3744, Vol. 1
ORNL/TM-9154/V1

4. TITLE AND SUBTITLE *(Add Volume No., if appropriate)*
Heavy-Section Steel Technology Program Semiannual Progress Report for October 1983–March 1984

2. *(Leave blank)*

3. RECIPIENT'S ACCESSION NO.

7. AUTHOR(S)
C. E. Pugh

5. DATE REPORT COMPLETED
MONTH: May | YEAR: 1984

9. PERFORMING ORGANIZATION NAME AND MAILING ADDRESS *(Include Zip Code)*
Oak Ridge National Laboratory
P.O. Box X
Oak Ridge, TN 37831

DATE REPORT ISSUED
MONTH: June | YEAR: 1984

6. *(Leave blank)*

8. *(Leave blank)*

12. SPONSORING ORGANIZATION NAME AND MAILING ADDRESS *(Include Zip Code)*
Division of Engineering Technology
Office of Nuclear Regulatory Research
U.S. Nuclear Regulatory Commission
Washington, DC 20555

10. PROJECT/TASK/WORK UNIT NO.

11. FIN NO.
B0119

13. TYPE OF REPORT
Semiannual

PERIOD COVERED *(Inclusive dates)*
October 1983 through March 1984

15. SUPPLEMENTARY NOTES

14. *(Leave blank)*

16. ABSTRACT *(200 words or less)*

The Heavy-Section Steel Technology (HSST) Program is an engineering research activity conducted by the Oak Ridge National Laboratory for the Nuclear Regulatory Commission. The program comprises studies related to all areas of the technology of materials fabricated into thick-section primary-coolant containment systems of light-water-cooled nuclear power reactors. The investigation focuses on the behavior and structural integrity of steel pressure vessels containing cracklike flaws. Current work is organized into ten tasks: (1) program management, (2) fracture-methodology and analysis, (3) material characterization and properties, (4) environmentally assisted crack growth studies, (5) crack arrest technology, (6) irradiation effects studies, (7) cladding evaluations, (8) intermediate vessel tests and analysis, (9) thermal-shock technology, and (10) pressurized thermal-shock technology.

17. KEY WORDS AND DOCUMENT ANALYSIS

17a. DESCRIPTORS

Pressure vessels
Ferritic steels
Weldments
Irradiation
Cladding
Flaws
Thermal shock
Fracture mechanics
Toughness
Crack arrest
Crack growth

17b. IDENTIFIERS/OPEN-ENDED TERMS

18. AVAILABILITY STATEMENT
Unlimited

19. SECURITY CLASS *(This report)*
Unclassified

21. NO. OF PAGES

20. SECURITY CLASS *(This page)*
Unclassified

22. PRICE
$